UNIVERSITY OF BARCELONA

Faculty of Earth Sciences

Department of Mineralogy, Petrology and Applied Geology

Geochemistry of rare earth elements in acid mine drainage precipitates

Thesis presented by

Alba Lozano Letellier

To obtain the degree of Doctor in Earth Sciences

Work conducted at the Institute of Environmental Assessment and Water Research (IDAEA-CSIC) under the supervision of

Dr. Carlos Ayora Ibáñez
IDAEA-CSIC

Dr. Alejandro Fernández Martínez
CNRS- Grenoble Alpes

Barcelona, September 2019

This thesis has been funded by the Ministry of Economy and Competitiveness with a FPI (Ayuda a Formación Personal Investigador) grant (BES- 2014-069978). The internships in Grenoble, France have been funded by the Ministry grants (EEBB-I-16-10975; EEBB-I-17-12025) and the "Make Our Planet Great Again" short-stay program. This work has also been funded by the European EIT "Morecovery" and the Spanish EMPATIA (CGL2013-48460-C2-2-R) and SCYRE (CGL2016-468 78783-C2-R) projects.

A mis padres Anastasio y Ana

A mi abuela Antonia

Acknowledgments/Agradecimientos

Una vez finalizada la tesis, quiero dar las gracias a todas las personas que en mayor o menor medida habéis puesto vuestro granito de arena a que este trabajo viera la luz y a que el paseo recorrido durante este tiempo haya merecido la pena.

Quiero empezar danto las gracias a Carlos, por la oportunidad que me brindó para hacer la tesis con él en Barcelona y por abrirme las puertas al mundo científico, y en concreto a la geoquímica, que sin duda es apasionante, a pesar de mi lucha constante en entenderla. Gracias por tu paciencia infinita, tu cercanía y confianza, que han hecho que todo el trabajo fuera más fácil y que sin tu ayuda esta tesis no habría salido adelante.

Quiero dar las gracias a Alex, porque sin dudarlo aceptó tomar las riendas de la parte de la tesis dedicada a experimentos de sincrotrón, y que sin su ayuda tampoco hubiera sido posible sacar adelante esta parte del trabajo. Gracias por abrirme las puertas del haz de electrones, a ese mundo apasionante de la física/química, de la espectroscopía… Gracias por haberme acogido en Grenoble y en el ISTerre.

Quiero dar las gracias a Jordi Bellès por las infinitas horas invertidas ayudándome en los experimentos de laboratorio y por su incansable ayuda, a Mercè Cabañas y Rafa Bartrolí, por todos los análisis de ICP que han hecho de los experimentos de laboratorio, y a Natalia Moreno, por su constante búsqueda de "bandas" y no picos en los difractogramas de rx de tantas muestras que le he pasado.

Y qué decir de los compañeros del IDAEA. Sin ellos nada hubiera sido igual desde que llegué a Barcelona, donde apenas conocía a gente. En estos años han pasado muchas personas de las que tengo muy buenos recuerdos, con unos más de monte y con otros más de tapeo y birras: Alex Serrano, Bayra, Mar, Alessandro, Silvia, Thomas, Sheila, Berta, Yoar, Laura S., MA, Tibaud, Alec, Vivien, Quim, Rotman, Jordi, Sonia, Jingjing, Nacho, Lidia, Robert, Ashkan, Max…

Y de Barcelona me voy a Grenoble, mi segunda casa durante la tesis, ya que durante los tres primeros años he hecho una estancia de varios meses por año. Quiero recordar en especial a Rosemarie, Rubén, Gökhan, Ariana y Rodrigo,

que de ser compañeros de piso o curro se han convertido en buenos amigos. A mi querido grupo de “españoles del ESRF” aunque no todos trabajarais allí: Edu, María, Ana, Pablo, Javilón, Aída, Rosalía, Antonio, Willy... Por último, pero no menos importante a tanta gente del ISTerre con la que he compartido horas de laboratorio y/o cafetería: Hugo, Jorge, Claudia, Bin, Ayumi, Nishant, Zhanar, Sander, Mapi, Sara, Luis, Rogier, Matthias…

Y desde Grenoble quiero mandar un saludo y mi agradecimiento a todas aquellos técnicos e investigadores que de algún modo han puesto su granito de arena en esta tesis en momentos de laboratorio, horas de sincrotrón y aportación en los artículos, algunos de ellos coautores: Sarah Bureau, Valerie Magnin, Nathaniel Findling, Agnieszka Poulain, Mauro Rovezzi, Carlo Marini y Devis di Tomasso.

Gracias a mis amigas de toda la vida, Cristina y María, por tener esta tesis tan presente, por vuestros ánimos constantes y por la suerte de haberos tenido, aunque en diferentes tiempos, en Barcelona o cerca de aquí. Gracias a todos los colegas que en cualquier momento me ha mandado ánimos para que continuara hasta el final y perdón a los que no menciono aunque sé que habéis estado ahí.

Gracias a mi familia, y en especial a mis padres y a mi hermano, por estar siempre apoyándome, animándome a no tirar la toalla y a escucharme en todo momento. Gracias por estar siempre ahí y por confiar en mí.

Gracias a Samuel, por tu cariño, tus ánimos, por escucharme siempre, por la confianza que siempre tienes en mí, y por esperarme. A pesar de la distancia y de lo duro que se ha hecho, aquí seguimos, y que sea por muchos años.

Table of contents

List of figures

List of tables

Abstract

Rare earth elements (REE) are known as the lanthanide series (La-Lu) plus yttrium (Y) and scandium (Sc). REE are essential materials for modern industries and especially for green technologies (wind turbines, batteries, lasers, catalysts, etc.). However, despite their high global demand, their supply is limited such that the EU has cataloged it as critical raw materials. In order to ensure the supply of REE in the future, the search for alternative sources of these elements worldwide has been promoted in recent years.

Acid mine drainage (AMD) produced by the Fe-sulphide weathering can effectively leach Fe, Al, SO_4, and REE from the host rock. This can lead to high concentrations of these liberated species in the affected waters. Thus, the REE concentrations in AMD can be between two and three orders of magnitude higher than natural waters, as such it can be considered as a complementary source of REE recovery. The increase of pH in AMD by mixing of neutral waters results in the precipitation of iron oxy-hydroxysulfate (schwertmannite) from pH 3-3.5, and aluminum oxy-hydroxysulfate (basaluminite) from pH 4-4.5 in the river channels, process which may be accompanied by REE scavenging.

Due to its acidity and high metal load, acid mine drainage presents a major environmental problem worldwide, therefore, different treatment systems have been developed to minimize its impact. Disperse Alkaline Substrate (DAS) passive remediation system neutralizes AMD by dissolving calcite, and allowing the sequential precipitation of schwertmannite and basaluminite in separated layers, where REE are preferably retained in the basaluminite-enriched waste. Despite this, there are still no studies describing the retention of REE on both basaluminite and schwertmannite in these environments.

The REE scavenging mechanism is studied by adsorption on synthetic minerals of basaluminite and schwertmannite as a result of variation to the both the pH and sulfate concentration. A thermodynamic adsorption model is proposed based on experimental results in order to predict and explain the

REE mobility in AMD mixtures with neutral waters and in a passive treatment system.

Basaluminite and schwertmannite have a nanocrystalline character. Further, schwertmannite has been observed to transform into goethite on weekly timescales, resulting in sulfate release. However, there is a gap of knowledge about basaluminite stability at variable sulfate concentration and pH and its possible transformation to other more crystalline Al-minerals. Basaluminite local order at different pH values and dissolved sulfate concentrations was characterized. The results demonstrate that basaluminite can transform to nanoboehmite in weeks under circumneutral pH values. However, the presence of sulfate can inhibit this transformation.

Separate adsorption experiments on both basaluminite and schwertmannite were performed with two different concentrations of SO_4 while varying the pH (3-7). Results show that the adsorption is strongly dependent on pH, and to a lesser extent on sulfate concentration. Lanthanide and yttrium adsorption is most effective near pH 5 and higher, while that of scandium begins around pH 4. Due to the high concentrations of sulfate in acidic waters, the predominant aqueous REE species are sulfate complexes (MSO_4^+). Notably, $Sc(OH)^{2+}$ represents a significant proportion of aqueous Sc. A surface complexation model is proposed in which predominant aqueous species (M^{z+}) adsorb on the mineral surface, XOH, following the reaction:

$$M^{z+} + nXOH = (XO)_nM^{z-n} + nH^+$$

The adsorption of the lanthanides and yttrium occurs through the exchange of one and two protons from the basaluminite and schwertmannite surface, respectively, with the aqueous sulfate complexes. The sorbed species form monodentate surface complexes with the aluminum mineral and bidentate with the iron mineral. In the case of Sc, the aqueous species $ScSO^{4+}$ and $Sc(OH)^{2+}$ form bidentate surface complexes with both minerals. EXAFS analysis of the YSO_4^+ complex adsorbed on the basaluminite surface suggests the formation of a monodentate inner sphere complex, in agreement with the proposed thermodynamic model.

Once the surface complexation model was validated, it was used to assess and predict the REE mobility in passive remediation systems and acidic water mixing zones with alkaline inputs from the field. The REE are preferentially retained in basaluminite-rich waste during passive remediation due to its sorption capacity between pH 5-6. In contrast, schwertmannite waste contains very little REE because the formation of this mineral occurs at pH lower than 4,

preventing REE adsorption. Further, Sc may be scavenged during schwertmannite precipitation as a result of this low pH

The model correctly predicts the absence of REE in schwertmannite precipitates and the enrichment of the heavy and intermediate REE with respect to the light REE in basaluminite precipitates collected in the water mixing zones. However, it cannot predict quantitatively the fractionation of rare earths in basaluminite precipitate. This inaccuracy is mainly due to the fact that the mineral precipitation and adsorption are not synchronous process, while basaluminite precipitates from pH 4, REE adsorption may occur at higher pH values, between 5 and 7, when the water mixture reaches these values and a fraction of the particles have been dispersed.

Resumen

Las tierras raras (en inglés *rare earth elements*, REE) son conocidas como el conjunto de la serie de los lantánidos (La-Lu), itrio (Y) y escandio (Sc). Las tierras raras son materiales indispensables para las industrias modernas y en especial para las tecnologías verdes (aerogeneradores, baterías, láseres, catalizadores, etc.). Sin embargo a pesar de su gran demanda mundial, su abastecimiento es limitado, por lo que han sido catalogadas por la UE como materias primas críticas (Critical Raw Materials). Con el objetivo de asegurar el abastecimiento de REE en el futuro, en los últimos años se ha promovido la búsqueda de fuentes alternativas de estos elementos en todo el mundo.

El drenaje ácido de mina (en inglés *acid mine drainage*, AMD) producido por la meteorización de sulfuros de Fe, tiene un alto poder de lixiviación de las rocas, por lo que las aguas afectadas adquieren elevadas concentraciones en disolución de Fe, Al, SO_4 y otros metales, como las REE. Así, las concentraciones de REE en AMD son entre dos y tres órdenes de magnitud superiores al resto de las aguas naturales y pueden suponer una fuente complementaria de recuperación de REE. El aumento de pH del AMD por mezcla con aguas neutras da lugar a la precipitación en los cauces de los ríos de oxy-hidroxisulfatos de hierro (schwertmannita), a partir de pH 3-3.5, y de aluminio (basaluminita), a partir de pH 4-4.5; acompañado de la eliminación de las tierras raras. Debido a su acidez y carga metálica, el drenaje ácido de mina presenta un problema medioambiental de primera magnitud, por lo que se han desarrollado diferentes sistemas de tratamiento para minimizar su impacto. El sistema de tratamiento pasivo *Disperse Alkaline Substrate* (DAS) produce la neutralización de las aguas ácidas por la disolución de la calcita presente en el sistema, permitiendo la precipitación secuencial, de schwertmannita y basaluminita. Las tierras raras quedan retenidas preferentemente en el residuo enriquecido en basaluminita. A pesar de ello, aún no existen estudios que describan la

adsorción de tierras raras tanto en basaluminita como schwertmannita en estos ambientes.

En esta tesis se estudia el mecanismo de retención de las tierras raras mediante adsorción en minerales sintéticos de basaluminita y schwertmannita, en función del pH y del contenido de sulfato disuelto. Con los resultados experimentales obtenidos, se propone un modelo termodinámico de adsorción para predecir y explicar la movilidad de las tierras raras observada en mezclas de AMD con aguas neutras y en un sistema de tratamiento pasivo.

La basaluminita y la schwertmannita presentan un carácter nanocristalino. Es conocido que la schwertmannita se transforma en goethita en semanas, liberando sulfato. Sin embargo, nada se sabe de la basaluminita y su posible transformación a otros minerales de Al más cristalinos. De este modo, la caracterización del orden local de la basaluminita a diferentes valores de pH y sulfato se expone en primer lugar. Dependiendo del pH y el sulfato en disolución, la basaluminita se transforma en diferentes grados a nanoboehmita en semanas, pero tiende a estabilizarse con la presencia de sulfato en solución.

Los experimentos de adsorción en basaluminita y schwertmannita con diferentes concentraciones de SO_4 realizados para cada mineral y en rangos de 3-7 de pH han demostrado que la adsorción es fuertemente dependiente del pH, y en menor medida del sulfato. La adsorción de los lantánidos y del itrio es efectiva a pH 5, mientras que la del escandio comienza a pH 4. Debido a las altas concentraciones de sulfato en aguas ácidas, las especies acuosas predominantes de las tierras raras son los complejos con sulfato, MSO_4^+. Además del complejo sulfato, el Sc presenta importantes proporciones de $Sc(OH)^{2+}$ en solución. En función de la dependencia del pH y de la importancia de la especiación acuosa, se propone un modelo de complejación superficial donde la especie acuosa predominante (M^{z+}) se adsorbe a la superficie libre el mineral, XOH, cumpliendo la siguiente reacción:

$$M^{z+} + nXOH = (XO)_n M^{z-n} + nH^+$$

La adsorción de los lantánidos y del itrio se produce a través del intercambio de uno o dos protones de la superficie de la basaluminita o de la schwertmannita, respectivamente, con los complejos sulfato acuoso, formando complejos superficiales monodentados con el mineral de aluminio y bidentados con el de hierro. En el caso del Sc, las especies acuosas $ScSO_4^+$ y $Sc(OH)^{2+}$ forman complejos superficiales bidentados con ambos minerales. Complementando el modelo propuesto, el análisis de EXAFS del complejo YSO_4^+ adsorbido en la superficie basaluminita sugiere la formación de un

complejo monodentado de esfera interna, coincidiendo con el modelo termodinámico propuesto.

El modelo de complejación superficial, una vez validado, ha permitido evaluar y predecir la movilidad de REE en los sistemas de tratamiento pasivos y en zonas de mezcla de aguas ácidas con aportes alcalinos estudiados en el campo. La preferente retención de las tierras raras en la zona de la basaluminita precipitada en los sistemas de tratamiento pasivo ocurre por adsorción de las mismas a pH entre 5-6. La ausencia de tierras raras en la zona de schwertmannita se debe al bajo pH de su formación, inferior a 4, que impide la adsorción de las mismas. Sin embargo, una fracción de Sc puede quedar retenida en la schwertmannita debido a su adsorción a pH más bajos.

El modelo también predice correctamente la ausencia de REE en los precipitados de schwertmannita y el enriquecimiento de las tierras raras pesadas e intermedias respecto a las ligeras en los precipitados de basaluminita recogidos en el campo en las zonas de mezcla de aguas. Sin embargo, el modelo no puede predecir de forma cuantitativa el fraccionamiento de las tierras raras en los precipitados de basaluminita. Este hecho se debe principalmente a que la precipitación del mineral no ocurre de forma síncrona con la adsorción, precipitando la basaluminita a partir de pH 4 y adsorbiendo tierras raras a pH más altos, entre 5 y 7, cuando las partículas sólidas han sido parcialmente dispersadas.

1 Introduction

Lanthanide series (from La to Lu) plus scandium (Sc) and yttrium (Y) are referred to as Rare Earth Elements (REE) according to recommendation by the International Union of Pure and Applied Chemistry (Connelly et al., 2005). They occur in nature as trivalent species with the exception of Ce and Eu which can also appear as Ce^{4+} and Eu^{2+}. Lanthanides group can be arbitrarily divided into light (LREE: La to Nd), medium (MREE: Sm to Gd) and heavy (HREE: Tb to Lu). Due to it atomic size similarity, Y is often considered with HREE, whereas Sc has been commonly set aside the group by its small ionic radius. Their similar atomic structure and chemical properties as well as the small differences among the elements in the group have traditionally converted their partition between water and minerals as tracers of geochemical processes (Henderson, 1984; McLennan, 1989; Elderfield et al., 1990; Chakhmouradian and Wall, 2012, among many others). Beyond their importance as geochemical tracers, in the last two decades, there has been an increasing interest in REE due to their higher demand by modern technology and industry, such as manufacturing in permanent magnets, batteries, light emitting diodes and alloys, among other technological advancements. Their low supply due to limited REE mining to find new sources of these elements (Alonso et al., 2012; Hatch, 2012) and where China dominates more than 90% of worldwide production (U.S. Geological Survey (USGS), 2019) has led to consider REE as Critical Raw Materials, boosting searches for alternative sources of REE worldwide (Alonso et al., 2012; Hatch, 2012; Massari and Ruberti, 2013). Moreover, although REE have been considered of minor environmental concern, due to their common use in modern industry, some toxicological studies suggest that they could have a pathogenic potential (Zhuang et al, 1996; Dai et al., 2002; Pagano et al., 2015; Roncati et al., 2018). Therefore, knowing the mobility constraints of REE in natural waters, and particularly in AMD is a target of interest.

Acid Mine Drainage (AMD) is one of the most widespread pollution affecting watersheds and ecosystems (Nordstrom, 2011; Nordstrom et al., 2015). However, the REE concentrations in AMD, including Sc, are several orders of magnitude higher than the rest of surface waters and could be a future supplementary source of some highly valuable REE (Ayora et al., 2016; Stewart et al., 2017; Zhang and Honaker, 2018). AMD also contains high concentrations of toxic elements in addition to REE, and represents a very important environmental threat that requires remediation. In mine operations, the active treatments of AMD are mainly based on its neutralization with alkaline reagents, usually limestone, sodium carbonate or ammonia (Evangelou and Zhang, 1995; Coulton et al., 2003). This treatment produces high amounts of an sludge formed by a mixture of Fe(III) and Al-sulfate-hydroxides which disposal represents a major operating cost for coal and metal mining operations (Ackamn, 1982; Viadero et al., 2006). Differently, the passive remediation systems, which have been developed extensively in recent decades, allow the AMD neutralization generating lower amounts of solid waste precipitates by driving AMD through a permeable system filled with grained limestone (Hedin et al., 1994; Cravotta and Trahan, 1999; Ayora et al., 2013). Along the process, a sequential precipitation of mainly schwertmannite ($Fe_8O_8(OH)_6SO_4$) and basaluminite ($Al_4SO_4(OH)_{10}{\cdot}5H_2O$) waste occurs in differentiated layers (Caraballo et al., 2011). There, lanthanide and Y have been proved to be entirely retained in the basaluminite-enriched solid and nearly absent in Fe-enrich solids (Ayora et al., 2016; Zhang and Honaker, 2018). Therefore, likewise in natural attenuation of AMD affected waters, a detailed understanding of the mechanism responsible for selective REE scavenging by basaluminite and/or schwertmannite, is necessary. Moreover, the passive treatment systems can work for several months to years with a constant pH evolution, so potential transformation of the minerals can be expected. Schwertmannite transformation to goethite with time has well characterized (Cruz-Hernández et al., n.d.; Schwertmann and Carlson, 2005; Acero et al., 2006; Burton et al., 2008). Basaluminite has reported to coexist with nanocrystals of $Al(OH)_3$ in aluminum precipitates formed in pit lakes, that suggest basaluminite partial transformation to nanoboehmite or gibbsite (Sánchez-España et al., 2016). However, no studies regarding basaluminite stability are present in the literature. Thus, a detailed characterization of the stability of basaluminite at different solution pH values becomes essential previous to study sorption mechanisms.

The REE distribution pattern normalized to the North American Shale Composite (NASC) has been used to prove the impact of Acid Mine Drainage (AMD) in groundwater, rivers and estuarine environments (Vallejo et al., 2012;

Grawunder et al., 2014; Morgan et al., 2016; Bonnail et al., 2017; Li and Wu, 2017). It is generally recognized that the REE concentration in water is largely controlled by solid surface and aqueous solution chemistry (Quinn et al., 2006a; Quinn et al., 2006b and refences therein). Besides, REE fractionation between minerals and AMD has been studied since the early 1990s as rock weathering (Auqué et al., 1993; Gimeno et al., 1999) and in mining areas (Gammons et al., 2003). Verplanck et al. (2004) observed REE scavenging from AMD by hydrous ferric oxides as the pH increased to 5.1 due to the water mixing in two AMD streams. The authors attributed the REE removal to sorption onto Fe(III) precipitates. Similar REE behavior was detected by Gammons et al. (2005a) in a mountain stream affected by AMD. Samplings conducted in at three stations: upstream station (pH 3.3), intermediate (pH 5.5) and downstream (pH 6.8), showed that REE remained in solution in the two first stations. The removal at high pH was interpreted as sorption on suspended particles of undifferentiated Fe and Al hydroxides. Concomitant to the previous study, Gammons et al. (2005b) collected samples along 40 km along the Patagonian Agrio river, which is initially acid due to volcanic discharges. Most of the decrease in REE load occurred immediately downstream of the confluence with a tributary that increased the pH of the Rio Agrio from 4.3 to 6.1. Again, these authors proposed sorption of REE on hydrous Al oxides as the mechanism responsible for the loss of REE with the drop in Al concentration. Similar observations were made by Ferreira da Silva et al. (2009) in the AMD of the Lousal mine (S. Portugal), where a decrease in REE concentrations was observed as the pH increased from 3 to 6 due to the confluence with a tributary stream. All the aforementioned studies suggested sorption mechanisms on Fe and Al hydroxysulfates as responsible for REE retention. Therefore, interaction with the most relevant solids formed in AMD environments, schwertmannite and basaluminite, is expected to play a relevant role in the characteristic water lanthanide distribution pattern.

Laboratory experiments of sorption and coprecipitation of REE onto ferric and manganese oxides/hydroxides have previously demonstrated the key role of pH in the geochemical mobility of REE (Bau, 1999; Ohta and Kawabe, 2000; Ohta and Kawabe, 2001; Quinn et al., 2004; Quinn et al., 2006a). REE are removed from solution as the pH increases from 4 to 9. In addition to pH, aqueous speciation is also an important factor that has been driven its attention in REE fractionation in marine environments. Thus, the formation of strong carbonate complexes with heavy REE (HREE) at neutral pH values prevents their sorption by ferric and manganese oxides. As a result, these solids show patterns with light REE (LREE) enrichment (Byrne and Kim, 1990;

Koeppenkastrop and De Carlo, 1992; Sholkovitz, 1995; Byrne and Sholkovitz, 1996; Kawabe, 1999a; Kawabe, 1999b).

In order to predict REE sorption behavior, surface complexation models (SCM) have developed to describe the sorption of some lanthanides (Yb, La, Eu) onto hematite and amorphous ferric oxides/hydroxides (Marmier et al., 1997; Rabung et al., 1998; Marmier et al., 1999; Quinn et al., 2006b; Quinn et al., 2006a; Estes et al., 2013; Pourret and Davranche, 2013; Liu et al., 2017). In contrast, aluminum phases are not as common as ferrous oxide phases, and there are few studies related to the REE uptake for aluminum oxides. For example, the uptake of Eu and Yb by alumina (Al_2O_3), at varying pH, ionic strength and acid fulvic concentrations, has been studied by soil scientists as an analogue for actinides in nuclear waste disposal (Xiangke et al., 2000). Experimental sorption edges for Yb and Eu(III) onto alumina were reproduced using SCM by Marmier et al. (1997) and Rabung et al. (2000), respectively.

In all these works, the REE scavenging is mainly explained by the sorption of free REE ions or their hydrolyzed species onto a solid surface with high dependence on pH. In addition to pH, sulfate has the potential to change the sorption behavior of REE and other metals in AMD systems. The presence of sulfate is ubiquitous in AMD systems, usually with concentrations reaching up to several grams per liter. Indeed, aqueous sulfate complexes are predominant in AMD over a wide range of pH values (Gimeno et al., 2000; Verplanck et al., 2004), and sulfate is a major constituent of the Fe and Al solid phases, schwertmannite and basaluminite. Similar to REE-carbonate speciation in seawater, sulfate complexes may explain REE fractionation in the solids precipitated from AMD environments. Therefore, sulfate is expected to play a major role in aqueous-solid partitioning. Despite their key role in AMD geochemistry, nor experimental and modeling studies of REE sorption on these two minerals have been investigated neither the role of pH and aqueous sulfate in REE sorption have quantitatively assessed.

1.1 Objectives

The main goal of this work is to understand the behavior of REE in AMD environments and its retention mechanism in basaluminite and schwertmannite, the two main minerals that precipitates in AMD neutralization processes.

Although both basaluminite and schwertmannite precipitates are common in AMD areas, the structure and stability of the former mineral has been less studied, so previous to sorption experiments, ageing experiments of synthetic

basaluminite in two different aqueous solutions has performed (paper 1). The objectives from this part are:

- To characterize the local structure of pure synthetic basaluminite and to compare it with amorphous $Al(OH)_3$ and nanoboehmite.
- To assess the role of pH and dissolved sulfate in the stability of synthetic basaluminite along the time.
- To understand how its metastable character and its transformation to more crystalline phases can affect its local structure.

Based on previous sorption experiments of REE onto both ferric and aluminum oxides/hydroxides, sorption of REE onto basaluminite and schwertmannite are carried out at different pH and sulfate concentrations (papers 2 and 3). The objectives from this part are:

- To assess the sorption capacity of each mineral as a function of pH and two different sulfate concentrations.
- To characterize the REE fractionation in these two minerals and compare with those observed in ferric/aluminum oxides/hydroxides.
- To develop a thermodynamic surface complexation model from experimental sorption results with higher sulfate concentration and 1g/L solid:liquid ratio.
- To validate the model proposed with other experimental sorption results performed at lower sulfate concentrations and different solid:liquid ratios, for each mineral.

The study of the thermodynamic model was complemented with synchrotron-based techniques in order to describe the sorption mechanism onto basaluminite at atomic scale (paper 4). This work was performed only with yttrium element, rather than with all REE since EXAFS is an atomic-selective technique. The objectives from this part are:

- To characterize the local structure of YSO_4^+ aqueous specie since the sorption model describes the REE sorption in terms of aqueous REE-sulfate complex onto the mineral surface. The study was performed using experimental EXAFs and PDF analyses and supported by the results of AIMD simulations.
- To define at atomic scale the surface complex formed by the aqueous specie YSO_4^+ and the surface of synthetic basaluminite. The

characterization was carried out performing EXAFS and PDFs analyses of synthetic solids.

- To determine the solid speciation of basaluminite-rich waste samples recovered from a passive remediation system performed at laboratory scale, comparing the local structure of these samples with different Al-precipitates, such as basaluminite and boehmite doped with Y and YSO_4.

A passive remediation treatment at column scale was performed in order to assess the mobility of REE in the system using the sorption model, focusing on the geochemistry of pore water and of the solid waste (paper 3). The specific objectives of this part are:

- To reproduce the aqueous REE evolution in pore water through column depth and along the time.
- To compare the profile of minerals precipitation and the mobility of REE in the model with the profile of REE in solid waste from column experiments.
- To explain the preferential retention of lanthanides and yttrium in basaluminite-rich solid waste.

The last part of the thesis is focused on the description of REE mobility in two AMD field sites of Spain (Odiel and Tinto catchments, SW Spain and Arroyo del Val, NE Spain) (paper 5). The objectives of this part are:

- To describe the REE mobility in AMD mixing with alkaline inputs from aqueous samples recovered from the field sites.
- To describe the solids precipitated in the mixing zones and the REE patterns observed in the solids.
- To reproduce the REE patterns analyzed in the solids recovered from AMD affected waters, using the aqueous data and the thermodynamic model.

2 Results

2.1 Local structure of basaluminite after ageing in solutions at different pH values and sulfate concentrations.[1]

The results of fast ageing experiments of suspensions of 1 g/L basaluminite in 0.01 M $NaNO_3$ showed clear SO_4:Al and H^+:Al linear correlations with ratios of 1.40 and -0.19, respectively. The saturation indices indicated that at the beginning of the ageing, the solution was undersaturated with respect to basaluminite, gibbsite and boehmite but quickly reached supersaturation with respect to these phases. These correlations are explained as an incongruent basaluminite dissolution with the subsequent Al hydrolysis and $Al(OH)_3$:

$$Al_4(SO_4)_{1.25}(OH)_{9.5} + 0.17\ H^+ \rightarrow$$
$$0.89\ Al^{3+} + 1.25\ SO_4^{2-} + 3.11\ Al(OH)_{3(s)} + 0.17\ H_2O \qquad \textit{Eq. 2.1}$$

In the slow ageing experiments, beyond the first 48 hours and after OH^- addition, a decrease in the pH was observed and the decrease was more accentuated when no sulphate was added to the initial suspensions (Figure 2.1). For pH values higher than 5.1, the Al in solution was below the detection limit, but he molar ratio between the SO_4 released and the excess OH^- was 4.

[1] *This part of the thesis is based on the article Lozano et al., 2018. Chem. Geol. 496, 25-33.*

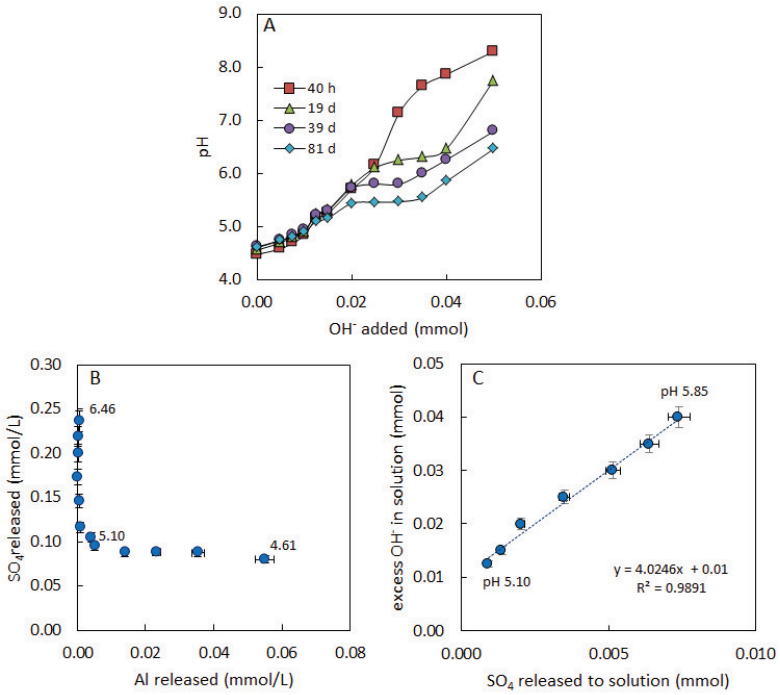

Figure 2.1 (A) Evolution of pH for the suspensions with different initial pH values. (B) Aluminium and SO_4 evolution of the different suspensions after 81 days of ageing. The values depicted inside are the final pH values. (C) Correlation between the OH^- excess and SO_4 concentration for the suspensions with higher pH values.

This result can be explained by a sequence of chemical reactions involving the dissolution of basaluminite and the formation of nanoboehmite and natroalunite, $NaAl_3(SO_4)_2(OH)_6$, according to the process reaction:

$$5Al_4(SO_4)(OH)_{10} \cdot 5H_2O + 2Na + 4OH^- \rightarrow 2NaAl_3(SO_4)_2(OH)_6 + 14AlOOH + SO_4^{2-} + 39H_2O \quad \textit{Eq. 2.2}$$

The structure factors showed that boehmite peaks appeared in the solids from the experiments with higher initial pH values (Figure 2.2). The differential PDFs, generated by subtracting the PDF of pure basaluminite from each sample, show a negative peak of increasing intensity at 1.49 Å, corresponding to the release of sulfate from samples as the pH increases, and a transition to more crystalline phase. Similar trends were observed in the differential PDFs of the experiment with added sulfate, although with less negative peaks at 1.49 Å. From these observations, a transformation of basaluminite to nanoboehmite with time can be inferred. Thus, the experiments demonstrated that basaluminite is a metastable precipitate that can transform into more stable Al hydroxide phases, when ageing in/near neutral waters. This process can affect the behaviour of trace elements, such as REE, that could be adsorbed onto its surface.

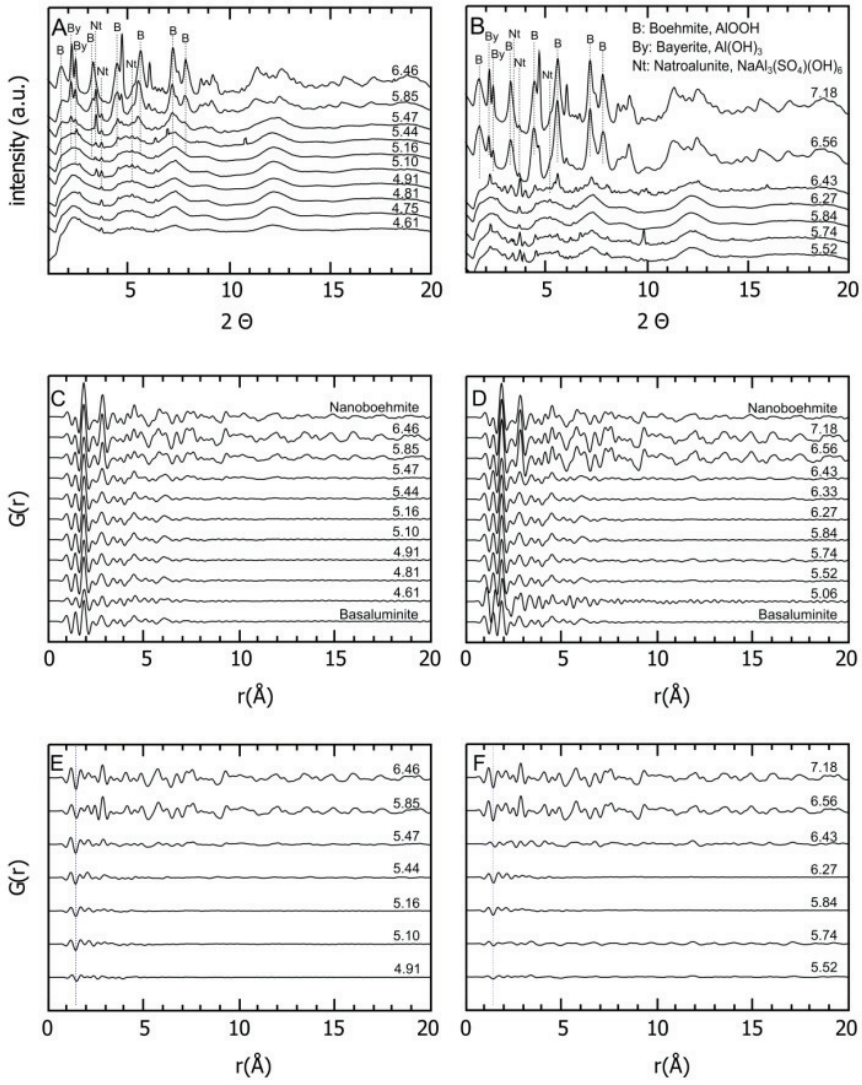

Figure 2.2 Structure factors with Q converted to 2θ for the solid samples equilibrated and aged during 81 days in the absence of sulfate (A) and with an initial sulfate content (B). The wavelength of the X-rays used was of λ=0.181 Å. (C, D) PDFs of the aged solids and synthetic nanoboehmite and basaluminite for the experiment in the absence of sulfate and with initial sulfate, respectively. (E, F) Differential PDFs the two both experiments. The vertical dotted line indicates the position of the S-O bond. Negative peaks reflect the decrease in the sulfate content in the solids.

2.2 Sorption experiments[2]

Sorption experiments of REE with synthetic basaluminite and schwertmannite was performed as a function of pH and sulfate concentrations. Two set of batch sorption experiments were performed with each mineral. For the first set, a solution of 1mg/L of each REE with 20 mM SO_4 was used with the two minerals. For the second set, a solution of 1 mg/L of each REE without sulfate was used with basaluminite, and a solution of 1 mg/L of each REE and 2 mM SO_4 was used with schwertmannite. The sets of experiments covered a pH range of 4-7 with basaluminite and 3-7 with schwertmannite, respectively. The sorption experiments were carried out for 6 hours since maximum sorption was reached for this time and to minimize a possible basaluminite transformation more crystalline Al-phases at high pH values, as showed in the results of basaluminite ageing experiments. The sorbed fractions were calculated as follows:

$$\text{Sorbed fraction} = \frac{[\text{REE}]_{\text{initial}} - [\text{REE}]_{\text{final}}}{[\text{REE}]_{\text{initial}}} \qquad \textit{Eq. 2.3}$$

where [REE] is the concentration of each REE. The initial concentration was measured in the stock solution and the final concentration after the experiment. The distribution coefficient, K_D (L/kg), for each REE was calculated from the [REE] sorbed onto the solid per the final [REE] remaining in solution and normalized per the solid:liquid ratio:

$$K_D = \frac{[\text{REE}]_{\text{initial}} - [\text{REE}]_{\text{final}}}{[\text{REE}]_{\text{final}}} \cdot \frac{V_{\text{solution}}}{M_{\text{solid}}} \qquad \textit{Eq. 2.4}$$

The XRD patterns of the synthetic solids confirmed that the minerals were pure and the BET indicated a surface area of 68 m^2/g and 173 m^2/g for basaluminite and schwertmannite, respectively. The site densities for basaluminite were therefore calculated from crystal structure of felsöbányaite, as basaluminite presents similar local order (Farkas and Pertlik, 1997; Carrero et al., 2017). Similarly, the site density for schwertmannite was obtained from crystal structure of proposed by (Fernández-Martínez et al., 2010). The averaged surface sites for the two solids calculated for each 100, 010 and 001 faces, are 4.6 and 4.7 nm^{-2} for basaluminite and schwertmannite, respectively. These values will be used for model validation in below sections.

[2] *This part of the thesis is based on the articles Lozano et al., 2019a. Geochim.Cosmochim. Acta 258, 50-62, and Lozano et al., 2019c. App. Geochem. Minor revision*.

2.2.1 Sorption edges

All final solutions for the four sets of experiments were subsaturated with respect to the REE hydroxides and, therefore, no REE hydroxide precipitation was expected. All the solutions, except one, from experiments with basaluminite were supersaturated with respect to basaluminite (saturation indices between 0.06 and 1.3). Small amounts of dissolved sulfate were present in the final solutions without initial sulfate. There, the amount of dissolved sulfate increased from 0.1 to 0.9 mM with increasing pH. This is interpreted as the exchange of sulfate from basaluminite with OH groups from the solution (Lozano et al., 2018). The experiments without initial sulfate will be hereafter noted as 0.5 mM SO_4, indicating the mean value.

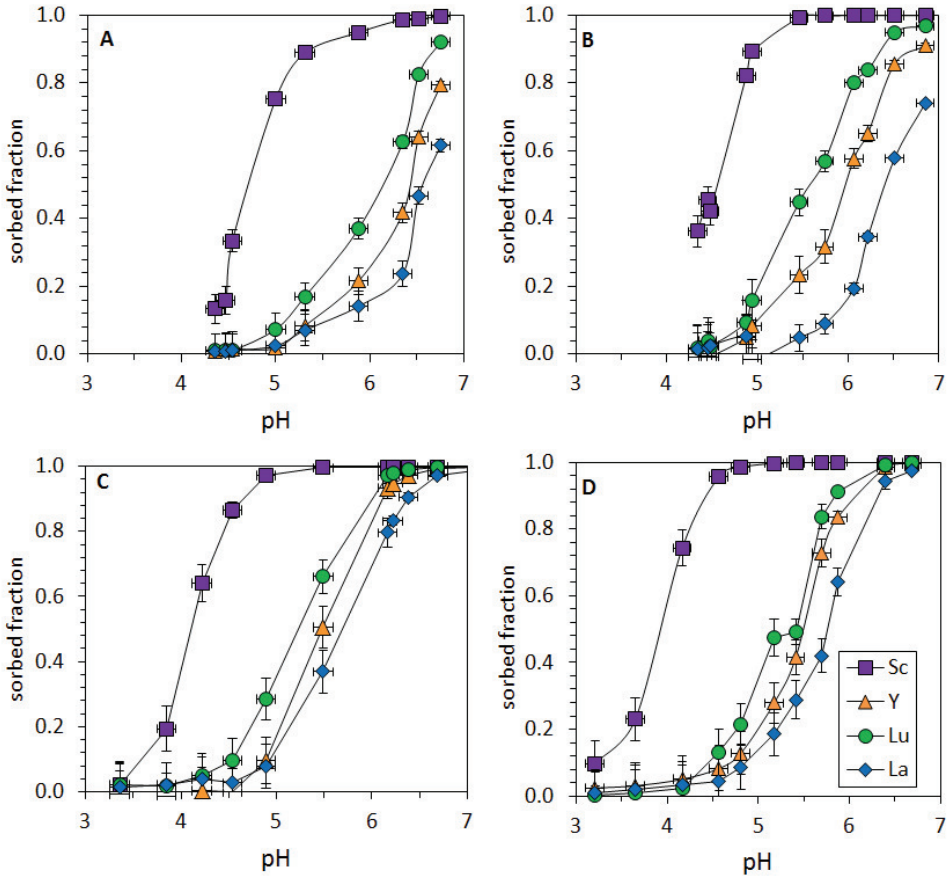

Figure 2.3 Experimental results (symbols) of four REE into 1g/L synthetic minerals (A, B) basaluminite and (C, D) schwertmannite in suspensions of 20 mM SO_4 (A,C) and 0.5 and 2 mMSO_4 (B, D, respectively).

The experimental results for the two set of experiments carried out with each mineral showed that REE sorption is highly dependent on pH, increasing with it (Figure 2.3). Sorption of lanthanides and yttrium is effective from around pH 5 for both minerals. Scandium, however, behaves different, being

sorbed from around pH 4. The experimental results of the sets with lower amounts of sulfate, 0.5 mM SO_4 with basaluminite and 2 mM SO_4 with schwertmannite, showed lower sorption fraction at the same pH values. The sorption decrease at lower sulfate content in solution suggests that sulfate may play a role in sorption process. The sorption also differs among the REE. At a specific pH value, the fraction of HREE (Lu or Y) sorbed in the solid is higher with respect to LREE (La).

The final solutions from experiments with schwertmannite were also subsaturated with respect to schwertmannite and almost in equilibrium with respect to goethite. Schwertmannite exists in a metastable phase that transforms to goethite over weeks at different pH values (Schwertmann and Carlson, 2005; Acero et al., 2006; Burton et al., 2009). However, the presence of sulfate in solution delays this transformation (Regenspurg and Peiffer, 2005), and no goethite was detected by XRD in schwertmannite solids after the sorption experiments.

2.2.2 REE fractionation patterns

The distribution coefficients (K_D) for both sets of experiments were calculated as described in Eq. (2.4) and they are shown in Figure 2.4. From pH 5 in basaluminite and pH 4.5 in schwertmannite upwards, the log K_D patterns reflect HREE enrichment relative to LREE in the solid phases varying close to 1 unit of log K_D along the lanthanide series in both sets of experiments and for both minerals, although less HREE enrichment is observed for schwertmannite. Similar patterns were observed by Bau (1999) for their coprecipitation experiments of REE and Fe at low pH values. Similar relative enrichment in heavy lanthanides was observed in aluminum and ferric hydroxides precipitated in acidic rivers after their neutralization via mixing with alkaline tributaries (Gammons et al. 2003, 2005; Verplanck et al., 2004) and in REEs coprecipitated with synthetic Fe(III)-hydroxides (De Carlo et al., 1998; Quinn et al., 2004).

The REE fractionation patterns showed four convex segments from La to Nd, from Nd to Gd, from Gd to Ho and from Ho to Lu, corresponding to the M-type tetrad effect (Masuda et al., 1987; Bau et al., 1996). However, these results contrast with those described in seawater environments, where a preferential LREE enrichment in the Fe oxides has been observed. Stable aqueous carbonate complexes with HREE formed in marine environments to prevent their adsorption (Koeppenkastrop and De Carlo, 1992; Kawabe et al., 1999b). In acid mine waters, however, sulfate complexes are the dominant aqueous

species, while carbonate complexes are only relevant at pH values higher than 6.5.

More specifically, patterns for basaluminite solids showed a small positive Ce only at low pH and low SO_4 concentration, possibly due to a partial/total oxidation of Ce^{3+} to Ce^{4+}, as Koeppenkastrop and De Carlo (1992) proposed for the positive anomalies observed in vernadite. However, this anomaly is not as evident as in the former mineral in the two patterns obtained for schwertmannite solids. Similarly, precipitates obtained after neutralizing acid mine waters with high sulfate concentration did not show this anomaly (Verplanck et al., 2004), which suggests that sulfate may inhibit Ce oxidation due to sulfate complexation. According to its ionic radius, Y is commonly displayed between Dy and Ho, where it presents a negative anomaly in both precipitates, as evidenced by the K_D^Y/K_D^{Dy} and K_D^Y/K_D^{Ho} ratios below unity. The Y anomalies in amorphous Fe(III)-hydroxides were attributed to covalent interactions with the Fe solids (Quinn et al., 2004).

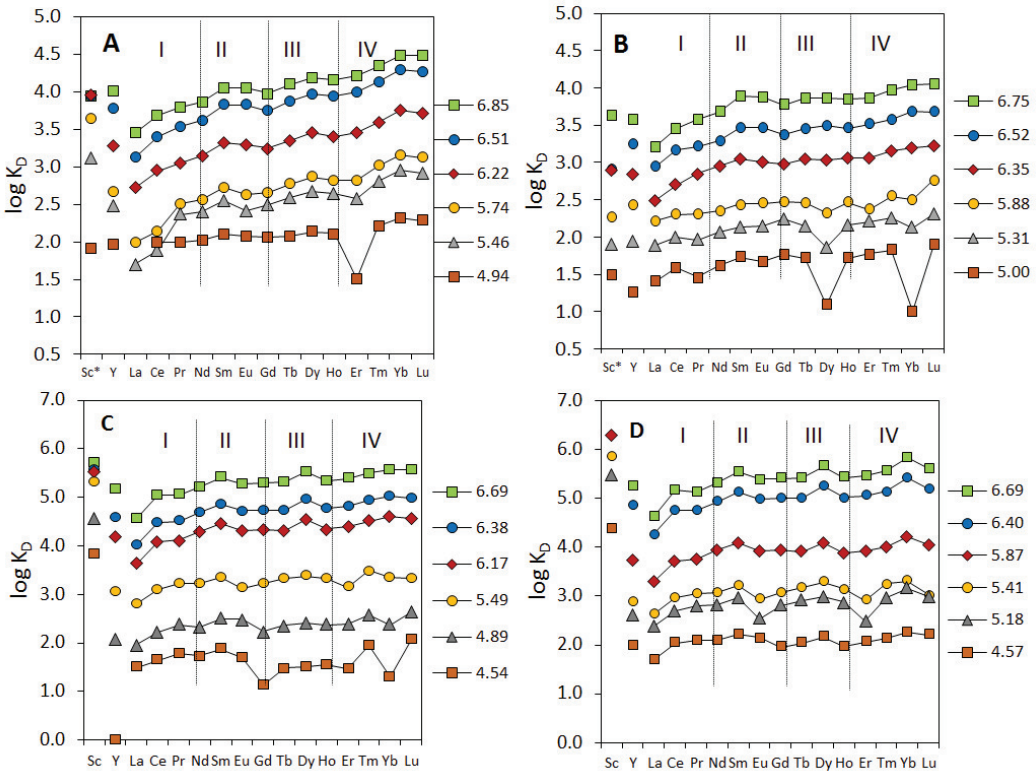

Figure 2.4 Log K_D values at different pH values showing the lanthanide M-type tetrad effect: (A,B) on basaluminite; (C,D) on schwertmannite and in solutions with 20 mM SO_4; (A,C) and with 0.5 and 2 mM SO_4 (B,D, respectively). (Sc = log K_D^{Sc}-2)*

Basaluminite precipitates from the experiments with low SO_4 concentration, displayed negative Yb and Dy anomalies that attenuated as the

pH increased. These anomalies were absent at high sulfate concentrations. In contrast, at higher sulfate concentrations, a negative Er anomaly was showed at lower pH values, that was attenuated when pH increased and this Er anomaly was not observed with lower sulfate content. These anomalies are not previously described in similar sorption/coprecipitation experiments using amorphous ferric hydroxides (Bau, 1999; Ohta and Kawabe, 2000; Quinn et al., 2006a). Finally, the negative Gd and Yb anomalies showed in schwertmannite precipitates at lower pH values from the experimental set with 20 mM SO_4 were not previously reported in the literature for similar experiments (Bau 1999; Quinn et al., 2006a,b) and are attributed to analytical errors.

2.3 Structure of YSO_4^+ aqueous complex and surface complex onto basaluminite[3]

2.3.1 Geometry of the aqueous YSO_4^+ complex

The major aqueous MSO_4^+ complexes formed in high sulfate concentration solutions, simulating AMD environments are expected to sorb in the surface of basaluminite and schwertmannite. Thus, a structural characterization of the aqueous complex is required previous to a local description of MSO_4^+ attached to the surface of these minerals. Extended X-ray Absorption spectroscopy was used to study the YSO_4^+ combined with pair distribution function (PDF) analyses and ab-initio molecular dynamics simulations (AIMD). Yttrium was selected due to its chemical characteristics with other HREEs and since it was of the most concentrated elements in waste samples analyzed.

The experimental PDF for solution with the aqueous YSO_4^+ specie (YSO4-sol) presented a peak at 2.37 Å, which corresponds to the Y-O interatomic distances to oxygen to the first shell (Figure 2.5). A small and sharp peak at 1.45 Å corresponds to the S-O interatomic distance in sulfate. Finally, another smaller peak at 3.7 Å, was concomitant to the analyses of the AIMD trajectories that showed a distance of 3.6 Å between Y and S. Fits of the EXAFS spectra of the YSO_4^+ aqueous solution were performed using atomistic models from the AIMD simulations as initial structural models for the generation of the scattering paths. The best fit yielded an average Y–O distance of 2.38 ± 0.01 Å and the coordination number (CN) of 7.9±0.9, close to 8, the expected for HREEs. The second shell observed in the FT was fitted with a Y-S distance of

[3] *This part of the thesis is based on the article Lozano et al., 2019b, Environ. Sci. Technol. 2019, 53, 11153-11161*

3.5 ± 0.04 Å, similar to that observed in the PDF of the same sample, with a CN =1. Thus, the structure of the aqueous YSO_4^+ forms a monodentate inner-sphere complex (one shared oxygen) between sulfur and yttrium.

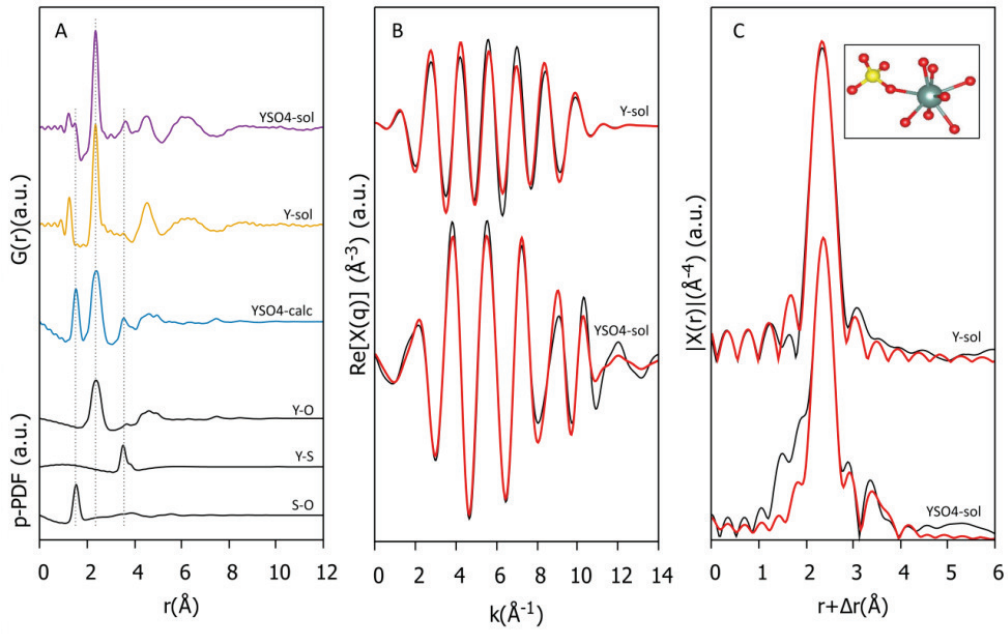

Figure 2.5 (A) Top: Experimental PDFs of YSO4-sol and Y-sol samples. Bottom: Simulated (AIMD) PDF (YSO4-calc) and its partial PDFs. (B) Fourier-filtered signal (1.8 to 4.2 Å) and (C) EXAFS FT amplitude functions EXAFS data. Black lines: experimental; red lines: fits. Simulated (AIMD) PDF and partial PDFs have been multiplied for visualization purposes: YSO4-cal (x3), Y-S (x5) and Y-O and S-O (x2). Dashed lines indicate the position of the Y-O, Y-S and S-O bonds in YSO4-sol sample.

2.3.2 Local order of yttrium adsorbed onto basaluminite

All the EXAFS spectra of solid references (B-YSO4-ads, B-Y-ads, B-Y-cop and A-Y-ads) are indistinguishable and differ from the aqueous Y-sol and YSO4-sol spectra in that a slight oscillation becomes visible at 5-6 $Å^{-1}$. In the B-YSO4-ads (YSO_4^+ sorbed onto basaluminite) the dominant Y species in solution is the YSO_4^+ complex (Figure 2.6). However, in B-Y-ads (Y^{3+} sorbed onto basaluminite), B-Y-cop (Y^{3+} coprecipitated in basaluminite) and A-Y-ads (Y^{3+} sorbed onto nanoboehmite), the dominant Y species is Y^{3+}. Since the common feature in these three samples is the presence of an Al adsorbent, and this feature agrees with that in the B-YSO4-ads EXAFS spectrum, we hypothesize that the higher frequency observed at 5-6 $Å^{-1}$ (arrow in Figure 2.6) may be related to the presence of an Al backscatterer, rather than to a signal from a close sulfate group. Both Al and S are light atoms with similar atomic numbers (Z = 13 and 16, respectively), which makes their backscattering functions

difficult to distinguish via fitting of the EXAFS signal. These observations lead us to assume that the EXAFS measurements have poor sensitivity to the presence of Y-S bonds in this system. However, a contribution from a sulfate shell for the two first samples cannot be ruled out.

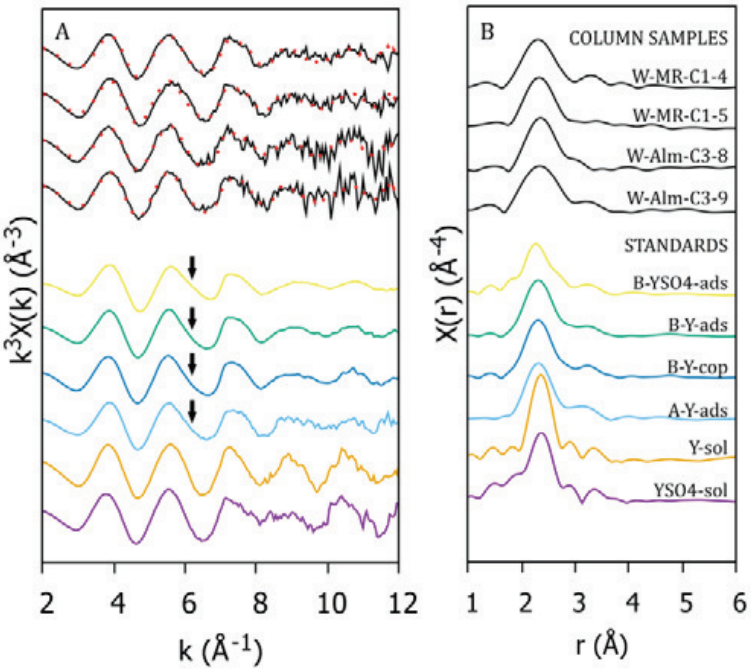

Figure 2.6 k³-weighted EXAFS (A) and FT amplitude functions (B) for four waste samples from column treatments W-MR-C1-3, W-MR-C1-4, W-Alm-C3-8, and W-Alm-C3-9 (upper part) and solid standards: B-YSO4-ads, B-Y-ads, B-Ycop; and aqueous solution standards: Y-sol and YSO4-sol (bottom part). The dashed lines in the EXAFS signals of the column samples represent LCF with B-YOS-ads and YSO4-sol.

Three different atomistic models were used to fit the EXAFS of a basaluminite sample with YSO_4^+ sorbed into its surface (B-YSO4-ads): (A) a monodentate surface complex, (B) a bidentate mononuclear surface complex and (C) a bidentate binuclear surface complex. The monodentate inner sphere complex was one of the best EXAFS fit, where the fit was performed assuming S and Al coordination numbers equal to 1 and 2, respectively. The fit yielded a first coordination shell with a Y-O distance range between 2.32 and 2.47 ± 0.02 Å with a fixed coordination number of 8. The second best fit, was the bidentate binuclear inner-sphere. The first shell was fitted with a coordination number of 10 ± 1.31 and a distance of 2.33 Å. The second shell was fitted with a S path yielding a Y-S distance of 3.34 Å with a fix coordination number of N = 1, similar to that for the monodentate hypothesis, and with an Al path with a fixed coordination number of N = 2 giving a distance a bit longer, 3.92 Å.

Table 2.1 Results of the EXAFS fits for B-YSO4 reference. Model 1: monodentate inner sphere. Model 2: bidentate mononuclear inner sphere. Model 3: bidentate binuclear inner sphere. Var.: independent variables. The best model is indicated with a star (*). The error is expressed in the parentheses after the last digit

Model	Neighbor	path	N	σ^2	ΔE_0	R	Var.	χ_ν^2
1*	1st shell	Y-O_1	6_{fix}	0.007(1)	-3(2)	2.32(1)	9	338
		Y-O_2	2_{fix}	0.004(8)	-3(2)	2.47(2)		
	2nd shell	Y-S	1_{fix}	0.008(5)	-3(2)	3.33(4)		
		Y-Al	2_{fix}	0.012(5)	-3(2)	3.52(5)		
2	1st shell	Y-O	10 (1)	0.012(2)	-6(2)	2.33 (1)	8	402
	2nd shell	Y-S	1 fix	0.009(5)	-6(2)	3.88 (5)		
		Y-Al	1 fix	0.006(3)	-6(2)	3.42 (3)		
3	1st shell	Y-O	10(1)	0.013(1)	-4(1)	2.33(1)	8	334
	2nd shell	Y-S	1_{fix}	0.008(3)	-4(1)	3.34(3)		
		Y-Al	2_{fix}	0.011(5)	-4(1)	3.92(4)		

2.4 REE distribution in the column experiment[4]

The results of the mobility of REE in a column experiment simulating a passive remediation system are shown in Figure 2.7. Only Sc, La and Y were compared due to their different sorption behavior in the column experiment results. Essentially, for a given time the pH increased with depth, and for a given depth the column was progressively invaded by more acidic water (Figure 2.7 A). For each time, Fe and Al concentrations decreased with depth to detection level suggesting the precipitation of schwertmannite and basaluminite (Figure 2.7 B-C). However, Al showed a peak of concentration higher than the input AMD. This was already observed in previous column experiments, and attributed to the re-dissolution of basaluminite by the percolating AMD once the calcite reagent was exhausted (Rötting et al., 2008). Practically no Al and Fe were detected at the end of the column in the four sampling events.

[4] *This part of the thesis is based on the article Sorption of rare earth elements on schwertmannite and their mobility in acid mine drainage treatments. App. Geochem. Minor revision*

The concentration of the three selected REE showed a similar distribution pattern (Figure 2.7 D-F) in depth. As described for Al, the concentration decreased with depth, but also showed a peak of concentration higher than the input AMD, which progressed downwards with time. This distribution suggests a close association of REE to basaluminite, as already observed for Y and lanthanides in previous experiments (Ayora et al., 2016). In subsequent samplings, the peak concentration decreased to the inflow AMD value. Scandium, however, showed a slightly different behavior. For the same sampling event (28 days), the Sc peak was observed to occur upstream with respect to those of La and Y, and for the same depth (10 cm), the Sc peak took longer time to disappear. As for Fe and Al, almost no REE concentration was detected at the end of the column during the experiment.

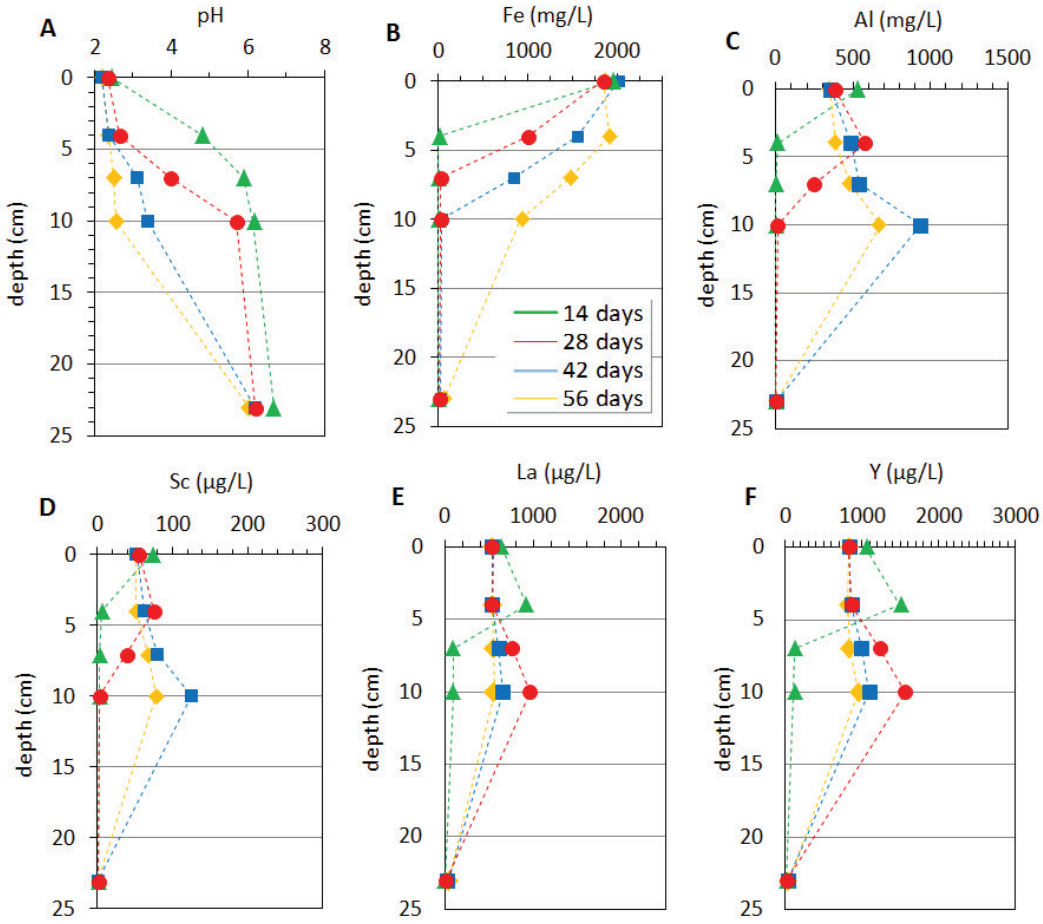

Figure 2.7 Depth profiles of pore water and solid composition at four different stages of column operation: (A) pH evolution; (B, C) Fe and Al concentrations in pore water; (D, E, F) concentrations of selected REE in pore water.

Once the column was stopped after 58 days of functioning, and the solid residue was dried and sliced for analysis, sequential extractions were carried out. As evidenced in Figure 2.8 D-E, a minor proportion of Sc and the rest of the

REE was found in the water-soluble step I, most likely linked to gypsum (Lin et al., 2019). However, most REE were found in steps II and III of the sequential extraction, which are representative of schwertmannite and basaluminite precipitates. However, some differences are evident in the depth distribution of Sc and the rest of the REE. Yttrium (and lanthanides) match the Al distribution along the column depth (Figure 2.8 E), indicating that they are attached to basaluminite. However, up to 25% Sc was located in the first 6 cm of the column, matching the Fe distribution and suggesting a link to schwertmannite.

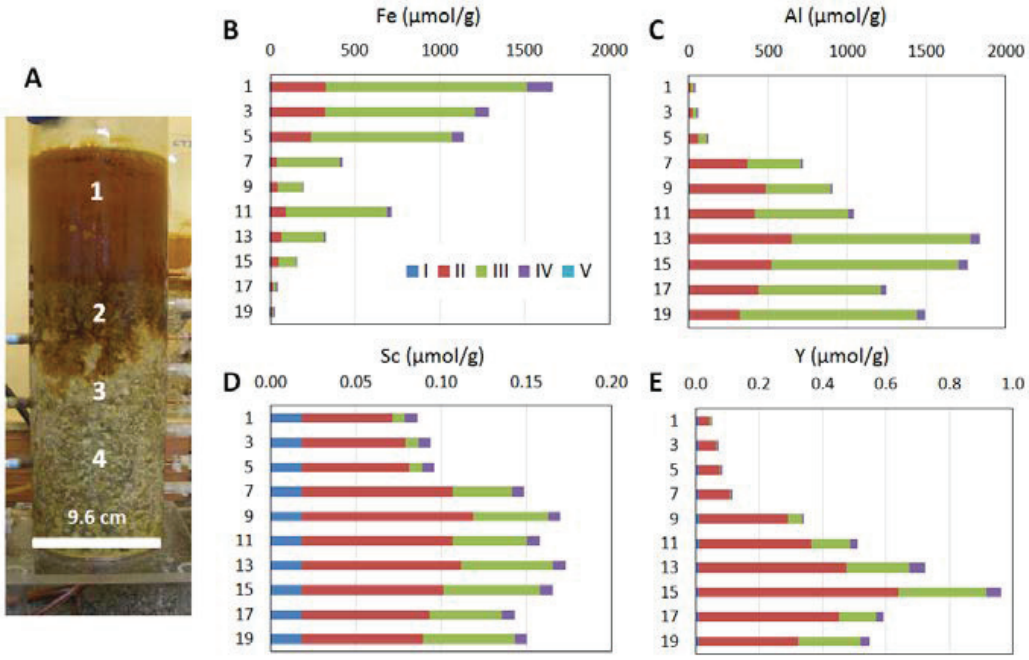

Figure 2.8 (A) View of the column after 28 days of the experiment: 1= supernatant AMD; 2= schwertmannite zone; 3= basaluminite zone 4= calcite zone. (B-E) Distribution of Fe, Al, Sc and Y concentration in the solid residue. The numbers on the vertical axes indicate the depth (cm) of the center of each slice of the column. The colors indicate the different steps of sequential extraction of the following phases: I) the water-soluble fraction; II) calcite and basaluminite, III) low crystalline Fe(III)-oxyhydroxides and remaining basaluminite, IV) crystalline Fe(III)-oxides, and V) the residual fraction.

2.5 REE behavior in the mixing streams[5]

2.5.1 Description of the field sites and sampling

2.5.1.1 Field sites in the Odiel-Tinto catchments

The Odiel River is a 122 km long and has a catchment area of 2300 km^2, from the Aracena Mountains in the North of Huelva province to Huelva estuary in the South, a region in the Southwest of Spain. In this area, about one hundred of ancient mines and wastes generating AMD have been detected in the Odiel watershed (Sánchez-España et al., 2005a; Nieto et al., 2013).

Water samples were collected from the five water discharges (CN, SP, ES, PO and AG) and from the Odiel river prior the discharges and more than 100 m downstream, when water mixing was apparently complete (Figure 2.9).

The field sampling was completed with several localities from the same area. Thus, water samples and precipitates from Dehesa Boyal (DB) and Torerera mine (TO) correspond to the mixing of a small acidic stream with less than 2 L/s with near-neutral water with higher flow (DB-neu and TO-neu, respectively). The Rio Tinto (RT) locality corresponds to the reverse situation. Upstream the village of Niebla, a small neutral stream of less than 5 L/s discharged into the Rio Tinto main stream (1 m^3/s).

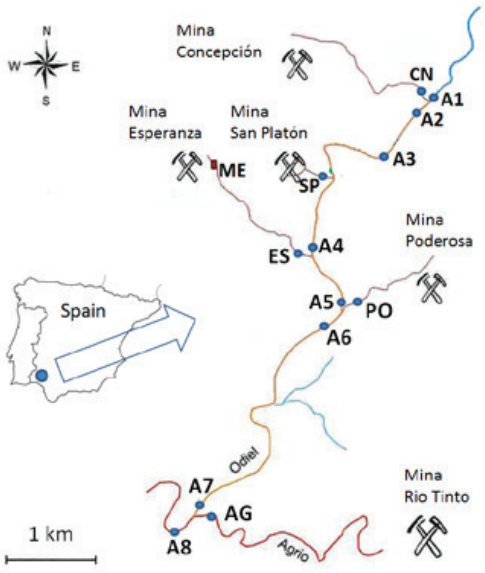

Figure 2.9 Stretch of the Odiel river and acidic tributaries with the sampling points.

[5] *This part of the thesis is based on the article Geochemical behavior of rare earth elements in acid drainages: modeling achievements and limitations. Submitted in Chem. Geol.*

Finally, a full scale passive remediation system was working in 2007-8 at Mina Esperanza site (ET in Figure 2.9). The system consisted of a limestone sand filter through which the acidic water flowed. A full description of the water and solid waste chemistry and mineralogy is provided in Caraballo et al. (2011a,b). Three solid samples of white precipitates were collected on different days at the outflow channel of treatment plant.

2.5.1.2 Arroyo del Val site

The information corresponding to Arroyo del Val area is mainly extracted from Auqué et al. (1993) and Gimeno (1999). The Arroyo del Val is located between Luesma and Fombuena villages, about 70 km SW Zaragoza, Spain. The studied section of the Arroyo del Val stream is about 3 km long, it carries more than 10 L/s after rain events, and less than 1 L/s during summer. The stream is excavated in a monotonous series of dark brown to black shale of Silurian age, that crop out in the drainage basin. The black shale contains dispersed abundant sulfides, mainly pyrite, which generates an ubiquitous acid rock drainage (ARD) after weathering. Differently from most of the Odiel sites, the Arroyo del Val is an acidic stream that receives several neutral tributaries of near neutral pH (Figure 2.10). The mixing of waters yields iron and especially aluminum rich flocculates that sediment at and downstream the confluences. Water (labeled with W) and solid (labeled with C) samples were collected in three different campaigns, and only those pairs of coexisting water and precipitates were selected: 1991 (W5-CV1), 1994 (W9-C9; W12-C12) and 1996 (Wexp-Cexp).

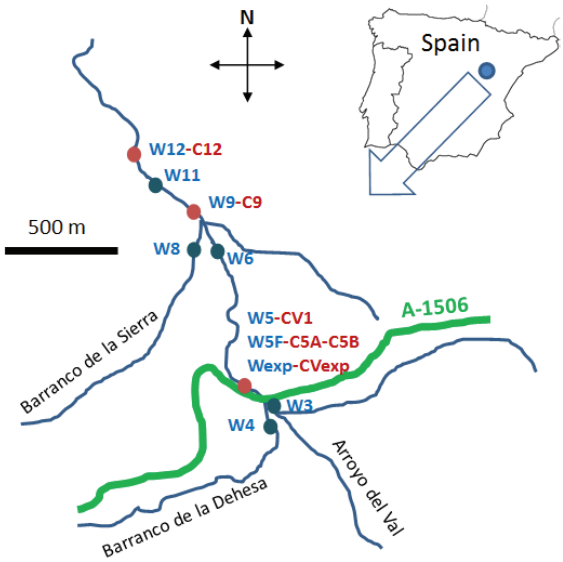

Figure 2.10 Sketch of the Arroyo del Val system. Each letter corresponds to different samples (W= water; C= precipitates).

2.5.2 Chemical evolution after mixing points

The chemical composition of the aqueous phase in each sampling point of the Odiel river stretch is compared with those resulting from the conservative mixing of the river and any acidic discharge (Figure 2.11). Although some amount of SO_4 was removed from water due to Fe and Al oxy-hydrosulfate precipitates, its high concentration made it a quasi-conservative solute (Figure 2.11 A). On the contrary, Fe and As are clearly not conservative at both acidic and neutral pH (Figure 2.11 B), indicating their removal by the precipitation of schwertmannite (Carlson et al 2002; Fukushi et al., 2004). Al and Cu showed an intermediate behavior (Figure 2.11 C). These elements are partially removed by precipitates in the upper part of the river, where pH remained always above 6.5, and they behaved conservatively at low pH when the Agrio acidic discharge caused a final pH of the river lower than 3.5.

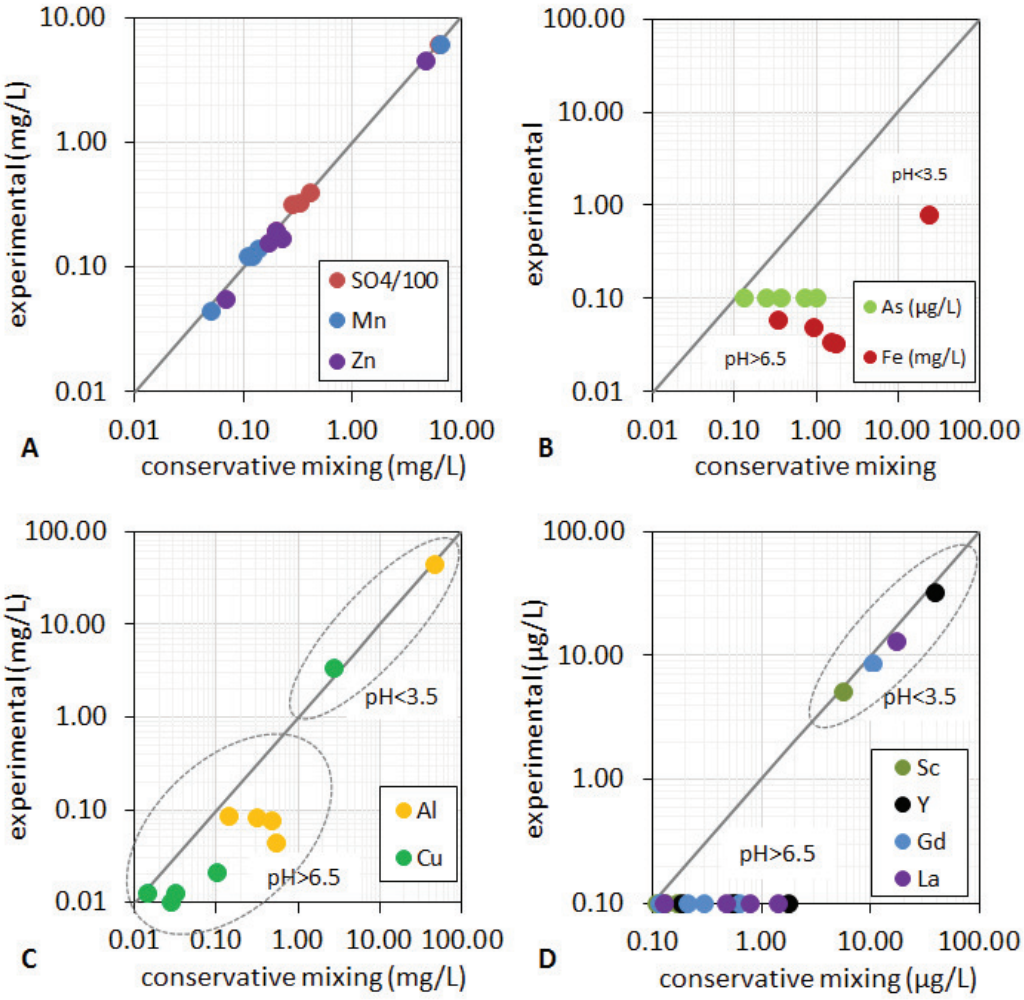

Figure 2.11 Comparative between experimental and conservative concentration of selected elements in samples from the Odiel river after receiving acid discharges.

Similar behavior was experienced by REE. They were completely removed by the precipitates at pH higher than 6.5 and they behaved conservatively at pH below 3.5. This observation is consistent with the behavior described by previous authors (Verplank et al., 2004; Gammons et al., 2005a, b; Ferreira-da-Silva et al., 2009), and suggests that, rather than schwertmannite, basaluminite is responsible for scavenging REE from water.

2.5.3 Precipitates

Reddish-ochreous and whitish precipitates or mixtures were taken from the two sampled localities. These materials are formed by aggregates of spherical particles of less than 1 μm forming aggregates of larger size. In most of the reddish precipitates, the pink-cushion texture typical of schwertmannite can be distinguished, whereas only aggregates of spheres were observed in the whitish precipitates. Schwertmannite was only clearly identified in AG, DB and TO reddish precipitates floating in the water, and basaluminite in whitish precipitates from AG, TO, DB and ET. In the rest of localities, the existence of basaluminite was deduced from the chemical analyses.

The whitish precipitates from AG, DB, TO and ET showed variable but minor Fe concentrations and Al/S ratios ranging from 4.32 to 6.26, higher than the theoretical basaluminite formula, $Al_4SO_4(OH)_{10}{\cdot}5H_2O$, probably due to mixtures with Al hydroxides and/or its partial transformation into low crystalline boehmite and the release of SO_4 (Lozano et al., 2018). The precipitates from PO and RT show high contents in both Al and Fe, and S concentrations below 3 wt%, and (Fe+Al)/S ratios from 7.5 to 12, far above what is expected for schwertmannite and basaluminite. These samples are associated with water mixtures with pH values above 6, and they are interpreted as mixtures of basaluminite and schwertmannite with Al and Fe hydroxides (Bigham et al., 1996; Nordstrom and Alpers, 1999).

The precipitates from Arroyo del Val were composed by Al (16 to 18 wt.%), Fe (25 to 29 wt.%) and S (6 to 11%), and minor amounts of Si (1 to 6 wt.%) (Gimeno, 1999). Moreover, microprobe analyses of the whitish amorphous phase always reveal the presence of S with ((Al+Fe)/S) ratios close to 4, which indicates that schwertmannite and basaluminite could be the major phases.

The results of the REE patterns from solids recovered in different field sites are plotted in Figure 2.12. The REE patterns of the original acid water are also plotted as a reference. As can be observed, the main trends of REE distribution of the water are transferred to the solid phase. Thus, all the NASC-normalized REE patterns of waters and precipitates show a typical convex curvature indicating enrichment in MREE with respect to LREE and HREE, which has

been also described for other acid drainages (Ferreira-da-Silva et al., 2009; Perez-Lopez et al., 2010; Sahoo et al., 2012). All the water samples from the Odiel-Tinto basins show a characteristic Eu negative anomaly, although this anomaly varies from being acute in AG and ET to less acute in other points of the Odiel -Tinto area (TO) (Figure 2.12 A-C). The Eu anomaly is absent in the samples from the Arroyo del Val site (Figure 2.12 D-F). The reason for this different pattern seems related to the different original rocks and mineralization types of both regions, felsic volcanics in Odiel-Tinto and sedimentary black shales in Arroyo del Val. As exception, some precipitates from Arroyo del Val show a negative anomaly in Gd that is not observed in the aqueous phase, and could be due to an analytical artifact.

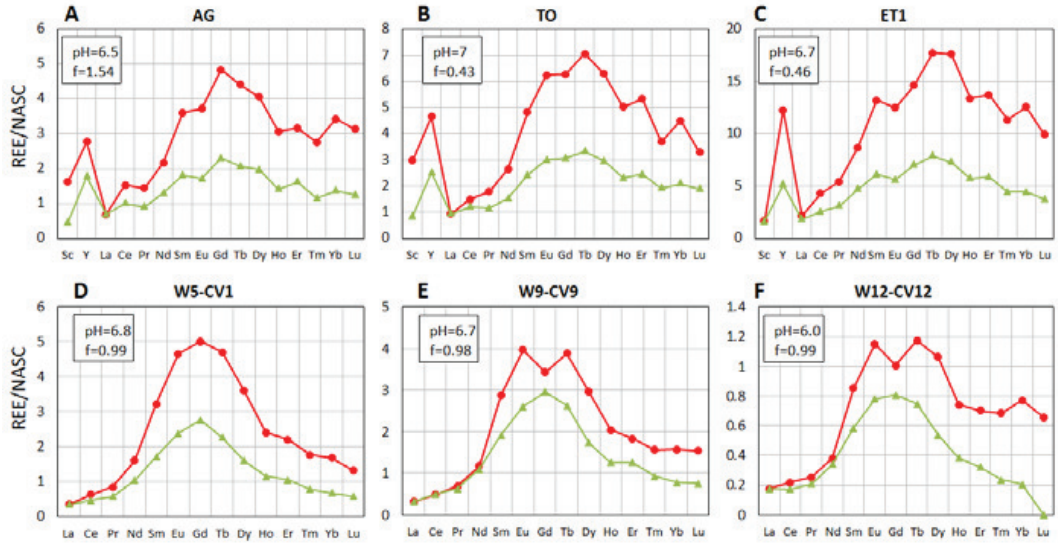

Figure 2.12 REE patterns of precipitates (red circles) and of the parent AMD (green triangles). All the concentrations normalized to North American Shale Composite (NASC). (A, B, C) Samples from Odiel-Tinto site, (D, E, F) Samples from Arroyo del Val site.

3 Discussion

3.1 Sorption model[6]

3.1.1 REE aqueous speciation

Sulfate is ubiquitous in AMD environments with concentrations that can range from mg/L to g/L. Moreover, sulfate strongly complexes with aqueous REE (Gimeno et al., 2000), forming the aqueous $REESO_4^+$ specie (MSO_4^+ hereinafter), and thus becoming the major aqueous specie in solution (Figure 3.1 A). Sc behaves some different since besides $ScSO_4^+$, the aqueous speciation showed a higher stability of the hydrolysis species $Sc(OH)^{2+}$ in the experiments with lower sulfate concentration (Figure 3.1 C,D). Thus, since sorption of REE increases with higher sulfate in solution, is expected that the sorption of MSO_4^+ occurs onto the basaluminite surface, with probably some exception to Sc sorption.

[6] *This part of the thesis is based on the articles Lozano et al., 2019a. Geochim. Cosmochim. Acta 258, 50-62, and Lozano et al., 2019c. App. Geochem. Minor revision.*

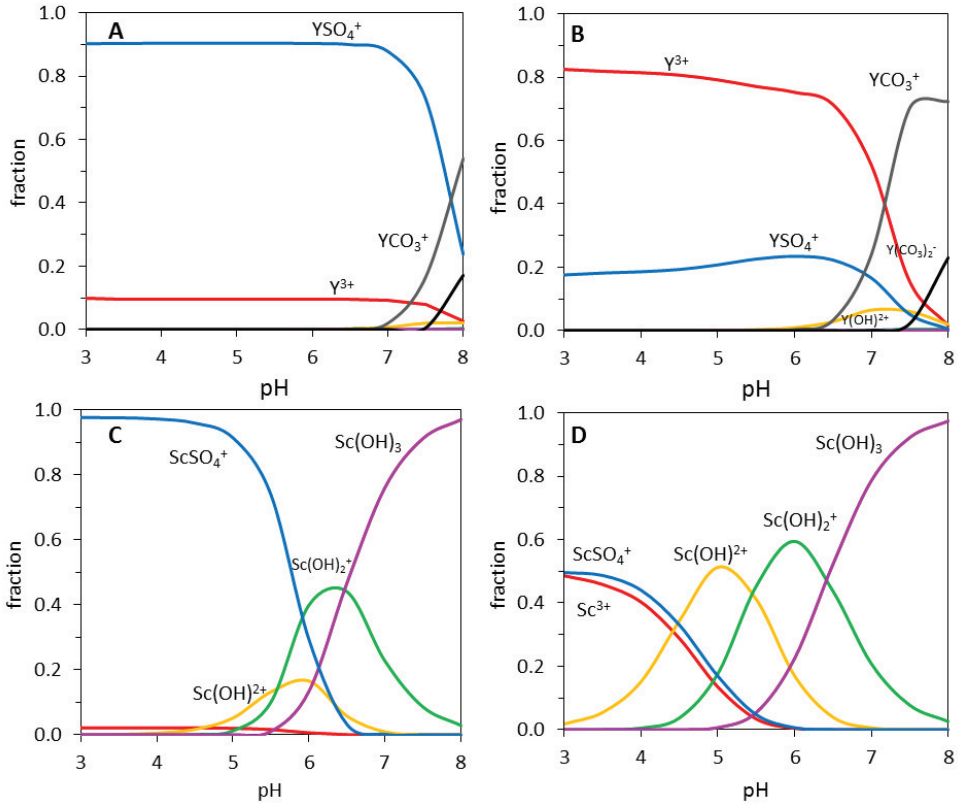

Figure 3.1 Aqueous species distribution of Y and Sc with pH for a solution with 20 mM (A, C) and 0.5 mM (B, D) of sulfate at 25 °C and atmospheric pCO_2.

3.1.2 Description of sorption model

A non-electrostatic model (NEM) is a type of Surface Complexation Model (SCM) in which the electrostatic term is ruled out when the chemical interaction of the cation adsorption is stronger than electrostatic forces (Davis and Kent, 1990). In particular, several works have modeled the sorption experimental data of some REE with NEM, discarding the electrostatic term, such as Marmier et al. (1999) to describe the sorption of lanthanum in hematite; Tertre et al. (2008) to describe REE adsorption on basaltic rock, or Rabung et al. (2000) and Quinn et al., (2006a,b) to describe Y and lanthanides sorption in amorphous iron hydroxides. The SCM models are characteristic in part due to its adjustable parameters, such as equilibrium constants, total number of reactive sites, and capacitance density. In the case of basaluminite and schwertmannite, its metaestable character of the mineral precluded the full determination of its surface properties and thus, a non-electrostatic model was used.

Owing to the predominance of aqueous sulfate complexes in the solutions (Figure 3.1), the sorption experiments were modeled by the reaction of the

aqueous sulfate complex MSO_4^+ with the free surface sites of the two studied minerals. This assumption is consistent with the observation of higher adsorption in the experiments with the SO_4-rich solutions (20 mM) with basaluminite. In the case of Sc, in addition to $ScSO_4^+$, the aqueous speciation showed a higher stability of the hydrolysis species $Sc(OH)^{2+}$ in the experiments with lower sulfate concentration and the sorption of this aqueous species was also considered. Although experiments were conducted at room conditions, carbonate complexation has not been considered experimentally since the proportion of carbonate species is very low at the experimental pH range (Figure 3.1).

The sorption reaction is proposed as the exchange of the M^{z+} aqueous complex (M^{z+} accounting for MSO_4^+ and $Sc(OH)^{2+}$) with n protons from n surface sites represented by XOH:

$$M^{z+} + nXOH = (XO)_nM^{z-n} + nH^+ \qquad K_M \qquad \textit{Eq. 3.1}$$

The equilibrium constant K_M of the reaction for each REE (M) would be:

$$K_M = \frac{\{(XO)_nM^{z-n}\} \cdot a_{H^+}^n}{a_{M^{z+}}\{XOH\}^n} \qquad \textit{Eq. 3.2}$$

where a_{Mz+} and a_{H+} are the activities of the aqueous complex and proton, respectively; and $\{(XO)_nM^{z-n}\}$ and {XOH} account for the mole fraction of the sorbed species ($[(XO)_nM^{z-n}]/[T_{XOH}]$) and the free surface sites ($[XOH]/T_{XOH}$), respectively.

From the total surface site concentration previously calculated for basaluminite and schwertmannite, the concentration of free surface sites was calculated as:

$$[XOH] = T_{XOH} - \sum n\,[(XO)_nM^{z-n}] \qquad \textit{Eq. 3.3}$$

The value of the equilibrium constant K_M for each element was obtained with data from the experiment with 20 mM SO_4, except for the case of the species $Sc(OH)^{2+}$, which was obtained from the experiments with 0.5 mM SO_4 basaluminite and 2 mM SO_4 for schwertmannite.

Thus, replacing the molar fraction by their values, taking logarithms of Eq. (4.2) and rearranging the order we obtain a linear expression (Eq.3.4):

$$\log\frac{[(XO)_nM^{z-n}]}{a_{M^{z+}}}\log = \log K_M + n\,pH + n\log[XOH] - (n-1)\log T_{XOH} \qquad \textit{Eq. 3.4}$$

For low occupancy of surface sites, [XOH] and T_{XOH} are practically coincident and Eq. 3.4 can be approximated as:

$$\log \frac{[(XO)_n M^{z-n}]}{a_{M^{z+}}} = \log K_M + n\ pH + \log T_{XOH} \qquad \textit{Eq. 3.5}$$

Therefore, the equilibrium constants determined here ($K_M \cdot T_{XOH}$) are those referred to as the K_3 according to the model 3 proposed by Wang and Giammar (2013).

By plotting the experimental data of the set of sorption experiments performed with 20 mM aqueous sulfate on basaluminite and schwertmannite minerals, linear correlations were obtained according to Eq. 3.5 for Y and lanthanide series (Figure 3.2).

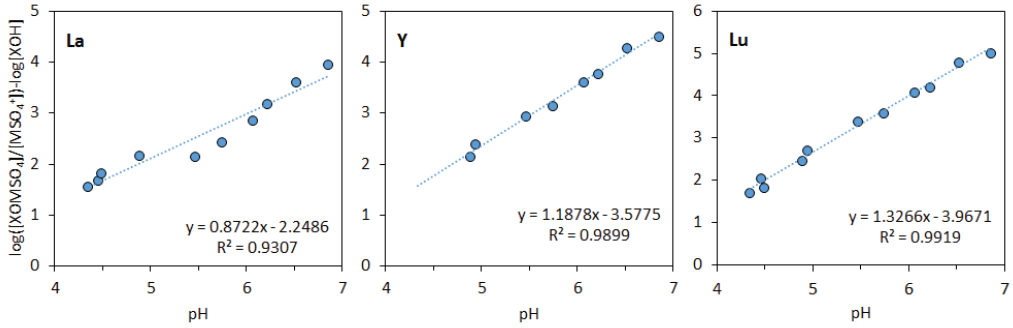

Figure 3.2 Regressions obtained from measured pH values and calculated activities from the final concentrations of experimental data following the Eq. 4.5 for the experimental set of 20 mM SO_4 for basaluminite Regressions for Y, La and Lu, from basaluminite.

The slope values of the regressions obtained from data of experiments with 20 mM SO_4 was close to 1 for yttrium and lanthanides in basaluminite mineral (Figure 3.2) and varied from 1.5 to 2 in schwertmannite. A slope close to 1 suggests the exchange of the MSO_4^+ with one surface proton and the formation of a monodentate surface complex, as indicated by the Eq. 3.1 (Rabung et al., 1998; Rabung et al., 2000). The results of EXAFS fits of a sample of basaluminite with sorbed YSO_4^+ on its surface indicated the formation of a monodentate inner sphere (Table 2.1) and are consistent with the model description of REE sorption onto basaluminite. Similar EXAFS results were obtained by Rabung et al. (2006), where Gd and Lu formed inner sphere surface complexes onto γ-Al_2O_3. Lu, which is considered a HREE such as Y, was shown to form a monodentate surface complex with a first shell of 7 atoms and a Lu-O distance of 2.28 Å.

Likewise, the values close to 2 from sorption experiments with schwertmannite were interpreted as the exchange with two surface protons and thus, the formation of a bidentate surface. Similar bidentate complexes

were obtained by EXAFS fitting analysis of Lu sorbed onto ferrihydrite and Eu sorbed onto hematite (Dardenne et al., 2001; Estes et al., 2013). However, due to the variation, a small proportion of monodentate complexes could also be present.

Unlike Y and the lanthanides, the linear regression for $ScSO_4^+$ data from the 20 mM SO_4 experiments with the two minerals resulted in a slope close to 2. Similar results were observed for $Sc(OH)^{2+}$ with a slope of 1.90 from the experiment with 0.5 mM SO_4 with basaluminite (Figure 3.3), and with a slope of 1.49 from the experiment with 2 mM SO_4 with schwertmannite. Again, in both cases, a slope of 2 suggests the formation of bidentate surface complexes.

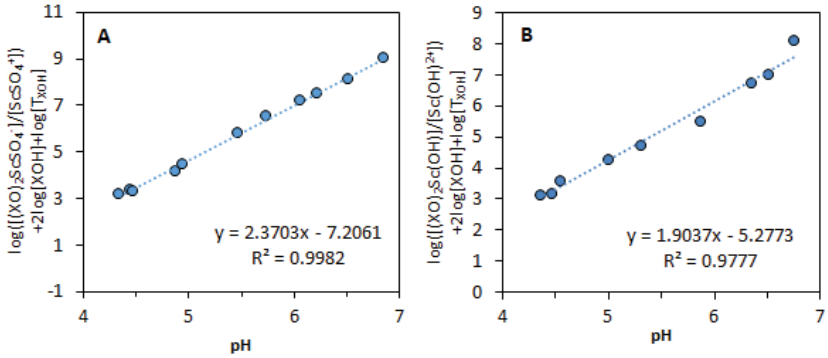

Figure 3.3 Regressions obtained from experimental data from Sc element plotted according the linearized equations (n = 2) for $ScSO_4^+$ (A) and for $Sc(OH)^{2+}$ (B).

To obtain surface sorption equilibrium constants, the regression slopes from experimental data sets of 20 mM SO_4 were forced to 1 for yttrium and lanthanides and to 2 for Sc, for the experiments performed with basaluminite; and forced to 2 for all REE for experiments carried out with schwertmannite, respectively, using Gnuplot v. 5.2.7 software (Williams and Kelley, 2019). The calculated log K_M values and the regression errors for surface complexation reactions for all REE are listed in Table 3.1. The log K_M values for both minerals increase from La to Lu in both minerals, indicating the higher HREE affinity over LREE.

Table 3.1 Equilibrium constants for the formation of surface complexes (K_M of Eq. 3.2) obtained by fitting the experimental values of the two set of sorption experiments with 20 mM SO_4 with basaluminite and schwertmannite solids, respectively. Concentration of the surface species calculated as their molar fractions (K_M is equal to the K_3 value of Wang and Giammar (2013).

Mineral	Basaluminite			Schwertmannite		
Element	Surface Complex	Log K_M	Error	Surface complex	Log K_M	Error
Sc	$(XO)_2ScSO_4^-$	-5.19	0.08	$(XO)_2ScSO_4^-$	-5.27	0.07
	$(XO)_2Sc(OH)$	-5.81	0.09	$(XO)_2ScOH$	-3.40	0.08
Y	$XOYSO_4$	-2.48	0.06	$(XO)_2YSO4^-$	-7.62	0.04
La	$XOLaSO_4$	-2.95	0.08	$(XO)_2LaSO4^-$	-7.96	0.15
Ce	$XOCeSO_4$	-2.81	0.07	$(XO)_2CeSO4^-$	-7.60	0.10
Pr	$XOPrSO_4$	-2.69	0.05	$(XO)_2PrSO4^-$	-7.52	0.13
Nd	$XONdSO_4$	-2.60	0.03	$(XO)_2NdSO4^-$	-7.44	0.09
Sm	$XOSmSO_4$	-2.48	0.05	$(XO)_2SmSO4^-$	-7.27	0.08
Eu	$XOEuSO_4$	-2.50	0.05	$(XO)_2EuSO4^-$	-7.41	0.09
Gd	$XOGdSO_4$	-2.50	0.04	$(XO)_2GdSO4^-$	-7.51	0.05
Tb	$XOTbSO_4$	-2.48	0.06	$(XO)_2TbSO4^-$	-7.42	0.06
Dy	$XODySO_4$	-2.37	0.06	$(XO)_2DySO4^-$	-7.27	0.03
Ho	$XOHoSO_4$	-2.40	0.05	$(XO)_2HoSO4^-$	-7.38	0.06
Er	$XOErSO_4$	-2.40	0.11	$(XO)_2ErSO4^-$	-7.39	0.05
Tm	$XOTmSO_4$	-2.27	0.08	$(XO)_2TmSO4^-$	-7.17	0.08
Yb	$XOYbSO_4$	-2.13	0.08	$(XO)_2YbSO4^-$	-7.26	0.04
Lu	$XOLuSO_4$	-2.19	0.09	$(XO)_2LuSO4^-$	-7.13	0.09

3.1.3 Model validation

Log K_M values from experimental data of sorption conducted at high sulfate concentration were tested with the results from sorption experiments with lower sulfate content: 0.5 mM (in the experiments with basaluminite) and 2 mM SO_4 (in the experiments with schwertmannite). The sorption fraction for each REE was calculated with the PHREEQC software, taking into account the experimental conditions (temperature of 25°C and a pCO_2 of 3.5) and the surface properties of the minerals calculated previously.

Only in basaluminite experimental results, at higher pH values than 6.5 a mismatch between the modeled sorbed fractions and the experimental ones

(symbols) for the experiment with the lower sulfate content is attributed to the presence of dissolved carbonate species. Thus, MCO_3^+ species form and take part in the sorption process. To show the possible role of carbonate complexes at pH higher than 6.5 and low sulfate concentration, the sorption of MCO_3^+ complexes has been included in the model. The equilibrium constants for the MCO_3^+ sorption reactions have been recalculated from those reported by Quinn et al. (2006b) for goethite. Including carbonate complexation, the model predicts sorption at near neutral pH when lower sulfate is present in solution, supporting the role of carbonate complexation at such particular conditions (Figure 3.4 A,B).

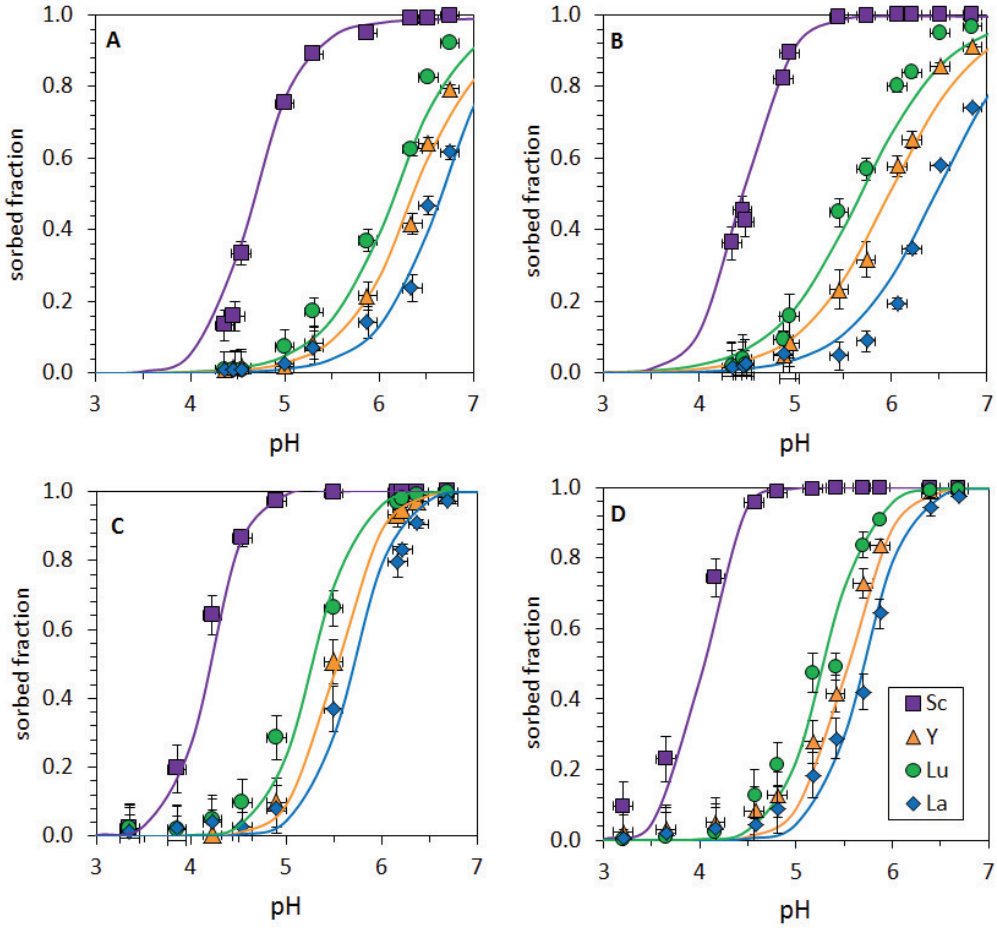

Figure 3.4 Experimental (symbols) and calculated fractions (lines) of the sorption curves for Sc, Y, La and Lu for the experiments (A,C) with 20 mM SO_4 and 0.5(B) and 2 mM SO_4 (D) in basaluminite (A, B) and schwertmannite (C,D) solids. Calculations at 25°C and atmospheric CO_2 pressure.

As expected, the model reproduces well the sorption edges in the experiments with 20 mM SO_4 (Figure 3.4 B,D) with occasional predictions outside the experimental error. Although worse, the model for the experiment

with lower sulfate concentration is also acceptable, and the predicted values in general fit the analyses within the experimental error (Figure 3.4 A,C). The good fit between the predicted and measured Sc values confirms a good model prediction for the formation of bidentate surface complexes with $ScSO_4^+$ and $ScOH^{2+}$ with the surfaces of the two minerals.

Finally, the model was also validated with data sets of new sorption experiments varying the solid:liquid ratios and keeping constant the concentration of 20 mM dissolved sulfate. As expected, the model predicts lower adsorption for the lower 0.25 g/L basaluminite suspensions (Figure 3.5A). In the case of schwertmannite, despite a slight overprediction at higher pH values for the 0.25 g/L solid:liquid ratio, the sorbed fractions for 2 g/L suspensions were successfully predicted by the model within the experimental errors (Figure 3.5 B).

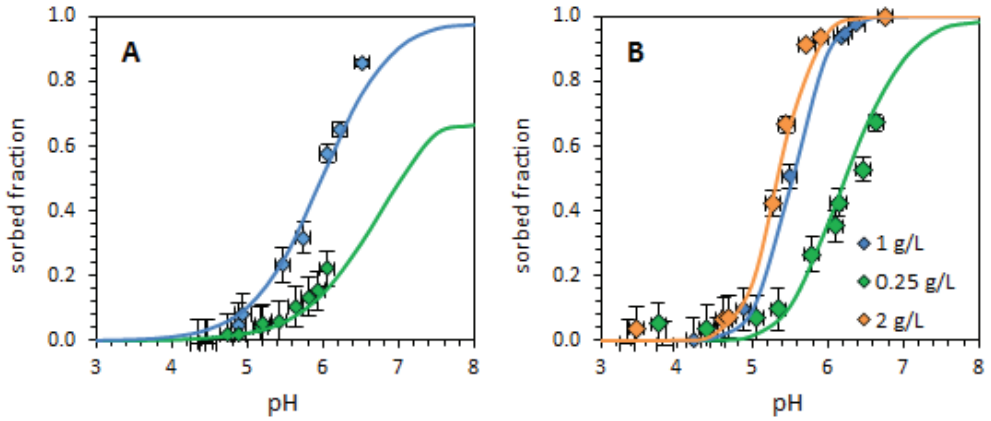

Figure 3.5 Comparison between experimental data (symbols) and calculated fraction (lines of the sorption edge curves for sorbed Y in 20mM SO_4 solutions with (A) basaluminite and (B) schwertmannite, at different solid liquid ratios. Calculations at 25°C and pCO_2 of 3.5.

3.2 REE behavior in passive remediation systems

The surface complexation model validated with experimental data let predict us the behavior of REE in laboratory-scale columns of passive remediation systems and explain the REE partition between solids and acidic waters when mixing with circumneutral streams in the field.

The prediction of the mobility of REE in pore water of a column system was performed with a reactive transport model accounting the calcite dissolution

according to the kinetic low described by Plummer et al., 1979. The results of the 1D reactive transport model (lines) were used to interpret the experimental data (symbols) (Figure 3.6). For a given time the pH increased with depth, and for a given depth the column was progressively invaded by more acidic water (Figure 3.6 A). A schwertmannite front appeared first, at lower pH values (pH 2.5), followed by a basaluminite front (pH 3.6 to 6). Both fronts advanced downwards as the column was progressively invaded by more acidic water (Figure 3.6 D,E). The calculations indicate that calcite was exhausted from the top of the column downwards (Figure 3.6 F), then the acid water extracted the alkalinity to form schwertmannite from the basaluminite already precipitated in previous times. As a consequence of the process, the Al concentration in the pore water increased above the inflow concentration (Figure 3.6 C).

According to Figure 3.4 C, sorption of yttrium and lanthanides would occur at pH higher than 4, far above the pH at which schwertmannite formed (from 2.5 to 3.5) and therefore, these REE are not expected to be sorbed on this mineral. Unlikely, scandium sorption on schwertmannite started at pH 3, and therefore a small fraction could be sorbed on this mineral. According to Figure 3.4 A, sorption of all REE including Sc, can take place on basaluminite, which formed at pH between 3.5 and 6. As a consequence, the REE sorption in the column occurred on basaluminite. As schwertmannite progressed at expenses of basaluminite dissolution at pH 3.5, a small fraction of Sc could als take place on schwertmannite. Thus, the similar La and Y distribution in pore water in contrast to the different behavior of Sc was evidence in both the measured and calculated pore water concentrations (Figure 3.6 G-I).

The calculated solid phase distribution at the end of the column life (Figure 3.6 D-E, 56 days) was also consistent with that deduced from sequential extraction analyses (Figure 2.8 B-E). Thus, schwertmannite was predicted to form between 0 and 11 cm, especially in the shallower 4 cm. A basaluminite zone was calculated to develop between 11 and 20 cm, comparable to the observed range between 7 and 20 cm. The calculated pH value in the lowermost 10 cm range from 3.8 to 6, indicating that La, Y and Sc could remain sorbed on basaluminite, in accordance with sequential extraction analyses and with the absence of REE in the column outflow. However, the presence of Sc analyzed in the upper 10 cm of solid residue indicates that desorption was not entirely reversible. The preferential lanthanides and yttrium retention by basaluminite has been also described by Ayora et al. (2016), where a similar AMD column experiment was carried out. Similarly, Zhang and Honaker (2018) also explained a REE enrichment in the Al-rich precipitate formed when neutralizing with NaOH the leachate from a coal refuse piles.

Interestingly, these authors also observed some Sc in the Fe-rich precipitates formed at pH between 3.3 and 4.6.

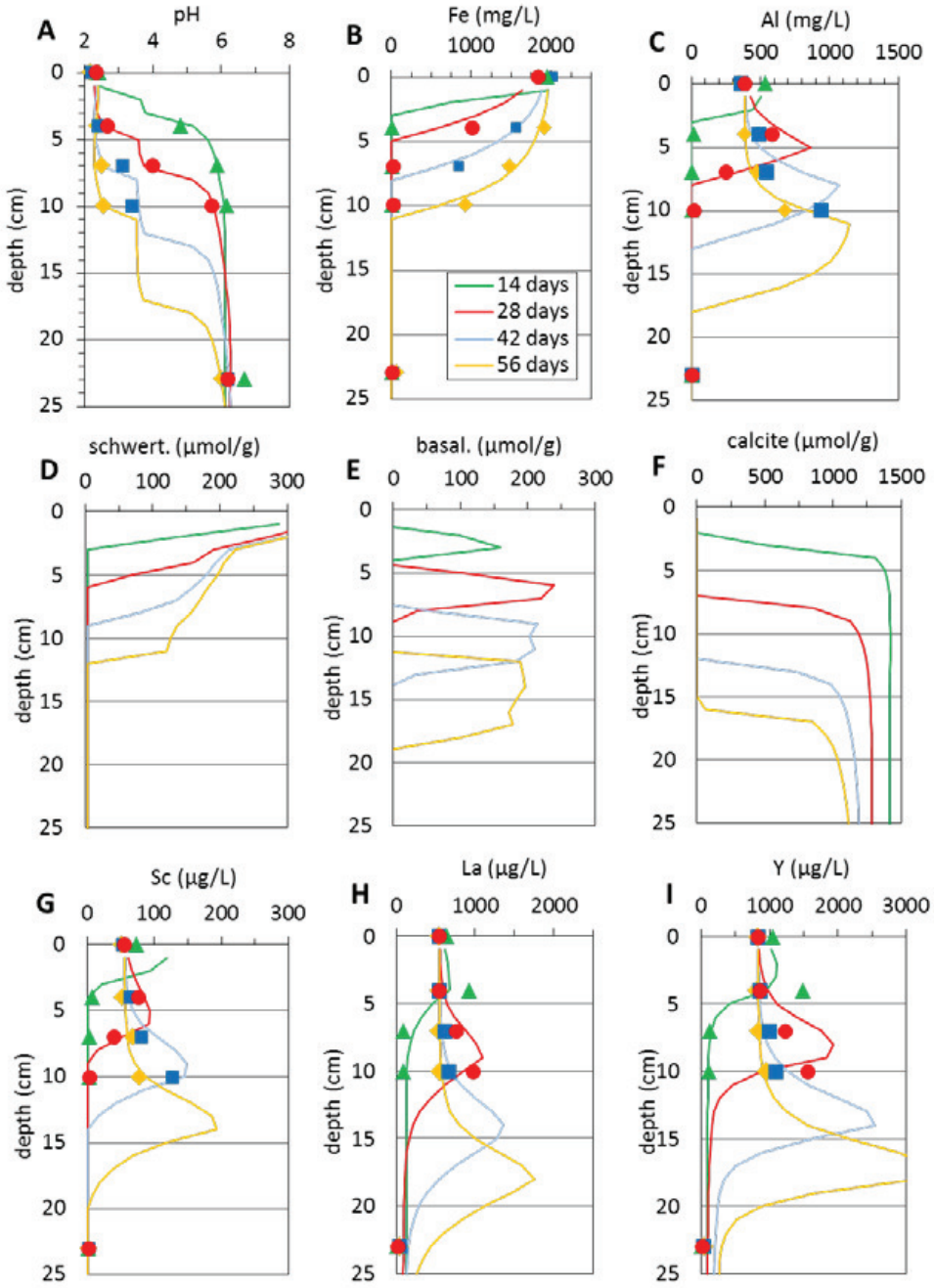

Figure 3.6 Depth profiles of experimental data (symbols) and the reactive transport model (lines) at four different stages of column operation: (A) pH evolution; (B, C) Fe and Al concentrations in pore water; (D, E, F) mineral distributions; (G, H, I) concentrations of selected REE in pore water.

3.2.1 Yttrium species in waste samples from passive treatments

The k^3-weighted EXAFS of the samples from other two laboratory-scale columns of passive remediation systems of the two AMD waters (Monte Romero: W-MR-C1-4, W-MR-C1-5 and Almagrera: W-Alm-C3-8, W-Alm-C3-9) and their Fourier transform (FT) envelope functions with corrected phase shifts are shown in Figure 2.6. The waste samples were selected from the depth where the major proportion of Al precipitated, assuming basaluminite precipitation. Visual comparisons of the EXAFS spectra of the column samples reveal a strong similarity between them, suggesting similar local order of Y in all the samples. In addition, the EXAFS spectra of the column samples are very similar to those of the solid references (B-YSO_4-ads, B-Y-ads, B-Y-cop, and A-Y-ads). They have a shoulder at ~6.5 $Å^{-1}$, indicating a higher frequency, which is absent in the aqueous samples (see the arrow in Figure 2.6).

The results of LCF of the waste samples with B-YSO4-ads and YSO4-sol references show that more than 72% of Y adopts a local geometry similar to that of the B-YSO4-ads reference (with the exception of sample W-Alm-C3-8) (Table 3.2). Thus, the majority of Y solid speciation present in the Al-rich waste from column treatments is expected to form monodentate-inner sphere complex with basaluminite surface, as indicated the best fit of the B-YSO4-ads EXAFS signal (Table 2.1), and which in turn is consistent with the sorption model of REE onto basaluminite.

Table 3.2 Percentages of Y species in the column samples obtained from LCF of the EXAFS spectra

Standard	W-MR-C1-4	W-MR-C1-5	W-Alm-C3-8	W-AlmC3-9
B-YSO4ads	0.719 ± 0.036	0.867 ± 0.038	0.495 ± 0.059	0.746 ± 0.061
YSO4-solution	0.281 ± 0.069	0.133 ± 0.071	0.505 ± 0.084	0.254 ± 0.085
R-factor	0.14	0.14	0.29	0.30
$\chi 2$	133	154	371	392

3.3 REE mobility in natural attenuation of AMD

The REE partition between aqueous and solid phase from samples of the two field sites are modeled assuming sorption onto basaluminite due to the higher Al concentration measured in the solid samples, in which basaluminite was the major solid phase. According to Eq. 3.1, the REE concentration of the aqueous phase and the free sorption sites were needed to predict the REE concentration in the solid phase, which were calculated from the acidic inputs.

The aqueous phase coexisting with the basaluminite precipitates at the mixing points from the Odiel-Tinto localities contained very low amount of REE and the REE concentration of the acidic stream was used as a base to calculate the activity of the aqueous species. In the case of Arroyo del Val, where the acidic water is the main flow, only a minor dilution took place and the acid water upstream the mixing was used in the calculations. To estimate the S:L ratio and the total sorption sites it was assumed that the Al transferred from the acid water to the solid phase and then converted stoichiometrically into basaluminite.

Both, the calculated and measured REE concentration in the solid phase were normalized to the NASC standard (Gromet et al., 1984) and compared. The predicted REE concentrations were higher or lower than the observed. This could be due to several uncertainties and it is discussed below. In order to facilitate the comparison of the measured and calculated REE patterns, the calculated concentrations were arbitrarily multiplied by a factor f until both observed and calculated Gd values coincided. Gadolinium was selected because it occupies a central location in the lanthanide series.

The pH value at which sorption occurred can be estimated from the REE distribution pattern. According to the sorption variation with pH calculated with the model (Figure 3.4), the different REE undergo very different sorption efficiencies at a given pH. For instance, at pH 6 the calculations predict more HREE and Sc to be sorbed than LREE, and their relative values are overpredicted with respect to measurements. Thus, the REE distribution pattern can provide information about the sorption pH and the final calculated patterns were obtained by manually selecting the factor f and pH values that allow the best fit between the predictions and the observations. The best fits of the measured REE patterns from solids together with the pH and factor f values are plotted in Figure 3.7.

A f value lower than 1 indicates that the calculated values of REE were in excess with respect to the observations, and the product by a factor lower than 1 was therefore required to fit the pattern. The reverse holds for f values higher than 1. The difference from the unity is attributed to uncertainties in one or several parameters used in the calculations: the specific surface area, the solid:liquid (S:L) ratio, calculated from the Al removal from the acidic source, and the exact pH at which sorption occurred.

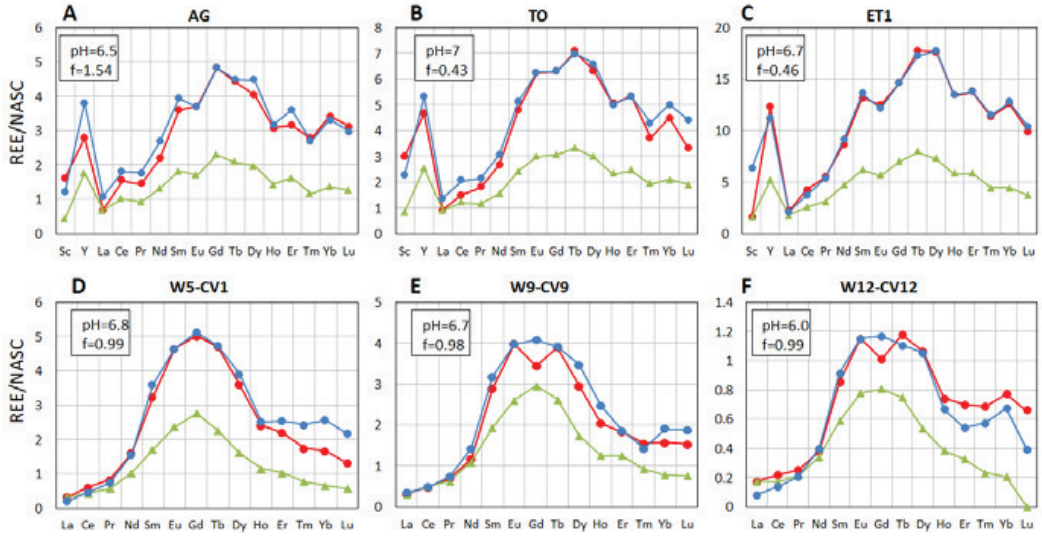

Figure 3.7 REE patterns of precipitates analyzed (red) and predicted (blue) of the parent AMD (green triangles). All the concentrations normalized to North American Shale Composite (NASC). (A, B, C) Samples from Odiel-Tinto site, (D, E, F) Samples from Arroyo del Val site.

The effect that parameter uncertainties have on the f factor value was evaluated varying each parameter and keeping the rest constant. Depending on the parameter, the f factor can change significantly with different changes in the parameter. For instance, f needs to increase by 1.54 times with a decrease of 2 decimals in the pH value, or f needs to double its value if the specific surface area is divided by two. Thus, the f factor is very sensitive with each parameter and it cannot differentiate individually.

Despite this inconvenience, the model matched the observed trend of REE values within the order of magnitude taking into account the f factor value. However, the feasibility of the model to anticipate the REE concentration in the precipitates from the composition of the aqueous phases and the mixing ratios is required. In this sense, the dilution process to mixing waters could affect the S:L sorption and thus account partially to the f factor value. The dilution of the acidic water in the final mixture was independently calculated using sulfate

concentrations. No correlations between dilution and f factor values were observed so the f factor value cannot be approximated from the mixing waters.

Another source of uncertainty is the pH at which sorption occurs. However, there is no correlation between the pH obtained from the calculated fitting of the measured REE patterns and the pH measured in the water coexisting the precipitates. All these calculations assume that all reactions are in a close system. However, since there is an open flow setting, reactions are not synchronous and total masses may not be conservative. Thus, basaluminite starts to form early as the pH increases above 4, whereas significant REE sorption occurs at pH vales between 5 and 7, at which point some of the basaluminite may have been transported downstream. Since the pH and f factor values required to fit the measured REE patterns cannot be independently anticipated from the composition and from proportions of the mixing waters, the model cannot be used for blind predictions of the REE concentrations of the precipitates in open flow settings.

4 General conclusions

The main goal of this thesis has been to understand the mechanism of REE retention in basaluminite and schwertmannite minerals that precipitates in AMD passive remediation systems and in mixing zones of AMD with neutral waters. Answering or developing a sum-up of the goals highlighted at the beginning of the thesis, we highlight the following general conclusions:

Batch sorption experiments confirm that basaluminite and schwertmannite scavenge REE through sorption mechanism. The REE sorption is highly dependent on the pH and it becomes effective for Y and lanthanides from around pH 5 and for Sc from around one pH unit lower in both minerals for solid:liquid ratios of 1g/L. Lanthanide fractionation occurs in basaluminite and schwertmannite precipates, yielding and HREE enrichment onto the solids. These results are analogous to the fractionation observed in Al and Fe oxide/hydroxide precipitates in the confluence of the AMD waters with natural streams and rivers.

A non-electrostatic surface complexation model has been proposed to explain the sorption mechanism. In the model description, sulfate plays a key role due to its strong complexation with REE leads to sorption of the aqueous sulfate complex MSO_4^+, rather than the free ion M^{3+}, as commonly described by other authors for REE sorption in oxides. Only Sc presents important fraction of aqueous $ScOH^{2+}$ at low sulfate concentrations and is also accounted in the sorption modeling. The equilibrium constants are validated with experiments with lower sulfate concentration (0.5 to 2 mM) and a different solid:liquid ratios (0.5-2 g/L) and the sorption model reproduces the sorption at the different experimental conditions.

The model describes sorption of lanthanides and yttrium as the exchange of one proton from the basaluminite surface, and as the exchange of two protons from schwertmannite surface with the aqueous sulfate complexes. Thus, the MSO_4^+ aqueous species form monodentate surface complexes with

basaluminite and bidentate with schwertmannite. In the case of Sc, both $ScSO_4^+$ and $ScOH^{2+}$ form bidentate surface complexes with the two minerals.

The results of the PDF and EXAFS analysis and AIMD simulations of the aqueous complex YSO_4^+ describe the formation of a monodentate inner sphere ion-pair between the Y and the S, with an interatomic distance of 3.5 Å.

The EXAFS fitting and PDF results of YSO_4 adsorbed onto basaluminite confirmed the strong interaction and the formation of inner-sphere complex between Y and basaluminite surface, as the sorption model described an exchange MSO_4^+ with one surface proton. However, EXAFS technique by itself cannot confirm the presence of the aqueous YSO_4^+ sorbed into its surface due to the low sensitivity to discern between Al and S neighbors.

The ageing experiments show that basaluminite is a metastable precipitate and its ageing in/near neutral waters can trigger its transformation into more stable Al hydroxide phases. However, basaluminite tends to stabilize when sulfate is present in solution, inhibiting its transformation to nanoboehmite. Moreover, the local structure of basaluminite is identical to $Al(OH)_3$ and sulfate is incorporated into the $Al(OH)_3$ without any effect on its local structure. The evolution of pure basaluminite with increasing pH, releasing sulfate into solution and transforming into nanoboehmite, would result in REE release or its restructuration into the surface of the mineral.

The sorption model combined with a 1D transport model successfully predicts the evolution of aqueous REE analyzed from the pore water of a laboratory column simulating a passive remediation system. The REE recovery is due to sorption mechanism carried out by basaluminite and schwertmannite precipitates, but also due to the REE desorption and/or basaluminite dissolution when the acid front progresses downwards the column along the time. The acid front progression affect less to schwertmannite precipitates, in which Sc preferentially remains sorbed because it is partially desorbed at lower pH, compared to the rest of REE. As practical consequence, REE preferentially accumulate in the basaluminite residue of AMD passive treatment systems, but a minor fraction of Sc can also be found in the schwertmannite waste. Thus, the pH control is essential to design a selective recovery.

When an AMD mixes with an alkaline stream, a mixture of schwertmannite and basaluminite precipitate. The behavior of REE during the mixing is conservative at low pH (pH<4), whereas they are scavenged by the flocculates at near neutral pH. This confirms the observations made by previous studies and suggests that Al-phases could be responsible for REE retention. When Fe

and Al phases can be sampled separately, schwertmannite does not contain REE, which are entirely retained in basaluminite, indicating that basaluminite phase is the main responsible for the REE removal. The lack of REE in schwertmannite is attributed to the formation of this mineral at pH values below 4, whereas basaluminite precipitation occurs at pH values higher than 4.

The sorption model applied with basaluminite surface is able to anticipate the main trends of the REE distribution patterns observed in the Al-rich solids recovered in the field sites, regardless the sulfate concentration in the acid drainage. The distribution patterns confirm the selective sorption of MREE, HREE and Y over LREE. However, the model fails to predict the REE concentrations in the precipitates from the composition and proportions of the mixing streams due to the asynchronous precipitation of basaluminite and REE sorption in an open fluid setting.

5 Bibliography

Acero P., Ayora C., Torrentó C. and Nieto J. M. (2006) The behavior of trace elements during schwertmannite precipitation and subsequent transformation into goethite and jarosite. *Geochim. Cosmochim. Acta* **70**, 4130–4139.

Alonso E., Sherman A. M., Wallington T. J., Everson M. P., Field F. R., Roth R. and Kirchain R. E. (2012) Evaluating Rare Earth Element a Vailability : a Case With Revolutionary Demand From Clean Technologies. *Environ. Sci. Technol.* **46**, 3406–3414.

Auqué L. F., Tena J. M., Gimeno M. J., Mandado J., Zamora A. and López Julián P. L. (1993) Distribución de tierras raras en soluciones y coloides de un sistema natural de aguas ácidas (Arroyo del Val, Zaragoza). *Estud. Geol.* **49**, 41–48.

Ayora C., Caraballo M. A., Macias F., Rötting T. S., Carrera J. and Nieto J. M. (2013) Acid mine drainage in the Iberian Pyrite Belt: 2. Lessons learned from recent passive remediation experiences. *Environ. Sci. Pollut. Res.* **20**, 7837–7853.

Ayora C., Macías F., Torres E., Lozano A., Carrero S., Nieto J. M., Pérez-López R., Fernández-Martínez A. and Castillo-Michel H. (2016) Recovery of Rare Earth Elements and Yttrium from Passive-Remediation Systems of Acid Mine Drainage. *Environ. Sci. Technol.* **50**, 8255–8262.

Bau M. (1999) Scavenging of dissolved yttrium and rare earths by precipitating iron oxyhydroxide: Experimental evidence for Ce oxidation, Y-Ho fractionation, and lanthanide tetrad effect. *Geochim. Cosmochim. Acta* **63**, 67–77.

Bonnail E., Pérez-López R., Sarmiento A. M., Nieto J. M. and DelValls T. Á. (2017) A novel approach for acid mine drainage pollution biomonitoring using rare earth elements bioaccumulated in the freshwater clam Corbicula fluminea. *J. Hazard. Mater.* **338**, 466–471.

Burton E. D., Bush R. T., Sullivan L. A. and Mitchell D. R. G. (2008)

Schwertmannite transformation to goethite via the Fe(II) pathway: Reaction rates and implications for iron-sulfide formation. *Geochim. Cosmochim. Acta* **72**, 4551–4564.

Byrne R. H. and Kim K.-H. (1990) Rare earth elements scavenging in seawater. *Geochim. Cosmochim. Acta* **54**, 2645–2656.

Byrne R. H. and Sholkovitz E. R. (1996) Chapter 158 Marine chemistry and geochemistry of the lanthanides. *Handb. Phys. Chem. Rare Earths* **23**, 497–593. Available at: https://www.sciencedirect.com/science/article/pii/S0168127396230090 [Accessed May 10, 2018].

Caraballo M. A., Macías F., Nieto J. M., Castillo J., Quispe D. and Ayora C. (2011) Hydrochemical performance and mineralogical evolution of a dispersed alkaline substrate (DAS) remediating the highly polluted acid mine drainage in the full-scale passive treatment of Mina Esperanza (SW Spain). *Am. Mineral.* **96**, 1270–1277.

Carrero S., Fernandez-Martinez A., Pérez-López R., Lee D., Aquilanti G., Poulain A., Lozano A. and Nieto J. M. (2017) The nanocrystalline structure of basaluminite, an aluminum hydroxide sulfate from acid mine drainage. *Am. Mineral.* **102**, 2381–2389.

Chakhmouradian A. R. and Wall F. (2012) Rare earth elements: Minerals, mines, magnets (and more). *Elements* **8**, 333–340.

Chakhmouradian A. R. and Zaitsev A. N. (2012) Rare earth mineralization in igneous rocks: Sources and processes. *Elements* **8**, 347–353.

Connelly N. G., Hartshorn R. M., Damhus T. and Hutton A. T. (2005) *Nomenclature of Inorganic Chemistry IUPAC Recommendations 2005*.,

Cravotta C. A. and Trahan M. K. (1999) Limestone drains to increase pH and remove dissolved metals from acidic mine drainage. *Appl. Geochemistry* **14**, 581–606.

Cruz-Hernández P., Carrero S., Pérez-López R., Fernandez-Martinez A., Lindsay M. B. J., Dejoie C. and Nieto J. M. Influence of As (V) on precipitation and transformation of schwertmannite in acid mine drainage-impacted waters. *Eur. J. Mineral.* **31**, 237–245.

Dai Y., Li Jian, Li Jie, Yu L., Dai G., Hu A., Yuan L. and Wen Z. (2002) Effects of Rare Earth Compounds on Growth and Apoptosis of Leukemic Cell Lines. *Vitr. Cell. Dev. Biol. - Anim.* **38**, 373–375.

Dardenne B. K., Schäfer T., Denecke M. A., Rothe J. and Kim J. I. (2001) Identification and characterization of sorbed lutetium species on 2-line ferrihydrite by sorption data modeling, TRLFS and EXAFS. *Radiochim. Acta* **89**, 469–479.

Davis J. A. and Kent D. B. (1990) Surface Complexation Modeling in Aqueous Geochemistry. In *Reviews in Mineralogy and Geochemistry* (eds. M. F. Hochella and A. F. White). pp. 177–260.

Elderfield H., Upstill-Goddard R. and Sholkovitz E. R. (1990) The rare earth elements in rivers , estuaries , and coastal seas and their significance to the composition of ocean ... *Geochim. Cosmochim. Acta* **54**, 971–991.

Estes S. L., Arai Y., Becker U., Fernando S., Yuan K., Ewing R. C., Zhang J., Shibata T. and Powell B. A. (2013) A self-consistent model describing the thermodynamics of Eu(III) adsorption onto hematite. *Geochim. Cosmochim. Acta* **122**, 430–447.

Evangelou V. P. and Zhang Y. L. (1995) A review: Pyrite oxidation mechanisms and acid mine drainage prevention. *Crit. Rev. Environ. Sci. Technol.* **25**, 141–199.

Farkas L. and Pertlik F. (1997) Crystal structure determinations of felsöbányaite and basaluminite, Al4(SO4)(OH)10·4H2O. *Acta Mineral.* **38**, 5–15.

Fernández-Martínez A., Timon V., Romaman-Ross G., Cuello G. J., Daniels J. E. and Ayora C. (2010) The structure of schwertmannite, a nanocrystalline iron oxyhydroxysulfate. *Am. Mineral.* **95**, 1312–1322.

Ferreira da Silva E., Bobos I., Xavier Matos J., Patinha C., Reis A. P. and Cardoso Fonseca E. (2009) Mineralogy and geochemistry of trace metals and REE in volcanic massive sulfide host rocks, stream sediments, stream waters and acid mine drainage from the Lousal mine area (Iberian Pyrite Belt, Portugal). *Appl. Geochemistry* **24**, 383–401. Available at: http://dx.doi.org/10.1016/j.apgeochem.2008.12.001.

Gammons C. H., Wood S. A., Jonas J. P. and Madison J. P. (2003) Geochemistry of the rare-earth elements and uranium in the acidic Berkeley Pit lake, Butte, Montana. *Chem. Geol.* **198**, 269–288.

Gammons C. H., Wood S. A., Pedrozo F., Varekamp J. C., Nelson B. J., Shope C. L. and Baffico G. (2005) Hydrogeochemistry and rare earth element behavior in a volcanically acidified watershed in Patagonia, Argentina. *Chem. Geol.* **222**, 249–267.

Gimeno M. J., Auqué Sanz L. F. and Nordstrom D. K. (2000) REE speciation in low-temperature acidic waters and the competitive effects of aluminum. *Chem. Geol.* **165**, 167–180.

Grawunder A., Merten D. and Büchel G. (2014) Origin of middle rare earth element enrichment in acid mine drainage-impacted areas. *Environ. Sci. Pollut. Res.* **21**, 6812–6823.

Gromet L. P., Dymek R. F., Haskin L. A. and Korotev R. L. (1984) The “North American Shale Composite”: Its compilations, major and trace element

characteristics. *Geochim. Cosmochim. Acta* **48**, 2469–2482. Available at: papers3://publication/uuid/4B96DB2E-EA61-4063-85C3-0C3E3AADE7FD.

Hatch G. P. (2012) Dynamics in the global market for rare earths. *Elements* **8**, 341–346.

Hedin R. S., Watzlaf G. R. and Nairn R. W. (1994) Passive Treatment of Acid Mine Drainage with Limestone. *J. Environ. Qual.* **23**, 1338–1345. Available at: https://www.agronomy.org/publications/jeq/abstracts/23/6/JEQ0230061338.

Henderson P. (1984) General Geochemical Properties and Abundances of the Rare Earth Elements. In *Developments in Geochemistry* (ed. P. Henderson). pp. 1–32. Available at: http://www.sciencedirect.com/science/article/pii/B978044442148750006X.

Kawabe I. (1999a) Hydration change of aqueous lanthanide ions and tetrad effects in lanthanide(III)-carbonate complexation. *Geochem. J.* **33**, 267–275.

Kawabe I. (1999b) Thermochemical parameters for solution of lanthanide (III) ethylsulphate and trichloride hydrate series: Tetrad effects and hydration change in aqua Ln3+ ion series. *Geochem. J.* **33**, 249–265.

Koeppenkastrop D. and De Carlo E. H. (1992) Sorption of rare-earth elements from sea water onto synthetic mineral particles: An experimental approach. *Chem. Geol.* **95**, 251–263.

Li X. and Wu P. (2017) Geochemical characteristics of dissolved rare earth elements in acid mine drainage from abandoned high-As coal mining area, southwestern China. *Environ. Sci. Pollut. Res.* **24**, 20540–20555.

Lin J., Nilges M. J., Wiens E., Chen N., Wang S. and Pan Y. (2019) Mechanism of Gd3+ uptake in gypsum (CaSO4·2H2O): Implications for EPR dating, REE recovery and REE behavior. *Geochim. Cosmochim. Acta* **258**, 63–78. Available at: https://doi.org/10.1016/j.gca.2019.05.019.

Liu H., Pourret O., Guo H. and Bonhoure J. (2017) Rare earth elements sorption to iron oxyhydroxide: Model development and application to groundwater. *Appl. Geochemistry* **87**, 158–166. Available at: https://doi.org/10.1016/j.apgeochem.2017.10.020.

Marmier N., Delise A. and Fromage F. (1999) Surface Complexation Modeling of Yb (III) and Cs (I) Sorption on Silica. **233**, 228–233.

Marmier N., Dumonceau J. and Fromage F. (1997) Surface complexation modeling of Yb(III) sorption and desorption on hematite and alumina. *J. Contam. Hydrol.* **26**, 159–167.

Massari S. and Ruberti M. (2013) Rare earth elements as critical raw materials: Focus on international markets and future strategies. *Resour. Policy* **38**, 36–43. Available at: http://dx.doi.org/10.1016/j.resourpol.2012.07.001.

McLennan S. M. (1989) Rare Earth Elements in Sedimentary Rocks: Influence of Provenance and Sedimentary Processes. *Rev. Mineral. Geochemistry* **11**, 169–200.

Morgan B., Johnston S. G., Burton E. D. and Hagan R. E. (2016) Acidic drainage drives anomalous rare earth element signatures in intertidal mangrove sediments. *Sci. Total Environ.* **573**, 831–840. Available at: http://dx.doi.org/10.1016/j.scitotenv.2016.08.172.

Nordstrom D. K. (2011) Hydrogeochemical processes governing the origin, transport and fate of major and trace elements from mine wastes and mineralized rock to surface waters. *Appl. Geochemistry* **26**, 1777–1791. Available at: http://dx.doi.org/10.1016/j.apgeochem.2011.06.002.

Nordstrom D. K., Blowes D. W. and Ptacek C. J. (2015) Hydrogeochemistry and microbiology of mine drainage: An update. *Appl. Geochemistry* **57**, 3–16. Available at: http://dx.doi.org/10.1016/j.apgeochem.2015.02.008.

Ohta A. and Kawabe I. (2000) Rare eath element partitioning between fe oxyhydroxide precipitates and aqueous NaCl solutions doped with NaHCO3: Determinations of rare earth element complexation constants with carbonate ions. *Geochem. J.* **34**, 439–454.

Ohta A. and Kawabe I. (2001) REE (III) adsorption onto Mn dioxide (δ-MnO2) and Fe oxyhydroxide: Ce(III) oxidation by δ-MnO2. *Geochim. Cosmochim. Acta* **65**, 695–703. Available at: http://linkinghub.elsevier.com/retrieve/pii/S0016703700005780.

Pagano G., Guida M., Tommasi F. and Oral R. (2015) Health effects and toxicity mechanisms of rare earth elements-Knowledge gaps and research prospects. *Ecotoxicol. Environ. Saf.* **115**, 40–48. Available at: http://dx.doi.org/10.1016/j.ecoenv.2015.01.030.

Plummer L. N., Parkhurst D. L. and Wigley T. M. L. (1979) Critical Review of the Kinetics of Calcite Dissolution and Precipitation. In *Chemical Modeling in Aqueous Systems* ACS Symposium Series. AMERICAN CHEMICAL SOCIETY. pp. 25–537. Available at: https://doi.org/10.1021/bk-1979-0093.ch025.

Pourret O. and Davranche M. (2013) Rare earth element sorption onto hydrous manganese oxide: A modeling study. *J. Colloid Interface Sci.* **395**, 18–23. Available at: http://dx.doi.org/10.1016/j.jcis.2012.11.054.

Quinn K. A., Byrne R. H. and Schijf J. (2004) Comparative scavenging of yttrium and the rare earth elements in seawater: Competitive influences of solution and surface chemistry. *Aquat. Geochemistry* **10**, 59–80.

Quinn K. A., Byrne R. H. and Schijf J. (2006a) Sorption of yttrium and rare earth elements by amorphous ferric hydroxide: Influence of solution complexation with carbonate. *Geochim. Cosmochim. Acta* **70**, 4151–4165.

Quinn K. A., Byrne R. H. and Schijf J. (2006b) Sorption of yttrium and rare earth elements by amorphous ferric hydroxide:Influence of pH and ionic strength. *Mar. Chem.* **99**, 128–150.

Rabung B. T., Geckeis H., Wang X. K., Rothe J., Denecke M. A., Klenze R. and Fanghänel T. (2006) Cm (III) sorption onto γ-Al2O3: New insight into sorption mechanisms by time-resolved laser fluorescence spectroscopy and extended X-ray absorption fine structure. *Radiochim. Acta* **94**, 609–618.

Rabung B. T., Stumpf T., Geckeis H., Klenze R. and Kim J. I. (2000) Sorption of Am (III) and Eu (III) onto γ-alumina : experiment and modelling. **88**, 711–716.

Rabung T., Geckeis H., Kim J. Il and Beck H. P. (1998) Sorption of Eu(III) on a natural hematite: Application of a surface complexation model. *J. Colloid Interface Sci.* **208**, 153–161.

Roncati L., Gatti A. M., Barbolini G., Piscioli F., Pusiol T. and Maiorana A. (2018) In Vivo Uptake of Rare Earth Metals by Triple-Negative Breast Cancer Cells. *Pathol. Oncol. Res.* **24**, 161–165.

Rötting T. S., Thomas R. C., Ayora C. and Carrera J. (2008) Passive treatment of acid mine drainage with high metal concentrations using dispersed alkaline substrate. *J. Environ. Qual.* **37**, 1741–1751.

Sánchez-España J., Yusta I., Gray J. and Burgos W. D. (2016) Geochemistry of dissolved aluminum at low pH: Extent and significance of Al-Fe(III) coprecipitation below pH 4.0. *Geochim. Cosmochim. Acta* **175**, 128–149.

Schwertmann U. and Carlson L. (2005) The pH-dependent transformation of schwertmannite to goethite at 25°C. *Clay Miner.* **40**, 63–66. Available at: http://www.scopus.com/inward/record.url?eid=2-s2.0-16344390427&partnerID=40&md5=1f29020dec377318ae72a6ea4a7a0bca.

Sholkovitz E. R. (1995) The aquatic chemistry of rare earth elements in rivers and estuaries. *Aquat. Geochemistry* **1**, 1–34.

Stewart B. W., Capo R. C., Hedin B. C. and Hedin R. S. (2017) Rare earth element resources in coal mine drainage and treatment precipitates in the Appalachian Basin, USA. *Int. J. Coal Geol.* **169**, 28–39. Available at: http://dx.doi.org/10.1016/j.coal.2016.11.002.

Tertre E., Hofmann A. and Berger G. (2008) Rare earth element sorption by basaltic rock: Experimental data and modeling results using the "Generalised Composite approach." *Geochim. Cosmochim. Acta* **72**, 1043–

1056.

U.S. Geological Survey (USGS) (2019) *Mineral Commodity Summaries*. 2019th ed. ed. U.S. Geological Surve, Reston, Virginia.

Vallejo J., Cano J., Castro I., Julve M., Lloret F., Fabelo O., Cañadillas-Delgado L. and Pardo E. (2012) Slow magnetic relaxation in carbonato-bridged dinuclear lanthanide(III) complexes with 2,3-quinoxalinediolate ligands. *Chem. Commun.* **48**, 7726–7728.

Verplanck P. L., Nordstrom D. K., Taylor H. E. and Kimball B. A. (2004) Rare earth element partitioning between hydrous ferric oxides and acid mine water during iron oxidation. *Appl. Geochemistry* **19**, 1339–1354.

Viadero R. C., Wei X. and Buzby K. M. (2006) Characterization and Dewatering Evaluation of Acid Mine Drainage Sludge from Ammonia Neutralization. *Environ. Eng. Sci.* **23**, 734–743.

Wang Z. and Giammar D. E. (2013) Mass action expressions for bidentate adsorption in surface complexation modeling: Theory and practice. *Environ. Sci. Technol.* **47**, 3982–3996.

Xiangke W., Wenming D., Xiongxin D., Aixia W., Jinzhou D. and Zuyi T. (2000) Sorption and desorption of Eu and Yb on alumina: Mechanisms and effect of fulvic acid. *Appl. Radiat. Isot.* **52**, 165–173.

Zhang W. and Honaker R. Q. (2018) Rare earth elements recovery using staged precipitation from a leachate generated from coarse coal refuse. *Int. J. Coal Geol.* **195**, 189–199.

Zhuang G., Zhou Y., Lu H., Lu W., Zhou M., Wang Y., Tan M. (1996). Concentration of rare earth elements, As, and Th in human brain and brain tumors, determined by neutron activation analysis. *Biol. Trace Elem. Res*. **53**, 45–49.

6 Annex

Article 1

Local structure and ageing of basaluminite at different pH values and sulphate concentrations

Published in: *Chemical Geology* 2018, 496, 25-35.

Chemical Geology 496 (2018) 25–33

Contents lists available at ScienceDirect

Chemical Geology

journal homepage: www.elsevier.com/locate/chemgeo

Local structure and ageing of basaluminite at different pH values and sulphate concentrations

Alba Lozano[a,*], Alejandro Fernández-Martínez[b], Carlos Ayora[a], Agnieszka Poulain[c]

[a] Institute of Environmental Assessment and Water Research, (IDAEA-CSIC), Jordi Girona 18-26, 08034 Barcelona, Spain
[b] Univ. Grenoble Alpes, Univ. Savoie Mont Blanc, CNRS, IRD, IFSTTAR, ISTerre, 38000 Grenoble, France
[c] ESRF, The European Synchrotron, 71 Avenue des Martyrs, Grenoble 38000, France

ARTICLE INFO

Editor: K Johannesson

Keywords:
Amorphous $Al(OH)_3$
Nanoboehmite
Pair Distribution Function (PDF)
Linear Combination Fitting (LCF)
Recrystallization
Felsöbányaite

ABSTRACT

Basaluminite is a poorly crystalline aluminium sulphate oxyhydroxide that precipitates in acid mine drainage waters and acid sulphate soils when pH increases above 4.5 approximately. The pH increase can be due to mixing with natural waters or by the addition of an alkaline reagent, a method commonly used in remediation treatments. Basaluminite is a scavenger of elements such as Se, As, Sb, Mo, P and rare earth elements (REEs) and acts as a vector for their transport in the environment. The retention of these elements has important environmental and economic impact due to their toxicity and to the potential extraction of REEs for technological applications. Despite the long history of basaluminite, initially described as a mineral in the late 40s, little is known about its stability and its eventual transformation in other less metastable phases. Here, the stability of synthetic basaluminite in aqueous solutions with different pH values and sulphate concentrations was studied for 81 days. Chemical analyses of the aqueous phase combined with High-Energy X-ray Diffraction and Pair Distribution Function (PDF) analyses of the solids were used to characterize the ageing process. In contact with water, basaluminite incongruently dissolves, precipitating amorphous Al-hydroxide and releasing sulphate to the solution. This process and the recrystallization of amorphous Al-hydroxide into nanoboehmite were enhanced with increasing pH. However, for high SO_4 concentrations, such as those found in acid mine waters, the transformation to nanoboehmite was partially inhibited. The ageing processes highlighted here point to a potential pathway for the desorption of trace elements upon neutralization of acid mine drainage. Furthermore, PDF analyses of basaluminite show a high similarity with the local structure of a synthetic amorphous Al-hydroxide.

1. Introduction

Hydrobasaluminite and basaluminite were first described as white precipitates from an ironstone mine (Bannister and Hollingworth, 1948; Hollingworth and Bannister, 1950). These precipitates have appeared together with allophane and other clay minerals. A difference between these materials was based on their water content, i.e., the water content is higher for hydrobasaluminite. Hydrobasaluminite, $(Al_4(SO_4)(OH)_{10}{\cdot}16\text{-}34H_2O)$, has been described as a white clay-like mineral, which losses water molecules yielding basaluminite, $(Al_4(SO_4)(OH)_{10}{\cdot}5H_2O)$, with a characteristic fine powder aspect and very broad diffraction peaks. Since then, most reports of basaluminite have been made from precipitates occurring in acidic sulphate-rich waters (Van Breemen, 1973; Adams and Rawajfih, 1977; Nordstrom, 1982; Bigham and Nordstrom, 2000) when the solution pH value increases in a range 4.0–4.5 due to mixing with natural waters or after the addition of an alkaline reagent, a common practice in treatment systems. Basaluminite, similar to its Fe(III)-bearing counterpart schwertmannite, is known for its high capability to retain both silica and toxic elements such as Se, As, Mo, Cr, Sb, V, Pb, U and P (Nordstrom and Alpers, 1999; Bigham and Nordstrom, 2000; Fukushi et al., 2004; Sibrell et al., 2009; Sánchez-España et al., 2016; Carrero et al., 2017a). Both precipitates are important phases in the waters where they are present due to their high reactivity with strong environmental implications. On the other hand, basaluminite and schwertmannite are responsible for the uptake of high concentrations of Rare Earth Elements (REEs) in acidic streams (Verplanck et al., 2004; Gammons et al., 2005). This process affects drastically the lanthanides partition pattern in these waters, impacting geochemical studies based on lanthanide distributions. Moreover, basaluminite has been proven to retain Sc, Y and lanthanides when it

* Corresponding author.
E-mail address: alba.lozano@idaea.csic.es (A. Lozano).

https://doi.org/10.1016/j.chemgeo.2018.08.002
Received 8 May 2018; Received in revised form 28 July 2018; Accepted 1 August 2018
Available online 02 August 2018

precipitates in passive remediation systems of acid mine drainage (Ayora et al., 2016). In these systems, AMD waters are neutralized using a reservoir of $CaCO_3$, reaching pH values higher than 6 in the output. The REE contents in the precipitated basaluminite are estimated to be approximately 2 to 12 μmol/g, depending on the initial REE water content, and represent an opportunity to recover REEs from basaluminite. These water treatment systems can work for several months to years with a constant pH evolution. Thus, a detailed characterization of the stability of basaluminite at different solution pH values becomes essential.

Literature reports on the structure of basaluminite are confusing. The first structure was proposed by Clayton (1980) from X-ray powder patterns using samples derived from acid water resulting from the oxidation of pyrite. These earlier studies described broad diffraction peaks such as those expected in nanocrystalline phases. However, a more recent report based on single-crystal X-ray diffraction (Farkas and Pertlik, 1997) gave unit cell parameters and atomic positions of basaluminite and felsöbanyáite, establishing that the first is just a nanocrystalline version of the second. This fact is confusing for two reasons: (i) the basaluminite formed in AMD is typically very disordered, and the occurrence of single crystals has never been reported; and (ii) felsöbanyáite is a rare mineral, never reported in AMD. As indicated by Carrero et al. (2017b), the similarity between the structures of basaluminite and felsöbanyáite could be due to a simple fortuitous coincidence. These authors used High-Energy X-ray Diffraction (HEXD) with Pair Distribution Function (PDF) analyses and Extended X-ray Absorption Fine Structure (EXAFS) to describe the local order in synthetic and natural (from AMD) basaluminite samples. The authors confirmed the Al-octahedral framework of the structure with sulphate coordinated as outer-sphere ligands, as previously proposed by Farkas and Pertlik (1997). Regarding its stability, some experiments where synthetic basaluminite aged in its mother solution showed that the mineral partially or totally recrystallizes with temperature forming alunite, depending on the conditions (Adams and Rawajfih, 1977; Prietzel and Hirsch, 1998). Therefore, the basaluminite formed in solution can be considered a metastable solid in a wide range of pH values, the formation of alunite being kinetically retarded (Nordstrom, 1982; Prietzel and Mayer, 2005).

In a more recent study of the solubility Al-solids based on chemical analysis and EXAFS spectroscopy, Jones et al. (2011) indicated that the synthetic and natural precipitates consisted of a mixture of basaluminite and amorphous $Al(OH)_3$ when the solution pH was approximately above 4.5, and the major phase present at pH 7 was basaluminite instead of $Al(OH)_3$ with adsorbed sulphate. Jolivet et al. (2011) proposed that amorphous $Al(OH)_3$ can recrystallize to gibbsite, bayerite or boehmite depending on pH and/or temperature. Similarly, recent SEM/TEM studies by Sánchez-España et al. (2016) have documented the coexistence of basaluminite globules with nanocrystals of $Al(OH)_3$ (gibbsite, bayerite) and allophane in natural Al precipitates formed at pH 4.0–4.5 in pit lakes. Based on the textural findings observed by SEM and TEM, these authors concluded that the nearly amorphous basaluminite globules partly transformed to gibbsite or bayerite during ageing. However, no ageing with detailed structural studies have been undertaken to confirm the transformation of basaluminite to more crystalline forms and to determine the parameters that control such a transformation.

The objective of the present work is to study the stability of basaluminite during ageing. Since basaluminite is a mineral that precipitates in acidic and rich sulphate waters, the second objective is to understand the role of pH and aqueous SO_4 in its stability. To achieve this, two set of suspensions of pure synthetic basaluminite were maintained in contact with solutions at different pH values and sulphate concentrations along different time spans. The resulting aqueous and solid phases were carefully characterized.

2. Materials and methods

2.1. Samples and experimental protocol

2.1.1. Pure solid synthesis

Basaluminite was synthesized following the method described by Adams and Rawajfih (1977), i.e., by adding 214 mL 0.015 M $Ca(OH)_2$ to 30 mL 0.05 M $Al_2(SO_4)_3{\cdot}18H_2O$ (both commercial reagents). The synthesis was performed by drop-by-drop addition, until an OH:Al molar ratio of 2.14 was reached under continuous stirring and at room temperature. The solid was washed three times to remove co-precipitated $CaSO_4{\cdot}2H_2O$ and dried 48 h at a maximum temperature of 40 °C.

Moreover, two $Al(OH)_3$ precipitates were synthesized in the laboratory to be used as references. The method described by Xu et al. (2011) was used, i.e., a 1 M NaOH solution was titrated into a 0.5 M $AlCl_3{\cdot}6H_2O$ solution. The titration was conducted by drop-by-drop addition until pH values of 8.1 and 7.3 were reached for each precipitate (samples labelled $Al(OH)_3$_pH 8 and $Al(OH)_3$_pH 7, respectively). The first solid (pH 8.1) was washed three times with deionized water and directly dried for 72 h at $T = 40$ °C. The second precipitate (pH 7.3) was washed seven times with deionized water, directly frozen and then lyophilized.

Digestion of 0.1 g of synthetic basaluminite in 5 mL HNO_3 65% was carried out for 12 h at 115 °C for chemical characterization. Systematic XRD analyses were conducted for all the synthetic solids to dismiss impurities.

2.1.2. Fast ageing experiments (high solid:liquid ratio)

A set of kinetic experiments was performed to understand the evolution of basaluminite solubility over a short period of time. To ensure the quantification of sulphate and aluminium in the aqueous phase by ICP-AES, a solid:liquid ratio of 1:1 was selected. However, only a minor fraction of the initial solid was expected to transform with such a high solid:liquid ratio. Thus, the set consisted of 10 suspensions of 10 mg of synthetic basaluminite in 10 mL of a 0.01 M $NaNO_3$ solution with a pH value of 5.8. The suspensions were aged for different short periods of time: 5, 10, 15, and 35 min and 1, 2, 6, 18, 48 and 96 h. At different times, each suspension was filtered to 0.22 μm, the pH was measured, and the solutions were acidified with HNO_3 65% for further chemical analyses of Al and SO_4.

2.1.3. Slow ageing experiments (low solid:liquid ratio)

A solid:liquid ratio of 1:10 was selected in this case to ensure that most of the initial solid was transformed at the end of the experiment, although some SO_4 and/or Al concentrations remained below detection levels. A set of 12 suspensions of 5 mg of synthetic basaluminite in 50 mL 0.01 M $NaNO_3$ solution was first equilibrated during 48 h with continuous stirring at room temperature. After this period, the pH was measured, and the suspensions were centrifuged at 4500 rpm for 10 min. An aliquot of 5 mL of the supernatant was collected, filtered to 0.22 μm and acidified with HNO_3 65% for further chemical analysis. Then, different amounts from 10 to 100 μL NH_4OH 0.5 M were added to reach initial pH values ranging between 4.9 and 9.2. The suspensions were aged under continuous stirring for 81 days. During this period, pH measurements were performed periodically. After this time, the suspensions were centrifuged at 4500 rpm for 10 min. Aliquots of supernatants were taken, filtered to 0.2 μm and acidified with HNO_3 65% for further chemical analysis. The solids were dried for 48 h at a temperature of 40 °C. These series of experiments were duplicated, and the average of the results from the two experiments is presented.

Another set of 12 suspensions was prepared, but in this case, the initial solution also contained 0.02 M Na_2SO_4. The same procedure, as described in the previous paragraph, was followed, although the pH

values of the starting solutions after adding different amounts of NH_4OH were lower and ranged between 5.08 and 6.16. The reproducibility of the experiment was confirmed by multiple runs at the highest pH (n = 4). This pH was chosen because it is the value at which larger changes in the solid are expected.

2.2. Analytical techniques

2.2.1. Aqueous phase analysis

Measurements of the initial and final pH solutions were made with a Crison® glass electrode calibrated with buffer solutions of pH 2, 4, 7 and 9. Sulphur, Al, and Na were measured by ICP-AES (Thermo Scientific – iCAP 6500, Radial acquisition). Certified solutions (CPI International-CCV standard 1-solution A) were intercalated within the samples to check the analytical accuracy. The detection limits were 1.6, 1.0 and 4.3 μmol/L for S, Al and Na, respectively. The analytical precision error was estimated to be approximately 2%.

Aqueous speciation and saturation indices of the solutions were calculated with PHREEQC code (Parkhurst and Appelo, 1999) using the WATEQ4F database (Ball and Nordstrom, 1991).

2.2.2. Solid phase analysis

The X-ray Diffraction (XRD) patterns of the solid phases were obtained by a Bruker D8 A25 Advance diffractometer θ-θ with CuKα$_1$ radiation. The diffractometer operated at 40 kV and 40 mA in a Bragg-Brentano geometry and was equipped with a linear LynxEye XE detector. The diffractograms were obtained from 4 to 60° in 2θ with a step size of 0.015° and a counting time of 0.1 s.

Thermogravimetric analyses (TGA) were performed to determine the water content of basaluminite from loss vs. temperature curves using a Mettler Toledo TGA/DSC3 + instrument with a N_2 flow rate of 20 mL/min. The temperature increased from room temperature to 900 °C at a rate of 10 °C/min. To this end, a few mg of each sample were loaded into alumina crucibles.

High Energy X-ray Diffraction (HEXD) experiments and Pair Distribution Function (PDF) analyses were performed at beamline ID31 at the European Synchrotron Radiation Facility (ESRF, Grenoble, France). Powder samples were loaded into polyamide capillaries. Scattering from samples and from background (empty capillary) were measured at room conditions and at 68.5 keV (λ = 0.181 Å) incident X-ray energy, which was calibrated using a CeO_2 standard (NIST 674b). The 2D images collected with a flat panel Pilatus3 XCdTe 2 M detector were corrected and integrated using pyFAI (Kieffer and Karkoulis, 2013). Structure factors S(Q) and PDFs were obtained using PDFGetX3 software (Juhás et al., 2013).

The resulting coherent scattered intensity, $I(Q)$, from the HEXD data is given by the Debye equation Eq. (1) and plotted as a function of the magnitude of the scattering vector Eq. (2) (Dinnebier and Billinge, 2008):

$$I(Q) = \sum_{m,n}^{N} f_m(Q) f_n(Q) \frac{sin(Qr_{mn})}{Qr_{mn}} \quad (1)$$

where f_m and f_n are atomic scattering factors and r_{mn} is the distance between a pair of atoms m and n. The scattering vector, Q, is described as follows:

$$Q = |Q| = 2ksin\theta = \frac{4\pi sin\ \theta}{\lambda} \quad (2)$$

The scattered intensity, $I(Q)$ is divided by the number of the scatterers, N, and the average scattering per atom, which is the square of the atomic form-factor, $\langle f \rangle^2$, Eq. (3):

$$\langle f \rangle^2 = \left(\sum_i c_i f_i \right)^2 \quad (3)$$

where c_i is the concentration of the element i, and f_i its atomic form factor. The total structure function or structure factor, $S(Q)$, is then obtained Eq. (4). In this work, the structure factors as a function of 2θ are shown.

$$S(Q) = \frac{I(Q)}{N \langle f \rangle^2} \quad (4)$$

The representation of the scattering data in real space allows an easier interpretation of the short-range order and comparison with other mineral or amorphous compounds. To do so, a Fourier Transform to real-space is performed and a Pair Distribution Function (PDF) is obtained. This function, also called $G(r)$, displayed in Eq. (5), represents the probability of finding pairs of atoms separated a distance, r:

$$G(r) = \frac{2}{\Pi} \int_0^\infty Q[S(Q) - 1] \sin(Qr) dQ \quad (5)$$

Linear Combination Fitting (LCF) analyses were conducted for the PDFs of solids recovered at the end of the experiment using synthetic pure standards. The LCF tool from the Athena IFFEFIT package (Ravel and Newville, 2005) was used to this end. A combinatory study of these standards was performed, and the best fit in terms of the R-factor was selected, Eq. (6). The factors obtained from the model represent the fraction of each standard needed to better describe the unknown sample. The model represents the least square fit to the sample spectrum. The relative weights of the components of the mixture can vary from 0 to 1 and are forced to sum to 1. An R-factor was calculated, where X_i is the set of variables:

$$R = \frac{\sum_i^{N_{fit}} [\chi_i^{data} - \chi_i^{model}(x)]^2}{\sum_i^{N_{fit}} [\chi_i^{data}]^2} \quad (6)$$

3. Results

3.1. Pure synthetic solids

3.1.1. Chemical characterization

The solid digestion and TGA analysis of the synthetic basaluminite yielded the formula $Al_4(SO_4)_{1.25}(OH)_{9.50}{\cdot}4.75H_2O$ with a higher sulphate content than the stoichiometry of $Al_4(SO_4)(OH)_{10}{\cdot}5H_2O$, reported by Hollingworth and Bannister (1950) and Farkas and Pertlik (1997). The TGA data showed a sigmoidal-like water desorption and decomposition step (Fig. S1) similar to that described in Carrero et al. (2017b). The weight loss observed between 150 °C and 342 °C is due to the vaporization of physisorbed H_2O and structural OH/H_2O.

3.1.2. Structural characterization

The XRD patterns of the synthetic pure solids obtained with CuKα$_1$ X-ray source are shown in Fig. S2. The basaluminite and $Al(OH)_3$_am at pH 7 samples show low-angle peaks and a large peak covering the range from 35 to 50°. The $Al(OH)_3$_am at pH 8 shows five very large peaks that correspond to the (020), (120), (031), overlapping (051) and (200), and (231) reflections of boehmite (γ-AlOOH) (Fig. S3, obtained with synchrotron HEXD data). The very broad width of these peaks suggests nanocrystalline boehmite. From here on, the two $Al(OH)_3$ samples will be labelled Al(OH)3_am (sample synthesized at pH 7.3) and nanoboehmite (sample synthesized at pH 8.1).

The PDFs for basaluminite, $Al(OH)_3$_am, nanoboehmite, and the two aged samples of $Al(OH)_3$_am and nanoboehmite (samples stored under atmospheric conditions and measured one month later) are displayed in Fig. 1. The two synthetic nanoboehmite samples show a higher degree of crystallinity than that of the amorphous and basaluminite samples. This crystallinity is reflected by the coherent domain size, which is approximately 10 Å for basaluminite and fresh amorphous $Al(OH)_3$ and increases to at least 25 Å for the aged samples. Individual atomic pairs can be identified in the PDFs. The peak at 1.49 Å in basaluminite corresponds to the S—O bonds. The remainder of the main peaks in the

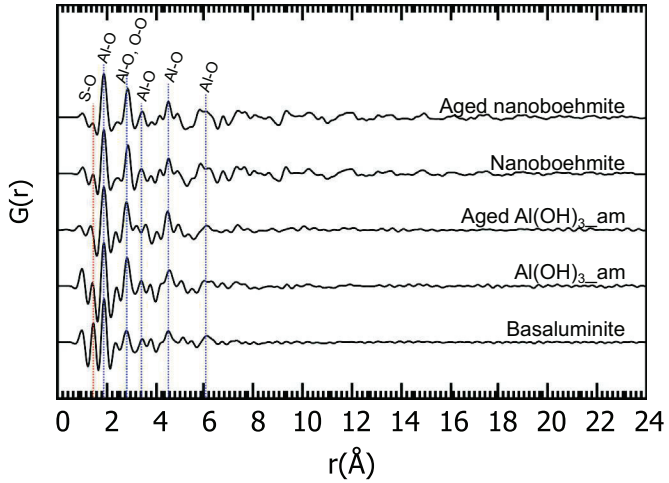

Fig. 1. PDFs of synthetic basaluminite, $Al(OH)_3$_am and nanoboehmite. $Al(OH)_3$_am and nanoboehmite were measured after one month, and a slight recrystallization is observed. Data are normalized to the Al-O peak.

three standards, corresponding to Al—Al, Al—O and O—O distances, are placed in the same positions for all the samples. The Al—O bond has an interatomic distance of 1.88 Å. Both Al—Al and O—O interatomic distances overlap and have the same interatomic distance of 2.8 Å. The peaks at 3.6, 4.6 and 6 Å are due to the Al—O distances. Differences in the relative peak intensities are due to the presence of point defects.

3.2. Fast ageing experiment

Prior to describe the ageing experiments, it is interesting to remark that the initial pH of the suspension depended on the solid:liquid ratio. Thus, the pH values of two suspensions of 10 mg of basaluminite in 10 and 100 mL of a 0.01 M $NaNO_3$ electrolyte solution after 2 h were 4.31 and 4.98, respectively. This effect is more evident if an amount of OH^- is added to raise the initial pH. Thus, NH_4OH was added to two solutions similar to those described to increase the initial pH to 10. After 2 h, the pH values of the solutions were 4.60 and 8.69 for solid:liquid ratios of 1.1 and 1:10, respectively. Moreover, the initial pH also depends on the amount of sulphate in the suspension. Thus, the pH values of two 1:1 suspensions without and with 0.02 M Na_2SO_4 after 2 h were 4.31 and 4.69, respectively. These features suggest a strong basaluminite-solute interaction.

Ten suspensions of 10 mg of basaluminite were in contact in 10 mL of a 0.01 M $NaNO_3$ background electrolyte solution. After the first five minutes, the pH decreased to 4.02 and then after 2 h, the pH increased to 4.31. From 2 to 96 equilibrating hours, the pH was maintained at a constant value of 4.30 ± 0.034 (Fig. 2A). The equilibrium conditions for ageing experiments were considered after 48 h.

During the time studied, the dissolved SO_4 was highly correlated with Al (R^2 = 0.99), which resulted in a SO_4:Al ratio of 1.40, (Fig. 2B) but also Al correlates with H^+ (R = 0.71) in a H^+:Al ratio of -0.19 (Fig. 2C), suggesting a basaluminite-water reaction that will be discussed below. The saturation index for basaluminite, boehmite, gibbsite ($Al(OH)_3$) and amorphous gibbsite are shown in Table S1 in Electronic Annex. At the beginning, the solution was undersaturated with respect to these phases but quickly reached supersaturation in basaluminite, gibbsite and boehmite.

3.3. Slow ageing experiments

3.3.1. Aqueous phase

Twelve suspensions of 5 mg of synthetic basaluminite in 50 mL of a 0.01 M $NaNO_3$ background solution were equilibrated for 48 h. After this time, the average solution pH for the twelve points was 4.98 ± 0.10, and the chemistry was 0.042 ± 0.001 mmol/L Al, 0.074 ± 0.002 mmol/L S and 10.030 ± 0.201 mmol/L Na (Table S2). The experimental molar ratio of aqueous SO_4:Al was 1.79. This value greatly differs from 0.31, the stoichiometric ratio expected from congruent dissolution, as will be discussed below. All the solutions were supersaturated with respect to basaluminite and undersaturated with respect to amorphous $Al(OH)_3$ (Table S3).

Increasing amounts of NH_4OH 0.5 M were added to each solution to adjust the pH to values ranging from 4.95 to 9.22 (Table S4). The main OH consumption occurred mainly during the first 19 days, and the solution pH continued to decrease for 81 days (Fig. 3A). At the end of the experiment, the pH values ranged between 4.61 and 6.46. The solution pH decreased 0.5 pH units for the suspension with the lowest amount of NH_4OH added and 3.0 pH units for the solution with the highest amount of NH_4OH added (Table S4). No NH_4OH was added to the first suspension, and after the ageing time, the pH decreased only 0.34 units.

At the end of the experiment, the aqueous Al and SO_4 concentrations did not correlate with the pH. At lower pH values (4.61–5.10) the amount of sulphate remained almost constant, whereas the aluminium concentration in the solution decreased slightly (Fig. 3B). For pH values higher than 5.10, the Al in solution was below the detection limit (0.001 mM), but the SO_4 increased constantly (Fig. 3B). At the pH range 5.10 to 5.85, a linear correlation between SO_4 release and excess $[OH^-]$ was observed (R^2 = 0.989) with a molar ratio OH:SO_4 of 4.0 (Fig. 3C). The excess $[OH^-]$ was calculated from the difference between the NH_4OH added and the final measured pH value.

To understand the influence of SO_4 in the behaviour of basaluminite, the ageing experiment was repeated adding 0.02 M Na_2SO_4 to 12 new suspensions. After 48 h, the average solution pH was 5.12 ± 0.10, and the elemental concentrations were 0.01 ± 0.0003 mmol/L Al, 21.16 ± 0.423 mmol/L of S and 49.05 ± 0.981 mmol/L Na. Detailed results can be found in Table S5. All the solutions were almost in equilibrium with respect to basaluminite and undersaturated with respect to amorphous $Al(OH)_3$ (Table S6).

The same amounts of NH_4OH (0 to 100 μL 0.5 M) were added. At the beginning, the pH values rose from 5.08 to 6.16, which is much less compared with the values in previous experiments without the addition of sulphate (compare Table S4, both experiments at time 0 h). The pH continued to increase for 40 h, although these values did not reach the pH values of the experiment without sulphate (Table S5). Then, the solution pH decreased during the remaining 81 days. The final pH ranged between 5.06 and 7.18 at the end of the experiment. The final pH values decreased to between 0.8 and 1.02 units. The pH decreased only 0.02 units in the first sample of the series, to which no NH_4OH had been added. Due to the amount of SO_4 added, no correlation between the released sulphate and aluminium and excess OH^- was observed in this case.

3.3.2. Solid phase

The structure factors extracted from the HEXD patterns, S(Q), for the solids aged during 81 days in the absence of sulphate are shown in Fig. 4A. The samples at lower pH values exhibit typical broad oscillations characteristic of amorphous or poorly crystalline materials. New broad peaks appear in the patterns of the solids formed at pH values higher than 5.47, clearly defined from pH 5.85. These peaks correspond to boehmite with two possible peaks belonging to bayerite and a possibly few peaks attributed to natroalunite ($NaAl_3(SO_4)_2(OH)_6$) (Fig. 4A). The characteristic broad bands for basaluminite are no longer present at these high pH values. These observations agree with those determined by Singh (1969) in the XRD patterns obtained after ageing basaluminite with and without gibbsite along 103 days, as well as those of $Al_2(SO_4)_3$ aged for 42 months, where a mixture of boehmite, gibbsite and alunite (as natroalunite) phases was identified in Singh (1982). The small peaks in the basaluminite patterns are due to the memory effects of the 2D detector. The structure factors of the solids equilibrated in the presence of sulphate (Fig. 4B) were in general similar to the ones shown

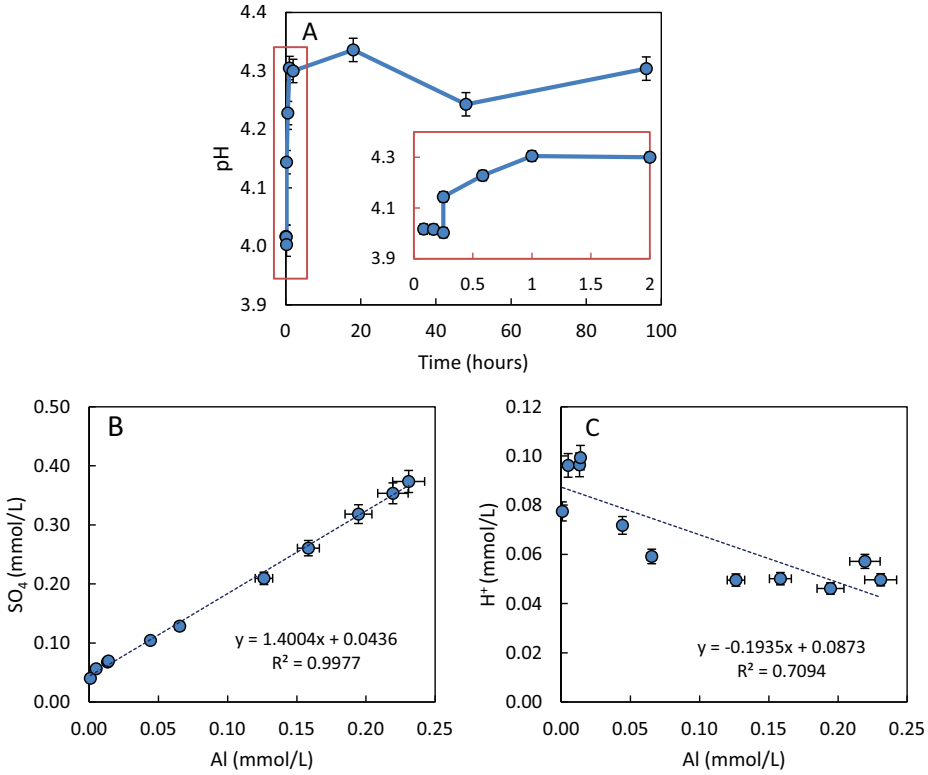

Fig. 2. (A) Evolution of pH during basaluminite stability with a background solution for 96 h. The inset depicts a magnified view of the first 2 h, where the pH increase is shown. (B) Correlation between SO_4 and Al with time. (C) Correlation between H^+ and Al with time. See the data in supporting information, Table S1.

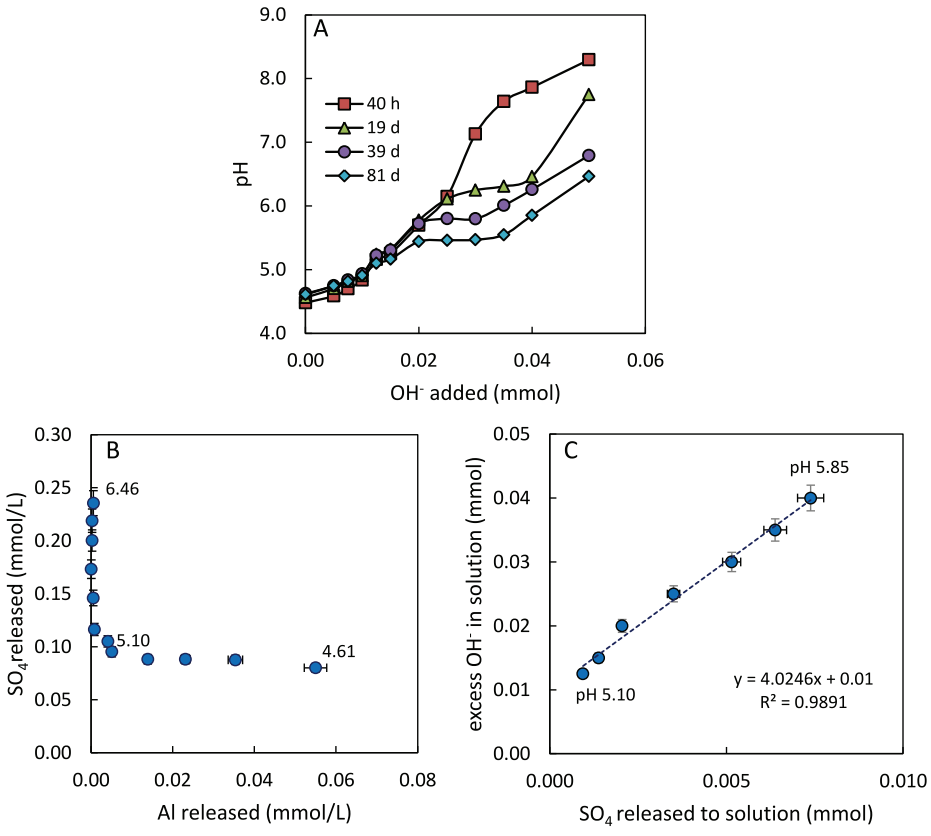

Fig. 3. (A) Evolution of pH for the suspensions with different initial pH values. (B) Aluminium and SO_4 evolution of the different suspensions after 81 days of ageing. The values depicted inside are the final pH values. (C) Correlation between the OH^- excess and SO_4 concentration for the suspensions with higher pH values. The OH^- excess is calculated as the difference between the added NH_4OH and the OH^- invested in the rising pH.

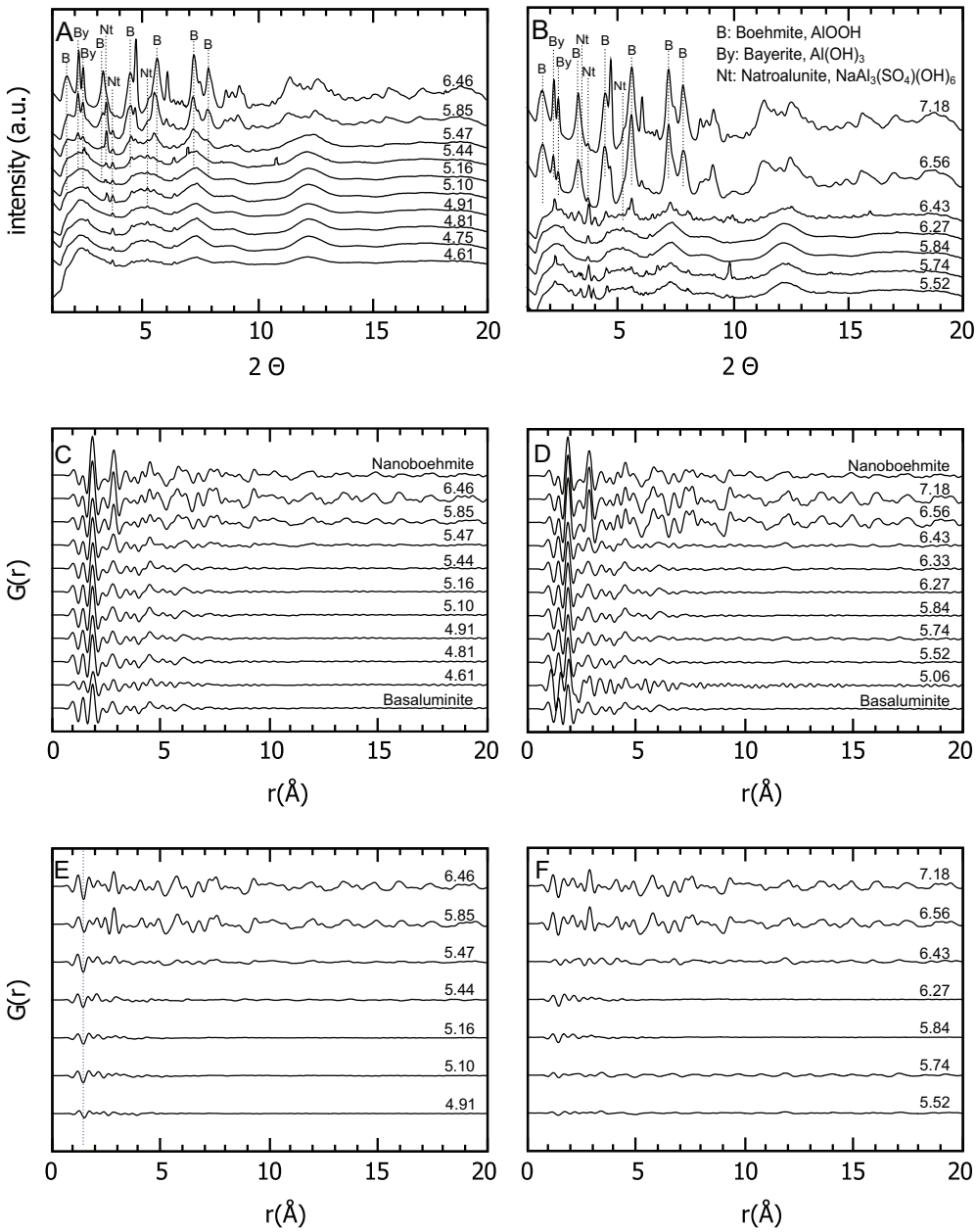

Fig. 4. Structure factors with Q converted to 2θ for the solid samples equilibrated and aged during 81 days in the absence of sulphate (A) and with an initial sulphate content (B). The wavelength of the X-rays used was of λ = 0.181 Å. (C, D) PDFs of the aged solids and synthetic nanoboehmite and basaluminite for the experiment in the absence of sulphate and with initial sulphate, respectively. (E, F) Differential PDFs for both experiments. The vertical dotted line indicates the position of the S—O bond. Negative peaks reflect the decrease in the sulphate content in the solids.

in Fig. 4A. Some peaks were identified as belonging to boehmite. From pH 6.56, the broad peaks indicate nanocrystalline boehmite, which were sharper than those for the experiment without sulphate, indicating an increase in the crystallinity. Again, residual $NaAl_3(SO_4)_2(OH)_6$ and some systematic peaks due to the memory effect of the detector were also present.

The PDFs of the solids equilibrated in the absence of initial sulphate in the solution together with those of pure synthetic basaluminite and nanoboehmite are shown in Fig. 4C. At lower pH values, the PDFs are very similar to the PDF of synthetic basaluminite, whereas at higher pH values, a transition to a nanoboehmite-like local structure is observed. Fig. 4D shows the differential PDF generated by subtracting the PDF of pure basaluminite from each sample. Two observations can be made: (i) a negative peak of increasing intensity (S-O peak at 1.49 Å) corresponding to the release of sulphate from the samples as the pH increases, and (ii) a transition to a more crystalline phase. The PDFs of the experiment with added sulphate show similar trends (Fig. 4E).

4. Discussion

4.1. Basaluminite ageing at different pH and SO_4

As stated in Section 3.1.1., the synthetic basaluminite had a S:Al ratio of 0.31, higher than the stoichiometry of 0.25 reported in the literature. In the long ageing experiments without added sulphate, 23% of the sulphate was transferred from the solid into the solution after 48 h of equilibration (Table S2), and the calculated SO_4:Al ratio in the residual solid reached a stoichiometric value of 0.25. This fast release of sulphate towards the stoichiometry has been interpreted as the desorption of sulphate from the outer-sphere surface complexes (Wang et al., 2015; Carrero et al., 2017b). Similar sulphate desorption was also proposed for the early ageing of schwertmannite (Burton et al., 2008). However, our fast ageing experiment showed clear correlations with SO_4:Al and H^+:Al ratios of 1.40 and −0.19, respectively (Fig. 2B, C). These relations are explained as an incongruent basaluminite

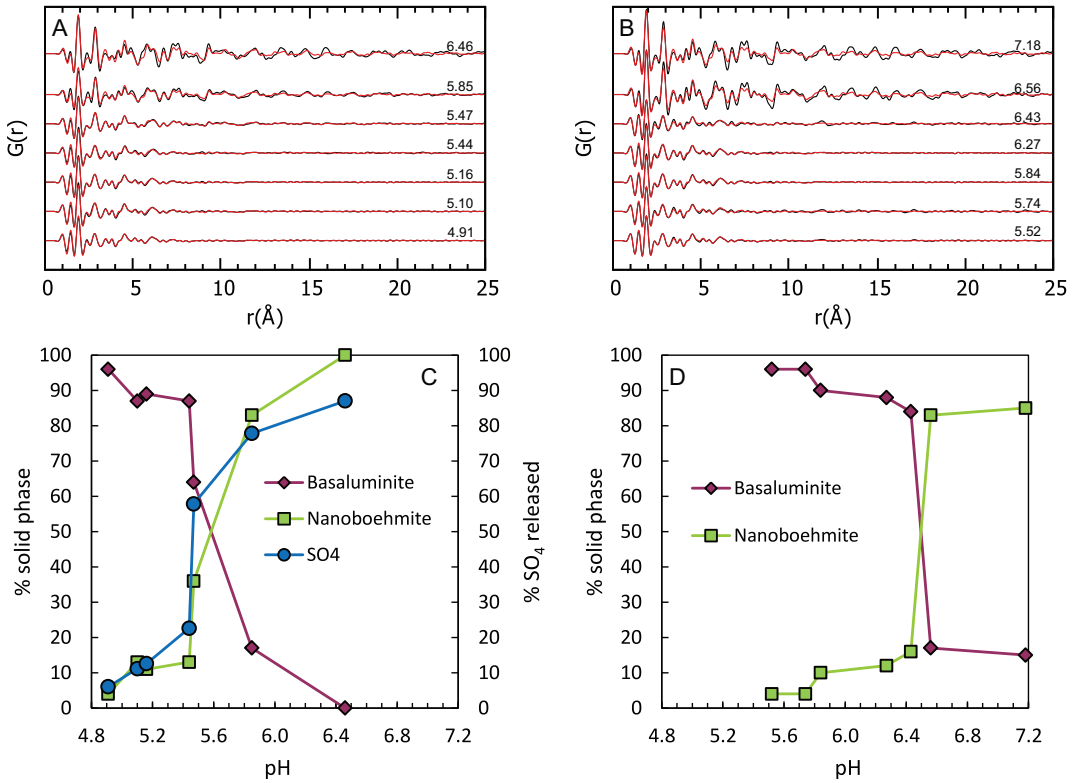

Fig. 5. (A, B) Experimental PDFs (black) and LCF fits of the PDFs (red) using pure basaluminite and nanoboehmite as end members for the fits of solids from the slow ageing experiments without initial sulphate (A) and with initial sulphate (B). (C, D) Percentages of the end members, basaluminite (rhomboids) and nanoboehmite (squares) calculated from the LCF fitting for experiments without (C) and with initial sulphate (D). Percentage of released sulphate calculated from aqueous chemistry (circles) in the experiment without initial sulphate (C). (For interpretation of the references to colour in this figure legend, the reader is referred to the web version of this article.)

dissolution with the subsequent Al hydrolysis and $Al(OH)_3$ precipitation, as expressed with the following process reaction:

$$Al_4(SO_4)_{1.25}(OH)_{9.5} + 0.17\ H^+ \rightarrow 0.89\ Al^{3+} + 1.25\ SO_4^{2-} + 3.11\ Al(OH)_3(s) + 0.17\ H_2O \quad (7)$$

Owing to the high amount of sulphate added, such a variation in sulphate concentration was not observed in the experiments where Na_2SO_4 was added to the initial suspensions.

Beyond the first 48 h, and after OH^- addition, a decrease in the pH was observed in the slow ageing experiments (Fig. 3A). This variation was more accentuated when no sulphate was added to the initial suspensions. The structure factors clearly showed that boehmite peaks appeared in the solids from the experiments with higher initial pH values (Fig. 4A, B). Concomitantly, the PDFs of these solids reflected an increase in the crystallinity at higher pH values (Fig. 4C, D). From these observations, a transformation of basaluminite to nanoboehmite with time can be inferred. This transformation was more evident when a higher amount of OH^- was added into the solution. Since the PDF spectrum at the lowest pH is very similar to basaluminite and at the highest pH to synthetic nanoboehmite, Linear Combination Fits (LCF) of the experimental PDFs were performed using these two synthetic solids as end members (Fig. 5A, B). The results of the fitting show a clear decrease in the proportion of basaluminite along with an increase in nanoboehmite as NH_4OH was added and the final pH value was higher (Fig. 5C, D). When it could be measured, this behaviour with pH is also consistent with the transfer of sulphate from the solid to the aqueous phase (Fig. 5C).

With respect to the aqueous phase, the increase in nanoboehmite in the solid phase was consistent with the amount of sulphate released from basaluminite. The molar ratio between the SO_4 released and OH^- consumed was 4 (Fig. 3C). This result can be explained by a sequence of chemical reactions involving the dissolution of basaluminite and the formation of nanoboehmite and natroalunite, $NaAl_3(SO_4)_2(OH)_6$, according to the process reaction:

$$5Al_4(SO_4)(OH)_{10}{\cdot}5H_2O + 2Na^+ + 4OH^- \rightarrow 2NaAl_3(SO_4)_2(OH)_6 + 14AlOOH + SO_4^{2-} + 39H_2O \quad (8)$$

Since in the first 48 h, 23% of SO_4 was released, and the basaluminite stoichiometry reported in the literature was used in the reaction. The solution reached supersaturation with respect to alunite (Table S3) at expense of the Al and SO_4 released by the dissolution of basaluminite and Na in the solution (0.01 M $NaNO_3$). Adams and Rawajfih (1977) obtained similar precipitates in ageing experiments of basaluminite titrated with NaOH. Prietzel and Hirsch (1998) observed a mixture of basaluminite and alunite after ageing suspensions of $Al_2(SO_4)_3$ solutions titrated with NaOH for 15 weeks and quantifying a mixture of 64% basaluminite and 36% alunite, respectively. Additionally, Nordstrom (1982) concluded that the formation of alunite is due the metastable behaviour of basaluminite.

Combining the presence of basaluminite determined by HEXD (Fig. 4) and the composition of the aqueous phase (Table S2), some insights on the solubility of basaluminite can be extracted. Indeed, after 81 days, the pH changes were almost negligible in all the solutions, and chemical equilibrium was assumed. Similar periods were considered in other solubility studies of aluminium phases (Adams and Rawajfih, 1977; Prietzel and Hirsch, 1998). For the final pH range of 4.61–5.16, basaluminite was confirmed in the solid phase by XRD-HEXD data (Fig. 4), and all major components in the solution were analysed (Table S2). The average Ion Activity Product (IAP) calculated from these 6 analyses was 23.09 ± 0.08. This value is close to 22.3, reported by several researchers for the crystalline material and has been summarized in Nordstrom (1982), and to 24, the value proposed by Singh and

Brydon (1969) and Adams and Rawajfih (1977) for amorphous basaluminite. Moreover, the value is also similar to the value of 23.9 reported by Sánchez-España et al. (2011) for precipitates from pit lakes with a pH range of 4.1–4.8. The existing experimental data for IAP converge towards a narrow window of 22.3–24.0. Nanoboehmite was identified in the solids from the two highest pH values (Fig. 3A). The IAP for the pH value 6.46 (the only one where Al could be analysed) was 9.74 ± 0.02. This value is higher than that reported in the WATEQ4F database for crystalline boehmite ($IAP_{boehmite}$ = 8.584), which makes sense due to the nanocrystalline character of the boehmite formed in our experiments.

In parallel to the long ageing experiments, HEXD patterns of synthetic amorphous $Al(OH)_3$ were measured again after one month. The resulting PDF showed an increase in the crystallinity (Fig. 1). This observation supports that not only basaluminite was metastable but also amorphous $Al(OH)_3$, which recrystallized into boehmite.

Comparing the results of both long ageing experiments without and with added sulphate (Fig. 5), for the same amount of OH^- added, the final pH was higher when sulphate was present in solution, and therefore, less OH^- consumption was observed. This effect occurred for all the pH points measured. Consequently, the solids obtained from sulphate-added suspensions were mixtures with a lower percentage of nanoboehmite (Fig. 5D) than those of the solids equilibrated without sulphate. Since there was a high amount of sulphate in solution, the activity of the $AlSO_4^+$ complex was one order of magnitude higher, and therefore, less $Al(OH)_3^0$ complexes were available to precipitate as amorphous $Al(OH)_3$ and subsequently recrystallize to nanoboehmite. Owing to its high concentration in solution, no released sulphate could be calculated. Thus, the presence of dissolved sulphate enhanced the stability of basaluminite, which not only hindered the formation of amorphous $Al(OH)_3$ at higher pH conditions but also retarded its recrystallization to nanoboehmite. This observation is apparently contradictory with that described by Sánchez-España et al. (2016). They report the coexistence of nearly amorphous basaluminite with some nanocrystals (< 100 nm) of $Al(OH)_3$ (gibbsite, bayerite) and allophane formed in the water column of two acid lakes with high sulphate concentration (pH 4.0–4.5, SO_4 = 100–200 mmol/L). However, no proof of ageing of the amorphous basaluminite to crystalline forms of $Al(OH)_3$ and allophane is actually given. Alternatively, some nanocrystals of $Al(OH)_3$ and allophane could also be originally present in what we call basaluminite precipitates, as described by Jones et al. (2011). Further research is needed to clarify this point.

Therefore, the transformation pathway from basaluminite to nanoboehmite includes basaluminite dissolution yielding $Al(OH)_3$ precipitation and its consequent OH^- consumption, resulting in the observed pH decrease. A comparison between the PDFs of pure synthetic basaluminite and amorphous $Al(OH)_3$ reveals an almost identical short-range structure. This fact is surprising and questions the existence of basaluminite as a mineral phase. Indeed, our results suggest that the presence of sulphate does not affect the structure of the amorphous $Al(OH)_3$ matrix. In contrast, our findings point to a stabilisation of amorphous $Al(OH)_3$ via sulphate adsorption. Upon an increase in the solution pH value, the amorphous solid is depleted in sulphate and further hydrolysis of the aluminium results in a crystallization process and the formation of nanoboehmite.

Our results contrast with previous observation from Jones et al. (2011). These authors studied precipitates from sulphate-rich acidic waters using X-ray absorption spectroscopy at the Al, S, and O K-edge. They also observed that both amorphous $Al(OH)_3$ and basaluminite were formed. However, these authors suggested that at pH higher than 7 the solubility of aluminium was controlled by basaluminite. This is in a clear disagreement with our results, which showed that, basaluminite transforms into nanoboehmite with increasing pH, and it was this latter phase which controlled the Al concentration in solution.

Although the influence of pH and sulphate was not systematically studied in the case of schwertmannite, the ageing of basaluminite to nanoboehmite (and natrojarosite) is consistent with that described for schwertmannite transformation to goethite (and jarosite) (Bigham et al., 1996; Acero et al., 2006). The ageing process could have important implications for the trace elements incorporated into basaluminite, whether they are toxic such as As, Se or Mo (Carrero et al., 2017a) or of economic value such as Sc, Y and lanthanides (Ayora et al., 2016), and therefore should be investigated. The instability of basaluminite (and schwertmannite) has to be considered in the use of sludge from AMD treatment to remove phosphorous from municipal and agriculture wastewater effluents (Wei et al., 2008; Sibrell et al., 2009) This process is particularly relevant in the conventional process of P strip and media regeneration by a strong base leaching (Sibrell and Kehler, 2016). Indeed, leaching with a strong base is the conventional procedure to strip the sorbed P and regenerate the sorbing medium (Sibrell and Kehler, 2016). Therefore, the fast transformation of basaluminite to boehmite at high pH would prevent its use as sorbing material for several times.

5. Concluding remarks

Our data support the reinterpretation of basaluminite as an amorphous precipitate. Past studies on the local structure of basaluminite were based on hypotheses that related the structure of basaluminite to that of felsöbanyáite, a rare mineral with the same chemical composition. The results from the PDF analyses show that the local order of both basaluminite and amorphous $Al(OH)_3$ are identical and sulphate is incorporated into the $Al(OH)_3$ structure without any effect on the local structure of the $Al(OH)_3$ precipitate. Owing to Occam's law of parsimony, the demonstrated hypothesis linking the nature of basaluminite to that of an amorphous solid, instead to a rare mineral phase, is therefore preferred.

Basaluminite undergoes several transformations when ageing in aqueous solutions. Considering that synthetic basaluminite has a SO_4:Al ratio higher than the stoichiometry reported in the literature, rather than releasing sorbed sulphate, basaluminite starts to dissolve immediately after its contact with water. The dissolution of basaluminite leads to the precipitation of amorphous $Al(OH)_3$, which, depending on pH and time, a different grade of transformation into boehmite is reached. The experiments demonstrated that basaluminite is a metastable precipitate and that its ageing in/near neutral waters can trigger its transformation into more stable Al hydroxide phases. However, basaluminite tends to stabilize when sulphate is present in solution, inhibiting the formation of $Al(OH)_3$. This process can affect the behaviour of trace elements, both toxic or of economic interest, frequently adsorbed or coprecipitated with basaluminite, and the technological use of this solid phase to remove phosphate from wastewater.

Acknowledgements

This work was funded by ERAMIN (PCIN2015-242-256) and SCYRE (CGL2016-78783-C2-2-R) projects and by Ministry of Economy, Industry and Competitiveness of Spain with a FPI grant (BES-2014-069978). The A.F.-M. and TGA measurements were supported by the LABEX OSUG@2020 (ANR10 LABX56). The authors wish to thank J. Bellés, M. Cabañas, R. Bartrolí and N. Moreno (IDAEA-CSIC) and N. Findling (ISTerre) for their analytical assistance. The ESRF data were acquired through an in-house research program at ID31 (ESRF). The authors also wish to thank the ID31 beamline personnel for their technical assistance during the data acquisition.

Appendix A. Supplementary data

Supplementary data to this article can be found online at https://doi.org/10.1016/j.chemgeo.2018.08.002.

References

Acero, P., Ayora, C., Torrentó, C., Nieto, J.M., 2006. The role of trace elements during schwertmannite precipitation and subsequent transformation into goethite and jarosite. Geochim. Cosmochim. Acta 70, 4130–4139.

Adams, F., Rawajfih, Z., 1977. Basaluminite and alunite: a possible cause of sulfate retention by acid soils. Soil Sci. Soc. Am. J. 41, 686–692.

Ayora, C., Macías, F., Torres, E., Lozano, A., Carrero, S., Nieto, J.M., Pérez-López, R., Fernández-Martínez, A., Castillo-Michel, H., 2016. Recovery of rare earth elements and yttrium from passive-remediation systems of acid mine drainage. Environ. Sci. Technol. 50 (15), 8255–8262.

Ball, J.W., Nordstrom, D.K., 1991. User's manual for WATEQ4F with revised thermodynamic database and test cases for calculating speciation of major, trace and redox elements in natural waters. In: U.S. Geological Survey Water-Resources Investigation Report, pp. 91–183.

Bannister, F.A., Hollingworth, S.E., 1948. Two new British minerals. Nature 162, 565.

Bigham, J.M., Nordstrom, D.K., 2000. Iron and aluminum hydroxysulfates from acid sulfate waters. Rev. Mineral. Geochem. 40, 351–403.

Bigham, J.M., Schwertmann, U., Traina, S.J., Winland, R.L., Wolf, M., 1996. Schwertmannite and the chemical modeling of iron in acid sulfate waters. Geochim. Cosmochim. Acta 60, 2111–2121.

Burton, E.D., Bush, R.T., Sullivan, L.A., Mitchell, D.R.G., 2008. Schwertmannite transformation to goethite via the Fe(II) pathway: Reaction rates and implications for iron-sulfide formation. Geochim. Cosmochim. Acta 72, 4551–4564.

Carrero, S., Fernández-Martínez, A., Pérez-López, R., Poulain, A., Salas-Colera, E., Nieto, J.M., 2017a. Arsenate and selenate scavenging by basaluminite: insights into the reactivity of aluminum phases in acid mine drainage. Environ. Sci. Technol. 51, 28–37.

Carrero, S., Fernández-Martínez, A., Pérez-López, R., Lee, D., Aquilanti, G., Poulain, A., Lozano, A., Nieto, J.M., 2017b. The nanocrystalline structure of basaluminite, an aluminum hydroxide sulfate from acid mine drainage. Am. Mineral. 102, 2381–2389.

Clayton, T., 1980. Hydrobasaluminite and basaluminite from Chickerell, Dorset. Mineral. Mag. 43, 931–937.

Dinnebier, R.E., Billinge, S.J.L., 2008. Local structure from total scattering and atomic Pair Distribution Function (PDF) analysis. In: Powder diffraction Theory and Practice. The Royal Society of Chemistry, pp. 464–493.

Farkas, L., Pertlik, F., 1997. Crystal structure determinations of felsöbányaite and basaluminite, $Al_4(SO_4)(OH)_{10}{\cdot}4H2O$. Acta Mineral. Petrogr. Szeged. 38, 5–15.

Fukushi, K., Sato, T., Yanase, N., Minato, J., Yamada, H., 2004. Arsenate sorption on schwertmannite. Am. Mineral. 89, 1728–1734.

Gammons, C.H., Wood, S.A., Pedrozo, F., Varekamp, J.C., Nelson, B.J., Shope, C.L., Baffico, G., 2005. Hydrogeochemistry and rare earth element behavior in a volcanically acidified watershed in Patagonia, Argentina. Chem. Geol. 222, 249–267.

Hollingworth, S.E., Bannister, F.A., 1950. Basaluminite and hydrobasaluminite, two new minerals from Northamptonshire. Mineral. Mag. 29, 1–17.

Jolivet, J.P., Chanéac, C., Chiche, D., Cassaignon, S., Durupthy, O., Hernandez, J., 2011. Basic concepts of the crystallization from aqueous solutions: the example of aluminum oxy(hydroxi)des and aluminosilicates. C. R. Geosci. 343, 113–122.

Jones, A.M., Collins, R.N., Waite, T.D., 2011. Mineral species control of aluminum solubility in sulfate-rich acidic waters. Geochim. Cosmochim. Acta 75, 965–977.

Juhás, P., Davis, T., Farrow, C.L., Billinge, S.J.L., 2013. PDFgetX3: a rapid and highly automatable program for processing powder diffraction data into total scattering pair distribution functions. J. Appl. Crystallogr. 46, 560–566.

Kieffer, J., Karkoulis, D., 2013. PyFAI, a versatile library for azimuthal regrouping. J. Phys. Conf. Ser. 425 (202012), 1–5.

Nordstrom, D.K., 1982. The effect of sulfate on aluminum concentrations in natural waters: some stability relations in the system Al2O3-SO3-H2O at 298 K. Geochim. Cosmochim. Acta 46, 681–692.

Nordstrom, D.K., Alpers, C.N., 1999. Geochemistry of acid mine waters. In: Plumlee, C.S., Logdson, M.J. (Eds.), The Environmental Geochemistry of Mineral Deposits. 6A. Rev. Econ. Geol. SEG, Littleton, Colorado, pp. 133–160.

Parkhurst, D.L., Appelo, C.A.J., 1999. User's Guide to PhreeqC (version 2.18) A Computer Program for Speciation, and Inverse Geochemical Calculations. U.S. Department of the Interior, U.S. Geological Survey.

Prietzel, J., Hirsch, C., 1998. Extractability and dissolution kinetics of pure and soil-added synthesized aluminium hydroxyl sulphate minerals. Eur. J. Soil Sci. 49, 669–681.

Prietzel, J., Mayer, B., 2005. Isotopic fractionation of sulfur during formation of basaluminite, alunite, and natroalunite. Chem. Geol. 215, 525–535.

Ravel, B., Newville, M., 2005. ATHENA, ARTEMIS, HEPHAESTUS: data analysis for X-ray absorption spectroscopy using IFEFFIT. J. Synchrotron Radiat. 12, 537–541.

Sánchez-España, J., Yusta, I., Diez-Ercilla, M., 2011. Schwertmannite and hydrobasaluminite: a re-evaluation of their solubility and control on the iron and aluminium concentration in acidic pit lakes. Appl. Geochem. 26, 1752–1774.

Sánchez-España, J., Yusta, I., Burgos, W.D., 2016. Geochemistry of dissolved aluminum at low pH: hydrobasaluminite formation and interaction with trace metals, silica and microbial cells under anoxic conditions. Chem. Geol. 441, 124–137.

Sibrell, P.L., Kehler, T., 2016. Phosphorus removal from aquaculture effluents at the Northeast Fishery Center in Lamar, Pennsylvania using iron oxide sorption media. Aquac. Eng. 72–73, 45–52.

Sibrell, P.L., Montgomery, G.A., Ritenour, K.L., Tucker, T.W., 2009. Removal of phosphorus from agricultural wastewater using adsorption media prepared from acid mine drainage sludge. Water Res. 43, 2240–2250.

Singh, S.S., 1969. Basic aluminum sulfate formed as a metastable phase and its transformation to gibbsite. Can. J. Soil Sci. 49, 383–388.

Singh, S.S., 1982. The formation and coexistence of gibbsite, boehmite, alumina and alunite at room temperature. Can. J. Soil Sci. 62, 321–332.

Singh, S.S., Brydon, J.E., 1969. Solubility of basic aluminum sulfates at equilibrium in solution and in the presence of montmorillonite. Soil Sci. 107, 12–16.

Van Breemen, N., 1973. Dissolved aluminum in acid sulfate soils and in acid mine waters. Soil Sci. Soc. Am. Proc. 37, 694–697.

Verplanck, P.L., Nordstrom, D.K., Taylor, H.E., Kimball, B.A., 2004. Rare earth element partitioning between hydrous ferric oxides and acid mine water during iron oxidation. Appl. Geochem. 19, 1339–1354.

Wang, X., Gu, C., Feng, X., Zhu, M., 2015. Sulfate local coordination environment in schwertmannite. Environ. Sci. Technol. 49, 10440–10448.

Wei, X., Viadero, R.C., Bhojappa, S., 2008. Phosphorus removal by acid mine drainage sludge from secondary effluents of municipal wastewater treatment plants. Water Res. 42, 3275–3284.

Xu, R., Xiao, S., Jiang, J., Wang, Y., 2011. Effects of Amorphous $Al(OH)_3$ on the Desorption of Ca^{2+}, Mg^{2+}, and Na^{+} from soils and minerals as related to diffuse layer overlapping. J. Chem. Eng. Data 56, 2536–2542.

Local structure and ageing of basaluminite at different pH values and sulphate concentrations

Alba Lozano[a,*], Alejandro Fernández-Martínez[b], Carlos Ayora[a], Agnieszka Poulain[c]

[a] Institute of Environmental Assessment and Water Research, (IDAEA-CSIC), Jordi Girona 18-26, 08034 Barcelona, Spain
[b] Univ. Grenoble Alpes, Univ. Savoie Mont Blanc, CNRS, IRD, IFSTTAR, ISTerre, 38000 Grenoble, France
[c] ESRF, The European Synchrotron, 71 Avenue des Martyrs, Grenoble, 38000, France

Corresponding author:
Alba Lozano (alba.lozano@idaea.csic.es)

Appendix A. Supplementary data

Contains 3 figures (Figure S1 - S3) and 6 tables (Table S1 – S6)

Figure S1. TGA analysis. Weight loss of pure synthetic basaluminite.

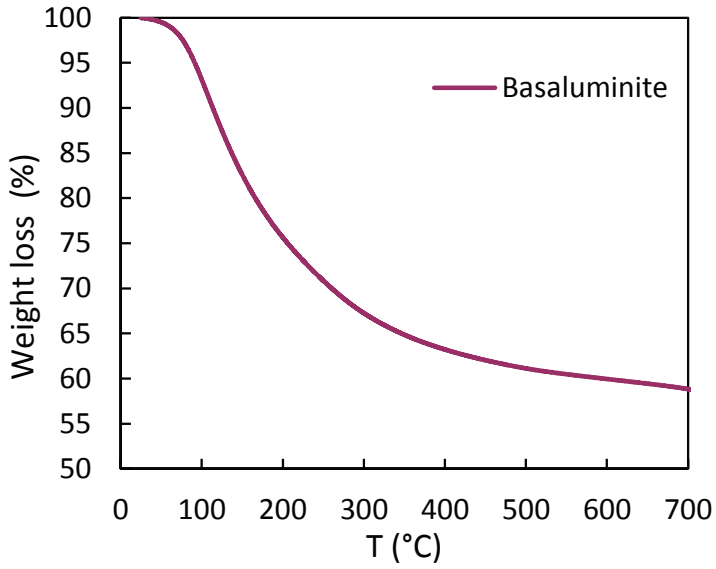

Figure S2. XRD patterns of pure synthetic solids.

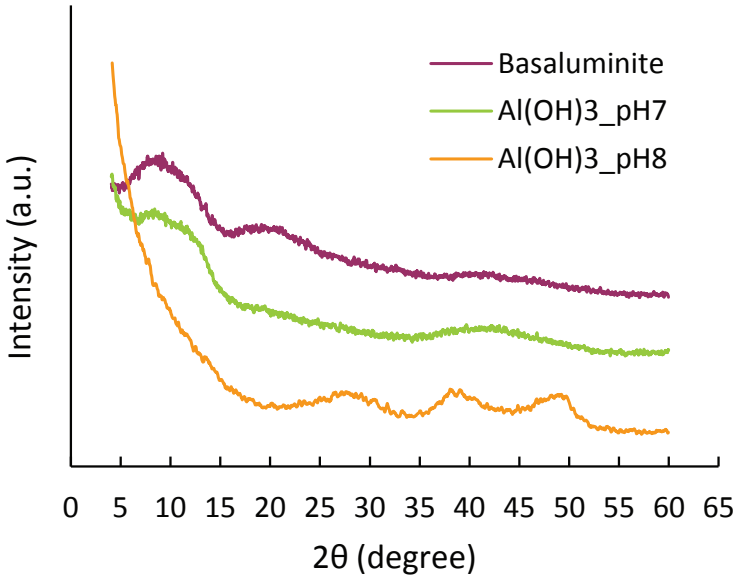

Figure S3. XRD pattern of pure synthetic AlOOH with peaks identified. Boehmite, AlO(OH)-01-083-2384 (C) –Amam (63)-a 3.69360 – b12.21400 – c2.86790- α 90.000 – β 90.000 – γ 90.000.

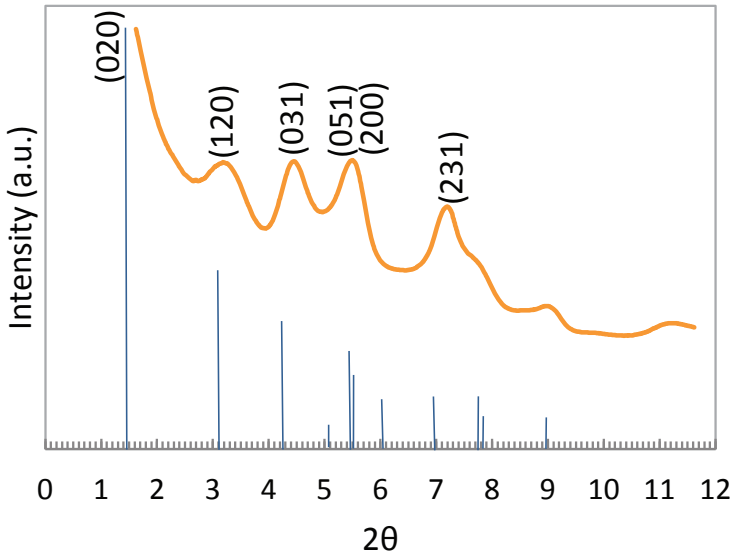

Table S1. Evolution of the aqueous chemistry (mmol/L), percentage of sulfate released from the solid phase and saturation indices for the fast aging experiment. Solid:liquid ratio of 1:1.

Sample	time (h)	pH	Aqueous concentration			% released	Saturation Indices			
			Al	Ca	S	S	Basaluminite	Boehmite	Gibbsite(am)	Gibbsite
B-5min	0.08	4.017	0.005	0.003	0.056	2.14	-6.96	-0.63	-3.66	-1.19
B-10min	0.17	4.016	0.013	0.003	0.068	2.57	-5.32	-0.24	-3.27	-0.80
B-15min	0.25	4.003	0.014	0.003	0.069	2.63	-5.36	-0.26	-3.29	-0.82
B-35min	0.58	4.144	0.044	0.006	0.104	3.96	-2.08	0.60	-2.43	0.04
B-1h	1	4.228	0.065	0.006	0.128	4.88	-0.65	0.99	-2.04	0.42
B-2h	2	4.305	0.126	0.006	0.209	7.95	1.08	1.42	-1.61	0.85
B-6h	6	4.300	0.158	0.007	0.261	9.89	1.34	1.46	-1.57	0.90
B-18h	18	4.336	0.195	0.009	0.318	12.08	1.97	1.62	-1.41	1.06
B-48h	48	4.243	0.219	0.009	0.353	13.42	1.23	1.38	-1.65	0.82
B-96h	96	4.304	0.231	0.009	0.373	14.18	1.88	1.57	-1.46	1.01

Table S2. Aqueous chemistry (mmol/L) at initial and final conditions for the long aging experiment without added sulfate. Solid:liquid ratio of 1:10.

	Initial conditions (48 hours)							Final Conditions (81 days)						
Sample Nº	pH	Al	Na	SO_4	SO_4:Al	% SO_4 released	Added NH_4OH 0.5 M (µL)	pH	Al	Na	SO_4	mmol SO_4 released	% SO_4 released	mmol excess OH
1	**4.95**	0.040	10.135	0.073	1.82	23.81	0	**4.61**	0.055	9.030	0.080	0.000	3.97	0.000
2	**4.95**	0.044	9.978	0.077	1.76	22.72	10	**4.75**	0.035	8.946	0.088	0.001	4.76	0.005
3	**4.98**	0.043	10.161	0.076	1.79	23.50	15	**4.81**	0.023	9.070	0.088	0.001	5.96	0.007
4	**4.98**	0.043	10.061	0.077	1.80	23.89	20	**4.91**	0.014	9.071	0.088	0.001	5.71	0.010
5	**4.98**	0.042	10.230	0.077	1.80	23.85	25	**5.10**	0.005	9.016	0.095	0.001	9.38	0.012
6	**4.99**	0.043	10.099	0.077	1.78	22.15	30	**5.16**	0.004	8.897	0.105	0.001	12.44	0.015
7	**4.98**	0.042	10.010	0.075	1.81	23.49	40	**5.44**	0.001	8.947	0.116	0.002	20.37	0.020
8	**4.98**	0.043	10.002	0.076	1.77	22.92	50	**5.46**	≤ D.L.	8.986	0.146	0.004	33.64	0.025
9	**4.99**	0.040	9.877	0.070	1.77	22.91	60	**5.47**	≤ D.L.	8.841	0.173	0.005	53.34	0.030
10	**4.99**	0.040	10.004	0.073	1.81	23.08	70	**5.55**	≤ D.L.	8.878	0.200	0.006	64.25	0.035
11	**4.99**	0.041	9.938	0.071	1.75	22.96	80	**5.85**	≤ D.L.	8.816	0.219	0.007	75.86	0.040
12	**4.99**	0.039	9.854	0.071	1.83	23.08	100	**6.46**	0.001	8.688	0.236	0.008	83.25	0.050

Table S3. Saturation indices at initial and final conditions for the long aging experiment without added sulfate.

Initial conditions (48 hours)						Final conditions (81 hours)					
pH	Basaluminite	$Al(OH)_3(a)$	Gibbsite	Boehmite	Alunite(Na)	pH	Basaluminite	$Al(OH)_3(a)$	Gibbsite	Boehmite	Alunite(Na)
4.89	2.47	-0.96	1.73	1.26	1.71	**4.61**	0.29	-1.68	1.01	0.53	0.59
4.93	2.66	-0.92	1.77	1.30	1.88	**4.74**	0.78	-1.50	1.19	0.71	0.80
4.97	2.83	-0.86	1.83	1.36	1.96	**4.77**	0.54	-1.54	1.15	0.68	0.54
4.95	2.84	-0.86	1.83	1.36	1.97	**4.86**	0.45	-1.51	1.18	0.71	0.33
4.98	2.79	-0.87	1.82	1.35	1.94	**5.12**	0.10	-1.51	1.18	0.71	-0.17
4.99	2.91	-0.83	1.86	1.38	2.01	**5.17**	0.14	-1.48	1.21	0.74	-0.18
4.99	2.79	-0.87	1.82	1.35	1.92	**5.44**	-1.00	-1.62	1.07	0.60	-1.46
4.98	2.84	-0.86	1.83	1.36	1.96	**5.43**	-1.50	-1.77	0.92	0.44	-1.68
4.99	2.76	-0.86	1.83	1.35	1.84	**5.47**	-4.86	-2.67	0.02	-0.45	-4.01
4.99	2.77	-0.86	1.83	1.35	1.88	**5.51**	-2.21	-1.94	0.75	0.27	-2.18
4.98	2.81	-0.85	1.84	1.36	1.89	**5.87**	-1.32	-1.58	1.11	0.64	-1.92
4.97	2.72	-0.87	1.82	1.34	1.82	**6.37**	-0.43	-1.06	1.63	1.16	-2.13

Table S4: Evolution of pH values for slow aging experiments.

		Without SO_4					With SO_4				
	µL 0.5M NH_4OH	0h	40h	19d	39d	81d	0h	40h	19d	39d	81d
1	0	4.95	4.48	4.56	4.62	4.61	5.08	5.75	5.13	5.13	5.06
2	10	5.20	4.59	4.70	4.75	4.75	6.00	5.35	5.33	5.27	5.20
3	15	5.38	4.70	4.81	4.84	4.81	7.06	5.66	5.51	5.51	5.38
4	20	5.86	4.84	4.91	4.93	4.91	7.09	5.89	5.70	5.57	5.52
5	25	7.19	5.16	5.24	5.23	5.10	7.09	6.34	6.06	5.93	5.74
6	30	7.72	5.25	5.32	5.30	5.16	6.62	6.50	6.16	6.10	5.84
7	40	8.21	5.70	5.78	5.72	5.44	6.60	7.24	6.68	6.53	6.27
8	50	8.64	6.15	6.11	5.80	5.46	6.04	7.76	6.97	6.67	6.33
9	60	8.93	7.13	6.25	5.80	5.47	6.08	8.30	7.37	6.85	6.43
10	70	9.00	7.64	6.31	6.01	5.55	6.12	8.36	7.67	7.06	6.50
11	80	9.10	7.86	6.46	6.26	5.85	6.14	8.58	8.24	7.69	6.56
12	100	9.22	8.29	7.75	6.79	6.46	6.16	8.70	8.82	8.62	7.18

Table S5. Aqueous chemistry (mmol/L) at initial and final conditions for the long aging experiment with sulfate added (18.73 mmol/L). Solid:liquid ratio of 1:10.

	Initial conditions (48 hours)				added	Final Conditions (81 days)			
	pH	Al	Na	SO_4	NH_4OH 0.5 M (µL)	pH	Al	Na	SO_4
1	**5.08**	-	-	-	0	**5.06**	0.02	49.053	20.827
2	**5.11**	-	-	-	10	**5.20**	≤ D.L.	49.123	20.806
3	**5.11**	0.012	48.818	21.456	15	**5.38**	≤ D.L.	47.226	20.378
4	**5.13**	0.013	50.057	21.191	20	**5.52**	≤ D.L.	48.060	20.966
5	**5.13**	0.012	46.314	20.526	25	**5.74**	≤ D.L.	49.065	21.401
6	**5.12**	0.015	49.561	20.891	30	**5.84**	≤ D.L.	47.284	20.245
7	**5.12**	0.013	48.685	21.184	40	**6.27**	≤ D.L.	46.006	20.701
8	**5.13**	0.012	48.432	21.042	50	**6.33**	≤ D.L.	47.296	21.089
9	**5.14**	0.013	48.480	21.362	60	**6.43**	≤ D.L.	49.135	21.139
10	**5.10**	0.012	49.542	21.251	70	**6.50**	≤ D.L.	49.952	21.695
11	**5.13**	0.012	49.745	21.165	80	**6.56**	≤ D.L.	50.303	21.756
12	**5.12**	0.011	50.904	21.566	100	**7.18**	≤ D.L.	49.094	21.335

Table S6. Saturation indices at initial and final conditions for the long aging experiment with sulfate added.

Initial conditions (48 hours)						Final conditions (81 hours)					
pH	Basaluminite	$Al(OH)_3(a)$	Gibbsite	Boehmite	Alunite(Na)	pH	Basaluminite	$Al(OH)_3(a)$	Gibbsite	Boehmite	Alunite(Na)
5.11	-0.25	-2.11	0.58	0.10	2.82	**5.06**	0.18	-2.03	0.66	0.19	3.20
5.13	0.08	-2.02	0.67	0.20	3.05	**5.20**	-1.09	-2.28	0.41	-0.06	2.04
5.13	-0.02	-2.05	0.64	0.17	2.93	**5.38**	-7.18	-3.71	-1.02	-1.49	-2.82
5.12	0.26	-1.98	0.71	0.24	3.18	**5.52**	-0.97	-2.08	0.61	0.13	1.65
5.12	-0.03	-2.05	0.64	0.16	2.97	**5.74**	0.59	-1.59	1.10	0.63	2.51
5.13	-0.15	-2.08	0.61	0.14	2.86	**5.84**	1.21	-1.38	1.31	0.84	2.79
5.14	0.06	-2.02	0.67	0.19	3.01	**6.27**	2.16	-0.93	1.76	1.29	2.85
5.10	-0.27	-2.12	0.57	0.09	2.81	**6.33**	2.09	-0.92	1.77	1.30	2.72
5.13	0.04	-2.03	0.66	0.19	3.00	**6.43**	1.85	-0.92	1.77	1.29	2.41
5.12	-0.33	-2.13	0.56	0.09	2.76	**6.50**	1.67	-0.94	1.75	1.28	2.19
5.13	-0.02	-2.05	0.64	0.17	2.96	**6.56**	1.43	-0.97	1.72	1.25	1.92
5.12	0.05	-2.03	0.66	0.18	3.04	**7.18**	-1.77	-1.46	1.23	0.76	-1.43

Article 2

Sorption of rare earth elements onto basaluminite: The role of sulfate and pH

Published in: *Geochimica et Cosmochimica Acta* 2019, 258, 50-62.

Available online at www.sciencedirect.com

ScienceDirect

Geochimica et Cosmochimica Acta 258 (2019) 50–62

Geochimica et Cosmochimica Acta

www.elsevier.com/locate/gca

Sorption of rare earth elements onto basaluminite: The role of sulfate and pH

Alba Lozano [a,b,*], Carlos Ayora [a], Alejandro Fernández-Martínez [c]

[a] Institute of Environmental Assessment and Water Research, (IDAEA-CSIC), Jordi Girona 18-26, 08034 Barcelona, Spain
[b] Grup de Mineralogia Aplicada i Geoquímica de Fluids, Departament de Cristal-lografia, Mineralogia i Dipòsits Minerals, Facultat de Geologia, Universitat de Barcelona (UB), C/Martí Franquès, S/N, Barcelona, Spain
[c] Univ. Grenoble Alpes, Univ. Savoie Mont Blanc, CNRS, IRD, IFSTTAR, ISTerre, 38000 Grenoble, France

Received 4 February 2019; accepted in revised form 12 May 2019; Available online 23 May 2019

Abstract

Scandium, yttrium and lanthanides (REE) are critical raw materials in increasing demand for modern technology, so identifying and developing new sources of REE has become a pressing need. REE concentrations in acid mine drainage (AMD) are several orders of magnitude higher than those in natural water, and their recovery is of economic interest. Passive remediation systems designed to minimize AMD impact on the ecosystem retain REE in solid waste, where basaluminite, $Al_4SO_4(OH)_{10}{\cdot}5H_2O$, is the mineral responsible for the scavenge. However, no information about the retention mechanisms of REE is currently available in the literature. The objective of the present work is to study the adsorption of lanthanides, yttrium and scandium onto synthetic basaluminite over a pH range of 4–7 at room conditions. Since sulfate is ubiquitous in AMD, the adsorption has been investigated with variable sulfate concentrations.

Experimental results show that sorption onto basaluminite is strongly dependent on pH, starting at pH 5 for lanthanides and yttrium and at pH 4 for scandium. At any given pH values, sorption increases with sulfate concentration. Distribution coefficients, defined as $K_D = [REE_{sorbed}]/[REE_{solution}]$, are higher for Sc, and across the lanthanide series, the distribution coefficients increase from La to Lu according to decreasing ionic radius, where yttrium is considered close to Ho. Experimental results were modeled using a sorption model that considers mass law equations where the strong sulfate aqueous complex, MSO_4^+, is adsorbed by exchanging a proton with the mineral surface. The dependence of the experimental results on pH suggests the formation of monodentate binding for Y and lanthanides. The bidentate complex for Sc is deduced by the two proton exchange per mol of Sc extracted from the experiments. The thermodynamic constants for the surface complexation reactions were obtained from experiments with high sulfate concentration and were successfully applied to the experiment with low sulfate content and different solid-liquid ratios. Therefore, the model can be applied to interpret the REE geochemistry in natural systems with variable pH and sulfate concentrations.

Keywords: Sorption model; Scandium; Yttrium; Lanthanides; Fractionation; Sorption edge; Non-electrostatic model; Monodentate surface species

1. INTRODUCTION

In the last two decades, there has been an increasing interest in REE, referred to here as the lanthanide series plus yttrium and scandium, due to their high demand in modern industries. The low supply is due to limited REE

* Corresponding author at: Institute of Environmental Assessment and Water Research, (IDAEA-CSIC), Jordi Girona 18-26, 08034 Barcelona, Spain.
E-mail address: alba.lozano@idaea.csic.es (A. Lozano).

https://doi.org/10.1016/j.gca.2019.05.016
0016-7037/

mining to find new sources of REE (Alonso et al., 2012; Hatch, 2012). Moreover, as a consequence of this industrial activity, new potential pollution sources of REE in natural waters have also emerged (Pagano et al., 2015; Isildar et al., 2018).

Noack et al. (2014) presented a comprehensive study of the REE distribution in groundwater, lakes, rivers and oceans. In particular, REE concentrations in acid mine drainage (AMD) are several orders of magnitude more abundant than other natural water. From the forensic point of view, the REE distribution pattern normalized to the North American Shale Composite (NASC), has been used to prove the impact of Acid Mine Drainage (AMD) in groundwater, rivers and estuarine environments (Delgado et al., 2012; Grawunder et al., 2014; Morgan et al., 2016; Bonnail et al., 2017; Li and Wu, 2017). It is generally recognized that the REE concentration in water is largely controlled by solid surface and aqueous solution chemistry (Quinn et al., 2006a,b and references therein).

REE fractionation between minerals and AMD has been studied since the early 1990s as rock weathering (Auqué et al., 1993, Gimeno et al., 1996) and in mining areas (Gammons et al., 2003). Verplanck et al. (2004) observed REE scavenging from AMD by hydrous ferric oxides as the pH increased to 5.1 due to the water mixing. Similar results were observed by Gammons et al. (2005a,b) when volcanic acidic water mixed with a tributary with neutral pH and the pH increased from 4.3 to 6.1, and when an acidic creek was mixed with a tributary river with circumneutral pH. There, mixtures of ferric and aluminum secondary precipitates were described as being responsible for REE scavenging, yielding Heavy REE (HREE) enrichment in the solids. Similar observations were made by Ferreira da Silva et al. (2009) in the AMD of the Lousal Mine (S. Portugal), where a decrease in REE concentrations was observed as the pH increased from 3 to 6 due to the confluence with a tributary stream. All the aforementioned studies suggested sorption mechanisms on Fe and Al hydroxysulfates as responsible for REE retention. Therefore, interaction with the most relevant solids formed in AMD environments, schwertmannite ($Fe_8O_8(OH)_6SO_4$) and basaluminite ($Al_4SO_4(OH)_{10}{\cdot}5H_2O$), is expected to play a relevant role in the characteristic water lanthanide distribution pattern.

On the other hand, the treatment of AMD in neutralization plants results in a high amount of sludge made up of schwertmannite and basaluminite. Due to its high water content, the disposal and storage of this waste represents a major operating cost and environmental concern for coal and metal mining operations (Ackman, 1982; Viadero et al., 2006). Similarly, passive mediation systems neutralize AMD by intercepting its natural flux with a permeable filter of limestone (Caraballo et al., 2011). Along this process, sequential precipitation of schwertmannite and basaluminite occurs, causing two well differentiated layers of the solids. Basaluminite retains Sc, Y and lanthanides in the system when it forms at pH values from 4.5 to 6 (Ayora et al., 2016). The REE concentration in basaluminite ranges from 2 to 12 μmol/g, depending on the REE values in the input, and these concentrations are comparable to the grades found in REE deposits and exploration targets (Berger et al., 2009). Despite the fact that schwertmannite precipitates before basaluminite (from pH 3–3.5), it does not retain REE. Therefore, a detailed understanding of the mechanism responsible for selective REE scavenging is necessary.

Currently, most REE sorption and fractionation studies have focused on hydrous ferric and manganese oxides in marine water (Byrne and Kim, 1990; Bau et al., 1996) and interactions between synthetic marine water and manganese and ferric oxides (Koeppenkastrop and De Carlo, 1992; Pourret and Davranche, 2013). Differences in solid origin and water source result in distinct fractionation. Light REE (LREE) enrichments were observed in silica phases (Byrne and Kim 1990) as well as in synthetic MnO_2 and α-FeOOH solids (Koeppenkastrop and De Carlo, 1992). In contrast, HREE enrichment was observed in synthetic FeOOH and MnO_2 (De Carlo et al., 1998) as well as hydrogenetic Mn-Fe crusts (Bau et al., 1996). With application to continental water, Liu et al. (2017) developed a surface complexation model (SCM) to interpret REE sorption in iron hydroxide. Additionally, other studies focused on REE interaction with organic matter and its affection with the organic acids of soils (Tang and Johannesson 2003; Verplanck et al., 2004; Pourret and Martinez, 2009).

Aluminum phases are not as common as ferrous oxide phases, and there are few studies related to the REE uptake for aluminum oxides. For example, the uptake of Eu and Yb by alumina (Al_2O_3), at varying pH, ionic strength and acid fulvic concentrations, has been studied by soil scientists as an analogue for actinides in nuclear waste disposal (Xiangke et al., 2000). Experimental sorption edges for Yb and Eu(III) onto alumina were reproduced by Marmier et al. (1997) and Rabung et al. (2000), respectively, using an SCM. In all of the studies, the REE sorption is dependent on pH.

In addition to pH, sulfate has the potential to change the sorption behavior of REE and other metals in AMD systems. Indeed, aqueous sulfate complexes are predominant in AMD over a wide range of pH values (Gimeno et al., 2000), and sulfate is a major constituent of the Fe and Al solid phases, schwertmannite and basaluminite. Therefore, sulfate is expected to play a major role in aqueous-solid partitioning. Despite their key role in AMD geochemistry, no experimental or modeling studies of REE sorption for these two minerals have been investigated. In this study, we present experimental results for adsorption of REE onto synthetic basaluminite as a function of pH and two different sulfate concentrations. To understand the REE sorption mechanism onto basaluminite, a surface complexation model is proposed from a sorption experiment with sulfate and subsequently validated with a second experiment at very low sulfate concentration.

2. MATERIALS AND METHODS

2.1. Experimental part

2.1.1. Preparation and characterization of synthetic basaluminite

Basaluminite was synthesized following the method described by Adams and Rawajfih (1977) by adding

214 mL of 0.015 M $Ca(OH)_2$ to 30 mL of 0.05 M $Al_2(SO_4)_3{\cdot}18H_2O$; both commercial reagents. The resulting solid was washed several times with Milli-Q water to remove the coprecipitated gypsum, and dried for 2 days at 40 °C. As shown by X-ray diffraction (XRD), the resulting solid was free of impurities (Fig. SI-1).

The specific surface area was obtained by the BET-N_2 sorption method, using a Micromeritics Gemini V analyzer. The sorption site density was calculated based from the crystal structure of felsöbanyáite, with a local order similar to that of basaluminite (Farkas and Pertlik, 1997; Carrero et al., 2017).

2.1.2. REE sorption as function of pH and sulfate

Two sets of batch experiments were performed to study the SO_4 dependence of REE adsorption onto synthetic basaluminite as a function of pH: low and high sulfate concentration. Two stock solutions were prepared from an ICP standard mix (Merck) of 16 elements –excluding Pm- with Milli-Q water (the total REE in the stock solution was 123.3 µM). The first stock solution consisted of 1 mg/L of each REE, whereas the second stock solution contained 1 mg/L of each REE plus 20 mg/L Na_2SO_4. The initial pH of the stock solutions was 2.5. A sequence of 10 mL aliquots of each stock solution were adjusted to a desired pH range of 4.5–7 via addition of a 0.05 M NH_4OH solution. The first set of experiments was carried out by adding 10 mg of synthetic basaluminite to each aliquot of the first stock solution. Despite aqueous sulfate is initially absent, this set of experiments will hereafter be referred to as a low sulfate (0.5 mM SO_4) due to the release of small amounts of sulfate adsorbed in the synthesis of basaluminite (see chapter 3.2). The second set of experiments was similar to the first one, but using the second stock solution (20 mM SO_4). Finally, a third set of batch experiments with a different solid:liquid ratio was performed to test the validity of the model developed. It consisted of suspensions of 10 mg of synthetic basaluminite in 40 mL of the second stock solution (20 mM SO_4).

The solid was added to each solution and the suspensions were shaken for 6 hours at room temperature. Previous kinetic experiments were performed at pH 6–6.5, and maximum adsorption was reached at 6 hours and continued from there on. Similar results were obtained by Koeppenksastrop and De Carlo (1992) with fast REE adsorption onto MnO_2, hydroxyapatite and goethite and amorphous FeOOH, reaching an uptake of 60–90% of the initial dissolved REE in 4 hours. Due to basaluminite instability (Lozano et al., 2018), equilibrium times longer than 6 hours were not used. Each pH was readjusted to the initial value after basaluminite addition because the pH drops when the mineral exchanges SO_4 with OH. Once the experiment finished, the suspensions were centrifuged for 15 min at 4500 rpm (4150 RCF). The supernatant was filtered through 0.22 µm nylon membranes into test tubes. The filtered supernatant samples were diluted fivefold with 1% HNO_3. The REE concentrations in the solutions were determined by ICP-MS. Raw data from each experiment were corrected by a dilution factor based on the amount of NH_4OH added. The solids were dried at 40 °C for 48 h. The reproducibility of the experiments was determined by replication at pH 6.7. The error of the final pH values was ±0.02. The sorbed fractions were calculated as follows:

$$\text{Sorbed fraction} = \frac{[\text{REE}]_{\text{initial}} - [\text{REE}]_{\text{final}}}{[\text{REE}]_{\text{initial}}} \quad (1)$$

where [REE] is the concentration of each REE. Initial concentration was measured from stock solution and final concentration in each different batch after experiment. The distribution coefficients K_D (L/kg) were calculated from the REE sorbed onto the solid per the concentration of REE remained in solution and normalized per volume of solution and mass of solid (solid to liquid ratio):

$$K_D = \frac{[\text{REE}]_{\text{initial}} - [\text{REE}]_{\text{final}}}{[\text{REE}]_{\text{final}}} \cdot \frac{V_{\text{solution}}}{M_{\text{solid}}} \quad (2)$$

2.1.3. Analytical techniques

Measurements of pH values from filtered aliquots were made with a Crison® glass electrode calibrated with buffer solutions of pH 2, 4, 7 and 9. Major cation (S, Al, and Na) concentrations were measured by ICP-AES (Thermo Scientific – iCAP 6500, Radial acquisition) and REE (La, Ce, Pr, Nd, Sm, Eu, Gd, Tb, Dy, Ho, Er, Tm, Yb, Lu, Y and Sc) were determined with ICP-MS (Perkin-Elmer®SciexElan 6000). The detection limits were 1.6, 1.0 and 4.3 µmol/L for S, Al and Na, respectively, and 0.2 µg/L for REE. The analytical precision error was estimated to be approximately 5% for ICP-AES and 2% for ICP-MS measurements. Certified solutions (CPI International-CCV standard 1-solution A) and two AMD laboratory standards supplied by P. Verplanck (USGS), were intercalated within the samples to check the analytical accuracy. The deviation from the recommended values was always lower than 5%, with the exception of Eu, giving values 20% below the value reported by Verplanck et al. (2001).

The solid phase prior and after the sorption experiments was investigated by High Energy X-ray Diffraction (HEXD) at the ID31 beamline at the European Synchrotron Radiation Facility (ESRF).

2.2. REE speciation

Chemical speciation of dissolved REE and surface complexation modeling was calculated by PHREEQC code (Parkhurst and Appelo, 1999) using the database of Donnee Thermoddem_V1.10 (Blanc et al., 2012). The database has been updated with the stability constants at zero ionic strength and 25 °C for the following inorganic complexes for lanthanides and yttrium (M): MCO_3^+, $M(CO_3)_2^-$ and $MHCO_3^{2+}$ (Luo and Byrne, 2004); MSO_4^+ (Schijf and Byrne, 2004); MOH^{2+} (Klungness and Byrne, 2000), $M(OH)_2^+$, $M(OH)_3^0$ (Lee and Byrne, 1992); MCl^{2+} (Luo and Byrne, 2001); MF^{2+}, MF_2^+ (Luo and Millero, 2004); and MNO_3^{2+} (Millero, 1992). Solubility products for REE solids, $M(OH)_3$ and $M(OH)_3$(am), were added from LLNL database (Johnson et al., 2000) database and Spahiu and Bruno (1995). Scandium aqueous complexes, $Sc(OH)^{2+}$,

$Sc(OH)_2^+$, $Sc(OH)_3^0$, $ScSO_4^+$; and the solubility product for $Sc(OH)_3$ by Wood and Samson (2006) were also added to Donnee Thermoddem_V1.10 database. Equilibrium constants for aqueous species are compiled in Table SI-1 of Supporting Information.

3. RESULTS

3.1. Basaluminite characterization

The BET method measured a specific surface area of 68 m^2/g. The potentiometric titrations of synthetic basaluminite have been attempted at three different ionic strengths, 0.1, 0.02 and 0.005 M of $NaNO_3$. However, the mineral is proved to release sulfate and transform into nanoboehmite as OH^- is incorporated to the solution (Lozano et al., 2018). This behavior prevented the acquisition of consistent titration curves and their prediction with current electrostatic models. Therefore, the surface properties could not be obtained. Then, the site densities were calculated from crystal structure of felsöbányaite, as basaluminite presents similar local order, as stated by Farkas and Pertlik (1997) and Carrero et al. (2017). The single coordinate sites (one oxygen atom linked to one Al atom) calculated were 4.94, 4.24 and 4.70 nm^{-2} for the 100, 010 and 001 faces, respectively, (5.5 sites/112.32 $Å^2$ for (100), 6.25/147.38^2 for (010) and 6.25/132.80^2 for (001)) from the unit cell of basaluminite, with a space group of P_21. The average surface site is 4.60 nm^{-2} (see Fig. SI-2 for structural details).

3.2. REE adsorption as a function of pH and sulfate

The chemical compositions of the initial and final solutions of the two sets of experiments with 1 g/L of solid:liquid ratio are compiled in Table SI-2. All final solutions were subsaturated with respect to the REE hydroxides (Table SI-3), and, therefore, no REE hydroxide precipitation was expected. All the final solutions except one were supersaturated with respect to basaluminite (Saturation indices between 0.06 and 1.3).

Small amounts of dissolved sulfate were present in the final solutions without initial sulfate. There, the amount of dissolved sulfate increased from 0.1 to 0.9 mM with increasing pH. This is interpreted as the exchange of sulfate from basaluminite with OH groups from the solution (Lozano et al., 2018). The experiments without initial sulfate will be hereafter noted as 0.5 mM SO_4, indicating the mean value.

Four elements were selected for representation: La as light REE (LREE), Lu as heavy REE (HREE), Sc and Y. The two sets of sorption experiments with different sulfate concentrations showed increasing REE sorption with pH (Fig. 1). The adsorption edges occur over a range of 2.0 to 2.5 pH units. Lanthanides and yttrium sorption became significant at pH 5. However, the pH values at which different REE are sorbed differ for each element. The sorption edges shifted to lower pH values for HREE with respect to LREE, and preferential sorption of HREE over LREE was observed. Scandium behaved differently, being scavenged at pH values considerably lower than the rest, and sorption of Sc became significant at pH 4. Similar pH dependence was observed in the experiment with 0.25 g/L of solid:liquid ratio. As expected, the sorption edges are shifter to higher pH values (Table SI-4), as it will be commented in Section 4.3.

The sulfate dependence of REE sorption is more evident by plotting the results of both experiments together by element (Fig. 2). REE sorption is greater when sulfate is present in solution along the entire pH range studied. Sorption enhancement varies with the pH range for each element. For instance, at pH 5.4 the sorption fraction for the higher sulfate in solution is 0.2 points higher for Lu, 0.1 points for Y, 0.1 for Sc and 0.05 for La. This enhancement increases at pH 6: for Lu (0.3 points higher) and for Y (0.2 points) but decreases for Sc (0.05) and for La, which has the same sorbed fraction. The effect for the enhancement of REE sorption with higher sulfate concentration has also been

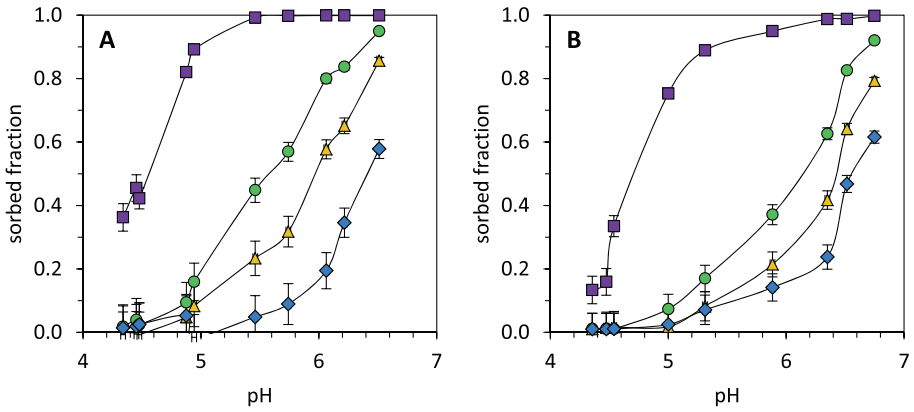

Fig. 1. Sorption edges of (A) sorption with 20 mM of sulfate, (B) sorption with 0.5 mM of sulfate in solution. (Sc: squares, Y: triangles, Lu: circles and La: diamonds). Uncertainties in pH measurements and in the sorbed fraction are considered as ±0.02 and from ±0.01 to ±0.08, respectively, indicated by error bars.

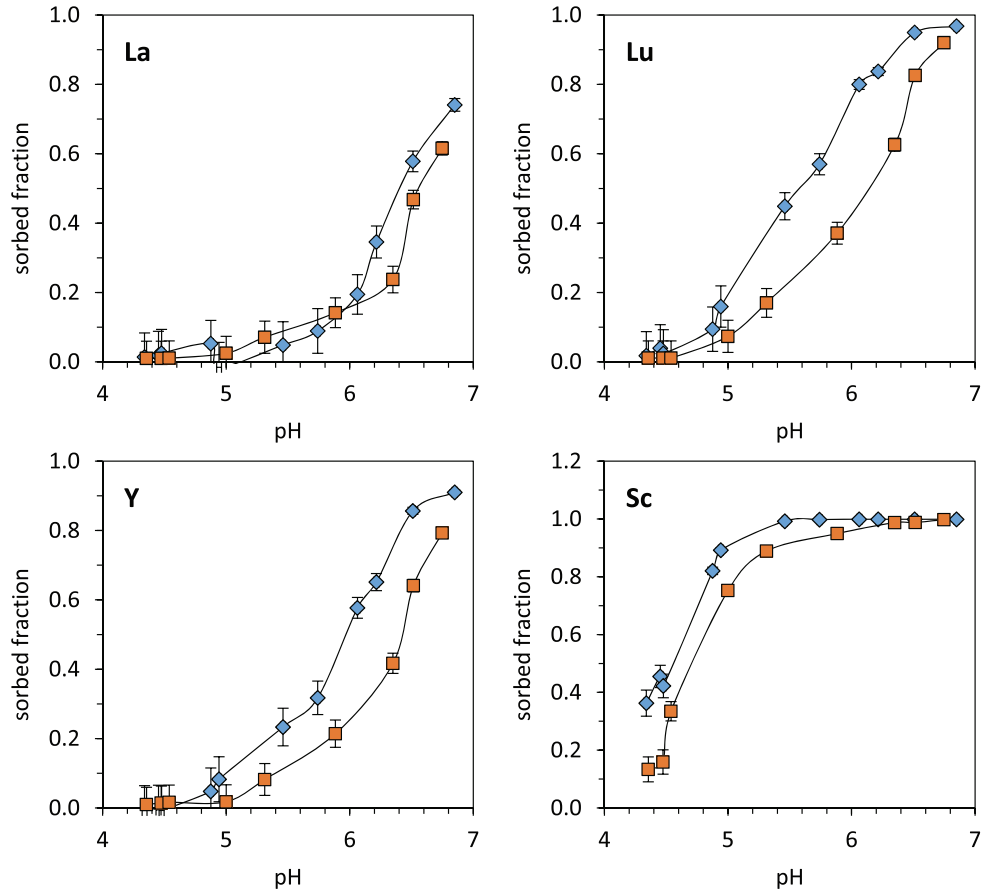

Fig. 2. Comparison of REE sorbed fraction dependence on sulfate concentration for four selected elements. Sorption with 0.5 mM SO_4 in red squares and sorption with 20 mM SO_4 in blue diamonds.

observed for other trace metal sorption, such as Cu and Pb, onto ferrihydrite and schwertmannite (Webster et al., 1998; Baleeiro et al., 2018). Webster et al. (1998) concluded that the enhanced sorption of Cu onto iron (III) oxy-hydroxy sulfate observed with higher sulfate in solution was due to the formation of ternary complexes with a ferric surface site, e.g., ≡FeOHCuSO_4. Similarly, Baleeiro et al. (2018) pointed out that these kinds of ternary surface complexes could explain the strong affinity of these trace metals with schwertmannite.

Values for the distribution coefficient (K_D) were calculated by Eq. (2) and are presented for the lanthanide series in Fig. 3. At pH values lower than 5, the distribution patterns are almost flat and from pH 5 upwards, when the sorbed fraction is significant, log K_D patterns reflect HREE enrichment relative to LREE in the solid phase (Fig. 3), varying 1 unit of log K_D along the series in both sets of experiments. Similar patterns were observed by Bau 1999 for their coprecipitation experiments of REE and Fe at low pH values. Similar relative enrichment in heavy lanthanides was observed in aluminum and ferric hydroxides precipitated in acidic rivers after their neutralization via mixing with alkaline tributaries (Gammons et al. 2003, 2005; Verplanck et al., 2004). Similar to those described by Masuda et al. (1987) and Bau (1996), the fractionation patterns showed an M-type tetrad effect (where they can be subdivided into four convex segments: from La to Nd, from Nd to Gd, from Gd to Ho and from Ho to Lu (Fig. 3). A small positive Ce anomaly was observed only at low pH and low SO_4 concentration, possibly due to a partial/total oxidation of Ce^{3+} to Ce^{4+}, as Koeppenkastrop and De Carlo (1992) proposed for the positive anomalies observed in vernadite. Yttrium has a similar ionic radius as Dy and Ho and can be placed between them (not shown in the figure). For the different pH values represented in Fig. 3, the log K_D patterns show a negative Y anomaly. This anomaly is expressed in K_D^Y/K_D^{Dy} and K_D^Y/K_D^{Ho} ratios below unity, which is observed along the pH range for both sets of experiments with 20 and 0.5 mM sulfate concentration (Table SI-5). In the experiments with low SO_4 concentration, Yb and Dy displayed negative anomalies that attenuated as the pH increased. These anomalies were absent at high sulfate concentrations. In contrast, at higher sulfate concentrations, Er showed a negative anomaly at lower pH values that was attenuated when pH increased and this Er anomaly was not observed with lower sulfate content. These anomalies are not previously described in similar sorption/coprecipitation

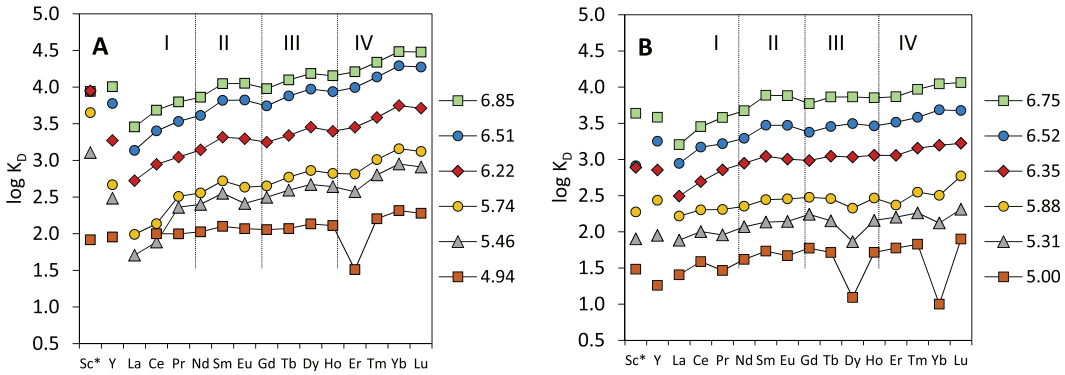

Fig. 3. Patterns of log K_D values showing lanthanide M-type tetrad effect. (A) solution with 20 mM SO_4; (B) solution with 0.5 mM SO_4. (log $K_D^{Sc*} = \log K_D^{Sc} - 2$).

experiments using amorphous ferric hydroxides (Bau, 1999; Ohta and Kawabe, 2000; Quinn et al., 2006a).

4. DISCUSSION

4.1. Aqueous speciation

The presence of sulfate in the solution affects the REE aqueous speciation since it strongly complexes with REE (Gimeno et al., 2000). The proportion of sulfate complexes increases with sulfate concentration and becomes predominant for SO_4 concentrations higher than 1 mM. The rest of the aqueous complexes, MOH^{2+}, MCO_3^+ and $M(CO_3)_2^-$ are only significant at pH values higher than 6.5 and low SO_4 concentrations, as represented for Y in Fig. 4A, B and extended for the rest of lanthanides. Scandium speciation differs from the rest, where Sc hydrolysis complexes are also significant at pH values higher than 4.6 (Fig. 4C, D). For Sc, there is no information about the carbonate complexation in the literature (Wood and Samson 2006), possibly because $ScCO_3^+$ formation is not thermodynamically favorable compared to the formation of strong hydrolysis products.

4.2. Model description

Surface Complexation Models (SCM) are commonly referred to as providing chemical and molecular descriptions of adsorption using equilibrium thermodynamics that can be applied to different conditions (Goldberg, 1992). The common characteristics of these models are the surface charge balance, electrostatic potential terms, as an effect of surface charge, and several adjustable parameters: equilibrium constants, total number of reactive sites and capacitance density.

In a non-electrostatic model (NEM), the electrostatic term is ruled out when the chemical interaction of the cations adsorption is stronger than electrostatic forces in the sorption process (Davis and Kent, 1990). For REE in particular, several works model the sorption experimental data with NEM, and thus, discard the electrostatic term. Marmier and Fromage (1999) reported a non-electrostatic surface complexation model to describe the sorption of lanthanum in hematite. Tertre et al. (2008) described a non-electrostatic model for REE adsorption on basaltic rock. Rabung et al., (2000) and Quinn et al., (2006a,b) also described a sorption model for Y and lanthanides in amorphous iron hydroxides without taking into account the electrostatic term. In our case, the metaestable character of the mineral precluded the full determination of basaluminite surface properties and thus, a non-electrostatic model will be used.

On the other hand, models proposed for REE sorption on amorphous ferric and manganese oxides, hematite, goethite, aluminum hydroxide and alumina are traditionally explained by the sorption of free ions onto surface sites (Tochiyama et al., 1996, Rabung et al., 1998; Marmier et al., 1997; Marmier and Fromage 1999; Quinn et al., 2006a). In the present work, owing to the predominance of sulfate complexes in the aqueous phase, the experiments were initially modeled by the reaction of the aqueous sulfate complex MSO_4^+ with surface sites. This result is consistent with the observation of higher adsorption in the experiments with the SO_4-rich solutions (20 mM). In the case of Sc, in addition to $ScSO_4^+$, the aqueous speciation showed a higher stability of the hydrolysis species $Sc(OH)^{2+}$ in the experiments with lower sulfate concentration (Fig. 4C, D), and the sorption of this aqueous species was also considered. Although experiments were conducted at room conditions, carbonate complexation has not been considered experimentally since the proportion of carbonate species is very low at the experimental pH range (Fig. 4).

The sorption reaction is proposed as the exchange of the M^{z+} aqueous complex (M^{z+} accounting for MSO_4^+ and $Sc(OH)^{2+}$) with n protons from n surface sites represented by XOH:

$$M^{z+} + nXOH = (XO)_nM^{z-n} + nH^+ \qquad K_M \tag{3}$$

The equilibrium constant K_M of the reaction for each REE (M) would be:

$$K_M = \frac{\{(XO)_nM^{z-n}\} \cdot a_{H^+}^n}{a_{M^{z+}}\{XOH\}^n} \tag{4}$$

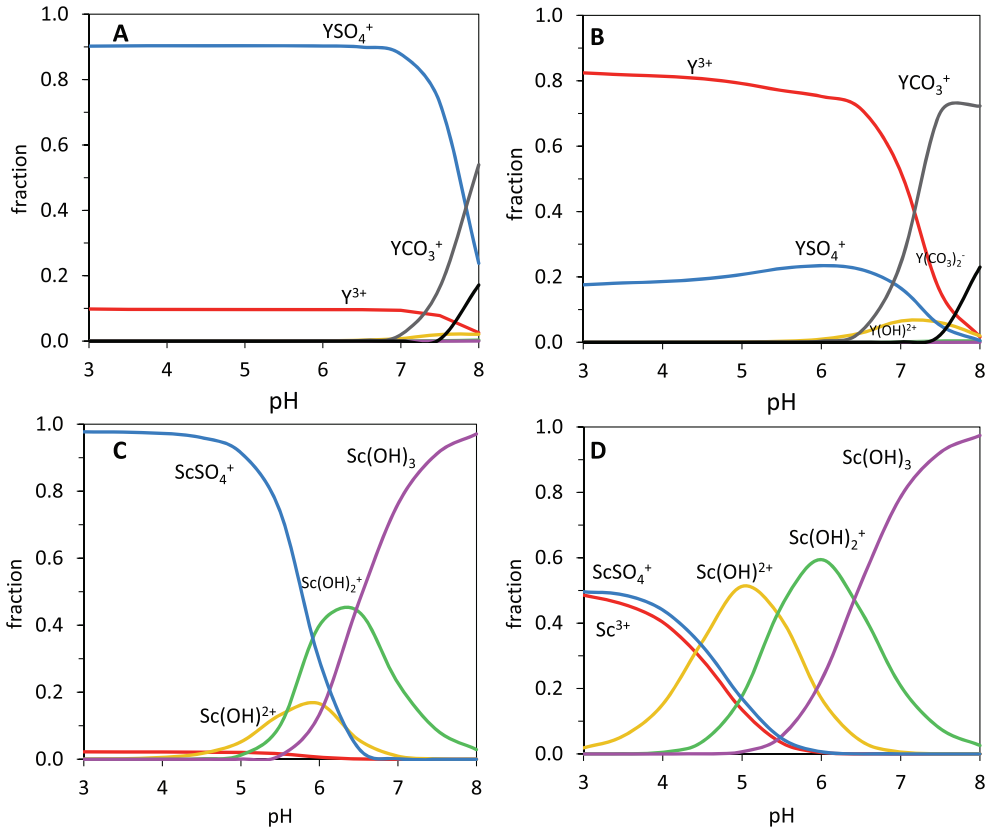

Fig. 4. Aqueous species distribution of Y and Sc with pH for a solution with 20 mM (A, C) and 0.5 mM (B, D) of sulfate at 25 °C and atmospheric pCO_2.

where a_{Mz+} and a_{H+} are the activities of the aqueous complex and proton, respectively; and $\{(XO)_nM^{z-n}\}$ and $\{XOH\}$ account for the mole fraction of the sorbed species ($[(XO)_nM^{z-n}]/[T_{XOH}]$) and the free surface sites ($[XOH]/T_{XOH}$), respectively.

A total surface site concentration T_{XOH} of 516 µmol/kg was obtained from the basaluminite site density of 4.6 site/nm^{-2}, the specific surface area of 68 m^2/g. The concentration of free surface sites was calculated as:

$$[XOH] = T_{XOH} - \sum n[(XO)_nM^{z-n}] \quad (5)$$

The value of the equilibrium constant K_M for each element was obtained with data from the experiment with 20 mM SO_4, except for the case of the species $Sc(OH)^{2+}$, which was obtained from the experiment with 0.5 mM SO_4.

Thus, replacing the molar fraction by their values, taking logarithms of Eq. (4) and rearranging the order we obtain a linear expression (Eq. (6)):

$$\log\frac{[(XO)_nM^{z-n}]}{a_{M^{z+}}} = \log K_M + npH + n\log[XOH] - (n-1)\log T_{XOH} \quad (6)$$

The term for total surface sites (T_{XOH}) is only discarded for monodentate surface complexes (n=1) but it must be accounted for multidentate surface complexes. For instance, when bidentante complexes (n = 2) are present, the Eq. (6) is rearranged as expressed in Eq. (7).

The equilibrium constants for bidentate surface complexes are those referred to as the K_3 according to the model 3 proposed by Wang and Giammar (2013), where $K_3 = K_1 \cdot T_{XOH}$.

$$\log\frac{[(XO)_nM^{z-n}]}{a_{M^{z+}}} = \log K_M + 2pH + 2\log[XOH] + \log T_{XOH} \quad (7)$$

By plotting the experimental data according to Eqs. (6) and (7), linear correlations were obtained. Except for Sc, the slope of the regression was close to 1, where only La showed a slope value below 1. For the rest of lanthanides, the slopes were higher than 1 and increased progressively from LREE to HREE, reaching up to 1.3 (Fig. 5). A slope close to 1 suggests that the sorption occurs as a monodentate complex as indicated by the Eq. (3) with n = 1 (Rabung et al., 1998 and 2000). Similar observations were obtained by Rabung et al. (2006), after fitting EXAFS spectra of a γ-Al_2O_3 sorbed with Lu, where Lu formed a monodentate inner sphere complex.

Unlike Y and the lanthanides, the linear regression for $ScSO_4^+$ data from the 20 mM SO_4 experiment resulted in a slope close to 2 (2.37) (Fig. 6A). Similar results were observed for $Sc(OH)^{2+}$ with a slope of 1.90 from the experiment with 0.5 mM SO_4, where it was the major species (Fig. 6B). In both cases, a slope of 2 suggests exchange with two surface protons and formation of a bidentate surface complex for both aqueous species. Despite the fact that

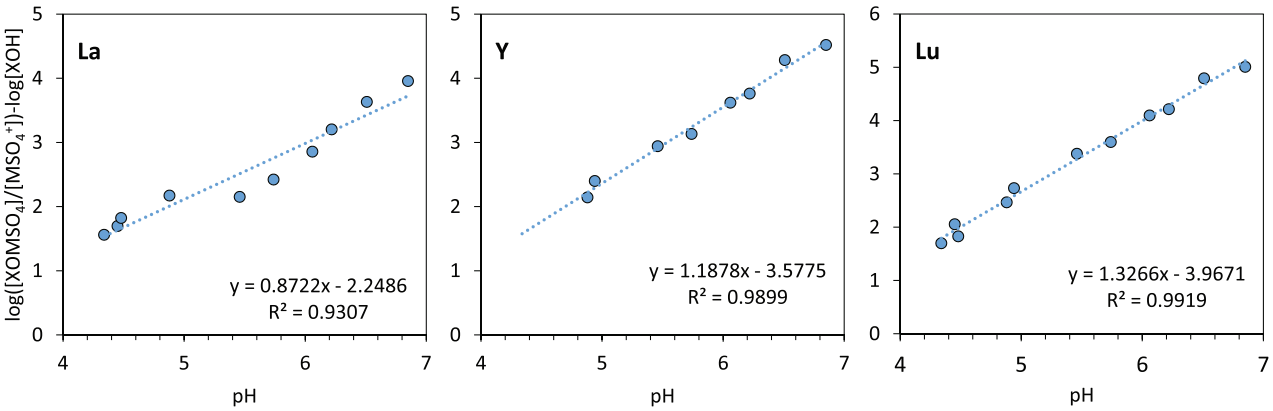

Fig. 5. Regressions obtained from the experimental data plotted as Eq. (6) considering n = 1. Measured pH values and activities calculated from the final concentrations. XOH are free available surface sites.

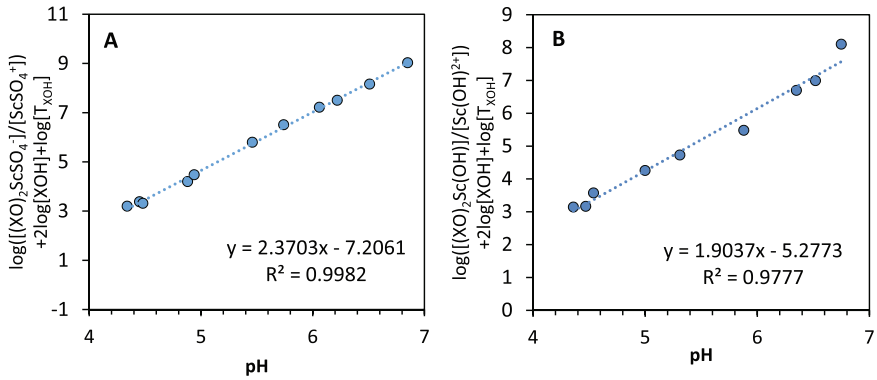

Fig. 6. Regressions obtained from experimental data from Sc element plotted according the linearized equations of reaction (7) (n = 2) for $ScSO_4^+$ (A) and for $Sc(OH)_2^+$ (B).

$Sc(OH)_2^+$ was predominant at pH 5.5, this aqueous species provided a very low slope and poorer correlation (not shown), and was not considered a sorbed species.

To obtain surface sorption constants, the regression slopes were forced to 1 for yttrium and lanthanides and to 2 for Sc via the Gnuplot v5.00 software (Williams and Kelley, 1986) using experimental data with higher sulfate content in solution. The resulting log K_M was obtained as the intercept. The error of the regression calculation was larger and enclosed the analytical error, and it was assumed to be the error of the log K_M value. The log K_M values and the regression errors for surface complexation reactions for all REE are listed in Table 1. Apart from values for Sc complexation, the equilibrium constants increased from −2.48 to −2.19 from La to Lu, indicating higher HREE than LREE affinity for the basaluminite surface. These log K_M values are close to those obtained by Quinn et al. (2006a) for complexation of free REE ions onto ferric oxide surfaces.

4.3. Validation

Log K_M values conducted at high sulfate concentration were validated with results from the experiment with lower

Table 1
Equilibrium constants for the formation of surface complexes (K_M of Eq. (3)) obtained by fitting the experimental values. Concentration of the surface species calculated as their molar fractions (i.e., K_M is the K_3 value of Wang and Giammar (2013)). Surface site density was 4.60 nm^{-2} and specific surface area 68 m^2/g.

Element	Surface Complex	Log K_M	Error
Sc	$(XO)_2ScSO_4^-$	−5.19	0.08
	$(XO)_2Sc(OH)$	−5.81	0.09
Y	$XOYSO_4$	−2.48	0.06
La	$XOLaSO_4$	−2.95	0.08
Ce	$XOCeSO_4$	−2.81	0.07
Pr	$XOPrSO_4$	−2.69	0.05
Nd	$XONdSO_4$	−2.60	0.03
Sm	$XOSmSO_4$	−2.48	0.05
Eu	$XOEuSO_4$	−2.50	0.05
Gd	$XOGdSO_4$	−2.50	0.04
Tb	$XOTbSO_4$	−2.48	0.06
Dy	$XODySO_4$	−2.37	0.06
Ho	$XOHoSO_4$	−2.40	0.05
Er	$XOErSO_4$	−2.40	0.11
Tm	$XOTmSO_4$	−2.27	0.08
Yb	$XOYbSO_4$	−2.13	0.08
Lu	$XOLuSO_4$	−2.19	0.09

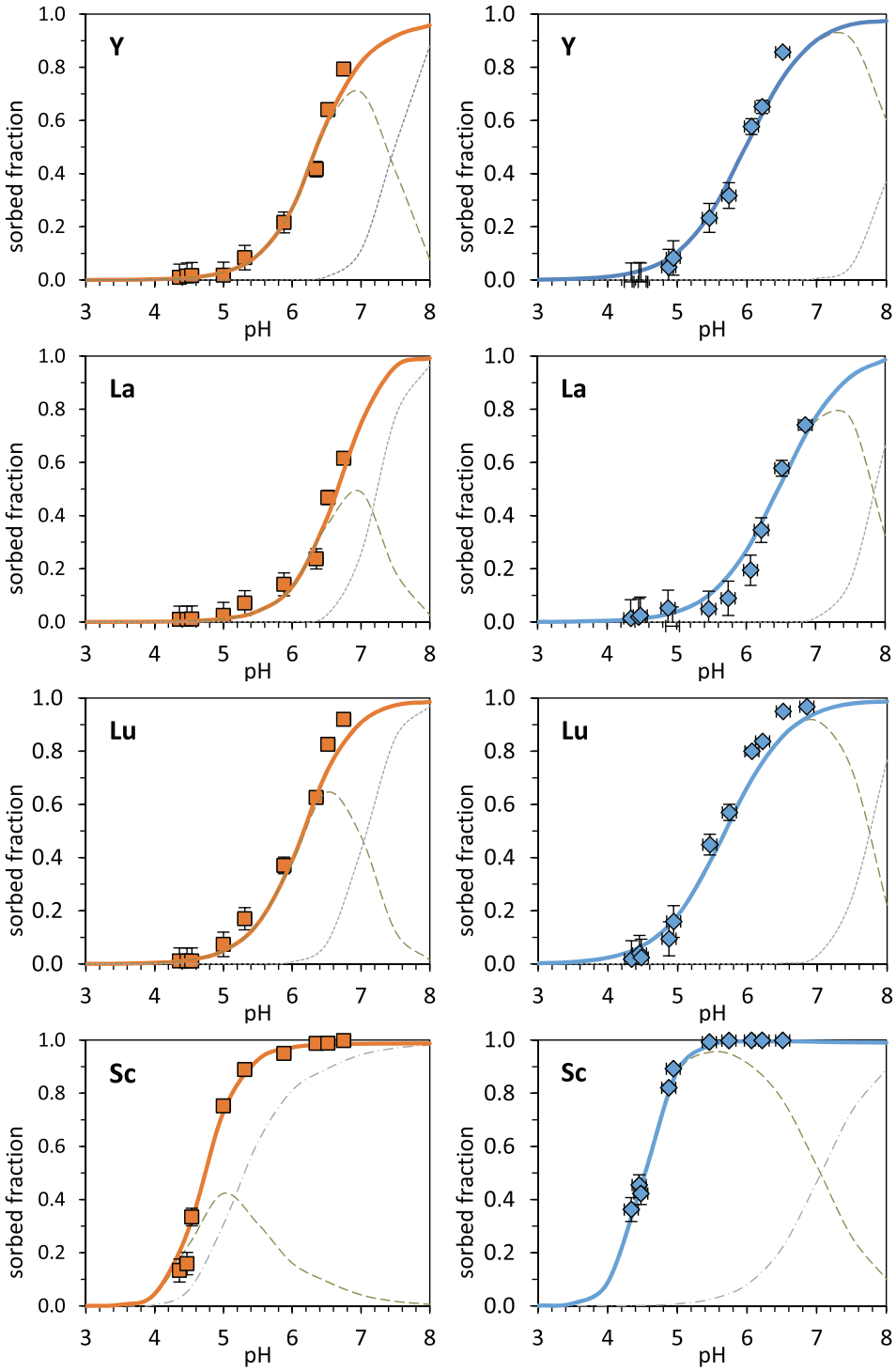

Fig. 7. Comparison between experimental data (symbols) and calculated fraction (lines) of the sorption edge curves for Sc, Y, La and Lu of the experiments with 20 mM SO_4 (diamonds) and with 0.5 mM SO_4 (squares). Continuous lines: total sorption, dashed lines: sorption of MSO_4^+ species and pointed lines: sorption of MCO_3^+. Calculations at 25 °C and pCO_2 of 3.5, including the carbonate complexation constants listed in Table SI-6.

sulfate content. In the case of Sc, the log K_M of reaction (7), obtained from the experiments with low sulfate content, was used to predict of the sorption edge curves for the 20 mM SO_4 experiment. The model results are plotted with continuous lines in Fig. 7. Model results for each REE are plotted in Figs. SI-3 and SI-4.

A temperature of 25 °C and a pCO_2 of 3.5 was considered to reproduce room conditions in the sorption models. At higher pH values than 6.5 a mismatch between the modeled sorbed fractions (solid lines in Fig. 7) and the experimental ones (symbols) for the experiment with the lower sulfate content is attributed to the presence of dissolved carbonate species. Thus, MCO_3^+ species can take part in the sorption process. To show the possible role of carbonate complexes at pH higher than 6.5 and low sulfate concentration, the sorption of MCO_3^+ complexes has been included in the model. The equilibrium constants for the MCO_3^+ sorption reactions have been recalculated from those reported by Quinn et al. (2006b) for goethite (Table SI-6). Including carbonate complexation, the model predicts sorption at near neutral pH when lower sulfate is present in solution, supporting the role of carbonate complexation at such particular conditions (pointed lines in Fig. 7).

As expected, the model reproduces the sorption edges in the experiment with 20 mM SO_4 (Fig. 7, left) well. Indeed, only adsorption very close or outside the experimental error is predicted for La and Ce at some pH values below 6.0. Although worse, the model for the experiment with lower sulfate content is also acceptable, and the predicted values in general fit the analyses within experimental error (Fig. 7, right). A slight overprediction of the adsorption at intermediate pH values and an underprediction at high pH values is systematically observed.

In addition to the sorption edges, the model also predicts the fractionation patterns of the lanthanide group (Fig. SI-5) and the M-type tetrad effect, within experimental error. As observed in the pH sorption edge curves, the model tends to underpredict the K_D values at pH 6.4. This is especially relevant for low sulfate concentration (Fig. SI-5B) and is attributed to the increasing importance of MCO_3^+ aqueous complexes at near neutral pH. In contrast, the model tends to overpredict the values for the intermediate pH (between 5.5 and 6.5), particularly for the intermediate lanthanides. The yttrium experimental K_D values are well predicted in all cases. However, the model fails to predict other anomalies. For instance, the positive Ce anomaly observed at pH values lower than 5.3 in the experiment without an initial sulfate concentration is not reproduced. Similar observations were described in Bau (1999) for REE scavenged in Fe oxyhydroxide at a pH lower than 5 and were attributed to a partial oxidation of Ce(III) at low pH. Similar poor fit is observed for the Er negative anomaly in sorption with high sulfate in solution and, the Dy and Yb negative anomalies detected with lower aqueous sulfate concentrations were not predicted by the model. In the latter case, no previous descriptions of these anomalies have been reported and they might be related to an analytical error for very low concentration.

The good fit between the predicted and measured Sc values confirms a good model prediction for the formation of

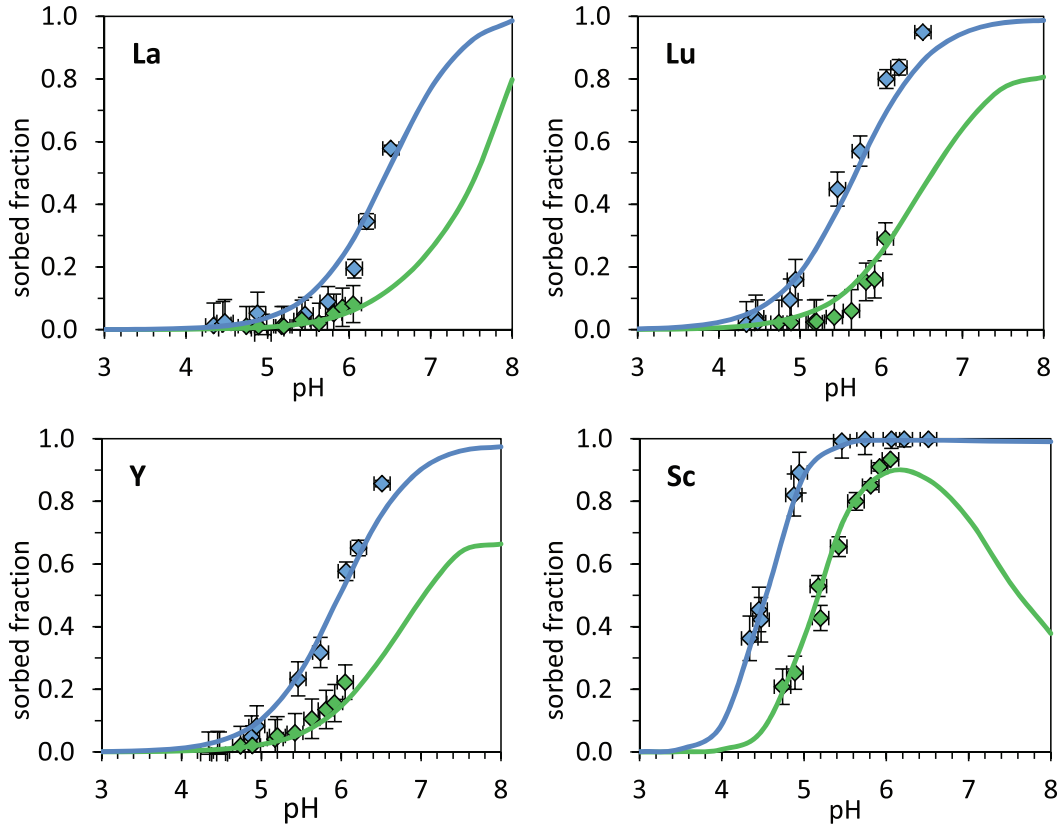

Fig. 8. Comparison between experimental data (symbols) and calculated fraction (lines of the sorption edge curves for Sc, Y, La and Lu at two different solid:liquid ratios (1 g/L the blue symbols and 0.25 g/L the green ones) and 20 mM SO_4. Calculations at 25 °C and pCO_2 of 3.5, including the carbonate complexation constants listed in Table SI-6.

bidentate surface complexes. As observed in Fig. 7, the $(XO)_2ScSO_4^-$ complex predominates in the experiment with 20 mM SO_4, and the $(XO)_2ScOH$ complex predominates in the experiment with a low SO_4 concentration. Again, Sc behaves differently due to the stronger hydrolysis effect than sulfate complexation. The higher ligand ratio for Sc may be due to its structural characteristics. Lanthanide cations are larger than Sc^{3+}, and have coordination numbers ranging from 8 (with a tricaped trigonal prism configuration) to 9 (with a distorted square antiprism or dodecahedron configuration of the hydration sphere) (Lindqvist-Reis et al., 2000; Rouse et al., 2001). On the contrary, Sc^{3+} (0.75 Å) has an ionic radius closer to that of Al^{3+} (0.53 Å), adopting an octahedral coordination (Lindqvist-Reis et al., 2006; Levard et al., 2018). This fact leads to similar interatomic distances to oxygen, allowing the formation of complexes with bidentate ligands. The different behavior of Sc suggests its potential segregation from the rest of the REE.

Finally, the model was also tested with experimental data for a solid:liquid ratio of 0.25 g/L. The results for four selected elements are included in Fig. 8 (the results for the initial ratio of 1 g/L are also included). The comparison between predicted and experimental values for the complete set of REE is in Fig. SI-6. As expected, the model predicts lower adsorption for lower solid:liquid ratio, showing a general consistency with experimental data. Comparing the prediction along the lanthanide series with experimental sorption data, the model better predicts HREE than LREE, where the predicted sorption was slightly lower than observed for La, Ce and Pr. Interestingly, Sc sorption by means of bidentate complexes was satisfactory predicted.

5. CONCLUSIONS

This work shows that basaluminite has a high capacity to retain REE by an adsorption mechanism, and this process is highly dependent on pH. Thus, REE sorption on basaluminite starts to be significant between pH 5–5.5 for lanthanides and yttrium and from pH 4–4.5 for Sc, depending on the solid:liquid ratio. Lanthanide fractionation also occurred from pH 5.3, yielding the M-type tetrad effect and reflecting HREE enrichment onto the solid. These results are analogous to the fractionation observed in Al and Fe oxide precipitates in the confluence of acid sulfate waters with natural streams and rivers and therefore could explain the mechanism of REE retention in natural precipitates. As expected from the overwhelming importance of the sulfate aqueous speciation (MSO_4^+), higher REE sorption was observed at higher sulfate concentrations. These results confirm that aqueous speciation and sorption onto basaluminite control the REE geochemistry in acid rock/mine drainages.

A non-electrostatic surface complexation model has been proposed to explain the sorption mechanism. In the model description, sulfate plays a key role since the strong complexation with REE leads to sorption of the aqueous sulfate complex MSO_4^+, rather than the free ion M^{3+}, as commonly described by other authors for REE sorption in oxides. Thanks to experimental data from the REE sorption experiment with high sulfate concentration (20 mM), surface constants were calculated and validated with experiments with low sulfate concentration (0.1 to 0.9 mM) and a lower solid:liquid ratio. Additionally, at near neutral pH and sulfate concentrations lower than 1 mM, the sorption of the aqueous carbonate complex, MCO_3^+, should be considered when mixing with natural water.

This work presents for the first time sorption equilibrium constants for REE sorption onto basaluminite, a very common mineral in mine discharge. Despite REE behaving as a group with similar chemical properties, their ionic radii vary along the series, and the different distances lead to slightly different positions on the basaluminite surface. This is clearly observed for Sc, which with a considerably smaller ionic radius than the other REE, forms bidentate surface complexes in comparison with the monodenate bonds formed by the rest of the REE group. Additionally, its aqueous speciation, with the formation of stable hydroxyl species, makes Sc behave differently and sorb at lower pH values. This knowledge could help design REE separation mechanisms and isolate cost-effective elements.

ACKNOWLEDGEMENTS

This work was funded by the European EIT 'Morerecovery' and the Spanish SCYRE (CGL2016-78783-C2-R)] projects. A. L. was also funded by the FPI grant (BES-2014-069978) Ministry of Science, Innovation and Universities (Spain). The authors wish to thank J. Bellés, M. Cabañas, R. Bartrolí and N. Moreno (IDAEA-CSIC) for their analytical assistance. The manuscript has been greatly improved with the comments of Prof. Villalobos and three anonymous reviewers.

APPENDIX A. SUPPLEMENTARY MATERIAL

Supplementary data to this article can be found online at https://doi.org/10.1016/j.gca.2019.05.016.

REFERENCES

Ackman, T., 1982. Sludge disposal from acid mine drainage treatment. Report of Investigation 8672. US Bureau of Mines, Pittsburgh.

Adams F. and Rawajfih Z. (1977) Basaluminite and alunite: a possible cause of sulfate retention by acid soils. *Soil Sci. Soc. Am. J.* **41**, 686–692.

Alonso E., Sherman A. M., Wallington T. J., Everson M. P., Field F. R., Roth R. and Kirchain R. E. (2012) Evaluating Rare Earth Element availability: A Case with revolutionary demand from clean technologies. *Environ. Sci. Technol.* **46**, 3406–3414.

Auqué L. F., Tena J. M., Gimeno M. J., Mandado J. M., Zamora A. and Lopez-Julian P. L. (1993) Distribución de tierras raras en soluciones y coloides de un sistema natural de aguas acidas (Arroyo del Val, Zaragoza). *Est. Geol.* **49**, 41–48.

Ayora C., Macías F., Torres E., Lozano A., Carrero S., Nieto J. M., Pérez-López R., Fernández-Martínez A. and Castillo-Michel H. (2016) Recovery of rare earth elements and yttrium from passive-remediation systems of acid mine drainage. *Environ. Sci. Technol.* **50**(15), 8255–8262.

Baleeiro A., Fiol S., Otero-Fariña A. and Antelo J. (2018) Surface chemistry of iron oxides formed by neutralization of acidic mine waters: removal of trace metals. *Appl. Geochem.* **89**, 129–137.

Bau M., Koschinsky A., Dulski P. and Hein J. R. (1996) Comparison of the partitioning behaviours of yttrium, rare earth elements, and titanium between hydrogenetic marine ferromanganese crusts and seawater. *Geochim. Cosmochim. Acta* **60**, 1709–1725.

Bau M. (1999) Scavenging of dissolved yttrium and rare earths by precipitating iron oxyhydroxide: experimental evidence for Ce oxidation, Y-Ho fractionation, and lanthanide tetrad effect. *Geochim. Cosmochim. Acta* **63**, 67–77.

Berger, V.I., Singer, D.A., Orris, G.J., 2009. Carbonatites of the world: explored deposits of Nb and REY. Database and grade and tonnage models. USGS Open-File Report, 11–39.

Blanc Ph., Lassin A., Piantone P., Azaroual M., Jacquemet N., Fabbri A. and Gaucher E. C. (2012) Thermoddem: Ageochemical database focused on low temperature water/rock interactions and waste materials. *App. Geochem.* **27**, 2107–2116.

Bonnail E., Pérez-López R., Sarmiento A. M., Nieto J. M. and DelValls T. Á. A. (2017) Novel approach for acid mine drainage pollution biomonitoring using rare earth elements bioaccumulated in the freshwater clam Corbicula fluminea. *J. Hazard. Mater.* **338**, 466–471.

Byrne R. H. and Kim K. H. (1990) Rare earth element scavenging in seawater. *Geochim. Cosmochim. Acta* **54**, 2645–2656.

Caraballo M. A., Macías F., Rötting T. S., Nieto J. M. and Ayora C. (2011) Long term Remediation of highly polluted acid mine drainage: A sustainable approach to restore the environmental quality of the Odiel river basin. *Environ. Pollut.* **159**(12), 3613–3619.

Carrero S., Fernández-Martínez A., Pérez-López R., Lee D., Aquilanti G., Poulain A., Lozano A. and Nieto J. M. (2017) The nanocrystalline structure of basaluminite, an aluminum hydroxide sulfate from acid mine drainage. *Am. Mineral.* **102**, 2381–2389.

Davis J. A. and Kent D. B. (1990) Surface Complexation modeling in aqueous. *Geochemistry* **23**, 177–260.

De Carlo E. H., Wen X. and Irving M. (1998) The influence of redox reactions on the uptake of dissolved Ce by suspended Fe and Mn oxide particles. *Aquat. Geochem.* **3**, 357–389.

Delgado J., Pérez-López R., Galván L., Nieto J. M. and Boski T. (2012) Enrichment of rare earth elements as environmental tracers of contamination by acid mine drainage in salt marshes: A new perspective. *Mar. Pollut. Bull.* **64**(9), 1799–1808.

Farkas L. and Pertlik F. (1997) Crystal structure determinations of felsöbányaite and basaluminite, $Al_4(SO_4)(OH)_{10}{\cdot}4H_2O$. *Acta Mineral.-Petrogr Szeged* **38**, 5–15.

Ferreira da Silva E., Ferreira E., Bobos I., Matos J., Patinha C., Reis A. P. and Fonseca E. C. (2009) Mineralogy and geochemistry of trace metals and REE in massive volcanic sulphide host rocks, stream sediments, stream waters and acid mine drainage from the Lousal mine area (Iberian Pyrite Belt, Portugal). *Appl. Geochem.* **24**, 383–401.

Gammons C. H., Wood S. A., Jonas J. P. and Madison J. P. (2003) Geochemistry of rare earth elements and uranium in the acidic Berkeley Pit lake, Butte,Montana. *Chem. Geol.* **198**, 269–288.

Gammons C. H., Wood S. A. and Nimick D. A. (2005a) Diel behavior of rare earth elements in a mountain stream with acidic to neutral pH. *Geochim. Cosmochim. Acta* **69**(15), 3747–3758.

Gammons C. H., Wood S. A., Pedrozo F., Varekamp J. C., Nelson B. J., Shope C. L. and Baffico G. (2005b) Hydrogeochemistry and rare earth element behavior in a volcanically acidified watershed in Patagonia Argentina. *Chem. Geol.* **222**, 249–267.

Gimeno M. J., Auque L. F., Lopez-Julian P. L., Gomez-Jime-nez J. and Mandado J. M. (1996) Pautas de distribución de especies de las tierras raras en soluciones ácidas naturales. *Est. Geol.* **52**, 11–22.

Gimeno M. J., Auque L. F. and Nordstrom D. K. (2000) REE speciation in low-temperature acidic waters and the competitive effects of aluminum. *Chem. Geol.* **165**, 167–180.

Goldberg S. (1992) Use of surface complexation models in soil chemical systems. *Adv. Agron.* **47**, 233–329.

Grawunder A., Merten D. and Büchel G. (2014) Origin of middle rare earth element enrichment in acid mine drainage-impacted areas. *Environ. Sci. Pollut. Res.* **21**(11), 6812–6823.

Hatch G. P. (2012) Dynamics in the global market for rare earths. *Elements* **8**, 341–346.

Isildar A., Rene E. R., van Hullenbusch E. D. and Lens P. N. L. (2018) Electronic waste as a secondary source of critical metals: Management and recovery technologies. *Resour. Conserv. Recycl.* **135**, 296–312.

Johnson J., Anderson G. and Parkhurst D. (2000) *Database 'thermo.com.V8.R6.230' Rev. 1.11*. Lawrence Livermore Natl, Lab, Livermore, California.

Klungness G. D. and Byrne R. H. (2000) Comparative hydrolysis behavior of the rare earths and yttrium: the influence of temperature and ionic strength. *Polyhedron* **19**, 99–107.

Koeppenkastrop D. and De Carlo E. H. (1992) Sorption of rare-earth elements from seawater onto synthetic mineral particles: an experimental approach. *Chem. Geol.* **95**, 251–263.

Lee J. H. and Byrne R. H. (1992) Examination of comparative rare earth element complexation behavior using linear free-energy relationships. *Geochim. Cosmochim. Acta* **56**, 1127–1137.

Levard C., Borschneck D., Grauby O., Rose J. and Ambrosi J.-P. (2018) Goethite, a tailor-made host for the critical metal scandium: The $Fe_xSc_{(1-x)}OOH$ solid solution. *Geochem. Perspect. Lett.* **9**, 16–20.

Li X. and Wu P. (2017) Geochemical characteristics of dissolved rare earth elements in acid mine drainage from abandoned high-As coal mining area, southwestern China. *Environ. Sci. Pollut. Res.* **24**(25), 20540–20555.

Lindqvist-Reis P., Lambe K., Pattanaik S., Persson I. and Sandström M. (2000) Hydration of the Yttrium(III) ion in aqueous solution. An X-ray diffraction and XAFS structural study. *J. Phys. Chem. B* **104**, 402–408.

Lindqvist-Reis P., Persson I. and Sandström M. (2006) The hydration of the Scandium(III) ion in aqueous solution and crystalline hydrates studied by XAFS spectroscopy, large-angle X-ray scattering and crystallography. *Dalt. Trans.* **32**, 3868–3878.

Liu H., Pourret O., Guo H. and Bonhoure J. (2017) Rare earth elements sorption to iron oxyhydroxide: Model development and application to groundwater. *Appl. Geochem.* **87**, 158–166.

Lozano A., Fernández-Martínez A., Ayora A. and Poulain A. (2018) Local structure and ageing of basaluminite at different pH values and sulphate concentrations. *Chem. Geol.* **496**, 25–33.

Luo Y. R. and Byrne R. H. (2001) Yttrium and rare earth element complexation by chloride ions at 25 degrees. *C. J. Solution Chem.* **30**(9), 837–845.

Luo Y. R. and Byrne R. H. (2004) Carbonate complexation of yttrium and the rare earth elements in natural rivers. *Geochim. Cosmochim. Acta* **68**, 691–699.

Luo Y. and Millero F. J. (2004) Effects of temperature and ionic strength on the stabilities of the first and second fluoride complexes of yttrium and the rare earth elements. *Geochim. Cosmochim. Acta* **68**(21), 4301–4308.

Marmier N., Dumonceau A. J. and Fromage F. (1997) Surface complexation modeling of Yb(III) sorption and desorption on hematite and alumina. *J. Contam. Hydrol.* **26**, 159–167.

Marmier N. and Fromage F. (1999) Comparing electrostatic and non-electrostatic surface complexation modeling of the sorption of lanthanum on hematite. *J. Colloid. Interface Sci.* **212**, 252–263.

Masuda A., Kawakami O., Dohmoto Y. and Takenaka T. (1987) Lanthanide tetrad effects in nature: two mutually opposite types, W and M. *Geochem. J.* **21**, 119–124.

Millero F. J. (1992) Stability constants for the formation of rare earth inorganic complexes as a function of ionic strength. *Geochim. Cosmochim. Acta* **56**, 3123–3132.

Morgan B., Johnston S. G., Burton E. D. and Hagan R. E. (2016) Acidic drainage drives anomalous rare earth element signatures in intertidal mangrove sediments. *Sci. Total Environ.* **573**, 831–840.

Noack C. W., Dzombak D. A. and Karamalidis A. K. (2014) Rare earth element distributions and trends in natural waters with a focus on groundwater. *Environ. Sci. Technol.* **48**, 4317–4326.

Ohta A. and Kawabe I. (2000) Rare earth element partitioning between Fe oxyhydroxide precipitates and aqueous NaCl solutions doped with $NaHCO_3$: Determinations of rare earth element complexation constants with carbonate ions. *Geochem. J.* **34**, 439–454.

Pagano G., Guida M., Tommasi F. and Orce R. (2015) Health effects and toxicity mechanisms of rare earth elements. Knowledge gaps and research prospects. *Ecotoxicol. Environ. Saf.* **115**, 40–48.

Pourret O. and Martinez R. E. (2009) Modeling lanthanide series binding sites on humic acid. *J. Colloid Interface Sci.* **330**(1), 45–50.

Pourret O. and Davranche M. (2013) Rare earth element sorption onto hydrous manganese oxide: A modeling study. *J. Colloid Interface Sci.* **395**(1), 18–23.

Parkhurst D. L. and Appelo C. A. J. (1999) *User´s guide to PhreeqC (version 2.18) A computer program for speciation, and inverse geochemical calculations, U.S. Department of the Interior*. Geological Survey, U.S.

Quinn K. A., Byrne R. H. and Schijf J. (2006a) Sorption of yttrium and rare earth elements by amorphous ferric hydroxide: influence of pH and ionic strength. *Mar. Chem.* **99**, 128–150.

Quinn K. A., Byrne R. H. and Schijf J. (2006b) Sorption of yttrium and rare earth elements by amorphous ferric hydroxide: influence of solution complexation with carbonate. *Geochim. Cosmochim. Acta* **70**, 4151–4165.

Rabung T., Geckeis G., Jim J. and Beck H. P. (1998) Sorption of Eu(III) on natural hematite: application of surface complexation model. *J. Colloid Interface Sci.* **208**, 153–161.

Rabung Th., Stumpf H., Geckeis R. Klenz and Kim J. I. (2000) Sorption of Am(III) and Eu(III) onto γ-alumina: experiment and modeling. *Radiochim. Acta* **88**, 711–716.

Rabung B. T., Geckeis H., Wang X. K., Rothe J., Denecke M. A., Klenze R. and Fanghänel T. (2006) Cm (III) sorption onto γ - Al_2O_3: New insight into sorption mechanisms by time-resolved laser fluorescence spectroscopy and extended X-Ray absorption fine structure. *Radiochim. Acta* **94**, 609–618.

Rouse R. C., Peacor D. R., Essene E. J., Coskren T. D. and Lauf R. J. (2001) The new minerals levinsonite-(Y) [(Y, Nd, Ce)Al (SO4)2(C2O4)·12H2O] and Zugshunstite-(Ce) [(Ce, Nd, La)Al (SO4)2(C2O4)·2H2O]: coexisting oxalates with different structures and differentiation of LREE and HREE. *Geochim. Cosmochim. Acta* **65**, 1101–1115.

Schijf J. and Byrne R. H. (2004) Determination of SO4β1 for yttrium and the rare earth elements at I = 0.66 m and t = 25° C—Implications for YREE solution speciation in sulfate-rich waters. *Geochim. Cosmochim. Acta* **68**(13), 2825–2837.

Spahiu K. and Bruno J. (1995) A selected thermodynamic database for REE to be used in HLNW performance assessment exercises. *SKB Technical Report* **95–35**, 88 pp.

Tang J. and Johannesson K. H. (2003) Speciation of rare earth elements in natural terrestrial waters: Assessing the role of dissolved organic matter from the modeling approach. *Geochim. Cosmochim. Acta* **67**(13), 2321–2339.

Tertre E., Hofmann A. and Berger G. (2008) Rare earth element sorption by basaltic rock: Experimental data and modeling results using the "Generalised Composite approach". *Geochim. Cosmochim. Acta* **72**(4), 1043–1056.

Tochiyama O., Yamazaki H. and Li N. (1996) Effect of the concentration of metal ions on their adsorption on various hydrous iron and aluminum oxides. *J. Nucl. Sci. Technol.* **33** (11), 846–851.

Verplanck P. L., Antweiler R. C., Nordstrom D. K. and Taylor H. E. (2001) Standard reference water samples for rare earth element determinations. *Appl. Geochem.* **16**, 231–244.

Verplanck P. L., Nordstrom D. K., Taylor H. E. and Kimball B. A. (2004) Rare earth element partitioning between hydrous ferric oxides and acid mine water during iron oxidation. *Appl. Geochem.* **19**, 1339–1354.

Viadero, Jr., R. C., Wei X. and Buzby K. M. (2006) Characterization and dewatering evaluation of acid mine drainage sludge from ammonia neutralization. *Environ. Eng. Sci.* **23**(4), 734–743.

Wang Z. and Giammar D. E. (2013) Mass action expressions for bidentate adsorption in surface complexation modeling: Theory and practice. *Environ. Sci. Technol.* **47**(9), 3982–3996.

Webster J. G., Swedlund P. J. and Webster K. S. (1998) Trace metal adsorption onto an acid mine drainage iron(III) oxy hydroxy sulfate. *Environ. Sci. Technol.* **32**, 1361–1368.

Williams T. and Kelley C. (1986) *An interactive*. Plotting Program.

Wood S. A. and Samson A. M. (2006) The aqueous geochemistry of gallium, germanium, indium and scandium. *Ore Geol. Rev.* **28**, 57–102.

Xiangke W., Dong W., Xiongxin D., Wang A., Du J. and Tao Z. (2000) Sorption and desorption of Eu and Yb on alumina: mechanisms and effect of fulvic acid. *Appl. Radiat. Isot.* **52**, 165–173.

Associate editor: Mario Villalobos

Supplementary material

Sorption of rare earth elements onto basaluminite: the role of sulfate and pH

Alba Lozano[a,b*], Carlos Ayora[a], Alejandro Fernández-Martínez[c]

[a] Institute of Environmental Assessment and Water Research, (IDAEA-CSIC), Jordi Girona 18-26, 08034 Barcelona, Spain

[b] Grup de Mineralogia Aplicada i Geoquímica de Fluids, Departament de Cristal-lografia, Mineralogia i Dipòsits Minerals, Facultat de Geologia, Universitat de Barcelona (UB), C/Martí Franquès, S/N, Barcelona, Spain

[c] Univ. Grenoble Alpes, Univ. Savoie Mont Blanc, CNRS, IRD, IFSTTAR, ISTerre, 38000 Grenoble, France

Corresponding author:

Alba Lozano (alba.lozano@idaea.csic.es)

TABLE CAPTIONS

Table SI-1. Aqueous speciation constants for Sc, Y and lanthanides (M) with different ligands. References: [a]: Klugness & Byrne, 2000 ; [b]: Lee & Byrne, 92; [c]: Luo & Byrne, 2004;[d]: Millero, 1992; [e]: Luo & Millero, 2004; [f]: Schijf & Byrne, 2004; [g]: Luo & Byrne,2001; [h]: Wood and Samson, 2006 (for Sc speciation).

Table SI-2. Initial and final concentrations (mg/L) of aqueous solution at each pH for the two sets of experiments with solid:liquid ratio of 1 g/L and 0.5 mM SO_4 and 20 mM SO_4, respectively.

Table SI-3. Saturation index (SI) for experiment with 20 mM SO_4 and 0.5 mM SO_4, respectively.

Table SI-4. Sorbed fraction calculated with data from the experiments with a 0.25 g/L solid:liquid ratio and 20 mM SO_4 in solution.

Table SI-5. Experimental log K_D (L/kg) from experiment with 20 mM SO_4 and 0.5 mM SO_4, respectively.

Table SI-6. REE surface complexation constants for aqueous carbonate complexes estimated from values obtained by Quinn et al., 2006 b (Table2).

FIGURE CAPTIONS

Fig. SI-1. X-ray Diffraction Pattern for synthetic basaluminite previous to sorption experiments (pure) and basaluminite after REE adsorption with sulfate presence at four different pH values obtained at ID-31 beamline, ESRF. The peaks observed are artifacts due to the panel detector (see Lozano et al., 2018 for details).

Fig. SI-2. Distribution of the surface sites in basaluminite structure.

Fig. SI-3. Predictions of REE adsorption in experiment with 20 mM sulfate using surface complexation constants in table 2.

Fig. SI-4. Predictions of REE adsorption in experiment with 0.5 mM sulfate using surface complexation constants in table 2.

Fig. SI-5. Experimental data (symbols) and model (lines) of fractionation constants (log K_D) for lanthanide series in (A) sorption experiment without 20 mM sulfate and (B) with 0.5 mM sulfate. Calculations at 25 C and pCO_2 of 3.5 including sorption of both MSO_4^+ and MCO_3^+ aqueous species.

Fig SI-6. REE sorption fraction for two different solid:solute ratios 1 g/L (blue), 0.25 g/L (green) obtained from experimental data (symbols) and the predicted model for each experiment (lines).

Table SI-1. Aqueous speciation constants for Sc, Y and lanthanides (M) with different ligands. References: [a]: Klugness & Byrne, 2000 ; [b]: Lee & Byrne, 92; [c]: Luo & Byrne, 2004;[d]: Millero, 1992; [e]: Luo & Millero, 2004; [f]: Schijf & Byrne, 2004; [g]: Luo & Byrne,2001; [h]: Wood and Samson, 2006 (for Sc speciation).

Equation	$\log {}_L\beta_n$	Sc	Y	La	Ce	Pr	Nd	Sm	Eu	Gd	Tb	Dy	Ho	Er	Tm	Yb	Lu	Ref
$M^{+3} + H_2O = M(OH)^{+2} + H^+$	$\log {}_{OH}\beta^*_1$	-4.31	-7.80	-8.81	-8.34	-8.32	-8.18	-7.84	-7.76	-7.83	-7.64	-7.59	-7.56	-7.52	-7.39	-7.45	-7.27	a
$M^{+3} + 2H_2O = M(OH)_2^+ + 2H^+$	$\log {}_{OH}\beta^*_2$	-9.70	-16.40	-18.14	-17.60	-17.27	-17.04	-16.51	-16.37	-16.37	-16.18	-16.10	-16.07	-15.96	-15.88	-15.74	-15.67	b,h
$M^{+3} + 3H_2O = M(OH)_3 + 3H^+$	$\log {}_{OH}\beta^*_3$	-16.10	-25.99	-27.90	-27.23	-26.63	-26.40	-25.91	-25.41	-25.28	-25.08	-24.83	-24.56	-24.35	-24.18	-23.85	-23.85	b,h
$M^{+3} + CO_3^{-2} = MCO_3^+$	$\log {}_{CO3}\beta_1$		7.48	6.73	7.06	7.23	7.28	7.46	7.48	7.39	7.46	7.56	7.55	7.61	7.68	7.81	7.75	c
$M^{+3} + HCO_3^- = MHCO_3^{+3}$	$\log {}_{HCO3}\beta_1$		2.32	2.34	2.31	2.25	2.28	2.34	2.47	2.36	2.46	2.50	2.46	2.49	2.52	2.53	2.49	c
$M^{+3} + 2CO_3^{-2} = M(CO3)_2^-$	$\log {}_{CO3}\beta_2$		12.63	11.30	11.76	12.08	12.17	12.53	12.63	12.48	12.78	12.91	13.00	13.12	13.27	13.30	13.37	c
$M^{+3} + NO_3^- = MNO_3^{+2}$	$\log {}_{NO3}\beta_1$			0.58	0.69	0.69	0.79	0.78	0.83	0.47	0.51	0.15	0.25	0.15	0.20	0.25	0.56	d
$M^{+3} + F^- = MF^{+2}$	$\log {}_F\beta_1$		3.97	3.11	3.29	3.35	3.29	3.61	3.72	3.71	3.83	3.88	3.78	3.77	3.77	3.84	3.74	e
$M^{+3} + 2F^- = MF_2^+$	$\log {}_F\beta_2$		6.35	5.16	5.48	5.66	5.66	5.99	6.11	6.07	6.24	6.29	5.98	5.96	6.09	6.31	6.31	e
$M^{+3} + SO_4^{-2} = MSO_4^+$	$\log {}_{so4}\beta_1$	4.18	3.50	3.61	3.61	3.62	3.60	3.63	3.64	3.61	3.59	3.57	3.54	3.51	3.48	3.46	3.44	f,h
$M^{+3} + Cl^- = MCl^{+2}$	$\log {}_{Cl}\beta_1$		0.65	0.65	0.65	0.65	0.65	0.65	0.65	0.65	0.65	0.65	0.65	0.65	0.65	0.65	0.65	g

Table SI-2. Initial and final concentrations (ppm) of aqueous solution at each pH for experiment with solid:liquid ratio of 1 g/L and 0.5 mM SO_4 and 20 mM SO_4, respectively.

Sorption with 20 mM SO_4 in solution																			
Initial concentration (ppm)																			
pH	Sc	Y	La	Ce	Pr	Nd	Sm	Eu	Gd	Tb	Dy	Ho	Er	Tm	Yb	Lu	Al	S	Na
4.34	0.957	0.960	0.872	0.874	0.890	0.948	0.954	0.937	0.942	0.945	0.997	0.951	0.901	0.947	0.963	0.950	0.00	665.80	957.09
4.45	0.943	0.946	0.859	0.861	0.877	0.934	0.940	0.923	0.928	0.931	0.983	0.937	0.887	0.933	0.949	0.936	0.00	665.80	957.09
4.48	0.928	0.930	0.846	0.847	0.863	0.919	0.925	0.908	0.913	0.916	0.967	0.922	0.873	0.919	0.934	0.921	0.00	665.80	957.09
4.88	0.919	0.921	0.838	0.839	0.855	0.911	0.916	0.900	0.905	0.908	0.958	0.914	0.865	0.910	0.925	0.912	0.00	665.80	957.09
4.94	0.916	0.918	0.834	0.836	0.852	0.907	0.913	0.897	0.901	0.904	0.954	0.910	0.862	0.907	0.922	0.909	0.00	665.80	957.09
5.46	0.905	0.908	0.845	0.826	0.842	0.896	0.902	0.886	0.891	0.894	0.943	0.899	0.852	0.896	0.911	0.898	0.00	665.80	957.09
5.74	0.900	0.902	0.820	0.822	0.837	0.891	0.897	0.881	0.885	0.888	0.938	0.894	0.847	0.891	0.906	0.893	0.00	665.80	957.09
6.06	0.891	0.894	0.812	0.813	0.829	0.882	0.888	0.872	0.877	0.880	0.929	0.885	0.839	0.882	0.897	0.884	0.00	665.80	957.09
6.22	0.891	0.895	0.813	0.814	0.829	0.883	0.889	0.873	0.877	0.880	0.929	0.886	0.839	0.883	0.898	0.885	0.00	665.80	957.09
6.51	0.876	0.879	0.799	0.800	0.815	0.868	0.874	0.858	0.863	0.865	0.914	0.871	0.825	0.868	0.882	0.870	0.00	665.80	957.09
6.85	0.876	0.879	0.799	0.800	0.815	0.868	0.874	0.858	0.863	0.865	0.914	0.871	0.825	0.868	0.882	0.870	0.00	665.80	957.09
Final concentration (ppm)																			
pH	Sc	Y	La	Ce	Pr	Nd	Sm	Eu	Gd	Tb	Dy	Ho	Er	Tm	Yb	Lu	Al	S	Na
4.34	0.61	0.967	0.86	0.868	0.883	0.936	0.941	0.921	0.927	0.934	0.98	0.934	0.885	0.931	0.939	0.933	14.780	580.13	832.37
4.45	0.514	0.951	0.843	0.84	0.86	0.911	0.913	0.898	0.903	0.905	0.95	0.907	0.891	0.898	0.903	0.899	8.485	585.95	840.73
4.48	0.536	0.937	0.825	0.827	0.847	0.895	0.899	0.883	0.886	0.897	0.938	0.897	0.947	0.896	0.905	0.899	9.720	584.65	838.86
4.88	0.165	0.877	0.794	0.792	0.803	0.853	0.853	0.841	0.838	0.848	0.881	0.849	0.886	0.83	0.824	0.826	0.685	583.98	837.89
4.94	0.099	0.842	0.847	0.76	0.775	0.82	0.811	0.803	0.809	0.809	0.84	0.806	0.835	0.782	0.764	0.764	0.220	579.83	831.94
5.46	0.007	0.696	0.804	0.767	0.685	0.716	0.665	0.704	0.678	0.642	0.642	0.625	0.62	0.548	0.481	0.495	0.000	565.05	810.74
5.74	0.002	0.616	0.747	0.723	0.633	0.655	0.588	0.616	0.611	0.558	0.543	0.537	0.513	0.44	0.371	0.384	0.000	553.60	794.31
6.06	0.001	0.378	0.654	0.539	0.466	0.457	0.358	0.363	0.388	0.343	0.298	0.312	0.267	0.223	0.164	0.177	0.000	538.90	773.22
6.22	0.001	0.312	0.532	0.432	0.393	0.369	0.289	0.293	0.316	0.276	0.242	0.253	0.219	0.182	0.136	0.144	0.000	551.25	790.94
6.51	0.001	0.126	0.337	0.227	0.185	0.17	0.115	0.112	0.132	0.101	0.088	0.09	0.076	0.059	0.043	0.044	0.000	562.85	807.58
6.85	0.001	0.079	0.207	0.137	0.112	0.105	0.072	0.07	0.082	0.064	0.056	0.057	0.048	0.038	0.028	0.028	0.000	570.38	818.38

Table SI-2. continuation

Sorption with 0.5 $mMSO_4$ in solution																			
Initial concentration (ppm)																			
pH	Sc	Y	La	Ce	Pr	Nd	Sm	Eu	Gd	Tb	Dy	Ho	Er	Tm	Yb	Lu	Al	S	Na
4.36	0.898	0.898	0.891	0.896	0.886	0.886	0.889	0.880	0.884	0.882	0.883	0.879	0.881	0.883	0.886	0.881	0.000	0.000	0.000
4.47	0.878	0.878	0.871	0.875	0.866	0.865	0.869	0.860	0.864	0.862	0.863	0.859	0.861	0.863	0.865	0.861	0.000	0.000	0.000
4.54	0.890	0.890	0.883	0.887	0.878	0.877	0.881	0.872	0.875	0.874	0.875	0.871	0.872	0.875	0.877	0.872	0.000	0.000	0.000
5.00	0.881	0.881	0.874	0.878	0.869	0.868	0.872	0.863	0.867	0.865	0.866	0.862	0.864	0.866	0.868	0.864	0.000	0.000	0.000
5.31	0.873	0.873	0.867	0.871	0.861	0.861	0.864	0.855	0.859	0.857	0.859	0.854	0.855	0.859	0.861	0.855	0.000	0.000	0.000
5.88	0.949	0.949	0.941	0.946	0.936	0.936	0.939	0.930	0.934	0.932	0.933	0.929	0.930	0.933	0.936	0.930	0.000	0.000	0.000
6.35	0.943	0.943	0.936	0.941	0.930	0.930	0.934	0.925	0.928	0.926	0.928	0.923	0.925	0.928	0.930	0.925	0.000	0.000	0.000
6.52	0.911	0.878	0.891	0.881	0.837	0.840	0.834	0.832	0.820	0.836	0.868	0.831	0.875	0.838	0.866	0.838	0.000	0.000	0.000
6.75	0.870	0.870	0.864	0.868	0.859	0.857	0.862	0.852	0.856	0.854	0.855	0.851	0.853	0.855	0.857	0.853	0.000	0.000	0.000
8.40	0.862	0.830	0.842	0.833	0.792	0.795	0.789	0.787	0.776	0.791	0.820	0.786	0.827	0.792	0.818	0.792	0.000	0.000	0.000
Final concentration (ppm)																			
pH	Sc	Y	La	Ce	Pr	Nd	Sm	Eu	Gd	Tb	Dy	Ho	Er	Tm	Yb	Lu	Al	S	Na
4.36	0.778	0.889	0.882	0.877	0.877	0.870	0.871	0.869	0.856	0.868	0.874	0.862	0.863	0.866	0.877	0.871	4.765	8.219	0.731
4.47	0.738	0.865	0.862	0.856	0.856	0.853	0.850	0.849	0.855	0.845	0.854	0.850	0.852	0.854	0.856	0.851	3.993	9.328	0.752
4.54	0.592	0.875	0.873	0.865	0.865	0.868	0.872	0.860	0.853	0.855	0.866	0.862	0.863	0.866	0.868	0.862	2.629	9.808	0.760
5.00	0.218	0.865	0.852	0.845	0.844	0.833	0.827	0.824	0.818	0.822	0.855	0.819	0.815	0.811	0.859	0.800	0.513	10.752	0.857
5.31	0.097	0.801	0.805	0.791	0.789	0.770	0.760	0.751	0.731	0.751	0.800	0.747	0.738	0.726	0.760	0.710	0.045	12.619	0.817
5.88	0.048	0.746	0.808	0.788	0.778	0.764	0.735	0.724	0.719	0.724	0.770	0.719	0.754	0.690	0.710	0.585	0.000	17.285	0.603
6.35	0.012	0.550	0.714	0.630	0.542	0.493	0.444	0.460	0.472	0.439	0.446	0.431	0.433	0.382	0.362	0.346	0.000	22.295	1.098
6.52	0.011	0.315	0.474	0.355	0.316	0.284	0.210	0.210	0.243	0.217	0.210	0.213	0.205	0.174	0.148	0.146	0.000	30.200	0.000
6.75	0.002	0.180	0.332	0.226	0.179	0.150	0.099	0.099	0.124	0.103	0.103	0.105	0.102	0.083	0.071	0.068	0.000	28.945	1.259
8.40	0.004	0.002	0.002	0.002	0.001	0.002	0.001	0.001	0.001	0.001	0.002	0.001	0.002	0.001	0.002	0.001	0.000	44.952	0.000

Table SI-3. Saturation index (SI) for experiment with 20 mM SO_4 and 0.5 mM SO_4, respectively.

	experiment with 20 mM SO_4										
pH	4.34	4.45	4.48	4.88	4.94	5.46	5.74	6.06	6.22	6.51	6.85
Basaluminite	0.7	0.8	1.3	0.6	-0.8	-	-	-	-	-	-
$Gibbsite_{(am)}$	-2.0	-1.9	-1.8	-1.8	-2.1	-	-	-	-	-	-
Alunite(Na)	4.5	4.5	4.8	3.6	2.5	-	-	-	-	-	-
$Y(OH)_{3(am)}$	-12.4	-12.1	-12.0	-10.9	-10.7	-9.2	-8.4	-7.6	-7.3	-6.8	-6.0
$La(OH)_{3(am)}$	-17.2	-16.9	-16.9	-15.7	-15.5	-13.9	-13.1	-12.2	-11.8	-11.1	-10.3
$Ce(OH)_{3(am)}$	-15.0	-14.7	-14.7	-13.5	-13.3	-11.7	-10.9	-10.1	-9.7	-9.1	-8.3
$Pr(OH)_{3(am)}$	-14.8	-14.5	-14.5	-13.3	-13.1	-11.6	-10.8	-9.9	-9.6	-9.0	-8.2
$Nd(OH)_{3(am)}$	-14.2	-13.9	-13.8	-12.7	-12.5	-11.0	-10.2	-9.3	-9.0	-8.4	-7.6
$Sm(OH)_{3(am)}$	-12.4	-12.0	-12.0	-10.8	-10.6	-9.2	-8.3	-7.6	-7.2	-6.8	-6.0
$Gd(OH)_{3(am)}$	-11.8	-11.5	-11.4	-10.2	-10.0	-8.6	-7.8	-7.0	-6.6	-6.1	-5.3
$Tb(OH)_{3(am)}$	-12.5	-12.2	-12.2	-11.0	-10.8	-9.4	-8.6	-7.8	-7.4	-7.0	-6.2
$Dy(OH)_{3(am)}$	-11.2	-10.9	-10.8	-9.7	-9.5	-8.1	-7.3	-6.6	-6.2	-5.8	-5.0
$Ho(OH)_{3(am)}$	-11.5	-11.2	-11.1	-10.0	-9.8	-8.3	-7.5	-6.8	-6.5	-6.0	-5.2
$Er(OH)_{3(am)}$	-12.7	-12.4	-12.3	-11.1	-11.0	-9.5	-8.7	-8.1	-7.7	-7.3	-6.5
$Tm(OH)_{3(am)}$	-11.0	-10.7	-10.6	-9.4	-9.3	-7.9	-7.1	-6.4	-6.1	-5.7	-4.9
$Yb(OH)_{3(am)}$	-12.7	-12.3	-12.3	-11.1	-11.0	-9.6	-8.9	-8.3	-7.9	-7.5	-6.7
$Lu(OH)_{3(am)}$	-12.7	-12.3	-12.3	-11.1	-10.9	-9.6	-8.8	-8.2	-7.8	-7.5	-6.7
$Y(OH)_3$	-10.9	-10.6	-10.5	-9.4	-9.2	-7.7	-6.9	-6.1	-5.8	-5.3	-4.5
$La(OH)_3$	-14.0	-13.7	-13.7	-12.5	-12.3	-10.7	-9.9	-9.0	-8.6	-7.9	-7.1
$Ce(OH)_3$	-13.7	-13.4	-13.4	-12.2	-12.0	-10.4	-9.6	-8.8	-8.4	-7.8	-7.0
$Pr(OH)_3$	-13.3	-13.0	-13.0	-11.8	-11.6	-10.1	-9.3	-8.4	-8.1	-7.5	-6.7
$Nd(OH)_3$	-11.8	-11.5	-11.4	-10.3	-10.1	-8.6	-7.8	-6.9	-6.6	-6.0	-5.2
$Sm(OH)_3$	-10.3	-9.9	-9.9	-8.7	-8.5	-7.1	-6.2	-5.5	-5.1	-4.7	-3.9
$Eu(OH)_3$	-9.1	-8.8	-8.8	-7.6	-7.4	-5.9	-5.1	-4.4	-4.0	-3.6	-2.7
$Gd(OH)_3$	-9.4	-9.1	-9.0	-7.8	-7.6	-6.2	-5.4	-4.6	-4.2	-3.7	-2.9
$Tb(OH)_3$	-9.4	-9.1	-9.1	-7.9	-7.7	-6.3	-5.5	-4.7	-4.3	-3.9	-3.1
$Dy(OH)_3$	-9.6	-9.3	-9.2	-8.1	-7.9	-6.5	-5.7	-5.0	-4.6	-4.2	-3.4
$Ho(OH)_3$	-9.1	-8.8	-8.7	-7.6	-7.4	-5.9	-5.1	-4.4	-4.1	-3.6	-2.8
$Er(OH)_3$	-8.7	-8.4	-8.3	-7.1	-7.0	-5.5	-4.7	-4.1	-3.7	-3.3	-2.5
$Tm(OH)_3$	-8.7	-8.4	-8.3	-7.1	-7.0	-5.6	-4.8	-4.1	-3.8	-3.4	-2.6
$Yb(OH)_3$	-8.4	-8.0	-8.0	-6.8	-6.7	-5.3	-4.6	-4.0	-3.6	-3.2	-2.4
$Lu(OH)_3$	-8.2	-7.8	-7.8	-6.6	-6.4	-5.1	-4.3	-3.7	-3.3	-3.0	-2.2
$Sc(OH)_3$	-6.3	-6.0	-5.9	-5.2	-5.3	-5.0	-4.8	-4.6	-4.4	-4.1	-4.0

Table SI-3. continuation

	experiment with 0.5 mM SO_4									
pH	4.36	4.47	4.54	5.00	5.31	5.88	6.35	6.52	6.75	8.40
Basaluminite	1.1	1.9	1.8	3.0	-	-	-	-	-	-
$Gibbsite_{(am)}$	-1.5	-1.3	-1.3	-0.8	-	-	-	-	-	-
Alunite(Na)	-0.1	0.4	0.3	0.6	-	-	-	-	-	-
$Y(OH)_{3(am)}$	-11.2	-10.9	-10.7	-9.3	-8.5	-6.9	-5.7	-5.5	-5.1	-4.5
$La(OH)_{3(am)}$	-15.9	-15.6	-15.4	-14.1	-13.2	-11.6	-10.3	-10.1	-9.5	-8.2
$Ce(OH)_{3(am)}$	-13.6	-13.4	-13.2	-11.8	-11.0	-9.3	-8.1	-8.0	-7.5	-6.3
$Pr(OH)_{3(am)}$	-13.5	-13.2	-13.0	-11.7	-10.8	-9.2	-8.0	-7.8	-7.4	-6.7
$Nd(OH)_{3(am)}$	-12.9	-12.6	-12.4	-11.1	-10.2	-8.6	-7.5	-7.3	-6.9	-5.9
$Sm(OH)_{3(am)}$	-11.0	-10.7	-10.5	-9.2	-8.4	-6.8	-5.6	-5.6	-5.2	-4.6
$Gd(OH)_{3(am)}$	-10.5	-10.2	-10.0	-8.6	-7.8	-6.2	-5.0	-4.9	-4.5	-3.9
$Tb(OH)_{3(am)}$	-11.3	-11.0	-10.8	-9.4	-8.6	-7.0	-5.9	-5.8	-5.4	-5.0
$Dy(OH)_{3(am)}$	-10.0	-9.7	-9.5	-8.1	-7.2	-5.6	-4.5	-4.5	-4.1	-3.5
$Ho(OH)_{3(am)}$	-10.3	-10.0	-9.7	-8.4	-7.6	-6.0	-4.9	-4.7	-4.4	-4.2
$Er(OH)_{3(am)}$	-11.5	-11.2	-10.9	-9.6	-8.8	-7.1	-6.0	-6.0	-5.6	-5.2
$Tm(OH)_{3(am)}$	-9.7	-9.4	-9.2	-7.9	-7.1	-5.5	-4.4	-4.3	-4.0	-3.9
$Yb(OH)_{3(am)}$	-11.4	-11.1	-10.9	-9.6	-8.7	-7.1	-6.1	-6.1	-5.8	-5.4
$Lu(OH)_{3(am)}$	-11.5	-11.1	-10.9	-9.6	-8.8	-7.2	-6.1	-6.1	-5.8	-5.7
$Y(OH)_3$	-9.7	-9.4	-9.2	-7.8	-7.0	-5.4	-4.2	-4.0	-3.6	-3.0
$La(OH)_3$	-12.7	-12.4	-12.2	-10.9	-10.0	-8.4	-7.1	-6.9	-6.3	-5.0
$Ce(OH)_3$	-12.3	-12.1	-11.9	-10.5	-9.7	-8.0	-6.8	-6.7	-6.2	-5.0
$Pr(OH)_3$	-12.0	-11.7	-11.5	-10.2	-9.3	-7.7	-6.5	-6.3	-5.9	-5.2
$Nd(OH)_3$	-10.5	-10.2	-10.0	-8.7	-7.8	-6.2	-5.1	-4.9	-4.5	-3.5
$Sm(OH)_3$	-8.9	-8.6	-8.4	-7.1	-6.3	-4.7	-3.5	-3.5	-3.1	-2.5
$Eu(OH)_3$	-7.8	-7.5	-7.3	-6.0	-5.1	-3.5	-2.4	-2.3	-2.0	-1.4
$Gd(OH)_3$	-8.1	-7.8	-7.6	-6.2	-5.4	-3.8	-2.6	-2.5	-2.1	-1.5
$Tb(OH)_3$	-8.2	-7.9	-7.7	-6.3	-5.5	-3.9	-2.8	-2.7	-2.3	-1.9
$Dy(OH)_3$	-8.4	-8.1	-7.9	-6.5	-5.6	-4.0	-2.9	-2.9	-2.5	-1.9
$Ho(OH)_3$	-7.9	-7.6	-7.3	-6.0	-5.2	-3.6	-2.5	-2.3	-2.0	-1.8
$Er(OH)_3$	-7.5	-7.2	-6.9	-5.6	-4.8	-3.1	-2.0	-2.0	-1.6	-1.2
$Tm(OH)_3$	-7.4	-7.1	-6.9	-5.6	-4.8	-3.2	-2.1	-2.0	-1.7	-1.6
$Yb(OH)_3$	-7.1	-6.8	-6.6	-5.3	-4.4	-2.8	-1.8	-1.8	-1.5	-1.1
$Lu(OH)_3$	-7.0	-6.6	-6.4	-5.1	-4.3	-2.7	-1.6	-1.6	-1.3	-1.2
$Sc(OH)_3$	-4.7	-4.4	-4.4	-3.7	-3.4	-2.9	-3.1	-3.0	-3.7	-3.2

Table SI-4. Sorbed fraction calculated with data from the experiments with a 0.25 g/L solid:liquid ratio and 20 mM SO_4 in solution.

Sorbed fraction from experiments with 0.25g/L ratio and 20 mM SO_4 in solution																
pH	**Sc**	**Y**	**La**	**Ce**	**Pr**	**Nd**	**Sm**	**Eu**	**Gd**	**Tb**	**Dy**	**Ho**	**Er**	**Tm**	**Yb**	**Lu**
4.74	0.21	0.02	0.01	0.02	0.02	0.03	0.05	0.06	0.07	0.07	0.02	0.01	0.00	-0.02	0.00	0.02
4.89	0.25	0.02	0.01	0.04	0.05	0.05	0.05	0.07	0.08	0.05	0.03	0.02	0.01	-0.04	0.00	0.02
5.17	0.53	0.04	0.01	0.04	0.05	0.05	0.05	0.09	0.07	0.05	0.05	0.02	0.01	0.00	0.02	0.02
5.20	0.43	0.05	0.01	0.07	0.05	0.08	0.07	0.09	0.09	0.04	0.05	0.03	0.01	0.00	-0.01	0.03
5.42	0.66	0.06	0.03	0.08	0.06	0.06	0.08	0.10	0.09	0.09	0.04	0.04	0.03	0.00	0.04	0.04
5.63	0.80	0.11	0.02	0.10	0.09	0.08	0.10	0.10	0.07	0.09	0.02	0.04	0.06	0.04	0.05	0.06
5.81	0.85	0.14	0.05	0.12	0.09	0.12	0.14	0.13	0.12	0.11	0.10	0.09	0.09	0.12	0.13	0.15
5.92	0.91	0.16	0.07	0.15	0.15	0.16	0.17	0.17	0.14	0.16	0.13	0.14	0.09	0.13	0.18	0.16
6.05	0.93	0.22	0.08	0.21	0.17	0.19	0.24	0.24	0.21	0.22	0.22	0.20	0.21	0.25	0.31	0.29

Table SI-5. Experimental log K_D (L/Kg) from experiment with 20 mM SO_4 and 0.5 mM SO_4, respectively.

	log K_D																	
	experiment with 20 mM SO_4																	
pH	Sc	Y	La	Ce	Pr	Nd	Sm	Eu	Gd	Tb	Dy	Ho	Er	Tm	Yb	Lu	K_D^Y/K_D^{Dy}	K_D^Y/K_D^{Ho}
4.34	2.75	-	1.14	0.84	0.90	1.11	1.14	1.24	1.21	1.07	1.24	1.26	1.26	1.24	1.41	1.26	-	-
4.45	2.92	-	1.28	1.40	1.30	1.40	1.47	1.44	1.44	1.46	1.54	1.52	0.00	1.59	1.71	1.61	-	-
4.48	2.86	-	1.41	1.38	1.28	1.43	1.46	1.45	1.48	1.33	1.49	1.45	0.00	1.41	1.51	1.39	-	-
4.88	3.66	1.70	1.74	1.77	1.81	1.83	1.87	1.85	1.90	1.85	1.94	1.88	0.00	1.98	2.09	2.02	0.58	0.66
4.94	3.92	1.96	-	2.00	2.00	2.03	2.10	2.07	2.06	2.07	2.13	2.11	1.51	2.20	2.32	2.28	0.66	0.70
5.46	5.11	2.48	1.71	1.89	2.36	2.40	2.55	2.41	2.50	2.59	2.67	2.64	2.57	2.80	2.95	2.91	0.65	0.69
5.74	5.65	2.67	1.99	2.14	2.51	2.56	2.72	2.63	2.65	2.77	2.86	2.82	2.81	3.01	3.16	3.12	0.64	0.70
6.06	5.95	3.13	2.38	2.71	2.89	2.97	3.17	3.15	3.10	3.19	3.33	3.26	3.33	3.47	3.65	3.60	0.64	0.74
6.22	5.95	3.27	2.72	2.95	3.05	3.14	3.32	3.30	3.25	3.34	3.45	3.40	3.45	3.59	3.75	3.71	0.66	0.75
6.51	5.94	3.78	3.14	3.40	3.53	3.61	3.82	3.82	3.74	3.88	3.97	3.94	3.99	4.14	4.29	4.27	0.64	0.69
6.85	5.94	4.01	3.46	3.68	3.80	3.86	4.05	4.05	3.98	4.10	4.19	4.15	4.21	4.34	4.48	4.48	0.66	0.71
	experiment with 0.5 mM SO_4																	
pH	Sc	Y	La	Ce	Pr	Nd	Sm	Eu	Gd	Tb	Dy	Ho	Er	Tm	Yb	Lu	K_D^Y/K_D^{Dy}	K_D^Y/K_D^{Ho}
4.36	2.19	1.00	1.00	1.33	1.00	1.26	1.31	1.09	1.51	1.20	1.00	1.29	1.31	1.29	1.00	1.05	1.00	0.52
4.47	2.28	1.17	1.00	1.34	1.05	1.13	1.34	1.09	1.00	1.29	1.00	1.00	1.00	1.00	1.00	1.05	1.47	1.47
4.54	2.70	1.23	1.05	1.40	1.17	1.00	1.00	1.13	1.40	1.34	1.00	1.00	1.00	1.00	1.00	1.05	1.69	1.69
5.00	3.48	1.26	1.41	1.59	1.46	1.62	1.73	1.67	1.77	1.71	1.09	1.72	1.78	1.83	1.00	1.90	1.47	0.35
5.31	3.90	1.95	1.88	2.00	1.96	2.07	2.13	2.14	2.24	2.15	1.86	2.16	2.20	2.26	2.12	2.31	1.22	0.62
5.88	4.27	2.44	2.22	2.30	2.31	2.35	2.44	2.45	2.48	2.46	2.33	2.47	2.37	2.55	2.50	2.77	1.29	0.93
6.35	4.89	2.85	2.49	2.69	2.86	2.95	3.04	3.00	2.99	3.05	3.03	3.06	3.06	3.16	3.20	3.22	0.66	0.63
6.52	4.91	3.25	2.94	3.17	3.22	3.29	3.47	3.47	3.38	3.46	3.50	3.46	3.51	3.58	3.69	3.68	0.57	0.62
6.75	5.64	3.58	3.20	3.45	3.58	3.67	3.89	3.88	3.77	3.86	3.86	3.85	3.87	3.97	4.04	4.06	0.52	0.54
8.40	5.33	5.62	5.62	5.62	5.90	5.60	5.90	5.90	5.89	5.90	5.61	5.89	5.62	5.90	5.61	5.90	1.01	0.53

Table SI-6. REE surface complexation constants for aqueous carbonate complexes estimated from values obtained by Quinn et al., 2006 b (table2).

Element	Surface Complex	Log K_M^{CO3}	Error	Log $K_{M(CO3)}$ - 1.75	Error
Y	$XOYCO_3$	-1.30		-3.05	-
La	$XOLaCO_3$	-0.39		-2.14	-
Ce	$XOCeCO_3$	-0.21		-1.96	-
Pr	$XOPrCO_3$	-0.22		-1.97	-
Nd	$XONdCO_3$	-0.20		-1.95	-
Sm	$XOSmCO_3$	-0.20		-1.95	-
Eu	$XOEuCO_3$	-0.26		-2.01	-
Gd	$XOGdCO_3$	-0.38		-2.13	-
Tb	$XOTbCO_3$	-0.40		-2.15	-
Dy	$XODyCO_3$	-0.51		-2.26	-
Ho	$XOHoCO_3$	-0.57		-2.32	-
Er	$XOErCO_3$	-0.59		-2.34	-
Tm	$XOTmCO_3$	-0.56		-2.31	-
Yb	$XOYbCO_3$	-0.62		-2.37	-
Lu	$XOLuCO_3$	-0.59		-2.34	-

Fig. SI-1 X-ray Diffraction Pattern for synthetic basaluminite previous to sorption experiments (pure) and basaluminite after REE adsorption with sulfate presence at four different pH values obtained at ID-31 beamline, ESRF. The peaks observed are artifacts due to the panel detector (see Lozano et al., 2018 for details).

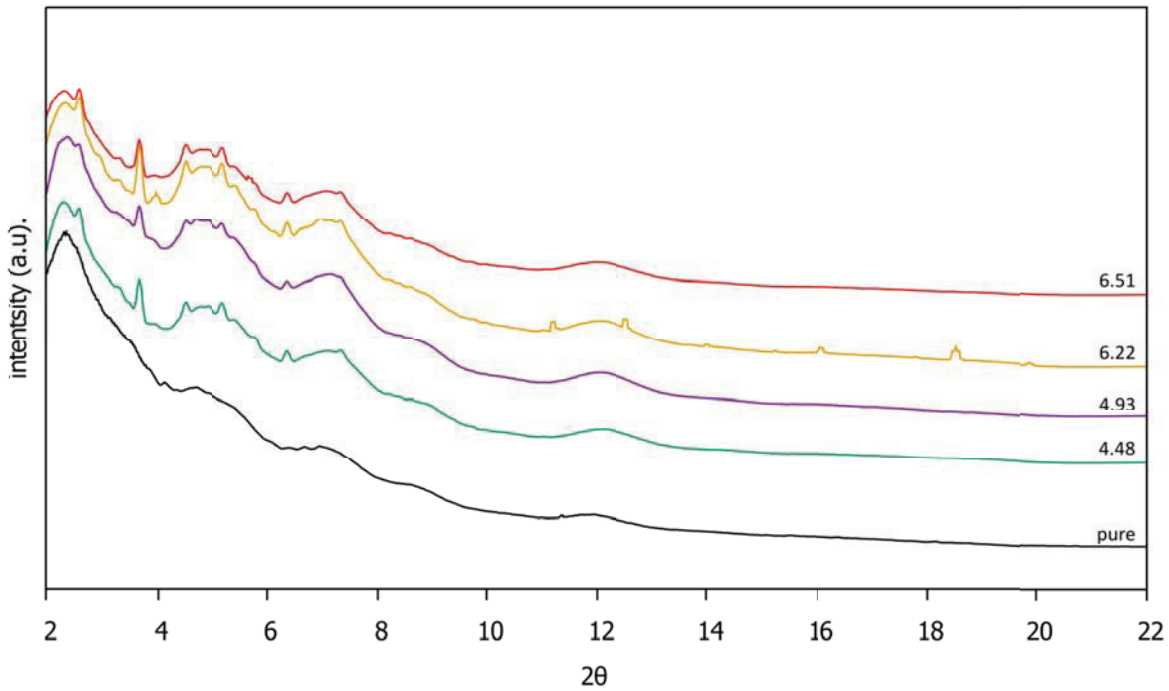

Fig. SI-2. Distribution of the surface sites in basaluminite structure.

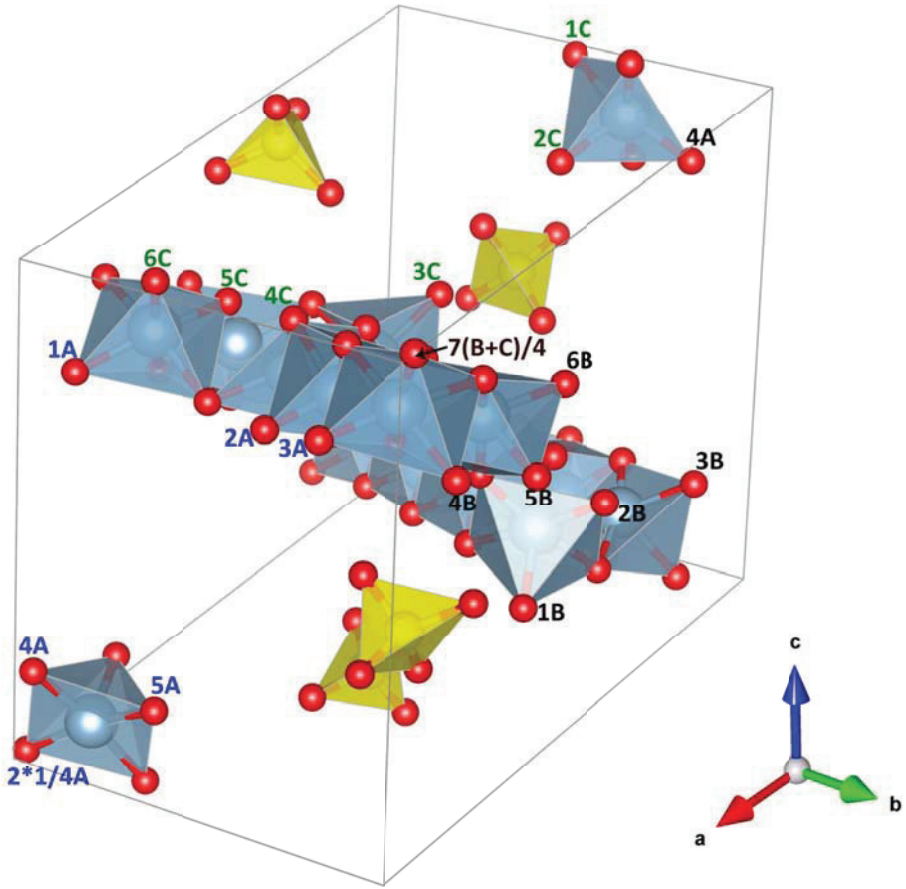

Fig. SI-3. Predictions of REE adsorption in experiment with 20 mM sulfate using surface complexation constants in table 2.

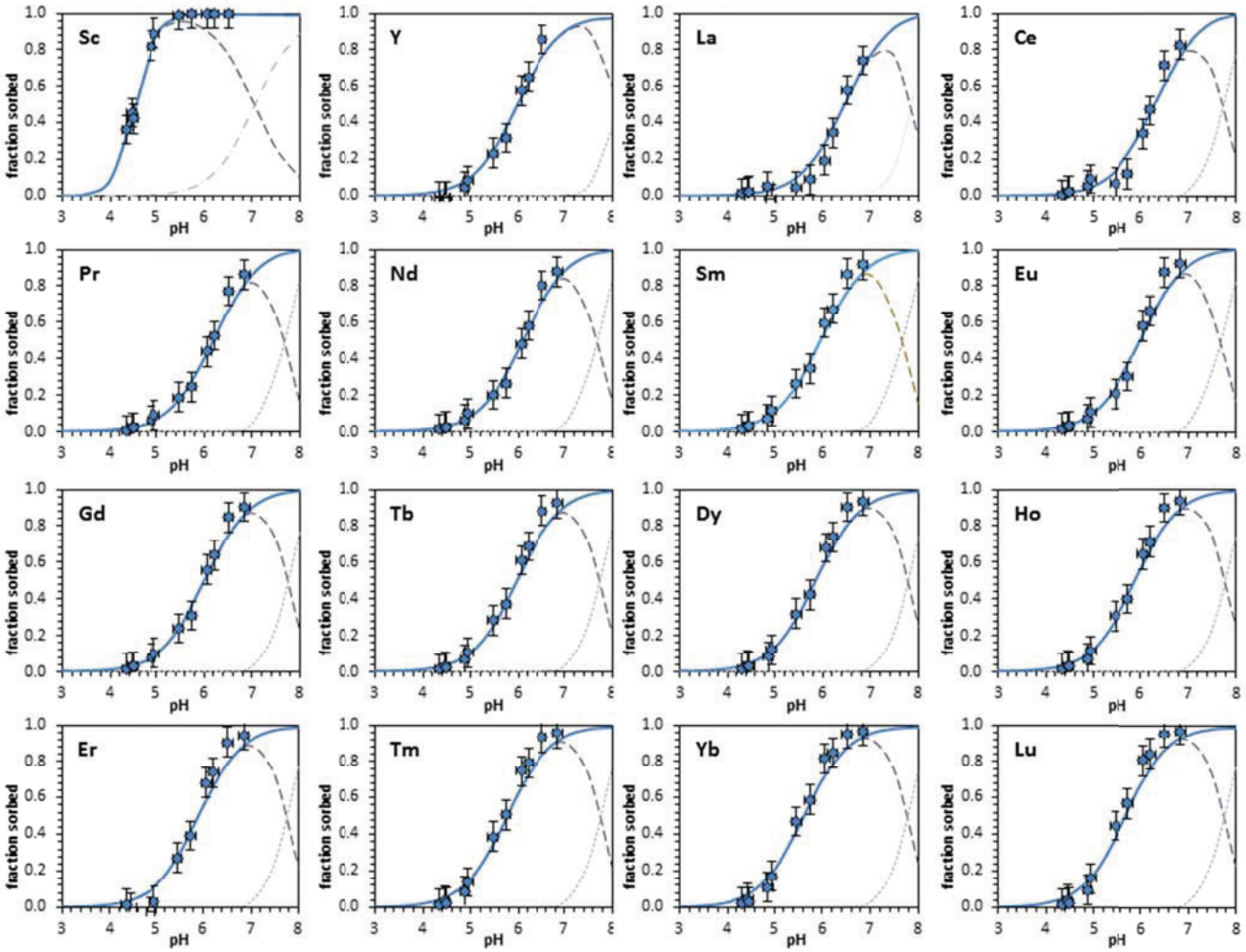

Fig SI-4. Predictions of REE adsorption in experiment with 0.5 mM sulfate using surface complexation constants in table 2.

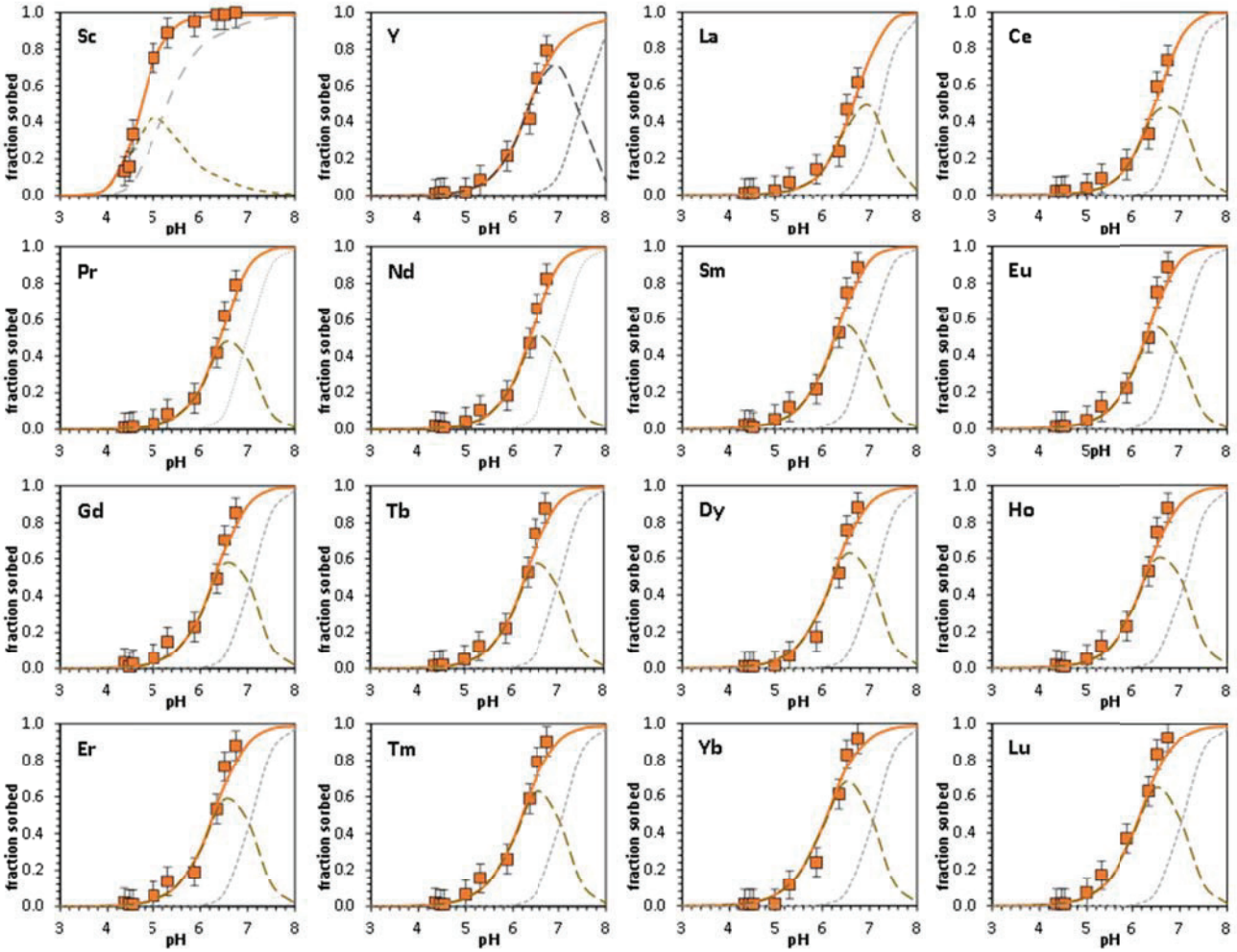

Fig. SI-5. Experimental data (symbols) and model (lines) of fractionation constants (log K_D) for lanthanide series in (A) sorption experiment without 20 mM sulfate and (B) with 0.5 mM sulfate. Calculations at 25 C and pCO_2 of 3.5 including sorption of both MSO_4^+ and MCO_3^+ aqueous species. Log K_D^{Sc*} represents Log K_D^{Sc}-2

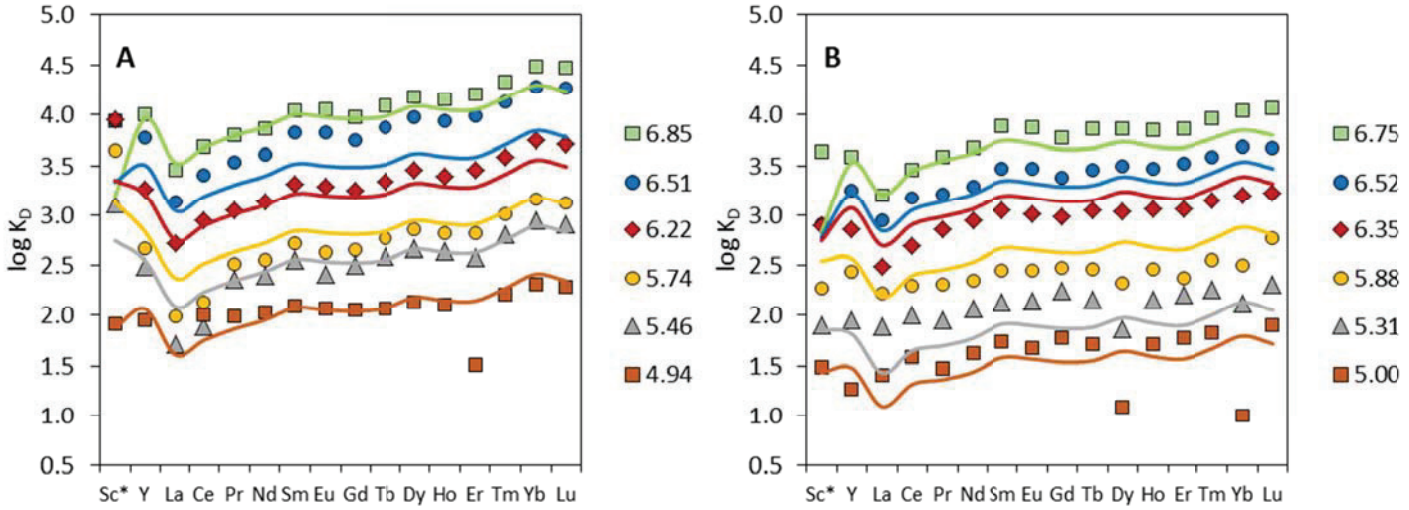

Fig SI-6. REE sorption fraction for two different solid:solute ratios 1 g/L (blue), 0.25 g/L (green) obtained from experimental data (symbols) and the predicted model for each experiment (lines).

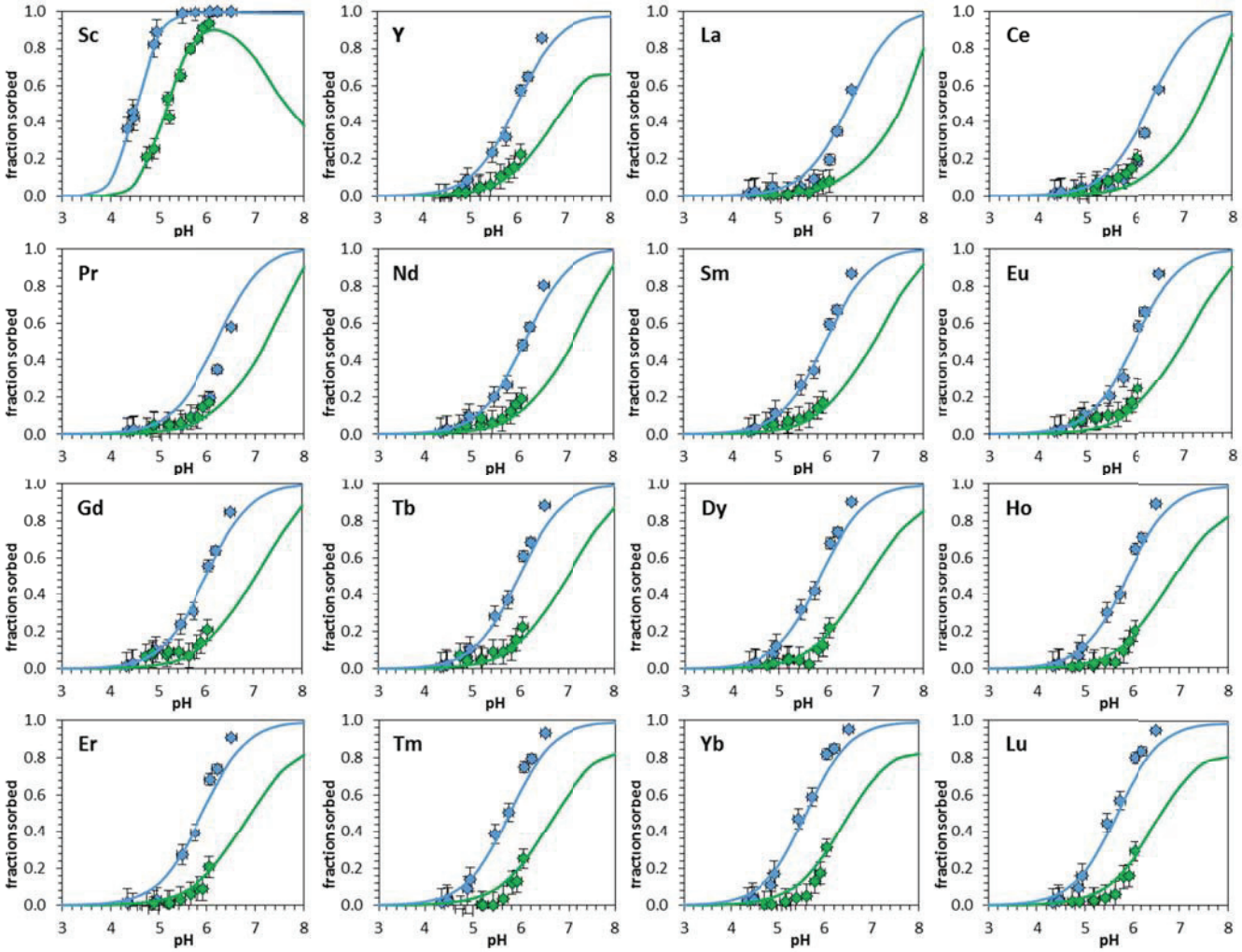

Article 3

Sorption of rare earth elements on schwertmannite and their mobility in acid mine drainage treatments

Published in: *Applied Geochemistry. Minor revision.*

Sorption of rare earth elements on schwertmannite and their mobility in acid mine drainage treatments

Alba Lozano[a,b*], Carlos Ayora[a,b], Alejandro Fernández-Martínez[c]

[a] Institute of Environmental Assessment and Water Research, (IDAEA-CSIC), Jordi Girona 18-26, 08034 Barcelona, Spain

[b] Grup de Mineralogia Aplicada i Geoquímica de Fluids, Departament de Cristal-lografia, Mineralogia i Dipòsits Minerals, Facultat de Geologia, Universitat de Barcelona (UB), C/Martí Franquès, S/N, Barcelona, Spain

[c] Univ. Grenoble Alpes, Univ. Savoie Mont Blanc, CNRS, IRD, IFSTTAR, ISTerre, 38000 Grenoble, France

Corresponding author:

Alba Lozano (alba.lozano@idaea.csic.es)

Abstract

Rare Earth Elements (REE) are nowadays considered critical raw materials due to their increasing use in modern industry and their shortage of supply. Acid mine drainage (AMD) contains REE concentrations several orders of magnitude higher than the rest of continental and marine waters, and the sludge from its treatment may become a supplementary source of REE. Schwertmannite, a Fe(III)-sulfate-hydroxide is the most common mineral precipitated from AMD and a main constituent of the neutralization sludge. The objective of this work is to study the mechanism of REE retention in synthetic schwertmannite and to predict the REE behavior in a column experiment emulating an AMD passive remediation system.

Suspensions of synthetic schwertmannite in sulfate solutions show that Y and the lanthanides are effectively sorbed at pH values higher than 4.5, and sorption is complete at pH values higher than 6.5. The experimental partition coefficients clearly show a preferential enrichment of heavy REE in the solid phase. Unlike the rest of the REE, Sc sorption occurred at a lower pH, from 3 to 5. The experimental results have been described with a non-electrostatic surface complexation model in which the aqueous complex MSO_4^+ exchanges with two H^+ from the surface of schwertmannite, forming a bidentate surface complex, $(XO)_2MSO_4^-$. Scandium sorption was also accurately predicted with the addition of a second bidentate surface complex, $(XO)_2MOH$.

The equilibrium constants for REE sorption on schwertmannite calculated in the present work, together with those for REE sorption on basaluminite (Lozano et al., 2019, GCA, 258, 50–62) were used to model the behavior of different REE observed in the pore water and solid of a column experiment. Schwertmannite and basaluminite were the main solid phases formed due to the progression of the neutralization. First schwertmannite precipitated at pH below 4 and then basaluminite precipitated at pH above 4. Both minerals have similar sorption edges for REE, but Y and the lanthanides sorbed at pH values higher than 5, and therefore their sorption only occurred on basaluminite. In contrast, the Sc sorption edge extended from pH 3 to 5 and Sc partially sorbed on schwertmannite. As a practical consequence, REE preferentially accumulated in the basaluminite residue of AMD neutralization systems, but a minor fraction of Sc can be retained in the schwertmannite waste.

Keywords

Scandium, yttrium, lanthanides, non-electrostatic model, bidentate surface complex, passive remediation, neutralization sludge

Highlights

- Sorption of REE on schwertmannite highly depends on pH
- Sorption affinity for schwertmannite increases from LREE to HREE and particularly to Sc
- A sorption model predicts the REE mobility in acid water treatments
- In AMD treatment plants REE are retained in basaluminite but a fraction of Sc accumulates in the schwertmannite sludge
- Sc can be segregated from the rest of REE by keeping the neutralization pH below 4.5

1 Introduction

The rare earth elements (REE) form the largest chemically coherent group in the periodic table. According to the International Union of Pure and Applied Chemistry, it is formed by the lanthanide series, yttrium and scandium. Their similar atomic structure and chemical properties as well as the small differences among the elements in the group have traditionally considered their partition between water and minerals as tracers of geochemical processes (Elderfield et al., 1990; Henderson, 1984; McLennan, 1989, among many others). Beyond their importance as geochemical tracers, in the last two decades, it has been an increasing interest in REE due to their higher demand by modern technology and industry. This demand, together with eventual shortages of supply has motivated the search for alternative sources of REE raw material worldwide (Hatch, 2012; Massari and Ruberti, 2013).

On the other hand, Acid Mine Drainage (AMD) is one of the most important and spread pollution affecting watersheds and ecosystems worldwide (Blowes et al., 2014; Choudhury et al., 2017; Lin et al., 2007; Nordstrom et al., 2015). However, AMD could also become a new and supplementary source for REE since their concentration in AMD, including scandium, is two to three orders of magnitude higher than in natural waters (Noack et al., 2014). In AMD, pH has been described as the key factor for REE mobility. Thus, the pH increase to circumneutral values when AMD mixes with alkaline waters leads to the precipitation of hydrous ferric/aluminum oxides and sulfate-hydroxides, accompanied with the REE scavenge (Ferreira da Silva et al., 2009; Gammons et al., 2005a, 2005b; Verplanck et al., 2004).

In addition to REE, AMD also contains high concentrations of toxic elements, and represents a very important environmental threat that requires remediation. In mine operations, the active treatments of AMD are mainly based on its neutralization with alkaline reagents, usually limestone, sodium carbonate or ammonia (Evangelou and Zhang, 1995; Coulton et al., 2003). This treatment produces high amounts of an sludge formed by a mixture of Fe(III) and Al-sulfate-hydroxides which disposal represents a major operating cost for the companies and an environmental concern (Ackman, 1982Viadero et al., 2006). Differently, the passive remediation systems neutralize the AMD by driving it through a permeable system filled with grained limestone (Heding et al., 1994; Ayora et al., 2013; Cravotta and Trahan, 1999). Along the process, the waste created is represented by a sequential precipitation of mainly schwertmannite ($Fe_8O_8(OH)_6SO_4$ and basaluminite ($Al_4SO_4(OH)_{10}\cdot 5H_2O$). Moreover, REE have been proved to be entirely retained in the solid waste resulting from AMD treatment with REE_2O_3 rates comparable to present day exploitations and prospects (Ayora et al., 2016; Zhang and Honaker, 2018). In Ayora et al. (2016) study, Sc was not included, but since its market value is one and two orders of magnitude higher than that of Heavy and Light REE, respectively (U.S. Geological Survey (USGS), 2019) this element deserves special attention nowadays. The retention of REEs on basaluminite and the dependence of this process on pH and sulfate availability has already been studied (Lozano et al., 2019a). However, despite the overwhelming presence as precipitates in AMD streams (Nordstrom, 2011), and being the other major constituent of AMD treatment sludge, the interaction between schwertmannite and REEs remains unknown.

Previous laboratory experiments of sorption and coprecipitation of REE onto ferric and manganese oxides/hydroxides have previously demonstrated the key role of pH in the

geochemical mobility of REE (Bau, 1999; De Carlo et al., 1998; Ohta and Kawabe, 2001, 2000; Quinn et al., 2006a, 2004). REE are removed from solution as the pH increases from 4 to 9. In addition to pH, the aqueous speciation is also an important factor that it has been driven its attention in the REE fractionation in marine environments. Thus, the formation of strong carbonate complexes with heavy REE (HREE) at neutral pH values prevents their sorption by ferric and manganese oxides. As a result, these solids show patterns with light REE (LREE) enrichment (Byrne and Kim, 1990; Byrne and Sholkovitz, 1996; Kawabe et al., 1999a, 1999b; Koeppenkastrop and De Carlo, 1992; Sholkovitz, 1995). More recently, some works have performed detailed sorption experiments and developed surface complexation models to describe the sorption of some lanthanides (Yb, La, Eu) onto hematite and amorphous ferric oxides/hydroxides (Estes et al., 2013; Liu et al., 2017; Marmier et al., 1997; Marmier and Fromage, 1999; Quinn et al., 2006b, 2006a; Rabung et al., 1998; Rillard et al., 2019). In these works, the REE scavenging is mainly explained by the sorption of free REE ions or their hydrolyzed species onto a solid surface.

The presence of sulfate is ubiquitous in AMD systems, usually with concentrations reaching up to several grams per liter. Rather than free ions or hydrolysis products, previous studies have highlighted the importance of aqueous sulfate complexes with REEs (Gimeno Serrano et al., 2000; Verplanck et al., 2004). Similar to REE-carbonate speciation in seawater, sulfate complexes may explain REE fractionation in the solids precipitated from AMD environments. Therefore, due to its importance in AMD chemistry the role of sulfate in REE sorption on schwertmannite must be quantitatively assessed.

Here, we present the results from REE sorption experiments on synthetic schwertmannite in an AMD setting. A non-electrostatic surface complexation model is developed to describe the experimental data for the sorption of a complete data set of REE (lanthanides, Y and Sc) at different pH values, sulfate concentrations and solid:liquid ratios. The model is then used to interpret the mobility of the different REE in a column experiment reproducing a scaled AMD passive treatment system.

2 Materials and methods

2.1 Experimental techniques

2.1.1 Structural characterization of synthetic schwertmannite

Synthetic schwertmannite was prepared following the procedure described by Schwertmann and Cornell (1991), where 10.8 g of $FeCl_3 \cdot 6H_2O$ and 3 g of Na_2SO_4 were mixed with 2 L of distilled water at 60°C. The suspension was stirred for 12 minutes at 60°C and then cooled to room temperature. The solid was dialyzed in a cellulose membrane against double-distilled water for 33 days. Once the water had conductivity less than 0.5 mS/cm, the precipitate was freeze-dried. Mineral purity was assessed by X-ray diffraction (XRD). The specific surface area was measured by the BET-N_2 sorption method (Micromeritics Gemini V analyzer; Micromeritics).

2.1.2 REE sorption as a function of pH and sulfate concentration

The REE sorption on synthetic schwertmannite was measured as a function of pH at two different sulfate concentrations in two separate sets of batch experiments using suspensions of 1 g/L. Two stock solutions with a pH of 2.5 were prepared for each set. The first stock solution consisted of 1 mg/L each REE and 20 mmol/L SO_4, whereas the second stock solution consisted of 1 mg/L each REE and 2 mmol/L SO_4. The solutions were prepared with an ICP standard mix of 16 elements, excluding Pm, and Na_2SO_4 (ACS reagent >99.9%, Merck). The stock solutions were intended to simulate acid mine waters with different sulfate concentrations. First, 10-mL aliquots of each stock solution were transferred to 50-mL centrifuge tubes, and the pH of each aliquot was adjusted to cover a pH range of 3-7 by adding small amounts of a 0.05 mol/L NH_4OH solution. After adding 10 mg of schwertmannite to each aliquot, the suspensions were shaken for 6 hours at room temperature. Then, the suspensions were centrifuged for 15 minutes at 4500 rpm (4150 RCF), and the supernatant was filtered through 0.22-µm nylon membranes and transferred to test tubes diluted fivefold with 1% HNO_3. The solids were dried at 40°C for 48 hours. The sorbed fractions were calculated as follows:

$$\text{Sorbed fraction} = \frac{[\text{REE}]_{\text{initial}} - [\text{REE}]_{\text{final}}}{[\text{REE}]_{\text{initial}}} \quad (1)$$

where [REE] is the concentration of each REE. The initial concentration was measured in the stock solution and the final concentration after the experiment. The distribution coefficient, K_D (L/kg), for each REE was calculated from the [REE] sorbed onto the solid per the final [REE] remaining in solution and normalized per the solid:liquid ratio:

$$K_D = \frac{[\text{REE}]_{\text{initial}} - [\text{REE}]_{\text{final}}}{[\text{REE}]_{\text{final}}} \cdot \frac{V_{\text{solution}}}{M_{\text{solid}}} \quad (2)$$

2.1.3 Description of the column experiment and waste characterization

A scaled column experiment was carried out with AMD from the field to obtain a vertical profile of REE distribution in the pore water and in the minerals precipitated along the passive AMD remediation system. The AMD was collected from for the Poderosa mine, located in the Iberian Pyrite Belt (IPB) in SW Spain. A scaled column experiment was carried out. The chemical composition of the acid input is described in Table S1. The column was built with transparent polymethyl methacrylate (9.6-cm inner diameter and 35 cm in height). A 3-cm layer of glass beads (3 mm in diameter) and a perforated drainpipe were installed at the bottom of the column. Lateral ports located at 3-cm intervals in the upper part of the column allowed pore water sampling. The column was filled with 20 cm of dispersed alkaline substrate consisting of 30 g of limestone sand (0.5-1 mm) and 300 g of pine-wood shavings (5-10 mm) (Rötting et al., 2008a). The role of the pine-wood shavings was to provide a porous matrix to allocate the minerals that precipitated inside the column and to prevent clogging. The proportion of limestone was decided to be small in order to exhaust the reagent within a few weeks. The initial total porosity of the filling was 0.46, determined by a gravimetric method.

The column was open to the atmosphere, and the input AMD was pumped into the top of the column with a peristaltic pump. The water flowed downward by gravity through the limestone substrate at a constant flow rate of 0.35 mL/min for a column section of 72 cm^2. This flow was similar to that of 2 L/s, which is the flow rate for a field-scale treatment of 2000 m^2 of surface

area to treat the discharge of the Poderosa mine. Water samples were collected every week from the supernatant and from 3 sampling points at 4, 7, 10 and 23 cm depth. Physical-chemical parameters (pH, redox potential and total alkalinity) were measured in situ. Filtered samples (0.2 µm nylon) were acidified with HNO_3 for chemical analysis of major elements by inductively coupled plasma optical emission spectroscopy (ICP-OES) and trace elements by inductively coupled plasma mass spectroscopy (ICP-MS). No pore water could be sampled between 10 and 23 cm. For each water sample, pH, redox potential, electrical conductivity, oxygen concentration and total alkalinity were measured in situ. The water was filtered through 0.22-µm nylon filters and stored at 4°C until analysis. The experiment lasted for 58 days and was stopped when the outflow showed a pH lower than 5.5, as an indication of reagent efficiency exhaustion.

Postmortem, the column was drained, and the residue was divided into 2-cm slices and dried at room temperature. The major mineral phases present in the solid residue were identified by XRD. To investigate the partitioning of Al, Fe, and trace elements into the solid phases, a sequential extraction procedure adapted from Torres and Auleda (2013) was applied to the residue samples to obtain the following fractions: 1) the water-soluble fraction, extracted with deionized water; 2) calcite and basaluminite, extracted with 1 mol/L ammonium acetate at pH 4; 3) low crystalline Fe(III)-oxyhydroxides and remaining basaluminite, extracted with 0.2 mol/L ammonium oxalate at pH 3; 4) crystalline Fe(III)-oxides, extracted with 0.2 mol/L ammonium oxalate at pH 3 in a water bath at 80°C for 2 hours; and 5) the residual fraction, extracted with concentrated $HClO_4$ and HNO_3 at 135°C. All the leachates resulting from the different extraction steps were filtered through 0.22-µm nylon syringe filters and stored at 4°C until analysis. Duplicates for 10% of the total samples were analyzed, showing a reproducibility of 90%. To validate the sequential extraction procedure, a total digestion (performed according to step 5 of the protocol) of all the samples was conducted. The addition of sequential extractions was compared with the total extraction from the digestion, and only element recovery rates between 80% and 120% were accepted.

2.2 Analytical techniques

Measurements of pH from filtered aliquots were made with a Crison® glass electrode calibrated with buffer solutions of pH 2, 4, 7 and 9. The redox potential was measured with a Pt combination electrode (ThermoOrionSureFlow®) which was calibrated with standard buffer solutions of 220 and 468 mV. Total (gross) alkalinity was measured following the acid titration method using an Alkalinity Test from Aquamerck® (the limit of detection was 0.1 mmol/L H^+ and the analytical was error of 0.1 mmol/L H^+). Major cations were measured by ICP-AES (Thermo Scientific – iCAP 6500, radial acquisition), and REEs (La, Ce, Pr, Nd, Sm, Eu, Gd, Tb, Dy, Ho, Er, Tm, Yb, Lu, Y and Sc) were measured with ICP-MS (Perkin-Elmer®SciexElan 6000). The detection limits were 0.2 µg/L for REEs and 0.1, 0.05, 0.1 and 0.1 mg/L for S, Fe, Al and Na, respectively. The analytical precision error was estimated to be approximately 2% for ICP-MS and ICP-AES measurements. Certified solutions (CPI International-CCV standard 1-solution A) were intercalated within the samples to check the analytical accuracy. Two AMD laboratory standards supplied by P. Verplank (USGS) were also analyzed for REE accuracy, yielding deviations lower than 4% of the recommended values, with the exception of Eu, which showed values 19% below the recommended value (Verplanck et al., 2001).

The XRD patterns of the solid phases after the experiments were obtained using a Bruker D8 A25 Advance Diffractometer θ-θ with CuKα1 radiation. The diffractometer operated at 40 kV and 40 mA in a Bragg-Brentano geometry and was equipped with a linear LynxEye XE detector. The diffractograms were obtained from 4° to 60° in 2θ with a step size of 0.015° and a counting time of 0.1 s.

2.3 Geochemical modeling

Chemical speciation of dissolved REE, saturation indexes of solid phases, surface complexation and 1D reactive transport modeling were calculated with the PHREEQC code (Parkhurst and Appelo, 1999) using the database Donnee Thermoddem_V1.10.dat (Blanc et al., 2012). The database has been updated with the stability constants at zero ionic strength and 25°C for the following inorganic complexes for the lanthanides and yttrium (M): MCO_3^+, MCO_3^{2-}, $MHCO_3^{2+}$ (Luo and Byrne, 2004); MSO_4^+ (Schijf and Byrne, 2004); MOH^{2+} (Klungness and Byrne, 2000); MOH_2^+, $M(OH)_3$ (Lee and Byrne, 1992); MCl^{2+} (Luo and Byrne, 2001); MF^{2+}, MF_2^+ (Luo and Millero, 2004); and MNO_3^{2+} (Millero, 1992). Solubility products for REE $M(OH)_3$ and $M(OH)_{3(am)}$ solids have been complementarily loaded from the LLNL database (Johnson et al., 1992; Spahiu and Bruno, 1995). Scandium aqueous complexes, $Sc(OH)^{2+}$, $Sc(OH)_2^+$, $Sc(OH)_3$, and $ScSO_4^+$, and the solubility product for $Sc(OH)_3$ by Wood and Samson (2006) were incorporated. The reactions and their equilibrium constants are compiled in Table S2 of the Supplementary Information. The solubility products of schwertmannite and basaluminite were obtained from Sánchez-España et al. (2011), are also included in Table S2.

The reactive transport model consisted of a 1-D domain of 20 cm divided into 25 elements of 1 cm each. The 20 initial elements consisted of calcite and the last 5 elements of an inert filling. An initial concentration of 0.25 mol/L of calcite was percolated by an inflow of AMD. As the acid water infiltrates, calcite dissolves according to the kinetic law described by Plummer et al. (1979) and included in the database of the PHREEQC code. The rest of minerals, schwertmannite, basaluminite and gypsum were assumed to precipitate in equilibrium. The reactive surface area of calcite was calibrated to 0.01 m^2/g in order to fit the observed pH profiles. The surface complexes and log K values described in Table 1 and those of Lozano et al. (2019a) for REE sorption on basaluminite (Table S3) were used to calculate the REE sorption onto schwertmannite and basaluminite precipitated on the column. As initial conditions, the number of sorption sites was deduced from the properties of schwertmannite (4.7 sites/nm^2; 173 m^2/g, as will be described in section 3.1) and basaluminite (4.6 sites/nm^2, 68 m^2/g according to Lozano et al., 2019a). The solid/liquid ratio for both minerals was calculated from their total amount formed, which were calculated in a previous run of the model without sorption reactions distributed in the column, and assuming a bulk solid density of 1.3 kg/L (including the wood shavings) and a porosity of 0.46.

3 Results

3.1 Characterization of synthetic schwertmannite

The XRD patterns of the solid phase prior to and after the sorption experiments confirmed that the mineral was pure schwertmannite (Fig. S1, S2). The measured specific surface area of pure schwertmannite was 173 m^2/g, close to the values reported by Antelo et al. (2012) and

Regenspurg et al. (2004) (171 m^2/g and 175-200 m^2/g, respectively). The site density was calculated from the crystal structure proposed by Fernández-Martínez et al. (2010), accounting for the single coordinated sites per face area, yielding values of 2 sites/63.22 $Å^2$ for (1 0 0), 7.5 sites/113.77 $Å^2$ for (0 1 0) and 2 sites/64.95 $Å^2$ for (0 0 1) (Fig. S3). These calculations resulted in a total site density of 4.75 sites/nm^2, a value similar to 4.7 sites/nm^2 reported by Fukushi et al. (2004). The resulting total concentration of surface sites was therefore 1367 µmol/g.

3.2 REE sorption as a function of pH and sulfate concentration

Prior to sorption experiments, the kinetics of the sorption reactions were determined using 10 suspensions of 1 g/L schwertmannite and a solution of REE at a concentration of 1 mg/L each and 20 mmol/L SO_4 at pH 5.5. The kinetics experiments showed a very fast initial sorption, which increased until a steady state was reached at 5 hours (Fig. S4). Similar equilibrium times were observed for ferric oxyhydroxide by Ohta and Kawabe (2001) and Koeppenkastrop and De Carlo (1992), with fast REE adsorption at approximately 4-6 hours. Therefore, sorption was considered almost complete after 6 hours of contact during the sorption experiments.

The chemical composition of the initial and final solutions of the two sets of sorption experiments with 20 and 2 mmol/L SO_4 are compiled in Tables S4 and S5, respectively. The hypothesis of hydroxide precipitation was rejected because the solutions were undersaturated with respect to REE hydroxides (Tables S6, S7). The solutions were also undersaturated with respect to schwertmannite and almost in equilibrium with respect to goethite. Schwertmannite is a metastable phase that transforms to goethite over weeks at different pH values (Acero et al., 2006; Burton et al., 2009; Schwertmann and Carlson, 2005). However, the presence of sulfate in solution delays this transformation (Regenspurg and Peiffer, 2005), and goethite was not detected by XRD in schwertmannite solids after the sorption experiments (Fig. S1, S2).

Sorption showed a high dependence on pH in the two sets of experiments, as the REE sorption increased with pH (Fig. 1). The sorption edges occurred within a range of 2.0 to 2.5 pH units and shifted to lower pH values for HREE than for LREE, showing that HREE sorption was favored over LREE sorption at the same pH value. Similar pH dependence was observed by Bau (1999) and Quinn et al. (2006a) in REE coprecipitation with amorphous ferric hydroxide and by Lozano et al. (2019a) in REE sorption on basaluminite.

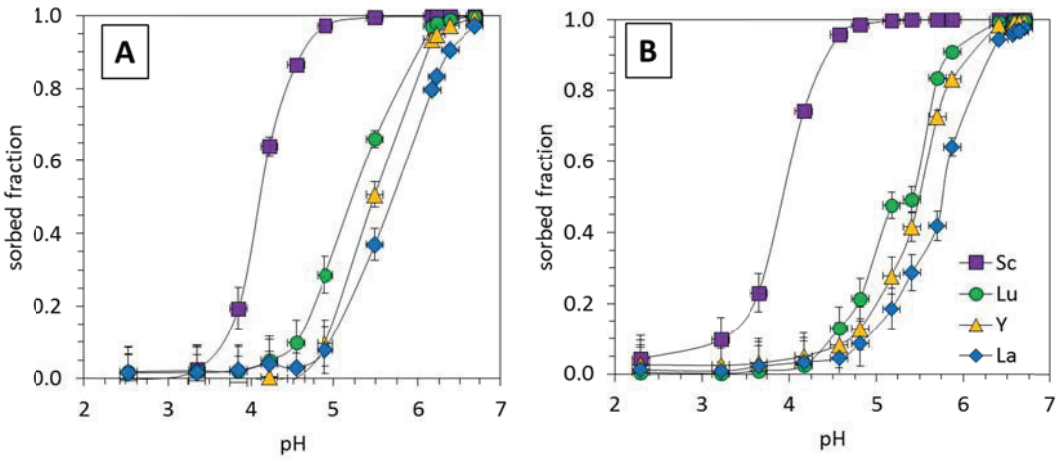

Fig. 1. Sorption edges of selected REE on schwertmannite in solutions with 20 mmol/L (A) and 2 mmol/L (B) sulfate. Legend: Sc: circles, Y: squares, Lu: squares and La: diamonds. The error bars indicate the uncertainties in pH measurements (± 0.02) and in the sorbed fraction (from ±0.01 to ±0.07).

The pH at which sorption becomes significant depends on the element. The lanthanides and Y started to sorb at pH 5, whereas Sc started at pH 3.5, a value considerably lower than the rest of the REE. In the experiment with 20 mmol/L SO_4 at pH 4.9, more than 95% of Sc was adsorbed on schwertmannite, whereas less than 20% of the remaining REE were adsorbed. A similar sorption preference of Sc over the lanthanides and yttrium for a given pH was also observed for basaluminite after REE sorption experiments (Lozano et al., 2019a), although here Sc sorption occurred at a pH lower than 4, at which basaluminite is not stable.

The distribution coefficients (K_D) for both sets of experiments were calculated as described in Eq. (2) and are shown in Fig. 2. The REE fractionation patterns showed four convex segments from La to Nd, from Nd to Gd, from Gd to Ho and from Ho to Lu, corresponding to the M-type tetrad effect (Bau et al., 1996; Masuda et al., 1987). The K_D values increased by 3 orders of magnitude as pH increases from 4.5 to 6.5, highlighting the REE sorption dependence on the pH. At pH values higher than 5, when sorption becomes significant, the K_D values clearly showed an enrichment of HREEs in the solid phase, which increased by 1 order of magnitude along the lanthanide series. Similar REE patterns with HREE enrichments appeared in free REEs that were coprecipitated with synthetic Fe(III)-hydroxides (De Carlo et al., 1998; Quinn et al., 2004). These results contrast with those described in seawater environments, where a preferential LREE enrichment in Fe oxides has been observed. Heavy REE formed stable aqueous carbonate complexes in marine environments preventing their adsorption (Kawabe et al., 1999b; Koeppenkastrop and De Carlo, 1992). In acid mine waters, however, sulfate complexes are the dominant aqueous species, while carbonate complexes are only relevant at pH values higher than 6.5.

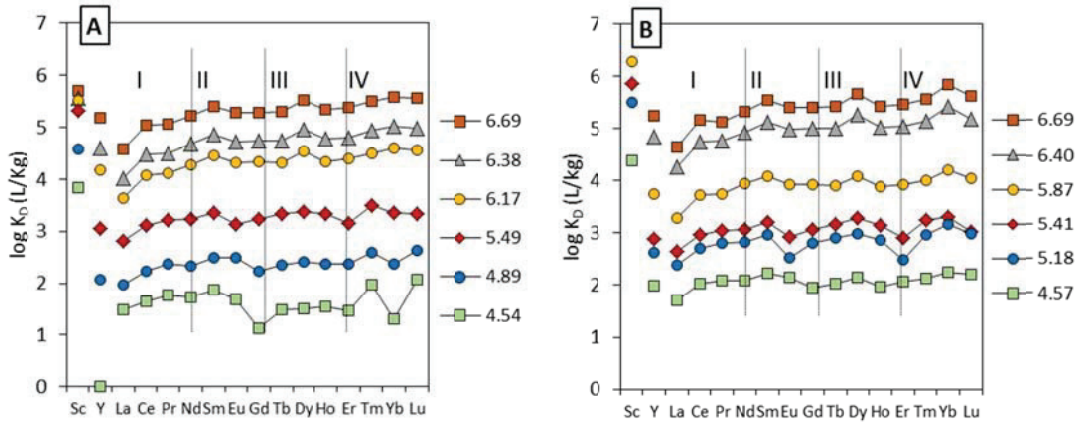

Fig. 2. Log K_D values at different pH values showing the lanthanide M-type tetrad effect: (A) solutions with 20 mmol/L SO_4; (B) solutions with 2 mmol/L SO_4.

Bau (1999) observed an important positive Ce anomaly in hydrous ferric oxide precipitated with REE in the absence of sulfate that was attributed to the oxidation of Ce and the precipitation of CeO_2. This anomaly was not observed in the present experiments (Fig. 2), nor it was observed by Verplanck et al. (2004) in precipitates obtained after neutralizing acid mine waters with high sulfate concentrations. This observation suggests that sulfate may inhibit Ce oxidation due to sulfate complexation.

According to its ionic radius, Y is commonly displayed between Dy and Ho, where it presents a negative anomaly (not shown in Fig. 2), as evidenced by the K_D^Y/K_D^{Dy} and K_D^Y/K_D^{Ho} ratios below unity (Table S7). The Y anomalies in amorphous Fe(III)-hydroxides were attributed to covalent interactions with the Fe solids (Quinn et al., 2004). The negative Gd and Yb anomalies at lower pH values in the experimental set with 20 mmol/L SO_4 were not previously reported in the literature for similar experiments (Bau, 1999; Quinn et al., 2006a, 2006b) and are attributed to analytical errors.

3.3 REE distribution in the column experiment

The complete set of pore water analyses can be found in Table S9 and a selection is plotted in Fig. 3, where depth 0 cm represents the supernatant inflow and depth 23 cm represents the outflow. Only Sc, La and Y were compared due to their different sorption-pH behavior. Both, La and Y were representative of the LREE and HREE, respectively, and their measured values were always above the detection limits.

Essentially, for a given time the pH increased with depth, and for a given depth the column was progressively invaded by more acidic water (Fig. 3A). For each time, Fe and Al concentrations decreased with depth to detection level indicating the precipitation of schwertmannite and basaluminite (Fig. 3B-C). However, Al showed a peak of concentration higher than the input AMD. This was already observed in previous column experiments, and attributed to the re-dissolution of basaluminite by the percolating AMD once the calcite reagent was exhausted (Rötting et al., 2008a). Practically no Al and Fe were detected at the end of the column in the four sampling events.

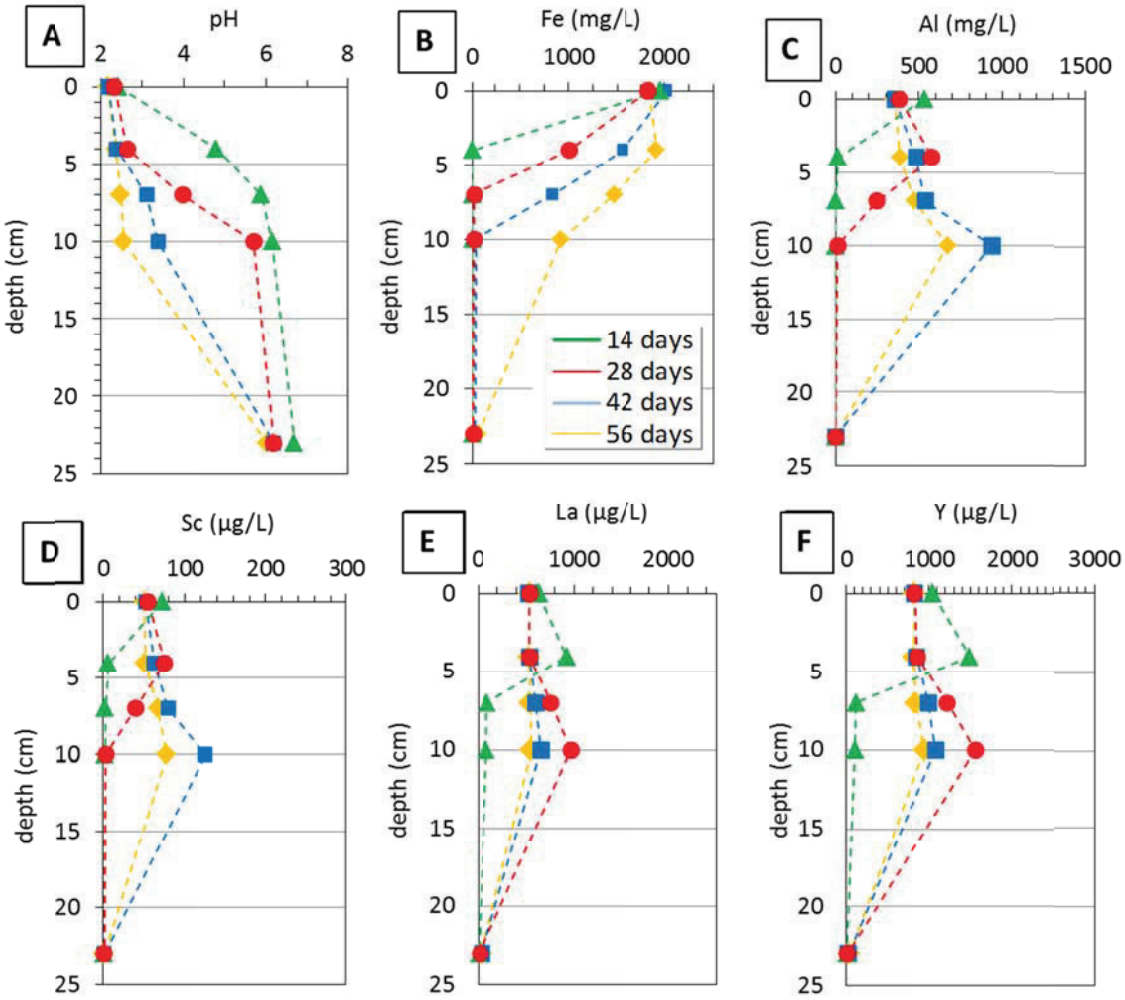

Fig. 3. Depth profiles of pore water and solid composition at four different stages of column operation: (A) pH evolution; (B, C) Fe and Al concentrations in pore water; (D, E, F) mineral distributions; (G, H, I) concentrations of selected REE in pore water.

The concentration of the three selected REE showed a distribution pattern similar to that of basaluminite (Fig. 3D-F). As described for Al, the REE concentration decreased with depth, but also showed a peak of concentration higher than the input AMD, which progressed downwards with time. This distribution suggests a close association of REE to basaluminite, as already observed for Y and lanthanides in previous experiments (Ayora et al., 2016). In subsequent samplings, the peak concentration of Y and lanthanides decreased to the inflow AMD value. Scandium, however, showed a slightly different behavior. For the same sampling event (28 days), the Sc peak was observed to occur at shallower depth (4cm) with respect to those of La and Y, and for the same depth (10 cm), so the Sc peak took longer time to disappear. As for Fe and Al, almost no REE concentration was detected at the end of the column during the experiment.

After a few weeks of functioning, the column showed a distinct zonation with depth (Fig. 4A). The experiment was stopped and the column dismantled after 58 days. The solid residue was drained, dried and sliced for analysis. The complete set of sequential extraction analyses can be found in Table S10, and a selection is plotted in Fig. 4B-E. The presence of schwertmannite in the samples from the uppermost half of the column was indicated by the amount of Fe

recovered in steps II and III of the sequential extraction (Fig. 4B). The presence of schwertmannite and minor goethite together with gypsum and residual calcite (data not presented) was confirmed by XRD. Although not identified on XRD due to its amorphous nature, the presence of basaluminite was evidenced by the amount of Al recovered in the second and third steps of the sequential extraction of samples of the lowermost half of the column (Fig. 4C). The presence of gypsum throughout the column was confirmed by the amount of Ca and S leached in extraction step I and the presence of calcite by the high amount of Ca present in extraction step II (data not presented). This solid phase distribution along the column is similar to that observed in other column experiments and field scale treatments (Caraballo et al., 2011, 2009; Rötting et al., 2008b, 2008a).

As evidenced in Fig. 4D-E, a minor proportion of Sc was found in the water-soluble step I, most likely linked to gypsum (Lin et al., 2019). However, most REE were found in steps II and III, which are representative of schwertmannite and basaluminite. However, some differences are evident in the depth distribution of Sc and the rest of the REE. Yttrium (and lanthanides) match the Al distribution along the column depth (Fig. 4E), indicating that they are attached to basaluminite. However, up to 25% Sc was located in the first 6 cm of the column, matching the Fe distribution and suggesting a link to schwertmannite.

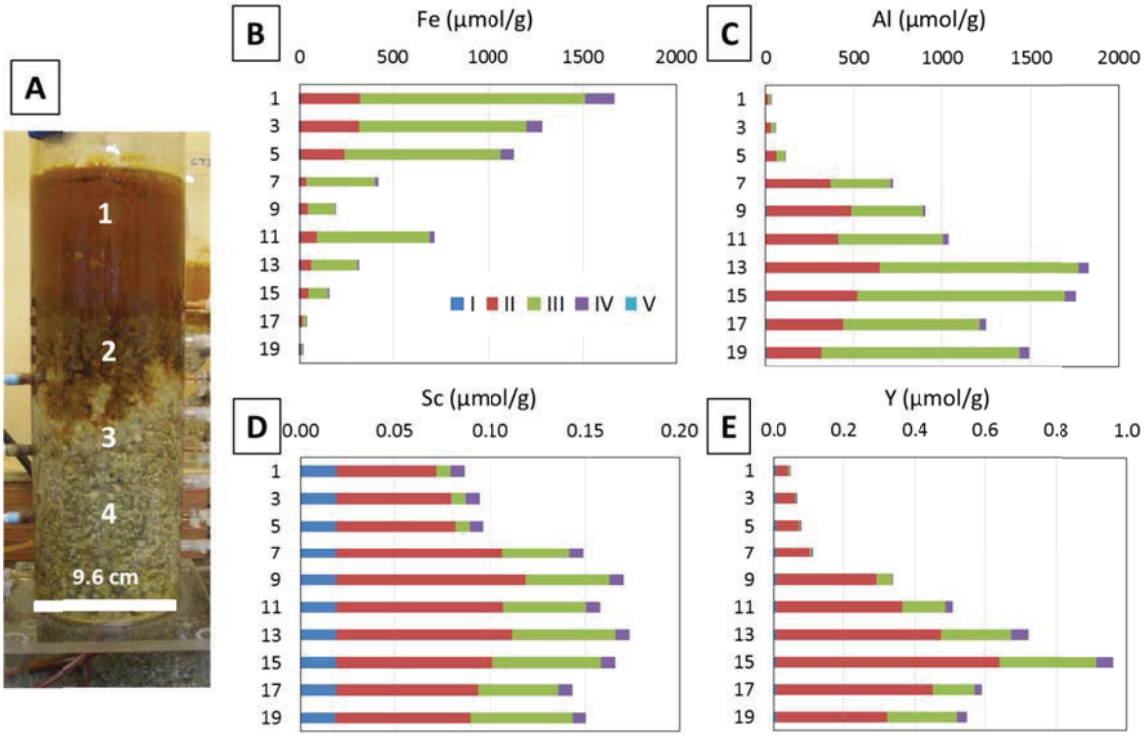

Fig. 4. A) View of the column after 28 days of the experiment: 1= supernatant AMD; 2= schwertmannite zone; 3= basaluminite zone 4= calcite zone. B-E) Distribution of Fe, Al, Sc and Y concentration in the solid residue. The numbers on the vertical axes indicate the depth (cm) of the center of each slice of the column. The colors indicate the different steps of sequential extraction of the following phases: I) the water-soluble fraction; II) calcite and basaluminite, III) low crystalline Fe(III)-oxyhydroxides and remaining basaluminite, IV) crystalline Fe(III)-oxides, and V) the residual fraction.

4 Discussion

4.1 Model description and validation

Different surface complexation models have been commonly used to reproduce experimental REE sorption onto amorphous ferric hydroxide, hematite and goethite. Traditionally, REE sorption onto ferric, manganese and/or aluminum hydroxides/oxides has been explained by the process of free ion sorption onto mineral surface sites. Some models consider the electrostatic term, which accounts for the effect of surface charge on the sorption of free ions or hydrolysis products (Marmier et al., 1997; Marmier and Fromage, 1999; Quinn et al., 2006a; Rabung et al., 1998; Tochiyama et al., 1996). In contrast, a non-electrostatic model can be used when the chemical interaction of the adsorbed cations is stronger than the electrostatic forces present during sorption (Davis and Kent, 1990) and the electrostatic term can be omitted. Here, a non-electrostatic model is proposed to describe the REE sorption based on the practical identity of the titration curves of schwertmannite suspensions under different ionic strengths (Fig. S5). Similarly, some previous studies have proposed a non-electrostatic model to predict REE adsorption on basaltic rock (Tertre et al., 2008) and the sorption of Y and the lanthanides onto amorphous iron hydroxides (Quinn et al., 2006a, 2006b; Rabung et al., 2000) and onto basaluminite (Lozano et al., 2019a).

Instead of developing a surface complexation model with free metal ions, sorption of aqueous sulfate complex MSO_4^+ is proposed because sulfate complexes are predominant in AMD waters and in the synthetic solutions prepared for the experiments (Fig. 5A,C). In contrast, REE-carbonate aqueous species were not considered because the proportion of carbonate species is very low at the pH range and sulfate concentrations used in the experiments.

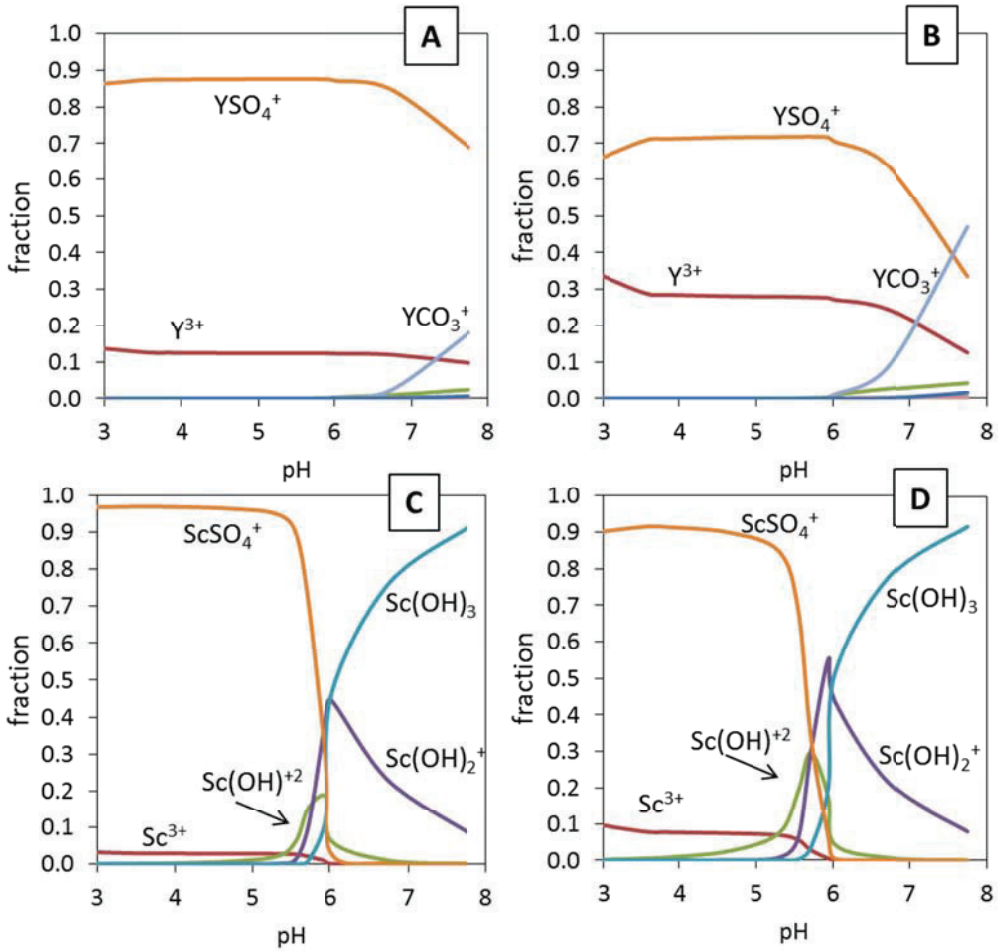

Fig. 5. Aqueous species distribution of Y and Sc (0.01 mmol/L) with different pH values in solutions of 20 mmol/L (A, C) or 2 mmol/L (B, D) sulfate at 25°C and atmospheric CO_2 pressure.

The sorption reaction consists of the exchange of the aqueous complex, (MSO_4^+, M accounts for each REE, or $Sc(OH)_2^+$) with n protons from the n surface sites (XOH), reflecting the pH dependence mentioned in section 3.2. In the case of MSO_4^+ sorption the following sorption reaction is described:

$$MSO_4^+ + nXOH = (XO)_nMSO_4^{1-n} + nH^+ \qquad K_M \qquad (3)$$

The equilibrium constant, K_M, of the surface complexation reaction for each REE aqueous complex (M) would be:

$$K_M = \frac{\{(XO)_nMSO_4^{1-n}\}\cdot a_{H^+}^n}{a_{MSO_4^+}\cdot\{XOH\}^n} \qquad (4)$$

where $\{(XO)_nMSO_4^{1-n}\}$ and {XOH} account for the mole fraction of the sorbed species ($[(XO)_nMSO_4^{1-n}]/T_{XOH}$), and of the free surface sites ($[XOH]/T_{XOH}$); and $a_{MSO_4^+}$ and a_{H^+} represents the activities of the aqueous complex and proton, respectively. Considering aqueous speciation previously described, the total dissolved REE is assumed to be MSO_4^+. A total surface site concentration T_{XOH} of 1.367 mmol/L was assumed according to the

schwertmannite surface properties described in section 3.1. The equilibrium constants expressed in this work are equivalent to those referred to as the K_3 in the model 3 proposed by (Wang and Giammar, 2013), where the surface mole fraction is proposed to better described the mass action expression for bidentate sorption. The concentration of free surface sites was calculated as the difference between the total surface site concentration and the total of REE sorbed:

$$[XOH] = T_{XOH} - \sum n\,[(XO)_n MSO_4^{1-n}] \quad (5)$$

Data from the experiment with 20 m SO_4 was used to calculate the equilibrium constant. Thus, Eq. 4 was rearranged after taking logarithms obtaining a linear expression showed in Eq. 6:

$$\log \frac{[(XO)_n MSO_4^{1-n}]}{a_{MSO_4^+}} - n \log[XOH] + (n-1) \log T_{XOH} = n\,pH + \log K_M \quad (6)$$

The amount of occupied sites with sorbed REE was lower than 10% at high pH experiments, and decreases for lower pH values. Therefore, the concentration of free sites [XOH] can be approximated to that of total sites T_{XOH}, and equation 6 can be simplified:

$$\log \frac{[(XO)_n MSO_4^{1-n}]}{a_{MSO_4^+}} - T_{XOH} = n\,pH + \log K_M \quad (7)$$

The experimental data was plotted according to Eq. (7) where the slope with respect to the pH indicated the denticity of the surface complex and the equilibrium constant was obtained from the intercept. The slope values increase with ionic radius from 1.4 to 2 (Fig. S6). Thus, bidentate surface complexes were assumed to form, although a proportion of monodentate complexes could also be present. The equilibrium constants were obtained as the intercept of a straight line of slope 2 by fitting the experimental data set of 20 mmol/L SO_4, according to equation (7). Gnuplot v. 5.7.2 software (Williams and Kelley, 2019) was used for the regression fitting. The error of the regression was larger and included the analytical error, and, therefore, it was assumed to be the error of log K_M value.

Scandium aqueous speciation showed that in addition to $ScSO_4^+$, $Sc(OH)^{2+}$ and $Sc(OH)_2^+$ species are also relevant in the pH range studied (Fig. 5C,D). The linear regression of Eq. (7) for $ScSO_4^+$ experimental data in sorption with high sulfate concentration showed a slope close to 2 (Fig. S7). Although $Sc(OH)_2^+$ species becomes relevant from pH 5, the correlation with pH was very poor and it was not considered. In contrast, $Sc(OH)^{2+}$ showed a good linear regression which resulted in a slope of 1.49 (Fig. S7). Thus, similar to Y and lanthanides, $ScSO_4^+$ and $Sc(OH)^{2+}$ are assumed to form bidentate surface complexes. The EXAFS fitting analysis of Lu sorbed onto ferrihydrite and Eu sorbed onto hematite described sorption of the free cations on the minerals forming bidentate surface complexes (Dardenne et al., 2001; Estes et al., 2013). Rabung et al. (2006) described the Lu^{3+} sorption γ-Al_2O_3 as the formation of monodentate surface complexes after fitting EXAFS spectra. The EXAFS fitting spectra of a basaluminite sample with YSO_4 sorbed on its surface indicated that the most probable configuration was the formation of a monodentate inner sphere complex (Lozano et al., 2019b), which is in agreement with the thermodynamic model suggested for REE sorption on this mineral (Lozano et al., 2019a). Similarly to basaluminite,MSO_4^+ aqueous species would form surface complexes

(here bidentate) with the hydroxyl groups of the schwertmannite surface through the REE cations. Further investigations are required to confirm the structure of the surface complex The differences between monodentate and bidentate formation depending on the mineral could be explained because the Fe-O bond is longer than Al-O, and it provides more space to allocate bidentate surface complexes.

The calculated log K_M values with the errors for the bidentate surface complexation reactions are displayed in Table 1. Equilibrium constants increased from -7.96 to -7.13 from La to Lu, indicating the higher affinity of HREE than LREE for schwertmannite surface.

Table 1. REE surface complexation constants for bidentate surface complexes obtained by fitting the experimental equation 7 with a concentration of 20 mmol/L SO_4 and a surface site d concentration of 1.367 mmol/L.

Element	Surface complex	Log K^2_M	Error
Sc	$(XO)_2ScSO_4^-$	-5.27	0.08
	$(XO)_2ScOH$	-3.4	0.11
Y	$(XO)_2YSO4^-$	-7.62	0.04
La	$(XO)_2LaSO4^-$	-7.96	0.15
Ce	$(XO)_2CeSO4^-$	-7.60	0.10
Pr	$(XO)_2PrSO4^-$	-7.52	0.13
Nd	$(XO)_2NdSO4^-$	-7.44	0.09
Sm	$(XO)_2SmSO4^-$	-7.27	0.08
Eu	$(XO)_2EuSO4^-$	-7.41	0.09
Gd	$(XO)_2GdSO4^-$	-7.51	0.05
Tb	$(XO)_2TbSO4^-$	-7.42	0.06
Dy	$(XO)_2DySO4^-$	-7.27	0.03
Ho	$(XO)_2HoSO4^-$	-7.38	0.06
Er	$(XO)_2ErSO4^-$	-7.39	0.05
Tm	$(XO)_2TmSO4^-$	-7.17	0.08
Yb	$(XO)_2YbSO4^-$	-7.26	0.04
Lu	$(XO)_2LuSO4^-$	-7.13	0.09

The sorption edge for each REE was calculated with the PHREEQC software. As expected, the calculations match the experimental data set of 20 mmol/L SO_4 (Fig. 6). The predicted and experimental sorption edges for the complete set of REE are shown in Fig. S8. With the exception of a slight overestimation for La, the model fit the concentration of the rest of the lanthanides and Y within the experimental error (Fig. S8). Regarding Sc, the good fit observed between the model-predicted outcome and the measured from experiments supported the existence of two different surface species. This result highlights the different behavior of Sc sorption with respect to the rest of the REE and it is a consequence of its different aqueous speciation. At the atomic scale, the Sc ionic radius is 0.75 Å (Rudolph and Pye, 2000), which is considerably lower than that of Lu, the smallest radius of the lanthanide series (0.98 Å), and thus it can better allocate to form bidentate surface complexes.

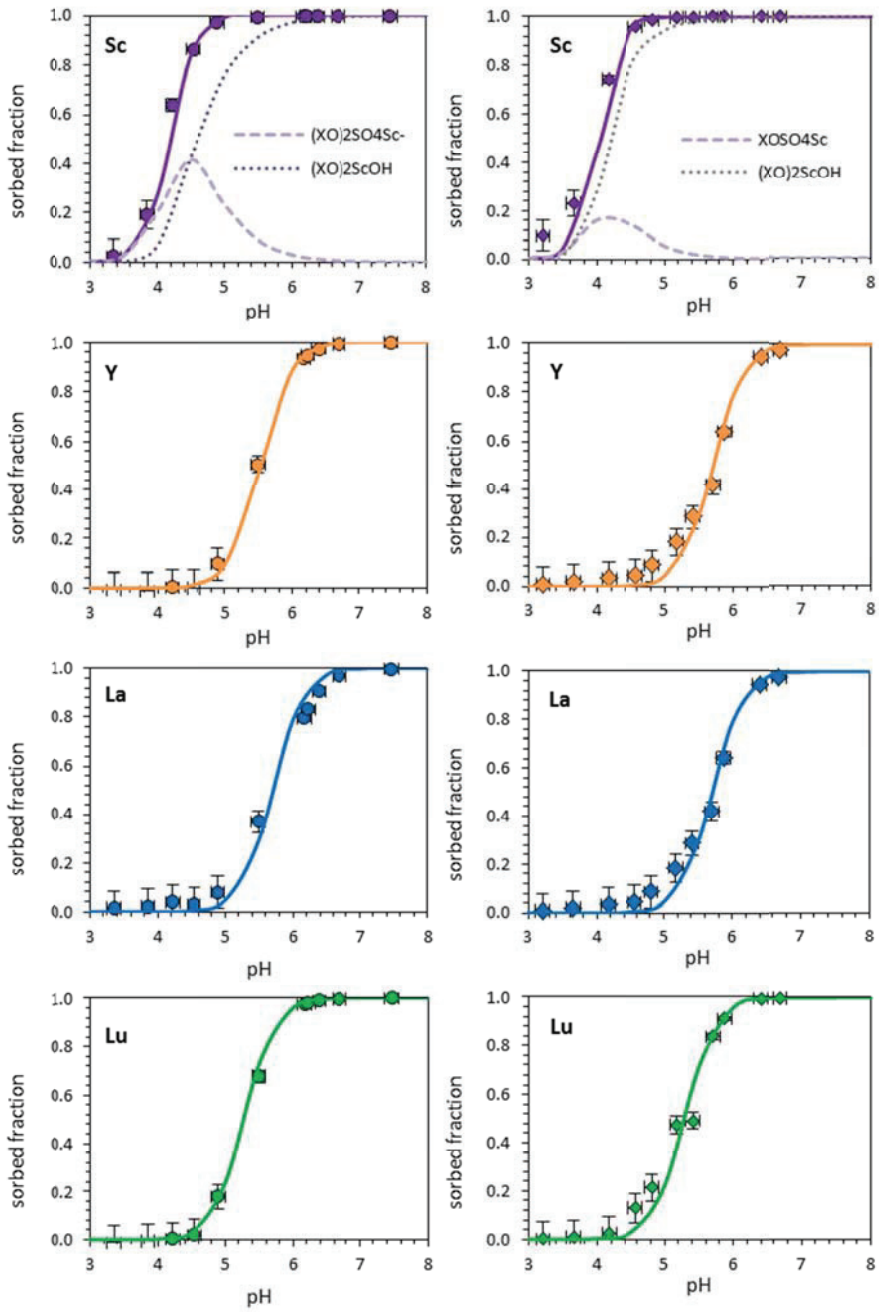

Fig. 6. Experimental (symbols) and calculated fractions (lines) of the sorption curves for Sc, Y, La and Lu for the experiments with 20 mmol/L SO_4 (left column) and with 2 mmol/L SO_4 (right column). Calculations at 25°C and atmospheric CO_2 pressure.

The model constructed with the 20 mmol/L SO_4 experimental data set was validated with three additional data sets: one set with 2 mmol/ SO_4 and a solid:liquid ratio of 1 g/L, and another two sets with 20 mmol/L SO_4 and solid:liquid ratios of 0.25 g/L and 2 g/L, respectively. The experimental and predicted values for Y, La, Lu and Sc for 2 mmol/L SO_4 and 1 g/L solid:liquid ratio are plotted in Fig. 6 (right column). The predicted and experimental values for the complete set of REE are shown in Fig. S9. Although with a slight underestimation at lower pH values, the modeled curves match the experimental sorption at lower sulfate

concentrations within the experimental error, supporting the formation of bidentate surface complexes.

The comparisons between the modeled and experimental data of selected elements for 1, 2 and 0.25 g/L solid:liquid ratios are shown in Fig. 7, and the data for the complete set of REE are plotted in Fig. S10. Despite a slight overprediction at higher pH values for the 0.25 g/L solid:liquid ratio, the sorbed fractions for the different suspension concentrations were successfully predicted by the model within the experimental errors.

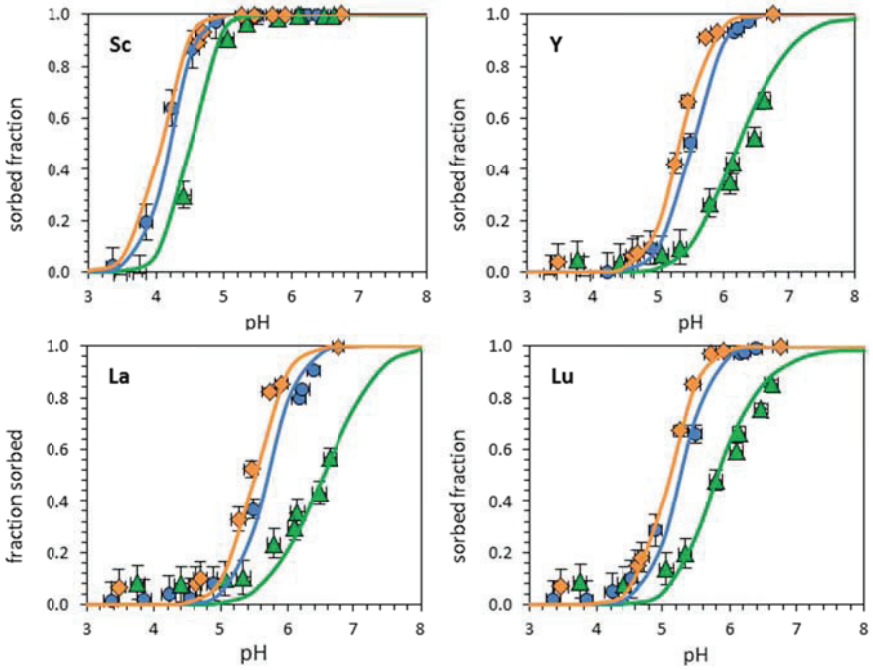

Fig. 7. Experimental data (symbols) and predicted sorbed fraction (lines) for sorption in 20 mmol/L SO_4 in solution and solid:liquid ratios of 2 g/L (orange diamonds), 1 g/L (blue circles) and 0.25 g/L (green triangles). Calculations at 25°C and atmospheric CO_2 pressure.

4.2 REE mobility in an AMD neutralization column

The results of the 1D reactive transport model were used to interpret the experimental data of Fig. 3 and Fig. 4. The results of the calculations for aqueous pH and for major solutes in pore water and the amount of mineral dissolved/precipitated are plotted in Fig. 8A-F. For a given time the pH increased with depth due to the limestone dissolution. A schwertmannite front appeared first, at lower pH values (pH 2.5), followed by a basaluminite front (pH from 3.6 to 6). Both fronts advanced to deeper parts of the columns with time (Fig. 8D,E) as the column was progressively invaded by more acidic water. The calculations indicate that calcite was exhausted from the top of the column downwards (Fig. 8F); then the acid water extracted the alkalinity to form schwertmannite from the basaluminite already precipitated in previous times. As a consequence of the process, the Al concentration in the pore water increased above the inflow concentration (Fig. 8C).

According to Fig. 9A, sorption of yttrium and lanthanides would occur at pH higher than 4, far above the pH at which schwertmannite formed (from 2.5 to 3.5) and therefore, these REE are not expected to be adsorbed on this mineral. Unlikely, scandium sorption on schwertmannite

started at pH 3, and therefore a small fraction could be sorbed on this mineral. According to Fig. 9B, sorption of all REE including Sc, can take place on basaluminite, which formed at pH between 3.5 and 6. As a consequence the REE sorption in the column occurred on basaluminite. As schwertmannite progressed at expenses of basaluminite dissolution at pH 3.5, a small fraction of Sc could also take place on schwertmannite. Thus, the similar La and Y distribution in pore water in contrast to the different behavior of Sc was evidenced in both the measured and calculated pore water concentrations (Fig. 8 G-I).

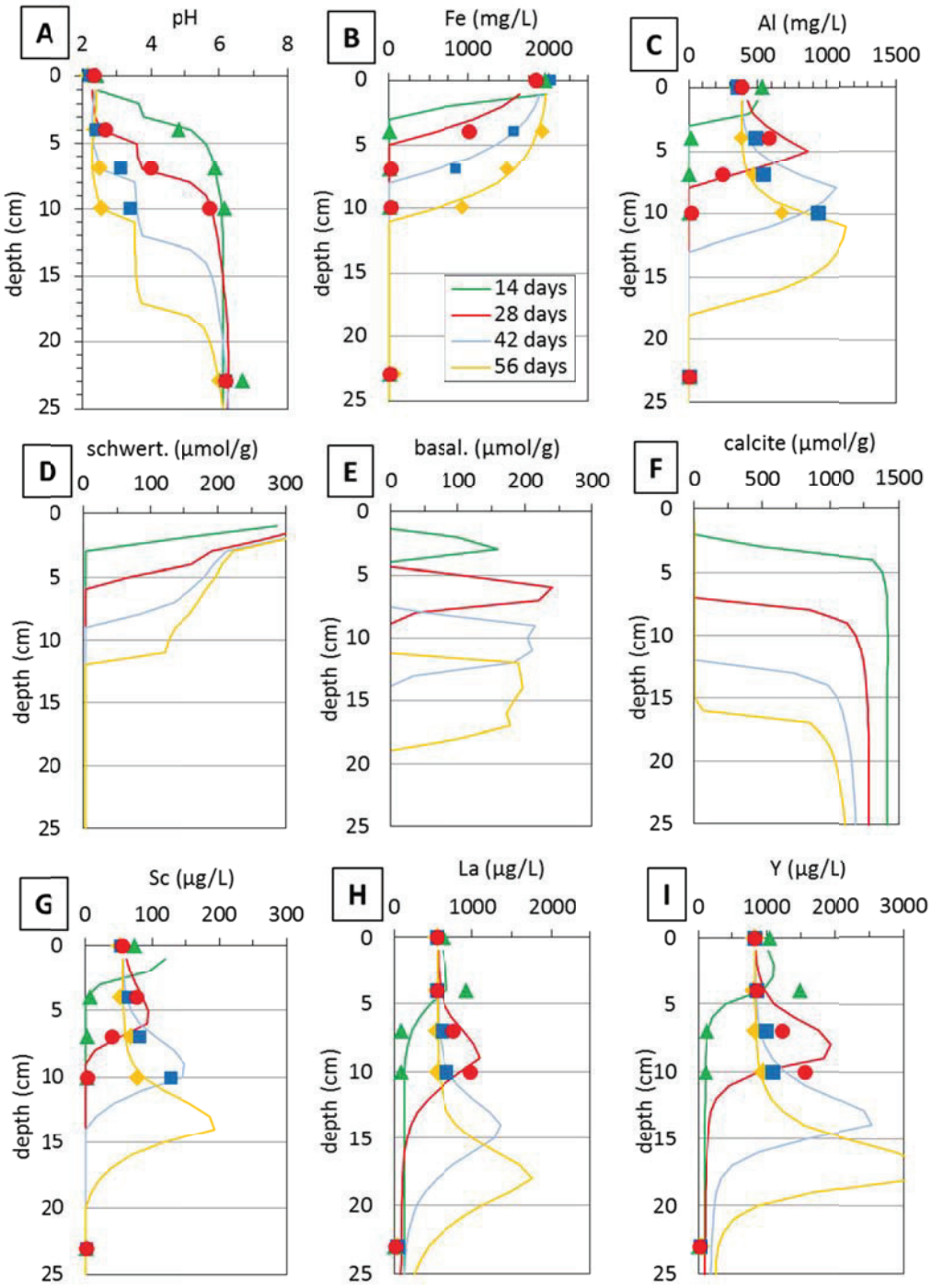

Fig. 8. Depth profiles of experimental data (symbols) and the reactive transport model (lines) at four different stages of column operation: (A) pH evolution; (B, C) Fe and Al concentrations

in pore water; (D, E, F) mineral distributions; (G, H, I) concentrations of selected REE in pore water.

Thus, after two weeks, at 4 cm deep, the pH was 4.8 and Sc was completely sorbed on basaluminite (and schwertmannite), whereas La and Y, which had previously sorbed at an earlier time and higher pH, were partially desorbing (notice their higher concentrations in the pore water than in the inflow). At 7 cm and deeper points, the pH was close to 6, and again, basaluminite precipitated and the three REE were sorbed. After four weeks and at 4 cm deep, the pH was 2.5, and La and Y were already desorbed (their concentrations were already equal to the inflow), whereas basaluminite was dissolving and releasing Sc and Al (notice the consistency of their peaks). At 7 cm deep, the pH decreased to 4.1 with respect to the value at the same depth in earlier time span. Thus, Sc was partially sorbed, as demonstrated by its concentration being lower than that in the inflow, and La and Y were desorbing from basaluminite, as shown again by their higher concentrations than those in the inflow. At 10 cm deep and with a pH of 5.7, Sc was entirely sorbed, whereas La and Y were already partially desorbing. After six weeks and at 4 cm deep, the pH remained at 2.5, and the three REE were completely released due to basaluminite dissolution under that pH condition. Meanwhile, at 7 and 10 cm deep with a pH of 3.5, Sc was still desorbing, whereas La and Y were practically desorbed. After eight weeks, all three REE were desorbed at all recorded depths, with the exception of Sc, which was partially released from basaluminite dissolution and partially sorbed by schwertmannite. At the end of the column (23 cm deep), the concentration of REE was very low throughout the experiment.

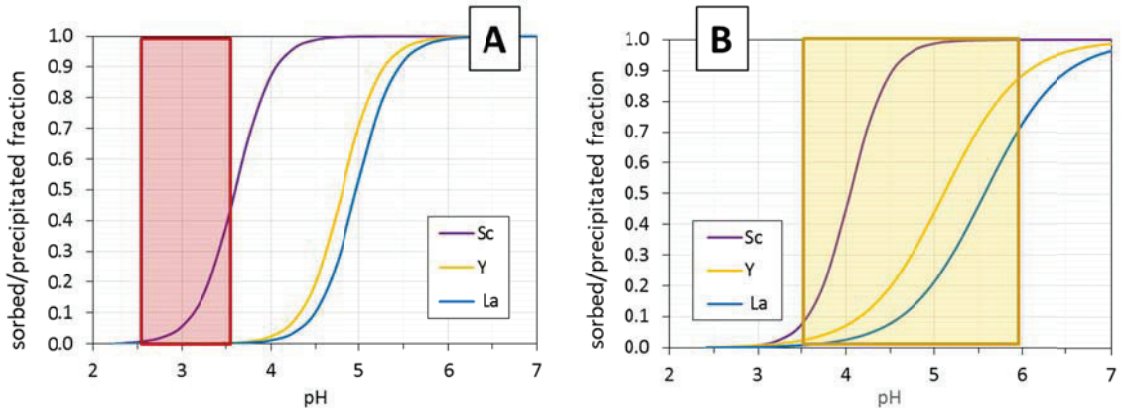

Fig.9 Sorbed fraction of REE on schwertmannite (A) and basaluminite (B) with respect to pH. The pH range of the main minerals precipitated is also plotted. Sorption parameters for schwertmannite and basaluminite are 4.7 and 4.6 sites/nm^2, 173 and 67 m^2/g and 23 and 7 g/L of solid:liquid ratio.

The calculated solid phase distribution at the end of the column life (Fig. 8D-E, 56 days) was also consistent with that deduced from sequential extraction analyses (Fig. 4B-C). Thus schwertmannite was predicted to form between 0 and 11 cm, especially in the shallower 4 cm. A basaluminite zone was calculated to develop between 11 and 20 cm, comparable to the observed range between 7 and 20 cm. The calculated pH value in the lowermost 10 cm ranged from 3.8 to 6, indicating that La, Y and Sc could remain sorbed on basaluminite, in accordance with sequential extraction analyses and with the absence of REE in the column outflow.

However, the presence of Sc (up to 25%) in the uppermost 10 cm of column deserves further discussion. The final pH value in the uppermost 10 cm was 2.5 (Fig. 8A). At such pH, if Sc was partially sorbed on schwertmannite would be desorbed (Fig. 9A). Therefore, the Sc analyzed in the upper 10 cm of solid residue indicates that desorption was not entirely reversible. Indeed, desorption has also been reported to be a very slow process in experiments of Yb sorption on hematite and alumina (Marmier et al., 1997). The preferential lanthanides and yttrium retention by basaluminite has been also described by Ayora et al. (2016), where a similar AMD column experiment was carried out. Similarly, Zhang and Honaker (2018) also explained a REE enrichment in the Al-rich precipitate formed when neutralizing with NaOH the leachate from a coal refuse piles. Interestingly, these authors also observed some Sc in the Fe-rich precipitates formed at pH between 3.3 and 4.6.

5 Conclusions

The experimental results showed that the sorption of REE onto schwertmannite was highly dependent on pH and to a lesser extent on the solid:liquid ratio. Thus, for a solid:liquid ratio of 1 g/L, the sorption of the lanthanides and Y was significant from pH 4.5, and they were almost totally sorbed at pH 6.5, depending on the element. Similar to other iron and aluminum oxides/hydroxides, preferential sorption was observed from La to Lu. The sorption of Y and lanthanides were not affected by the amount of sulfate in solution, probably because MSO_4^+ was the overwhelming aqueous species above 1 mmol/L SO_4. Scandium sorbed at distinctly lower pH, from 3 to 6.5, and its sorption slightly increased with a decrease in the sulfate content because in addition to $ScSO_4^+$, the $ScOH^{2+}$ aqueous species was also sorbed. As a consequence, the Sc sorbed fraction was significant at pH values at which the sorption of the rest of REE was almost negligible. This suggests that, in active treatment plants, Sc can be segregated from the rest of REE by keeping the pH of the process below 4.5 and solid:liquid ratios around 1 g/L.

The results of the sorption experiments were satisfactorily described by a non-electrostatic model in which MSO_4^+ (and $ScOH^{2+}$) exchanged with two surface protons, forming a bidentate surface complex. The sorption model successfully predicted the analyses of REE in pore water and solid phases from a laboratory column emulating a passive AMD remediation system. Although schwertmannite and basaluminite have similar sorption edges, Y and lanthanides only sorbed at pH values higher than 4.5, and sorption only occurred on basaluminite because schwertmannite formed at pH values lower than 3.5. In contrast, the Sc sorption edge extended from pH 3 to 5 (at the high solid:liquid ratios of a porous medium) and therefore Sc can be partially sorbed on schwertmannite. As a practical consequence, REE preferentially accumulate in the basaluminite residue of AMD passive treatment systems, but a Sc can be partially found in the schwertmannite waste.

Acknowledgments

This work was funded by the European EIT-Raw materials 'Morecovery' and the Spanish SCYRE (CGL2016-78783-C2-R)] projects. A. L. was also funded by the FPI grant (BES-2014-069978) from the Ministry of Science, Innovation and Universities (Spain). The authors thank J. Bellés, M. Cabañas, R. Bartrolí and N. Moreno (IDAEA-CSIC) for their analytical assistance.

References

Acero, P., Ayora, C., Torrentó, C., Nieto, J.M., 2006. The behavior of trace elements during schwertmannite precipitation and subsequent transformation into goethite and jarosite. Geochim. Cosmochim. Acta 70, 4130–4139. https://doi.org/10.1016/j.gca.2006.06.1367

Antelo, J., Fiol, S., Gondar, D., López, R., Arce, F., 2012. Comparison of arsenate, chromate and molybdate binding on schwertmannite: Surface adsorption vs anion-exchange. J. Colloid Interface Sci. 386, 338–343. https://doi.org/10.1016/j.jcis.2012.07.008

Ayora, C., Caraballo, M.A., Macias, F., Rötting, T.S., Carrera, J., Nieto, J.M., 2013. Acid mine drainage in the Iberian Pyrite Belt: 2. Lessons learned from recent passive remediation experiences. Environ. Sci. Pollut. Res. 20, 7837–7853. https://doi.org/10.1007/s11356-013-1479-2

Ayora, C., Macías, F., Torres, E., Lozano, A., Carrero, S., Nieto, J.M., Pérez-López, R., Fernández-Martínez, A., Castillo-Michel, H., 2016b. Recovery of Rare Earth Elements and Yttrium from Passive-Remediation Systems of Acid Mine Drainage. Environ. Sci. Technol. 50, 8255–8262. https://doi.org/10.1021/acs.est.6b02084

Bau, M., 1999. Scavenging of dissolved yttrium and rare earths by precipitating iron oxyhydroxide: Experimental evidence for Ce oxidation, Y-Ho fractionation, and lanthanide tetrad effect. Geochim. Cosmochim. Acta 63, 67–77. https://doi.org/10.1016/S0016-7037(99)00014-9

Bau, M., Koschinsky, A., Dulski, P., Hein, J.R., 1996. Comparison of the partitioning behaviours of yttrium, rare earth elements, and titanium between hydrogenetic marine ferromanganese crusts and seawater. Geochim. Cosmochim. Acta 60, 1709–1725. https://doi.org/10.1016/0016-7037(96)00063-4

Blanc, P., Lassin, A., Piantone, P., Azaroual, M., Jacquemet, N., Fabbri, A., Gaucher, E.C., 2012. Thermoddem: A geochemical database focused on low temperature water/rock interactions and waste materials. Appl. Geochemistry 27, 2107–2116. https://doi.org/10.1016/j.apgeochem.2012.06.002

Blowes, D.W., Ptacek, C.J., Jambor, J.L., Weisener, C.G., Paktunc, D., Gould, W.D., Johnson, D.B., 2014. The Geochemistry of Acid Mine Drainage, 11th ed, Treatise on Geochemistry: Second Edition. Elsevier Ltd. https://doi.org/10.1016/B978-0-08-095975-7.00905-0

Burton, E.D., Bush, R.T., Johnston, S.G., Watling, K.M., Hocking, R.K., Sullivan, L.A., Parker, G.K., 2009. Sorption of arsenic (V) and arsenic (III) to schwertmannite. Environ. Sci. Technol. 43, 9202–9207. https://doi.org/10.1021/es902461x

Byrne, R.H., Kim, K.-H., 1990. Rare earth elements scavenging in seawater. Geochim. Cosmochim. Acta 54, 2645–2656.

Byrne, R.H., Sholkovitz, E.R., 1996. Chapter 158 Marine chemistry and geochemistry of the lanthanides. Handb. Phys. Chem. Rare Earths 23, 497–593. https://doi.org/10.1016/S0168-1273(96)23009-0

Caraballo, M.A., Macías, F., Nieto, J.M., Castillo, J., Quispe, D., Ayora, C., 2011. Hydrochemical performance and mineralogical evolution of a dispersed alkaline substrate (DAS) remediating the highly polluted acid mine drainage in the full-scale passive treatment of Mina Esperanza (SW Spain). Am. Mineral. 96, 1270–1277. https://doi.org/10.2138/am.2011.3752

Caraballo, M.A., Rötting, T.S., Nieto, J.M., Ayora, C., 2009. Sequential extraction and DXRD applicability to poorly crystalline Fe- and Al-phase characterization from an acid mine water passive remediation system. Am. Mineral. 94, 1029–1038. https://doi.org/10.2138/am.2009.3137

Choudhury, B.U., Malang, A., Webster, R., Mohapatra, K.P., Verma, B.C., Kumar, M., Das, A., Islam, M., Hazarika, S., 2017. Acid drainage from coal mining: Effect on paddy soil and productivity of rice. Sci. Total Environ. 583, 344–351. https://doi.org/10.1016/j.scitotenv.2017.01.074

Cravotta, C.A., Trahan, M.K., 1999. Limestone drains to increase pH and remove dissolved metals from acidic mine drainage. Appl. Geochemistry 14, 581–606. https://doi.org/10.1016/S0883-2927(98)00066-3

Dardenne, B.K., Schäfer, T., Denecke, M.A., Rothe, J., Kim, J.I., 2001. Identification and characterization of sorbed lutetium species on 2-line ferrihydrite by sorption data modeling, TRLFS and EXAFS. Radiochim. Acta 89, 469–479.

Davis, J.A., Kent, D.B., 1990. Surface Complexation Modeling in Aqueous Geochemistry, in: Hochella, M.F., White, A.F. (Eds.), Reviews in Mineralogy and Geochemistry. pp. 177–260.

De Carlo, E.H., Wen, X.Y., Irving, M., 1998. The influence of redox reactions on the uptake of dissolved Ce by suspended Fe and Mn oxide particles. Aquat. Geochemistry 3, 357–389. https://doi.org/10.1023/A:1009664626181

Elderfield, H., Upstill-Goddard, R., Sholkovitz, E.R., 1990. The rare earth elements in rivers , estuaries , and coastal seas and their significance to the composition of ocean ... Geochim. Cosmochim. Acta 54, 971–991. https://doi.org/10.1016/0016-7037(90)90432-K

Estes, S.L., Arai, Y., Becker, U., Fernando, S., Yuan, K., Ewing, R.C., Zhang, J., Shibata, T., Powell, B.A., 2013. A self-consistent model describing the thermodynamics of Eu(III) adsorption onto hematite. Geochim. Cosmochim. Acta 122, 430–447. https://doi.org/10.1016/j.gca.2013.08.023

Evangelou, V.P., Zhang, Y.L., 1995. A review: Pyrite oxidation mechanisms and acid mine drainage prevention. Crit. Rev. Environ. Sci. Technol. 25, 141–199. https://doi.org/10.1080/10643389509388477

Fernández-Martínez, A., Timon, V., Romaman-Ross, G., Cuello, G.J., Daniels, J.E., Ayora, C., 2010. The structure of schwertmannite, a nanocrystalline iron oxyhydroxysulfate. Am. Mineral. 95, 1312–1322. https://doi.org/10.2138/am.2010.3446

Ferreira da Silva, E., Bobos, I., Xavier Matos, J., Patinha, C., Reis, A.P., Cardoso Fonseca, E., 2009. Mineralogy and geochemistry of trace metals and REE in volcanic massive sulfide host rocks, stream sediments, stream waters and acid mine drainage from the Lousal mine area (Iberian Pyrite Belt, Portugal). Appl. Geochemistry 24, 383–401. https://doi.org/10.1016/j.apgeochem.2008.12.001

Fukushi, K., Sato, T., Yanase, N., Minato, J., Yamada, H., 2004. Arsenate sorption on schwertmannite. Am. Mineral. 89, 1728–1734. https://doi.org/10.2138/am-2004-11-1219

Gammons, C.H., Wood, S.A., Nimick, D.A., 2005a. Diel behavior of rare earth elements in a mountain stream with acidic to neutral pH. Geochim. Cosmochim. Acta 69, 3747–3758.

https://doi.org/10.1016/j.gca.2005.03.019

Gammons, C.H., Wood, S.A., Pedrozo, F., Varekamp, J.C., Nelson, B.J., Shope, C.L., Baffico, G., 2005b. Hydrogeochemistry and rare earth element behavior in a volcanically acidified watershed in Patagonia, Argentina. Chem. Geol. 222, 249–267. https://doi.org/10.1016/j.chemgeo.2005.06.002

Gimeno Serrano, M.J., Auqué Sanz, L.F., Nordstrom, D.K., 2000. REE speciation in low-temperature acidic waters and the competitive effects of aluminum. Chem. Geol. 165, 167–180. https://doi.org/10.1016/S0009-2541(99)00166-7

Hatch, G.P., 2012. Dynamics in the global market for rare earths. Elements 8, 341–346. https://doi.org/10.2113/gselements.8.5.341

Henderson, P., 1984. General Geochemical Properties and Abundances of the Rare Earth Elements, in: Henderson, P. (Ed.), Developments in Geochemistry. pp. 1–32. https://doi.org/10.1016/B978-0-444-42148-7.50006-X

Johnson, J.W., Oelkers, E.H., Helgeson, H.C., 1992. SUPCRT92: a soft- ware package for calculating the standard molal thermodynamic properties ofminerals, gases, aqueous species, and reactions from 1 bar to 5000 bar and 0Cto 1000C, Computers and Geosciences. https://doi.org/Doi 10.1016/0098-3004(92)90029-Q

Kawabe, I., Ohta, A., Miura, N., 1999a. Distribution and coefficients NaCl solutions of REE affected between Fe oxyhydroxide precipitates by REE-carbonate complexation. Geochem. J. 33, 181–197.

Kawabe, I., Ohta, A., Tokumura, M., Miyauchi, K., 1999b. REE partitioning betweem Fe-Mn oxyhydroxide precipitates and weakly acid NaCl solutions : Convex tetrad effect and fractionation of Y and Sc from heavy lanthanides. Geochem. J. 33, 167–179.

Klungness, G.D., Byrne, R.H., 2000. Comparative hydrolysis behaviour of the rare earths and yttrium: the influence of temperature and ionic strength. Polyhedron 19, 99–107.

Koeppenkastrop, D., De Carlo, E.H., 1992. Sorption of rare-earth elements from sea water onto synthetic mineral particles: An experimental approach. Chem. Geol. 95, 251–263.

Lee, J.H., Byrne, R.H., 1992. Examination of comparative rare earth element complexation behavior using linear free-energy relationships. Geochim. Cosmochim. Acta 56, 1127–1137.

Lin, C., Wu, Y., Lu, W., Chen, A., Liu, Y., 2007. Water chemistry and ecotoxicity of an acid mine drainage-affected stream in subtropical China during a major flood event. J. Hazard. Mater. 142, 199–207. https://doi.org/10.1016/j.jhazmat.2006.08.006

Lin, J., Nilges, M.J., Wiens, E., Chen, N., Wang, S., Pan, Y., 2019. Mechanism of Gd3+ uptake in gypsum (CaSO4·2H2O): Implications for EPR dating, REE recovery and REE behavior. Geochim. Cosmochim. Acta 258, 63–78. https://doi.org/10.1016/j.gca.2019.05.019

Liu, H., Pourret, O., Guo, H., Bonhoure, J., 2017. Rare earth elements sorption to iron oxyhydroxide: Model development and application to groundwater. Appl. Geochemistry 87, 158–166. https://doi.org/10.1016/j.apgeochem.2017.10.020

Lozano, A., Ayora, C., Fernández-Martínez, A., 2019a. Sorption of rare earth elements onto basaluminite: The role of sulfate and pH. Geochim. Cosmochim. Acta 258, 50–62.

https://doi.org/10.1016/j.gca.2019.05.016

Lozano, A., Fernández-Martínez, A., Ayora, C., Di-Tomamaso, D., Poulain, A., Rovezzi, M., Marini, C., 2019b. Solid and Aqueous Speciation of Yttrium in Passive Remediation Systems of Acid Mine Drainage. Environ. Sci. Technol. https://doi.org/10.1021/acs.est.9b01795

Luo, Y., Millero, F.J., 2004. Effects of temperature and ionic strength on the stabilities of the first and second fluoride complexes of yttrium and the rare earth elements. Geochim. Cosmochim. Acta 68, 4301–4308. https://doi.org/10.1016/j.gca.2004.05.025

Luo, Y.R., Byrne, R.H., 2004. Carbonate complexation of yttrium and the rare earth elements in natural waters. Geochim. Cosmochim. Acta 68, 691–699. https://doi.org/10.1016/S0016-7037(03)00495-2

Luo, Y.R., Byrne, R.H., 2001. Yttrium and Rare Earth Element Complexation by Chloride Ions at 25°C. J. Solution Chem. 30, 837–845.

Marmier, N., Dumonceau, J., Fromage, F., 1997. Surface complexation modeling of Yb(III) sorption and desorption on hematite and alumina. J. Contam. Hydrol. 26, 159–167.

Marmier, N., Fromage, F., 1999. Comparing electrostatic and nonelectrostatic surface complexation modeling of the sorption of lanthanum on hematite. J. Colloid Interface Sci. 212, 252–263. https://doi.org/10.1006/jcis.1998.6039

Massari, S., Ruberti, M., 2013. Rare earth elements as critical raw materials: Focus on international markets and future strategies. Resour. Policy 38, 36–43. https://doi.org/10.1016/j.resourpol.2012.07.001

Masuda, A., Kawakami, O., Dohmoto, Y., Takenaka, T., 1987. Lanthanide tetrad effects in nature : two mutually opposite types, W and M. Geochem. J. 21, 119–124.

McLennan, S.M., 1989. Chapter 7: Rare Earth Elements in Sedimentary Rocks: Influence of provenance and sedimentary processes. Rev. Mineral. Geochemistry 11, 169–200.

Millero, F.J., 1992. Stability constants for the formation of rare earth inorganic complexes as a function of temperature and ionic strength. Geochim. Cosmochim. Acta 56, 3123–3132. https://doi.org/10.1016/j.gca.2006.09.019

Noack, C.W., Dzombak, D.A., Karamalidis, A.K., 2014. Rare earth element distributions and trends in natural waters with a focus on groundwater. Environ. Sci. Technol. 48, 4317–4326. https://doi.org/10.1021/es4053895

Nordstrom, D.K., 2011. Hydrogeochemical processes governing the origin, transport and fate of major and trace elements from mine wastes and mineralized rock to surface waters. Appl. Geochemistry 26, 1777–1791. https://doi.org/10.1016/j.apgeochem.2011.06.002

Nordstrom, D.K., Blowes, D.W., Ptacek, C.J., 2015. Hydrogeochemistry and microbiology of mine drainage: An update. Appl. Geochemistry 57, 3–16. https://doi.org/10.1016/j.apgeochem.2015.02.008

Ohta, A., Kawabe, I., 2001. REE (III) adsorption onto Mn dioxide (δ-MnO2) and Fe oxyhydroxide: Ce(III) oxidation by δ-MnO2. Geochim. Cosmochim. Acta 65, 695–703. https://doi.org/10.1016/S0016-7037(00)00578-0

Ohta, A., Kawabe, I., 2000. Rare eath element partitioning between fe oxyhydroxide precipitates and aqueous NaCl solutions doped with NaHCO3: Determinations of rare earth element complexation constants with carbonate ions. Geochem. J. 34, 439–454. https://doi.org/10.2343/geochemj.34.439

Parkhurst, D.L., Appelo, C.A.J., 1999. User's Guide to PHREEQC (VERSION 2) A Computer Program for Speciation, Batch Reaction, One Dimensional Transport, and Inverse Geochemical Calculations.

Plummer, L.N., Parkhurst, D.L., L., W.T.M., 1979. Critical Review of the Kinetics of Calcite Dissolution and Precipitation. https://doi.org/10.1021/bk-1979-0093.ch025

Quinn, K.A., Byrne, R.H., Schijf, J., 2006a. Sorption of yttrium and rare earth elements by amorphous ferric hydroxide:Influence of pH and ionic strength. Mar. Chem. 99, 128–150. https://doi.org/10.1021/es0618191

Quinn, K.A., Byrne, R.H., Schijf, J., 2006b. Sorption of yttrium and rare earth elements by amorphous ferric hydroxide: Influence of solution complexation with carbonate. Geochim. Cosmochim. Acta 70, 4151–4165. https://doi.org/10.1021/es0618191

Quinn, K.A., Byrne, R.H., Schijf, J., 2004. Comparative scavenging of yttrium and the rare earth elements in seawater: Competitive influences of solution and surface chemistry. Aquat. Geochemistry 10, 59–80. https://doi.org/10.1023/B:AQUA.0000038959.03886.60

Rabung, B.T., Geckeis, H., Wang, X.K., Rothe, J., Denecke, M.A., Klenze, R., Fanghänel, T., 2006. Cm (III) sorption onto γ-Al2O3: New insight into sorption mechanisms by time-resolved laser fluorescence spectroscopy and extended X-ray absorption fine structure. Radiochim. Acta 94, 609–618. https://doi.org/10.1524/ract.2006.94.9.609

Rabung, B.T., Stumpf, T., Geckeis, H., Klenze, R., Kim, J.I., 2000. Sorption of Am (III) and Eu (III) onto γ-alumina : experiment and modelling 88, 711–716.

Rabung, T., Geckeis, H., Kim, J. Il, Beck, H.P., 1998. Sorption of Eu(III) on a natural hematite: Application of a surface complexation model. J. Colloid Interface Sci. 208, 153–161. https://doi.org/10.1006/jcis.1998.5788

Regenspurg, S., Brand, A., Peiffer, S., 2004. Formation and stability of schwertmannite in acidic mining lakes. Geochim. Cosmochim. Acta 68, 1185–1197. https://doi.org/10.1016/j.gca.2003.07.015

Regenspurg, S., Peiffer, S., 2005. Arsenate and chromate incorporation in schwertmannite. Appl. Geochemistry 20, 1226–1239. https://doi.org/10.1016/j.apgeochem.2004.12.002

Rillard, J., Pourret, O., Censi, P., Inguaggiato, C., Zuddas, P., Toulhoat, P., Gombert, P., Brusca, L., 2019. Behavior of rare earth elements in an aquifer perturbed by CO2 injection: Environmental implications. Sci. Total Environ. 687, 978–990. https://doi.org/10.1016/j.scitotenv.2019.05.490

Rötting, T.S., Caraballo, M.A., Serrano, J.A., Ayora, C., Carrera, J., 2008a. Field application of calcite Dispersed Alkaline Substrate (calcite-DAS) for passive treatment of acid mine drainage with high Al and metal concentrations. Appl. Geochemistry 23, 1660–1674. https://doi.org/10.1016/j.apgeochem.2008.02.023

Rötting, T.S., Thomas, R.C., Ayora, C., Carrera, J., 2008b. Passive treatment of acid mine drainage with high metal concentrations using dispersed alkaline substrate. J. Environ.

Qual. 37, 1741–1751. https://doi.org/10.2134/jeq2007.0517

Rudolph, W.W., Pye, C.C., 2000. Raman Spectroscopic measurements of scandium(III) hydration in aqueous perchlorate solution and ab initio molecular orbital studies of scandium(III) water clusters: Does Sc(III) occur as a hexaaqua complex? J. Phys. Chem. A 104, 1627–1639. https://doi.org/10.1021/jp9916541

Sánchez-España, J., Yusta, I., Diez-Ercilla, M., 2011. Schwertmannite and hydrobasaluminite: A re-evaluation of their solubility and control on the iron and aluminium concentration in acidic pit lakes. Appl. Geochemistry 26, 1752–1774. https://doi.org/10.1016/j.apgeochem.2011.06.020

Schijf, J., Byrne, R.H., 2004. Determination of SO4β1 for yttrium and the rare earth elements at I = 0.66 m and t = 25°C- Implications for YREE solution speciation in sulfate-rich waters. Geochim. Cosmochim. Acta 68, 2825–2837. https://doi.org/10.1016/j.gca.2003.12.003

Schwertmann, U., Carlson, L., 2005. The pH-dependent transformation of schwertmannite to goethite at 25°C. Clay Miner. 40, 63–66. https://doi.org/10.1180/0009855054010155

Sholkovitz, E.R., 1995. The aquatic chemistry of rare earth elements in rivers and estuaries. Aquat. Geochemistry 1, 1–34. https://doi.org/10.1007/BF01025229

Spahiu, K., Bruno, J., 1995. A selected thermodynamic database for REE to be used in HLNW performance assessment exercises. https://doi.org/10.1016/S0007-8506(07)90004-9

Tertre, E., Hofmann, A., Berger, G., 2008. Rare earth element sorption by basaltic rock: Experimental data and modeling results using the "Generalised Composite approach." Geochim. Cosmochim. Acta 72, 1043–1056. https://doi.org/10.1016/j.gca.2007.12.015

Tochiyama, O., Yamazaki, H., Li, N., 1996. Effect of the concentration of metal ions on their adsorption on various hydrous iron and aluminum oxides. J. Nucl. Sci. Technol. 33, 846–851. https://doi.org/10.1080/18811248.1996.9732019

Torres, E., Auleda, M., 2013. A sequential extraction procedure for sediments affected by acid mine drainage. J. Geochemical Explor. 128, 35–41. https://doi.org/10.1016/j.gexplo.2013.01.012

U.S. Geological Survey (USGS), 2019. Mineral Commodity Summaries, 2019th ed. Reston, Virginia.

Verplanck, P.L., Antweiler, R.C., Nordstrom, D.K., Taylor, H.E., 2001. Standard reference water samples for rare earth element determinations. Appl. Geochemistry 16, 231–244. https://doi.org/10.1016/S0883-2927(00)00030-5

Verplanck, P.L., Nordstrom, D.K., Taylor, H.E., Kimball, B.A., 2004. Rare earth element partitioning between hydrous ferric oxides and acid mine water during iron oxidation. Appl. Geochemistry 19, 1339–1354. https://doi.org/10.1016/j.apgeochem.2004.01.016

Viadero, R.C., Wei, X., Buzby, K.M., 2006. Characterization and Dewatering Evaluation of Acid Mine Drainage Sludge from Ammonia Neutralization. Environ. Eng. Sci. 23, 734–743. https://doi.org/10.1089/ees.2006.23.734

Wang, Z., Giammar, D.E., 2013. Mass action expressions for bidentate adsorption in surface complexation modeling: Theory and practice. Environ. Sci. Technol. 47, 3982–3996. https://doi.org/10.1021/es305180e

Wood, S.A., Samson, I.M., 2006. The aqueous geochemistry of gallium, germanium, indium and scandium. Ore Geol. Rev. 28, 57–102. https://doi.org/10.1016/j.oregeorev.2003.06.002

Zhang, W., Honaker, R.Q., 2018. Rare earth elements recovery using staged precipitation from a leachate generated from coarse coal refuse. Int. J. Coal Geol. 195, 189–199. https://doi.org/10.1016/j.coal.2018.06.008

Supplementary material

Sorption of rare earth elements on schwertmannite and their mobility in acid mine drainage treatments

Alba Lozano[a,b*], Carlos Ayora[a], Alejandro Fernández-Martínez[c]

[a] Institute of Environmental Assessment and Water Research, (IDAEA-CSIC), Jordi Girona 18-26, 08034 Barcelona, Spain

[b] Grup de Mineralogia Aplicada i Geoquímica de Fluids, Departament de Cristal-lografia, Mineralogia i Dipòsits Minerals, Facultat de Geologia, Universitat de Barcelona (UB), C/Martí Franquès, S/N, Barcelona, Spain

[c] Univ. Grenoble Alpes, Univ. Savoie Mont Blanc, CNRS, IRD, IFSTTAR, ISTerre, 38000 Grenoble, France

Corresponding author:

Alba Lozano (alba.lozano@idaea.csic.es)

FIGURE CAPTIONS

Fig. S1. XRD pattern of pure schwertmannite prior to and after the sorption experiments at 20 mmol/L SO_4 and different pH values. Notice that no goethite peaks are observed.

Fig. S2. XRD pattern of pure schwertmannite prior to and after the sorption experiments at 2 mmol/L SO_4 and different final pH values. Notice that no goethite peaks are observed.

Fig. S3. Surface site distribution in schwertmannite. Atoms labeled "A" form the face (1 0 0), "B" form (0 1 0) and "C" form (0 0 1). Data from Fernandez-Martinez et al. (2010).

Fig. S4. Evolution of REE sorbed on schwertmannite (µmol/g) over time at pH 5.5 ±0.2 for selected REEs. (Sc: circles, Lu: diamonds, Y: squares, La: triangles, and dotted line: pH value; Sc*=Sc/2).

Fig. S5. Titration of schwertmannite suspensions (1 g/L) under different $NaNO_3$ concentrations. Symbols: Suspensions with different NH_4OH and HCl addition and kept under stirring for 24 hours. Solid lines: titrations conducted using a 848 Titrino plus titrator with addition of NH_4OH 0.1 mol/L (OH>0) and HCl 0.1 mol/L (OH<0). After each titrant addition, the electrode reading was set between 60 to 120 seconds, and the drift was lower than 50 mV/min. All the experiments were made at 25°C and atmospheric CO_2 pressure.

Fig. S6 Regressions obtained from measured pH values and calculated activities from the final concentrations of the experimental data set of 20 mmol/L SO_4. (A, B, C) Regressions for Y, La and Lu, respectively, plotted as Eq. (S5).

Fig. S7 Regressions obtained from experimental data of Sc plotted according to Eq. (S5) for $ScSO_4^+$ (A) and $ScOH^{2+}$ (B) species.

Fig. S8. Sorbed fractions measured (symbols) and calculated (lines) for 20 mmol/L SO_4 and a 1 g/L solid:liquid ratio. Calculations performed at 25°C and pCO_2 of 3.5.

Fig. S9. Sorbed fractions measured (symbols) and calculated (lines) for 2 mmol/L SO_4 and a 1 g/L solid:liquid ratio. Calculations performed at 25°C and pCO_2 of 3.5.

Fig. S10. Sorbed fractions measured (symbols) and calculated (lines) for 20 mmol/L SO_4 and three different solid:liquid ratios: 2 g/L (orange diamonds), 1 g/L (blue circles) and 0.25 g/L (green triangles). Calculations performed at 25°C and pCO_2 of 3.5.

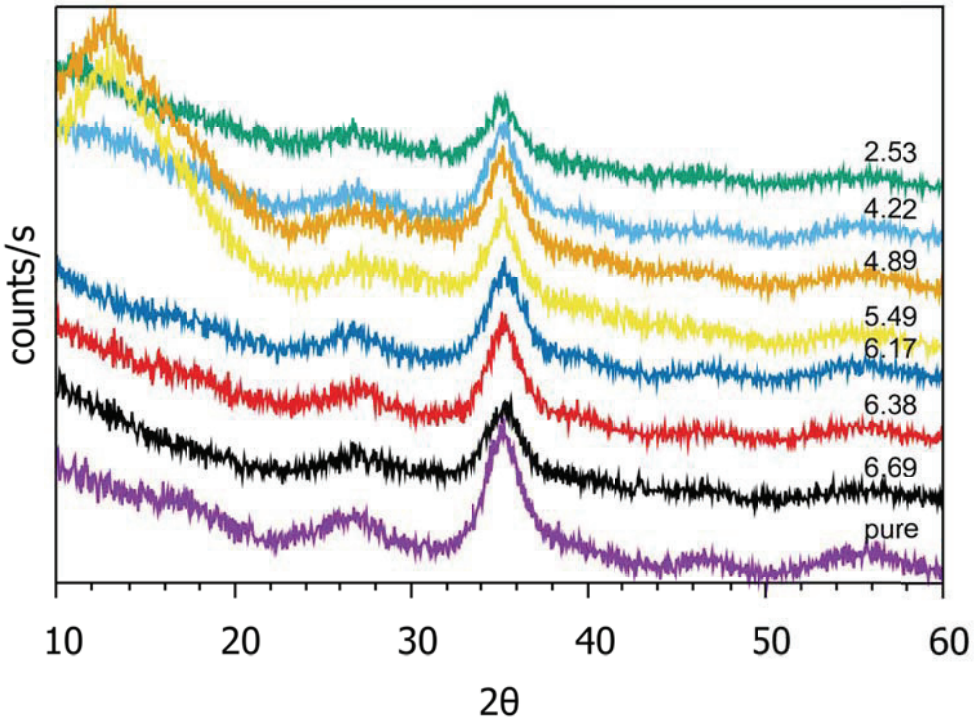

Fig. S1. XRD pattern of pure schwertmannite prior to and after the sorption experiments at 20 mmol/L SO_4 and different pH values. Notice that no goethite peaks are observed.

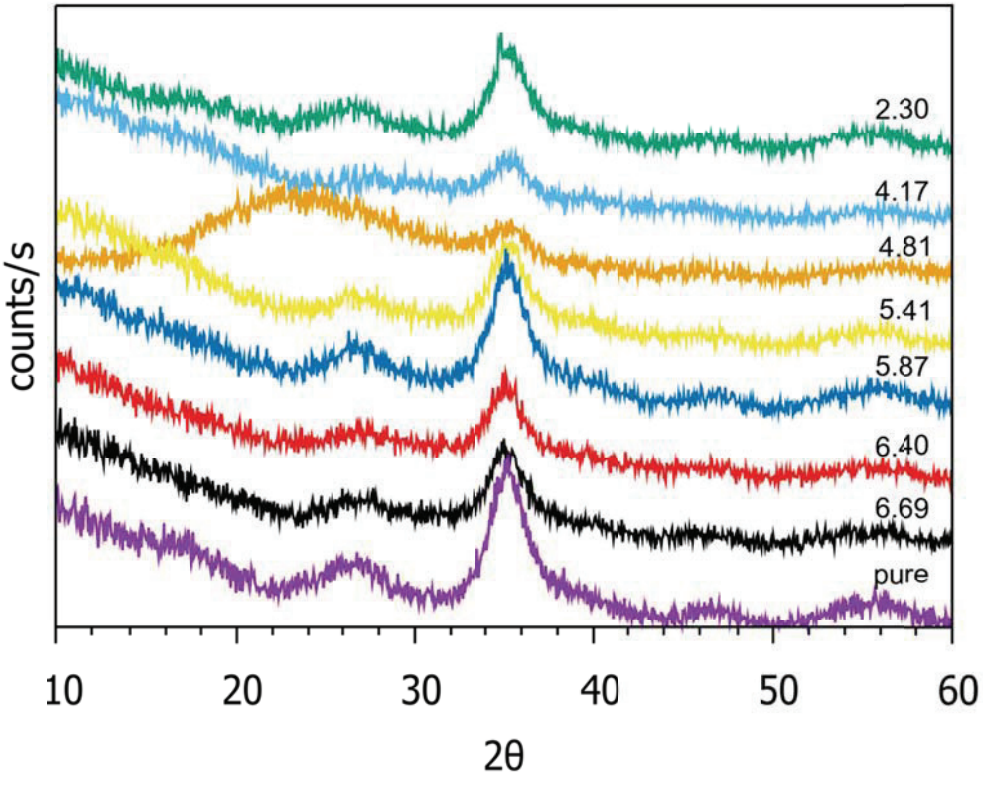

Fig. S2. XRD pattern of pure schwertmannite prior to and after the sorption experiments at 2 mmol/L SO_4 and different final pH values. Notice that no goethite peaks are observed.

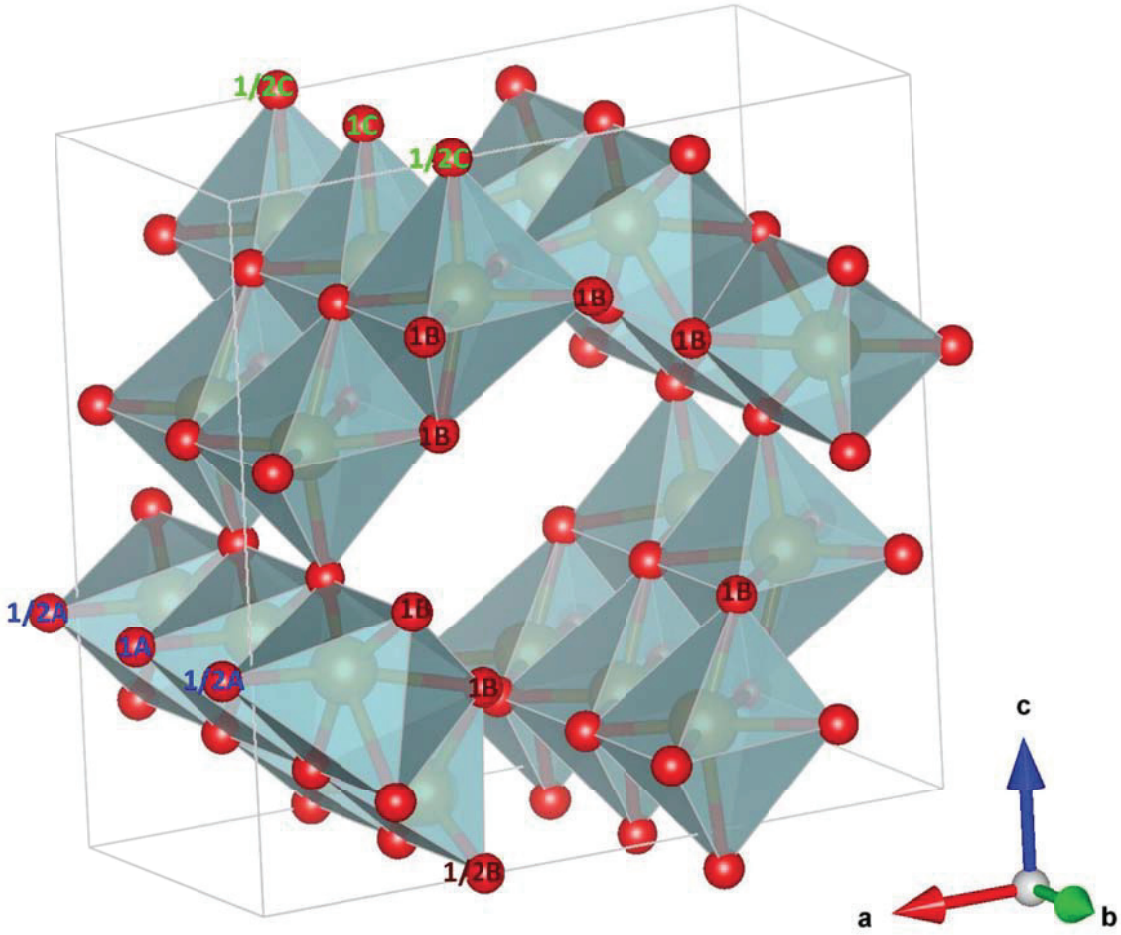

Fig. S3. Surface site distribution in schwertmannite. Atoms labeled “A” form the face (1 0 0), “B” form (0 1 0) and “C” form (0 0 1). Data from Fernandez-Martinez et al. (2010).

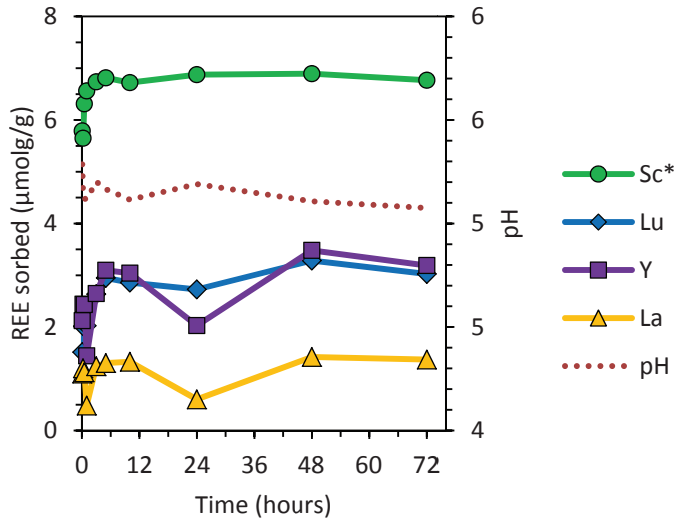

Fig. S4. Evolution of REE sorbed on schwertmannite (µmol/g) over time at pH 5.5 ±0.2 for selected REEs. (Sc: circles, Lu: diamonds, Y: squares, La: triangles, and dotted line: pH value; Sc*=Sc/2).

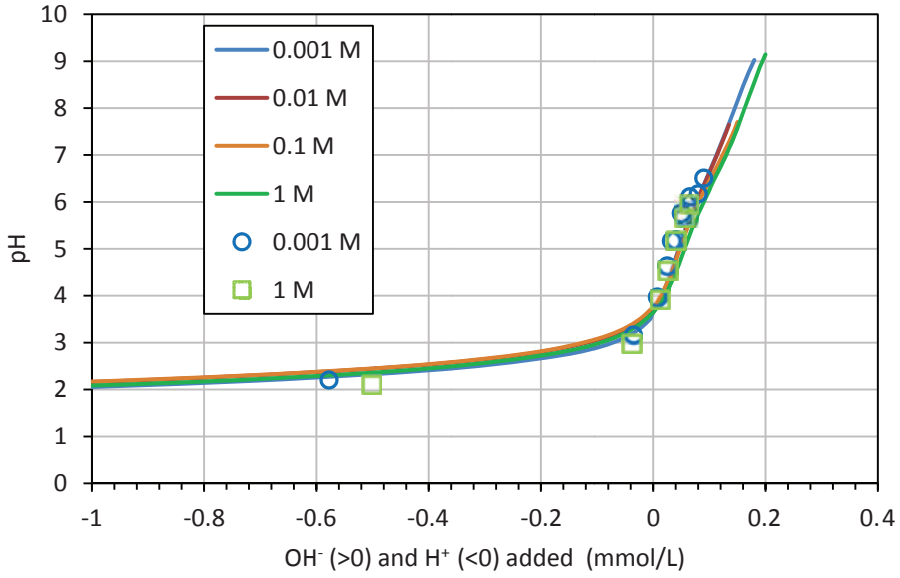

Fig. S5. Titration of schwertmannite suspensions (1 g/L) under different $NaNO_3$ concentrations. Symbols: Suspensions with different NH_4OH and HCl addition and kept under stirring for 24 hours. Solid lines: titrations conducted using a 848 Titrino plus titrator with addition of NH_4OH 0.1 mol/L (OH>0) and HCl 0.1 mol/L (OH<0). After each titrant addition, the electrode reading was set between 60 to 120 seconds, and the drift was lower than 50 mV/min. All the experiments were made at 25°C and atmospheric CO_2 pressure.

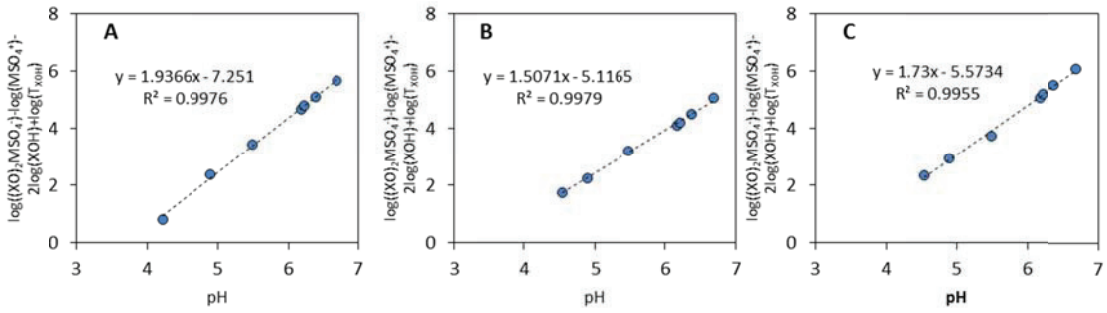

Fig. S6 Regressions obtained from measured pH values and calculated activities from the final concentrations of the experimental data set of 20 mmol/L SO_4. (A, B, C) Regressions for Y, La and Lu, respectively, plotted as Eq. (S5).

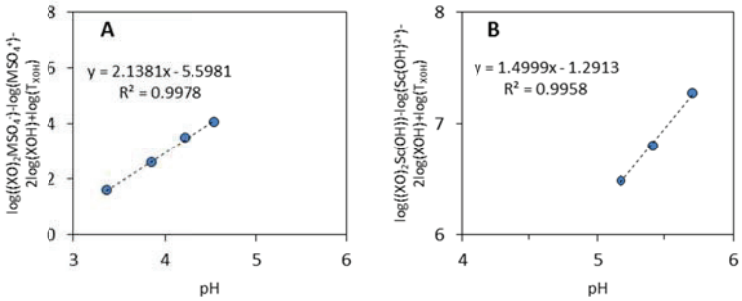

Fig. S7 Regressions obtained from experimental data of Sc plotted according to Eq. (S5) for $ScSO_4^+$ (A) and $ScOH^{2+}$ (B) species.

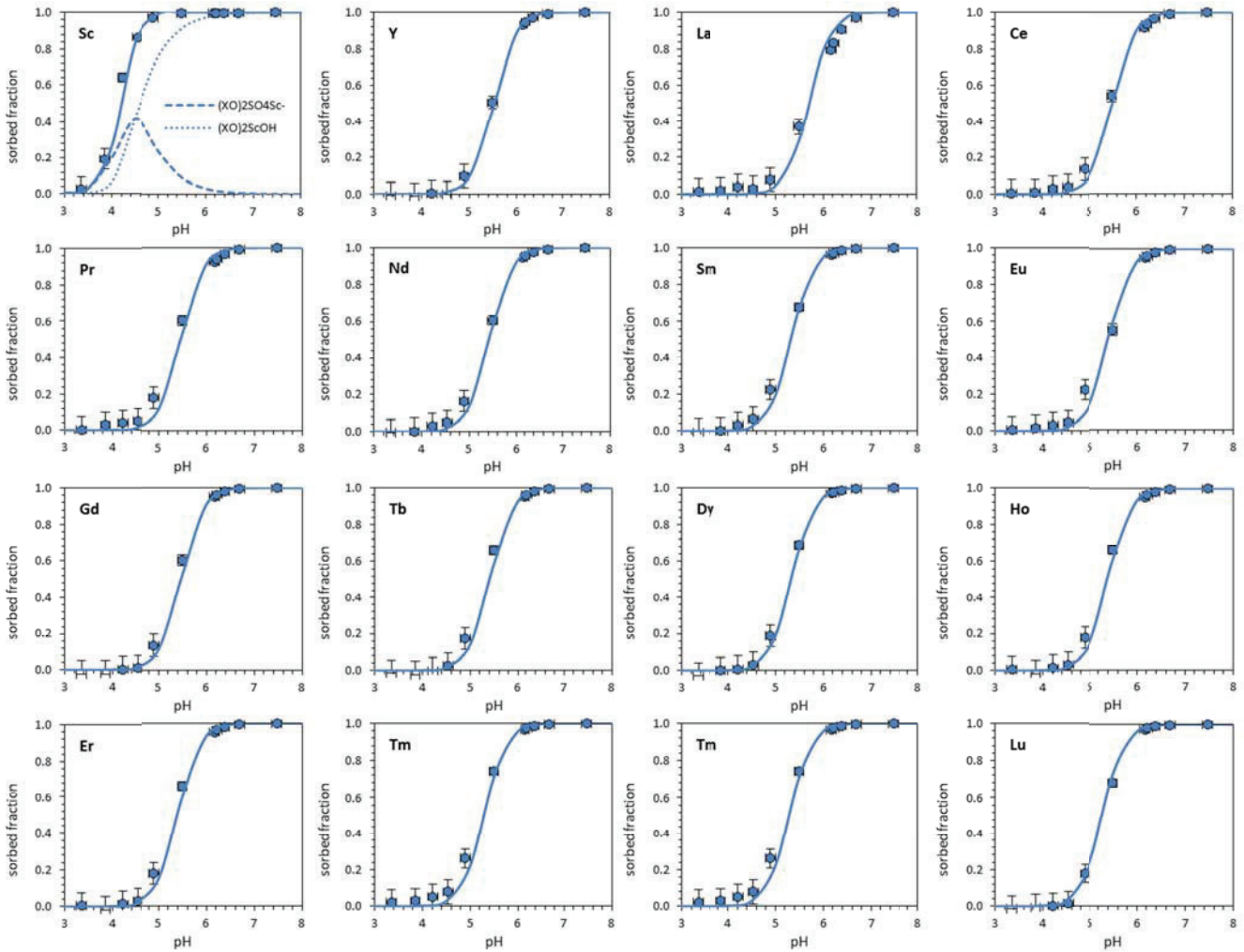

Fig. S8. Sorbed fractions measured (symbols) and calculated (lines) for 20 mmol/L SO_4 and a 1 g/L solid:liquid ratio. Calculations performed at 25°C and pCO_2 of 3.5.

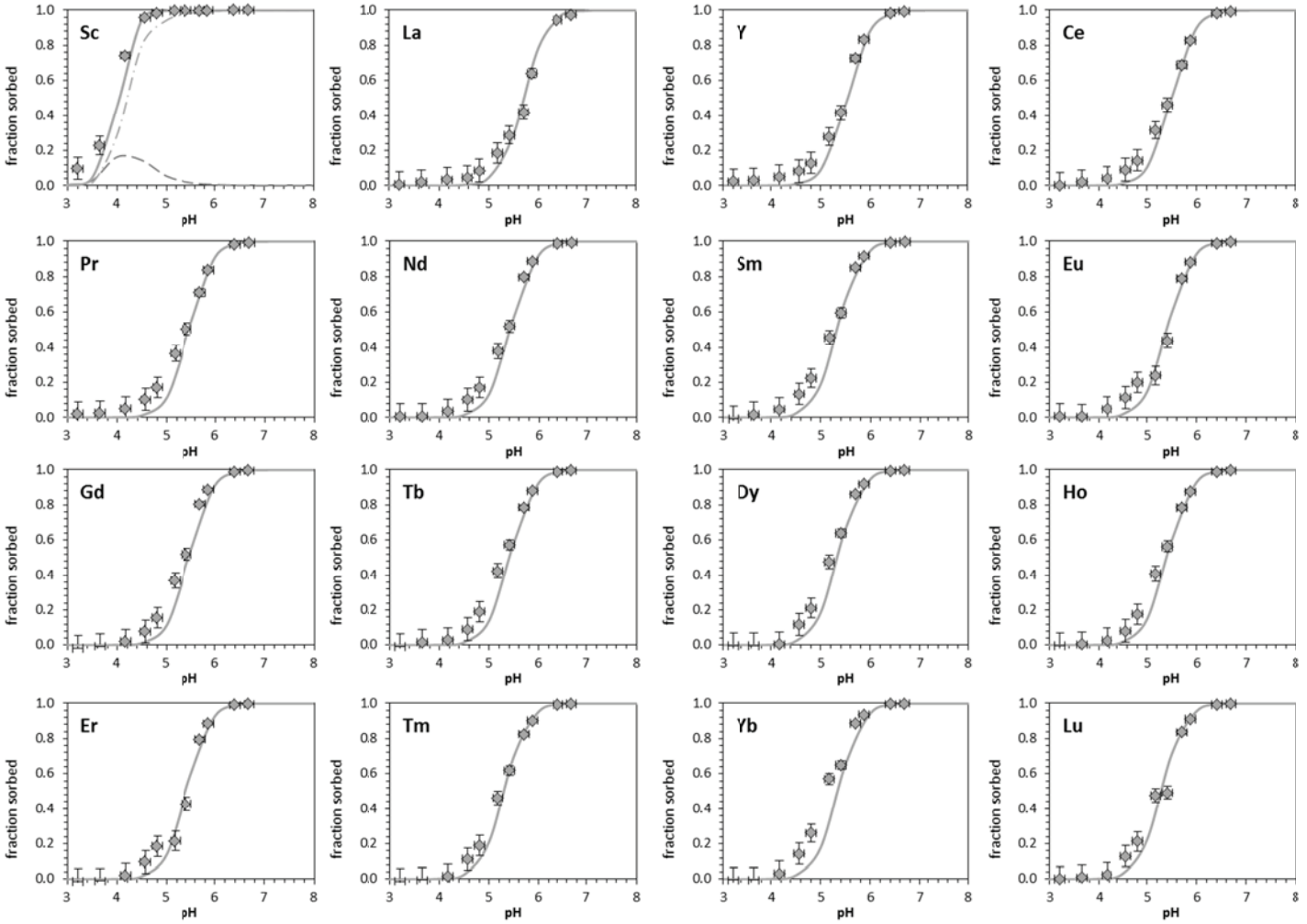

Fig. S9. Sorbed fractions measured (symbols) and calculated (lines) for 2 mmol/L SO_4 and a 1 g/L solid:liquid ratio. Calculations performed at 25°C and pCO_2 of 3.5.

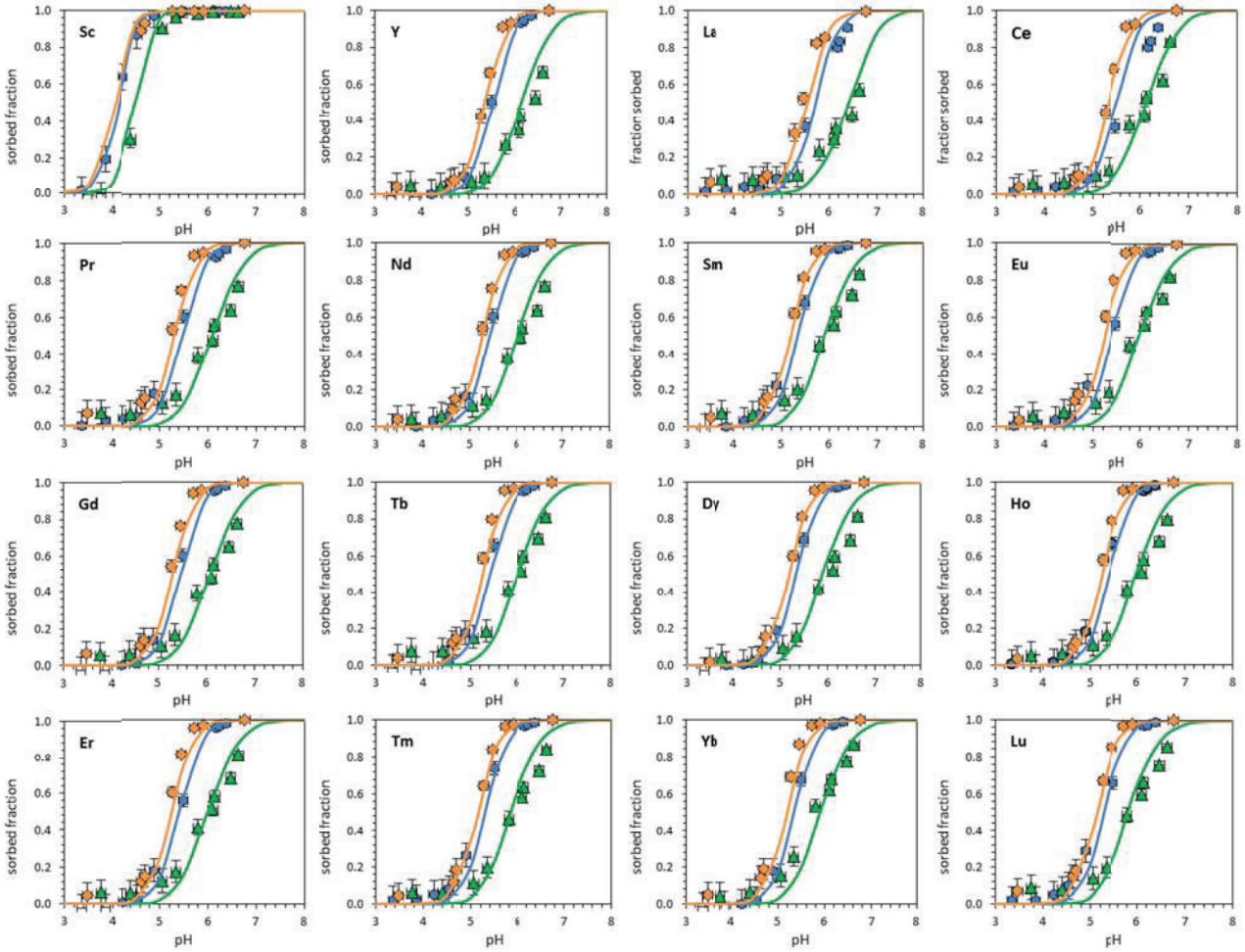

Fig. S10. Sorbed fractions measured (symbols) and calculated (lines) for 20 mmol/L SO_4 and three different solid:liquid ratios: 2 g/L (orange diamonds), 1 g/L (blue circles) and 0.25 g/L (green triangles). Calculations performed at 25°C and pCO_2 of 3.5.

Article 4

Solid and aqueous speciation of yttrium in passive remediation systems of acid mine drainage

Published in: *Environmental Science and Technology* 2019, 53, 11153-11161.

Environmental Science & Technology

Article

Cite This: Environ. Sci. Technol. 2019, 53, 11153−11161

pubs.acs.org/est

Solid and Aqueous Speciation of Yttrium in Passive Remediation Systems of Acid Mine Drainage

Alba Lozano,*[,†,‡] Alejandro Fernández-Martínez,[§] Carlos Ayora,[†] Devis Di Tommaso,[∥] Agnieszka Poulain,[⊥] Mauro Rovezzi,[#] and Carlo Marini[▽]

[†]Institute of Environmental Assessment and Water Research, (IDAEA-CSIC), Jordi Girona 18-26, 08034 Barcelona, Spain

[‡]Grup de Mineralogia Aplicada i Geoquímica de Fluids, Departament de Cristal-lografia, Mineralogia i Dipòsits Minerals, Facultat de Geologia, Universitat de Barcelona (UB), C/Martí Franquès, S/N, 08028 Barcelona, Spain

[§]Univ. Grenoble Alpes, Univ. Savoie Mont Blanc, CNRS, IRD, IFSTTAR, ISTerre, 38000 Grenoble, France

[∥]Thomas Young Centre, Materials Research Institute, Department of Chemistry, Queen Mary University of London, Mile End Road, E1 4NS London, U.K.

[⊥]ESRF, The European Synchrotron, 71 Avenue des Martyrs, 38000 Grenoble, France

[#]Univ Grenoble Alpes, CNRS, IRD, Irstea, Météo France, OSUG, FAME, 38000 Grenoble, France

[▽]CELLS-ALBA Synchrotron Radiation Facility, Carrer de la Llum 2-26, Cerdanyola del Valles, 08290 Barcelona, Spain

Supporting Information

ABSTRACT: Yttrium belongs to the rare earth elements (REEs) together with lanthanides and scandium. REEs are commonly used in modern technologies, and their limited supply has made it necessary to look for new alternative resources. Acid mine drainage (AMD) is a potential resource since it is moderately enriched in REEs. In fact, in passive remediation systems, which are implemented to minimize the environmental impacts of AMD, REEs are mainly retained in basaluminite, an aluminum hydroxysulfate precipitate. In this study, the solid and liquid speciation and the local structure of yttrium are studied in high-sulfate aqueous solutions, basaluminite standards, and samples from remediation columns using synchrotron-based techniques and molecular modeling. Pair distribution function (PDF) analyses and ab initio molecular dynamics density functional theory models of the yttrium sulfate solution show that the YSO_4^+ ion pair forms a monodentate inner-sphere complex. Extended X-ray absorption fine structure (EXAFS) and PDF analyses show that Y is retained by basaluminite, forming a monodentate inner-sphere surface complex on the aluminum hydroxide surface. EXAFS of the column samples shows that more than 72% of their signal is represented by the signal of basaluminite with which YSO_4^+ forms an inner-sphere complex. The atomic view of the REE configuration in AMD environments could facilitate a deeper research of REE recovery from waste generated in AMD remediation systems.

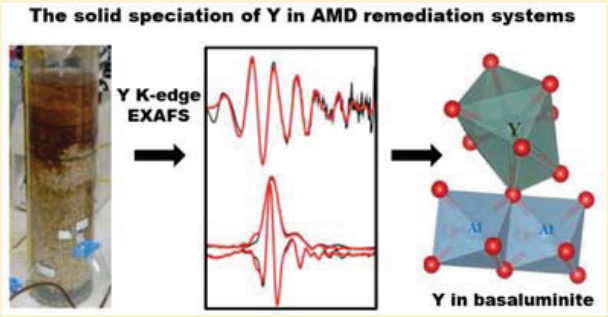

INTRODUCTION

Yttrium belongs to the rare earth element (REE) group, also composed of lanthanides and scandium. REEs are necessary for the development of modern technologies, and specifically, yttrium has important applications, for instance, in fluorescent lamps as phosphors,[1] and in the aircraft industry, used in the thermal barrier coatings for jet engines.[2] The increasing demand for REEs and their low worldwide supply have led to considering REEs as critical raw materials, boosting searches for alternative resources, such as recycling used stocks or identifying new geological sources of these elements. Because the REE concentrations in acid mine drainage (AMD) are from one to two orders of magnitude higher than the average concentrations in natural waters,[3] it may be possible to perform secondary REE recovery from precipitates from AMD neutralization in passive remediation systems. These active systems were developed to minimize the environmental impacts of AMD and they are used worldwide.[4,5] However, due to the high water content, sludge storage has substantial operational costs and environmental concerns.[6,7] In contrast, passive remediation systems, which have been developed extensively in recent decades,[8−11] allow the AMD neutralization generating lower amounts of solid waste precipitates. Ayora et al. documented nearly complete aqueous REE retention in two laboratory columns, simulating a disperse

Received: March 25, 2019
Revised: August 18, 2019
Accepted: August 22, 2019
Published: August 22, 2019

DOI: 10.1021/acs.est.9b01795
Environ. Sci. Technol. 2019, 53, 11153−11161

alkaline substrate (DAS), a passive treatment already implemented in the field, for two highly acidic AMDs (SW Spain).[12,13] The REEs were scavenged by basaluminite, a mineral precipitated in the columns, which also presented Y enrichment due to the higher yttrium concentration with respect to the rest of REEs in the two treated AMDs. Basaluminite, an aluminum oxyhydroxysulfate ($Al_4(SO_4)(OH)_{10}\cdot 5H_2O$), precipitates in acidic environments as a consequence of the natural attenuation of the AMD when mixed with more alkaline waters, or due to the induced neutralization of the acid waters, when the solution pH reaches ~4.[14] Basaluminite is considered a nanomineral, with a short-range order, around 1 nm of coherent domain size, which is described as layers of Al-octahedra with structural point defects and with sulfate groups as outer-sphere complexes between the Al layers.[15]

Similarly to the REE uptake by basaluminite in DAS treatments, Gammons et al. reported the precipitation of hydrous aluminum oxides accompanied by a decrease in REE concentration from AMD when mixed with natural water.[16] Recently, the scavenging of REEs by basaluminite precipitates has been described as a sorption mechanism.[17] AMD is characterized to contain high loads of dissolved sulfate and the affinity of REEs to form aqueous species with sulfate is very high, the MSO_4^+ aqueous complex being more abundant in AMD solutions.[18] Sorption of dissolved REEs from sulfate-rich waters onto basaluminite is thus described as the sorption of the MSO_4^+ aqueous complex via ligand exchange with a surface site of basaluminite, forming a monodentate surface complex with the Al-octahedron as one proton is released.[17] Here, a structural description of the aqueous YSO_4^+ complex and of the local environment of the surface complex formed upon adsorption onto basaluminite are reported.

Most of the previous studies reporting the adsorption mechanisms of REEs using X-ray absorption spectroscopy and extended X-ray absorption fine structure (EXAFS) described the adsorption of free REE ions onto the surface of metal oxides.[19−22] However, the AMD environments show a high concentration of dissolved sulfate, which presents high affinity for aqueous REEs (M). Thus, the MSO_4^+ aqueous complex is the major REE species in solution, and hence, the sorption models of REEs in AMD precipitates might be better explained in terms of MSO_4^+ sorption.

The structure of the first hydration shell of lanthanides and yttrium has been well characterized.[23−28] The coordination number (CN) of the first hydration shell changes from an average of CN ~ 9 oxygen atoms for light REEs (LREEs La to Pm) to CN ~ 8 oxygen atoms for heavy REEs (HREEs Tb to Lu), with intermediate values for medium REEs (MREEs Pm to Gd).[27] This behavior is explained by the continuous decrease in ionic radii with the atomic number.[27,29,30] The ionic radius of yttrium is between those of Ho and Dy, so it is typically considered an HREE with a first hydration shell of CN ~ 8 oxygen atoms. There are several studies describing aqueous complexes of REEs with different ligands. REEs easily form inner-sphere complexes with carbonate and phosphate in solution,[31−33] whereas chloride and nitrate form inner-sphere complexes at concentrations higher than 10 M.[23,25] In the case of sulfate, no information about the geometry of MSO_4^+ complexes has been reported so far despite their strong binding affinity.[18]

The objective of this study is to elucidate the structure of Y adsorbed onto basaluminite. Its chemical similarities with HREEs allow us to assume similar structural configuration for this subgroup. Moreover, this element was one of the most concentrated in waste samples allowing performing X-ray absorption spectroscopy experiments. Since the YSO_4^+ aqueous complex is adsorbed onto the mineral,[17] a previous characterization of the geometry of the aqueous complex has been carried out. Finally, a quantification of Y-species in basaluminite solids precipitated from AMD treatments has been performed. Structural studies were performed using EXAFS and pair distribution function (PDF) analyses of aqueous and solid samples combined with ab initio molecular dynamics (AIMD) simulations of the aqueous YSO_4^+ complexes.

Two hypotheses are used to investigate the local structure of the aqueous YSO_4^+ ion pair: (1) an outer-sphere complex, with water located between Y^{3+} and SO_4^{2-}, and (2) an inner-sphere complex. In the latter case, two more hypotheses must be considered: (a) a monodentate complex, with one oxygen atom shared between the sulfate and the first coordination sphere of Y^{3+}, and (b) a bidentate complex, with two oxygen atoms shared between the yttrium hydration sphere and the sulfate group.

Once the structure of the aqueous solution is fully described, different hypotheses have been considered to interpret the YSO_4^+ surface complexation onto the Al-oxyhydroxysulfate: the formation of (1) a monodentate inner-sphere complex, (2) a bidentate mononuclear inner-sphere complex, and (3) a bidentate binuclear inner-sphere complex.

Finally, to determine semiquantitatively the yttrium species in solids from column samples, linear combination fits were performed using the most representative references.

MATERIALS AND METHODS

Synthetic Samples (Standards). Different basaluminites doped with Y were prepared for high-energy X-ray scattering (HEXS) and EXAFS experiments. To ensure maximum Y incorporation into the solid, sorption and coprecipitation experiments were performed at pH 6,[17] avoiding higher pH values where YCO_3^+ aqueous species could be present.[34] A basaluminite sample with sorbed YSO_4^+ (B-YSO_4-ads) was obtained from a suspension of 1 g/L of solid in 0.11 $Y(NO_3)_3\cdot 6H_2O$ and 0.25 M Na_2SO_4 solution in 5 h at a constant pH of 6. Under these conditions, the major species in solution was YSO_4^+, which is supposedly the aqueous Y species sorbed on the solid surface.[17] A basaluminite sample coprecipitated with Y (B-Ycop) was obtained using the basaluminite synthesis method adding 1 M $Y(NO_3)_3\cdot 6H_2O$ in the acid solution of 0.05 M $Al_2(SO_4)_3\cdot 18H_2O$ (see Chapter S1 of the SI). Basaluminite and nanoboehmite samples with sorbed Y^{3+} (B-Yads and A-Yads, respectively) were also prepared from a suspension of 1 g/L of solid in 0.011−0.11 M $Y(NO_3)_3\cdot 6H_2O$ solution in 5 h, and the pH was maintained at ~6 at room temperature (the synthesis protocol is described in detail in Chapter S1 of the SI). Under these conditions, the major species of Y was Y^{3+}. In all cases, the suspensions were centrifuged at 4500 rpm for 15 min; the supernatant was filtered through 0.2 μm membranes and kept for inductively coupled plasma (ICP) analysis. The solids were rinsed several times with deionized water and oven-dried for 48 h at a maximum temperature of 40 °C.

High-energy X-ray scattering (HEXS) and EXAFS experiments of aqueous solutions with Y and YSO_4^+ were carried out. For the HEXS measurements, an aqueous solution of free

DOI: 10.1021/acs.est.9b01795
Environ. Sci. Technol. 2019, 53, 11153−11161

yttrium ions (Y-sol) was prepared with 0.1 M $Y(NO_3)_3{\cdot}6H_2O$ at pH 3.2, and a solution containing YSO_4^+ as the major aqueous complex (YSO_4-sol) was prepared by mixing equal amounts of 0.2 M $Y(NO_3)_3{\cdot}6H_2O$ and 0.2 M Na_2SO_4 at pH 3. For the EXAFS measurements, a solution with the free Y^{3+} ion (Y-sol) with a composition of 0.01 M $YCl_3{\cdot}6H_2O$ at pH 4.6 and a solution of the YSO_4^+ complex (YSO_4-sol) with a composition of 0.01 M $YCl_3{\cdot}6H_2O$ and 0.01 M Na_2SO_4 at pH 2.9 were prepared, respectively. Under these conditions, the major species in solution were Y^{3+} and YSO_4^+ (Figure S1). The yttrium concentrations of the references are listed in Table S1, and a more comprehensive description of the syntheses is given in the Supporting Information S1.

Waste Samples from Column Treatments. Column samples were collected from two laboratory column experiments of disperse alkaline substrate (DAS), as described in Ayora et al.,[12] simulating the remediation systems of the two AMDs from the Iberian Pyrite Belt region (SW Spain). The columns (9.6 cm in inner diameter and 39 cm in height) consisted of a permeable mixture of grained limestone and wood shavings at a 1:1 weight ratio. Samples W-MR-C1-4 and W-MR-C1-5 belonged to columns which treated AMD from Monte Romero mine, and the W-Alm-C3-8 and W-Alm-C3-9 samples belonged to columns which treated leaching of Almagrera mine tailing dam. Y concentration in different AMDs at the inlet ranged from 9 to 42 ppm, and sulfate concentrations were 3.5 and 11.7 mg/L. Physical-chemical parameters and water samples were collected every 2 weeks. Once the treatment was completed after 18 weeks, the solid was divided into 2 cm thick slices and dried. The partitioning of Al, Fe, and REEs was studied by performing a sequential extraction adapted from Torres and Auleda to the solid residues.[35] The results shown in Ayora et al. concluded that REEs were retained in basaluminite.[10] The W-MR-C1-4, W-MR-C1-5, W-Alm-C3-8, and W-Alm-C3-9 samples were selected from the depth where maximum Al concentration was extracted from the solids, assuming the solid slice that was the most enriched in basaluminite. These waste samples were used for EXAFS measurements, and the Y concentrations for these samples are shown in Table S2.

Analytical Techniques. Measurements of the pH values of the initial and final solutions were made with a Crison glass electrode calibrated with buffer solutions of pH 2, 4, and 7. The Al and S concentrations were measured by inductively coupled plasma optical emission spectroscopy (ICP-OES), and the Y concentration was measured by inductively coupled plasma mass spectrometry (ICP-MS). The aqueous speciation and saturation index of the solid phases were calculated with the PHREEQC code[36] using the Donnee Thermoddem_V1.10 database[37] provided by the Bureau de Recherches Géologiques et Minières (BRGM). Details of the analytical procedures and the database for the REE speciation are described in the Supporting Information S2.

The HEXS measurements were performed at the ID31 beamline at the European Synchrotron Radiation Facility (ESRF). The samples were loaded into 1.5 or 2 mm Kapton capillaries, and the HEXS patterns were obtained using a Pilatus3 X CdTe 2M detector. The data correction and generation of structure factors and pair distribution functions were performed with the PDFgetX3 software.[38] PDFs for aqueous solutions were obtained by subtracting the scattering signal of pure water from the total scattering signal of the YSO_4-sol sample and the Y-sol sample, respectively. The differential pair distribution functions (d-PDFs) for the B-Ycop sample were obtained by subtracting the PDF signal of a pure synthetic basaluminite from the PDF of the B-Ycop sample.

The EXAFS measurements of samples B-Y-ads, B-Y-cop, A-Y-ads, Y-sol, and YSO_4-sol were performed at the Y K-edge (17.038 keV) at the FAME beamline,[39] BM30B, at the ESRF. The EXAFS measurements of the B-YSO_4-ads sample was performed at the Y K-edge (17.038 keV) at the CLÆSS beamline (ALBA synchrotron). Atomistic models of YSO_4^+ and Y^{3+} complexes adsorbed on a basaluminite surface with different initial configurations were employed in the data analysis to extract the Y local order parameters, including the neighbor distances, R, coordination number, N, and Debye–Waller factors, σ^2. The proportion of Y species present in each waste sample from column treatments was obtained by linear combination fitting (LCF) of the EXAFS spectra using the most representative reference compounds as the basis set. The experimental setup and the details of the data analysis are given in the Supporting Information S3.

The ab initio molecular dynamics (AIMD) simulations of an aqueous solution of yttrium(III) sulfate were carried out on a Y^{3+}–SO_4^{2-}–OH^- system embedded in a box of 61 water molecules. The simulations were conducted with the electronic structure code, CP2K/Quickstep code, version 5.1.[40] CP2K implements density functional theory (DFT) based on a hybrid Gaussian plane wave. The revPBE generalized gradient approximations for the exchange and correlation terms were used together with the general dispersion correction termed DFT-D3.[41,42] The simulations were carried out for 15 ps in the canonical (constant NVT) ensemble to maintain the average temperature at T = 300 K. An in-house Python code using DiffPy-CMI was developed to convert the AIMD trajectories to PDF signals.[43] Details of the MD simulations are described in Supporting Information S4.

RESULTS AND DISCUSSION

Geometry of the Aqueous YSO_4^+ Complex. The experimental (YSO_4-sol, Y-sol) and theoretical (YSO_4-calc) PDFs of the Y-containing aqueous solutions, 0.1 M YNO_3 and YSO_4, are shown in Figure 1. Background subtraction of the aqueous samples was performed using a deionized water background, which implies that the experimental PDFs shown here are differential PDFs (water-subtracted). The background scale factor was adjusted to minimize the O–O correlation (~2.8 Å) in the PDFs. All spectra show an intense peak at 2.37 Å, which corresponds to the Y–O interatomic distances to oxygen in the first coordination shell. The experimental PDF of the YSO_4-sol sample shows a small and sharp peak at 1.45 Å, which corresponds unequivocally to the S–O interatomic distance in sulfate, and another smaller peak at ~3.6 Å, which is absent in the Y-sol sample. The DFT-based PDFs obtained from AIMD simulations of the YSO_4^+ aqueous complex also reproduced this latter peak. Analyses of the AIMD trajectories show that the 3.6 Å distance between Y and S is consistent with the formation of a monodentate inner-sphere complex (one shared oxygen) between the coordination shells of the sulfur and yttrium.

Fits of the EXAFS spectra of the aqueous solutions were performed using atomistic models from the AIMD simulations as initial structural models for the generation of the scattering paths. The results yielded an average Y–O distance of 2.37 ± 0.02 Å for the Y-sol sample and 2.38 ± 0.01 Å for YSO_4-sol (Table 1). The intense peak in the FT function at 2.38 Å for

DOI: 10.1021/acs.est.9b01795
Environ. Sci. Technol. 2019, 53, 11153–11161

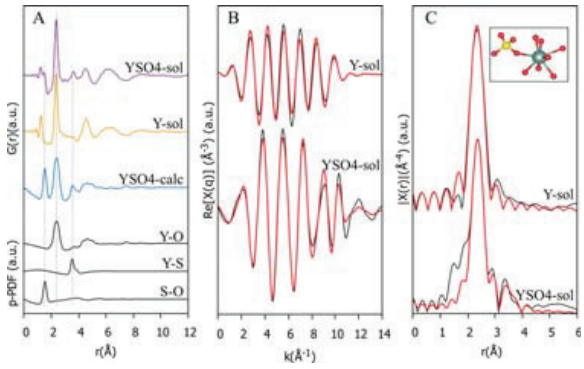

Figure 1. (A) Top: Experimental PDFs of the YSO_4-sol and Y-sol samples. Bottom: Simulated (AIMD) PDF (YSO_4-calc) and partial PDFs of a YSO_4^+ aqueous complex. (B) Fourier-filtered signal from 1.8 to 4.2 Å for the EXAFS data. (C) EXAFS Fourier transform (FT) amplitude functions of the YSO_4-sol sample. Black lines: experimental; red lines: fits. Simulated (AIMD) PDF and partial PDFs have been multiplied for visualization purposes: YSO_4-calc (3×), Y−S (5×), and Y−O and S−O (2×). Dashed lines indicate the position of the Y−O, Y−S, and S−O bonds in the YSO_4-sol sample.

the two aqueous references represents the first solvation shell, and its asymmetry reveals a distribution of Y−O interatomic distances, as reported previously by Lindqvist-Reis et al.[24] The coordination numbers (CN) were 7.6 ± 1.9 and 7.9 ± 0.9 for Y-sol and YSO_4-sol, respectively, which are close to the expected value of 8 for HREEs. A second shell is visible in the FT of the YSO_4-sol sample. It was fitted with a Y−S distance of 3.50 ± 0.04 Å, similar to that observed in the PDF of the same sample, and a CN = 1. This corresponds to a monodentate coordination, matching the geometry obtained from the AIMD simulations. The coordination number CN = 1 was kept fixed in the EXAFS fitting to increase the stability of the fitting procedure, minimizing the number of parameters and excessive correlations between them. A multiple scattering path (Y−S−O) was included and was found to be relevant and to improve the fit. The fitting parameters matched both the PDF and modeling results and indicated that the YSO_4^+ aqueous species forms a monodentate inner-sphere complex.

The determined Y−O first shell coordination numbers and interatomic distances are consistent with those in previous reports describing yttrium coordination shells with N = 8 and Y−O distances of 2.36 Å.[23,24,28] Similar to aqueous REE carbonate and phosphate complexes,[31−33] aqueous Y−SO_4 ion pairs form inner-sphere complexes. This result contrasts with other ligands, such as chloride, which hardly form inner-sphere complexes at similar concentrations to those used in this study.[23] Only the formation of monodentate complexation between Dy and NO_3 with a distance of 3.57 Å has been reported using MD simulations.[26]

Local Order of Yttrium Adsorbed onto Basaluminite.

HEXS measurements were performed on a pure basaluminite sample (B-pure) and on a sample of basaluminite coprecipitated with Y (B-Ycop). The PDFs are shown in Figure 2 with

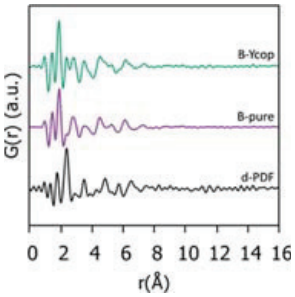

Figure 2. PDFs of basaluminite coprecipitated in the presence of Y (B-Ycop) and pure basaluminite (B-pure) and differential PDF (d-PDF). The d-PDF spectrum has been amplified (3×) for visualization purposes.

the differential PDF obtained by subtracting the PDF of the pure sample from that of the coprecipitated one. This approach has been previously used to examine the local order of different anions incorporated into poorly crystalline minerals, such as schwertmannite and basaluminite, and the desorption of sulfate from basaluminite when ageing at circumneutral pH values.[15,46] The PDFs of the two samples are similar and show characteristic basaluminite peaks that correspond to the known interatomic distances (S−O bond at ∼1.46 Å; Al−O bonds at 1.88, 4, 4.8, and 6 Å; and Al−Al bonds at 3 Å).[15,45] The differential PDF shows a main peak at 2.37 Å, which corresponds to the Y−O distance. This peak matches the distance from Y to the first solvation shell obtained from the EXAFS and PDF of the Y^{3+} and YSO_4^+ aqueous solutions (Figure 1). Another peak is present at 1.7 Å, which is tentatively assigned to a new Al−O distance of the Al-octahedra, due to probable distortions of the basaluminite. The existence of deformations in the structures of mineral nanoparticles upon oxyanion adsorption has been previously observed.[44,46] A smaller peak appears at 3.48 Å, which can be assigned to a Y−S distance, though it is shorter than the Y−S distance reported for the YSO_4^+ aqueous complex (Table 1 and Figure 1A). This peak may also correspond to a Y−Al interatomic distance, which would be consistent with the formation of an inner-sphere ligand, as suggested by Lozano et al.[17] This hypothesis will be tested using different atomistic models for the fitting of the EXAFS data. Other peaks at longer distances are difficult to assign in the absence of a more detailed structural model.

The k^3-weighted EXAFS spectra for the solid references, B-YSO_4-ads, B-Y-ads, B-Y-cop, and A-Y-ads (Figure 3), are indistinguishable and differ from the aqueous Y-sol and YSO_4-

Table 1. Modeling Parameters of the Y K-Edge EXAFS Spectra of the 0.1 M YSO_4 Aqueous Solution[a]

sample	neighbor	path	N	σ^2	ΔE_0	R (Å)	Var.	χ_ν^2
Y sol	1st shell	Y−O	7(2)	0.005(3)	−2(3)	2.37(2)	4	354
Y−SO_4 sol	1st shell	Y−O_1	7.9(9)	0.007(2)	−1(1)	2.38(1)	8	498
	2nd shell	Y−S	1_{fixed}	0.003(6)		3.50(4)		
	3rd shell	Y−S−O	1_{fixed}	0.015(19)		3.18(10)		

[a]The error is expressed in parentheses after the last digit.

DOI: 10.1021/acs.est.9b01795
Environ. Sci. Technol. 2019, 53, 11153−11161

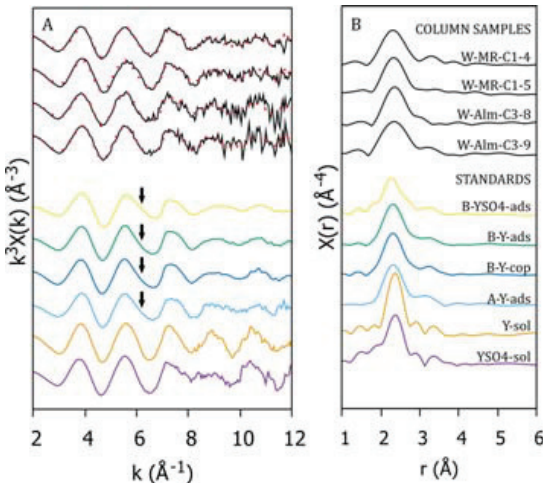

Figure 3. k^3-Weighted EXAFS (A) and FT amplitude functions (B) for four waste samples from column treatments, W-MR-C1-3, W-MR-C1-4, W-Alm-C3-8, and W-Alm-C3-9 (upper part); solid standards (basaluminite sorbed with YSO_4 (B-YSO_4), basaluminite sorbed and coprecipitated with Y: B-Yads and B-Ycop, respectively); and aqueous solution (free ion and sulfate complex: Y-sol and YSO_4-sol, respectively) (bottom part). The dashed lines in the EXAFS signals of the column samples represent LCF with B-Yads (basaluminite with sorbed yttrium) and YSO_4-sol (solution of Y with SO_4) standards as the most representative references (results in Table 3). The arrows indicate a frequency present in the solid standards.

sol spectra in that a slight oscillation becomes visible at 5−6 $Å^{-1}$. In B-YSO_4-ads, the dominant Y species in solution is the YSO_4^+ complex. However, in B-Y-ads, B-Ycop, and A-Yads, the dominant Y species is Y^{3+}. Still, these four samples show similar spectra. Since the common feature in these three samples is the presence of an Al adsorbent, and this feature agrees with that in the B-YSO_4-ads EXAFS spectrum, we hypothesize that the higher frequency observed at 5−6 $Å^{-1}$ (arrow in Figure 3) may be related to the presence of an Al backscatterer, rather than to a signal from a close sulfate group. Both Al and S are light atoms with similar atomic numbers (Z = 13 and 16, respectively), which makes their backscattering functions difficult to distinguish via fitting of the EXAFS signal. These observations lead us to assume that the EXAFS measurements have poor sensitivity to the presence of Y−S bonds in this system. However, a contribution from a sulfate shell for the first two samples cannot be ruled out.

Based on the previous information of the aqueous species and on the thermodynamic model of REE sorption,[17] the B-YSO_4-ads EXAFS signal was fitted with three models of different geometries of the YSO_4^+ aqueous complex adsorbed onto basaluminite surfaces via inner-sphere complexes (Figure 4), to obtain an atomistic model representation: (A) a monodentate surface complex, (B) a bidentate mononuclear surface complex, and (C) a bidentate binuclear surface complex.

The EXAFS fits for B-YSO_4-ads for the different models and the calculated parameters are given in Figure 5 and Table 2,

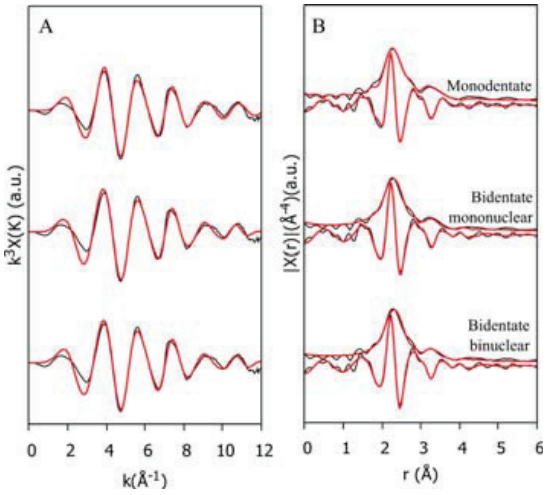

Figure 5. (A) k^3-Weighted EXAFS spectra at the Y K-edge of the basaluminite with YSO_4 sorbed (B-YSO_4-ads reference) and (B) its Fourier transform amplitude. The experimental and fitted curves are shown in black and red, respectively.

respectively. The first model represents a monodentate inner-sphere surface complex. The coordination number of the shells has been fixed based on information from other sources: the major aqueous species in solution is YSO_4^+, which, as supported by PDF and DFT data, forms a monodentate

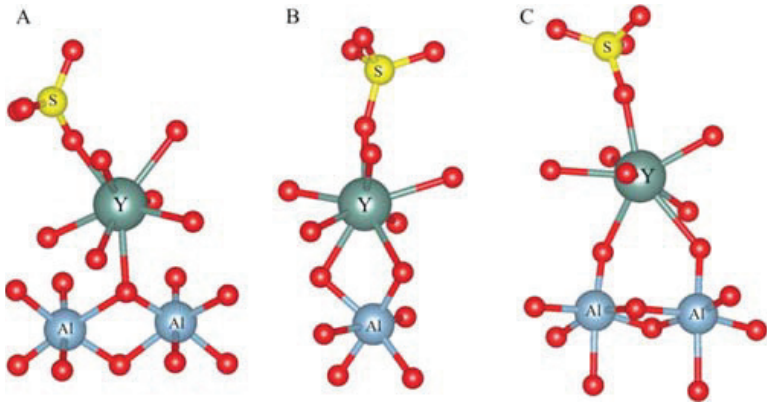

Figure 4. Atomistic representations of the three models of YSO_4 aqueous complexes adsorbed on the basaluminite−water interface. The different atomic positions of YSO_4 to octahedral-Al are used to fit the EXAFS signal of the B-YSO_4 sample. The three models show different inner-sphere surface complexes: (A) monodentate, (B) bidentate mononuclear, and (C) bidentate binuclear.

DOI: 10.1021/acs.est.9b01795
Environ. Sci. Technol. 2019, 53, 11153−11161

Table 2. Results of the EXAFS Fits for the B-YSO_4-ads Reference[a]

model	neighbor	path	N	σ^2	ΔE_0	R	Var.	χ_ν^2
1*	1st shell	Y−O_1	6_{fix}	0.007(1)	−3(2)	2.32(1)	9	338
		Y−O_2	2_{fix}	0.004(8)	−3(2)	2.47(2)		
	2nd shell	Y−S	1_{fix}	0.008(5)	−3(2)	3.33(4)		
		Y−Al	2_{fix}	0.012(5)	−3(2)	3.52(5)		
2	1st shell	Y−O	10(1)	0.012(2)	−6(2)	2.33 (1)	8	402
	2nd shell	Y−S	1_{fix}	0.009(5)	−6(2)	3.88 (5)		
		Y−Al	1_{fix}	0.006(3)	−6(2)	3.42 (3)		
3	1st shell	Y−O	10(1)	0.013(1)	−4(1)	2.33(1)	8	334
	2nd shell	Y−S	1_{fix}	0.008(3)	−4(1)	3.34(3)		
		Y−Al	2_{fix}	0.011(5)	−4(1)	3.92(4)		

[a]Model 1: monodentate inner sphere. Model 2: bidentate mononuclear inner sphere. Model 3: bidentate binuclear inner sphere. Var. indicates independent variables. The best model is indicated with an asterisk (*). The error is expressed in parentheses after the last digit.

aqueous complex. Besides, the thermodynamic model of REE sorption on basaluminite indicated monodentate complexation of the YSO_4^+ aqueous complex.[17] With this information, the fit was performed assuming S and Al coordination numbers equal to 1 and 2, respectively, as is shown in Figure 4A. Besides, two oxygen paths were considered due to the Y−O length variation improving the fit. Thus, the fit yielded a first coordination shell with a Y−O distance range between 2.32 and 2.47 ± 0.02 Å with a fixed coordination number of 8. The second shell was fitted yielding a Y−Al distance of 3.52 Å, with a fixed coordination number of N = 2, and a Y−S distance of 3.33 Å, with a fixed number of N = 1. This result is consistent with the monodentate inner-sphere complex of Y with one oxygen shared with two surface Al sites (Figure 4A). The second model, the bidentate binuclear inner-sphere complex configuration, gave poorer results without structural significance and with higher χ_ν^2 values (Table 2), so it was discarded. The third model was the bidentate binuclear complex; the first shell was fitted with a coordination number of 10 ± 1.31 and a distance of 2.33 Å. The second shell was fitted with a S path yielding a Y−S distance of 3.34 Å with a fix coordination number of N = 1, similar to that for the monodentate hypothesis, and with an Al path with a fixed coordination number of N = 2 giving a longer distance of 3.92 Å.

Overall, the monodentate inner-sphere surface complex, which gave one of the best fit results, was in accordance with the thermodynamic sorption model. Moreover, the bidentate binuclear inner-sphere surface complexes also yielded a good fit with similar χ_ν^2 values to those of the monodentate hypothesis, making this configuration also possible (Figure 4C). In both fits, the distances between Y−S are similar, 3.33 and 3.34 Å, which is also observed in the differential PDF of the B-Ycop reference. From the EXAFS data, the presence of a bidentate binuclear surface complex cannot be ruled out. However, the thermodynamic modeling and the EXAFS data both agree on the monodentate surface complex being the one present at the basaluminite−water interface.

The EXAFS of the B-YSO_4-ads standard was also fitted with the same three atomistic models presented in Figure 4 but without sulfate included (Figure S2) to analyze the sensitivity of the fit to the presence of sulfate. The Y−Al distances obtained with these new fits (Table S3) were almost identical to those calculated when including sulfate shells (Table 2), with the exception in the monodentate inner-sphere configuration, which was a bit longer. Thus, the presence of Al is consistent in the two models, with and without sulfate. However, the fits obtained including sulfate group showed lower values of the agreement factor (reduced chi-square) (compare Tables 2 and S3). This discussion highlights the difficulties of the EXAFS technique to discern the presence of low-Z backscatterers, in particular in disordered systems such as the one present here.

These results are consistent with those presented by Rabung et al., where Gd and Lu were shown to adsorb onto γ-Al_2O_3 to form inner- sphere complexes.[47] Lu, which is considered a HREE as Y, was shown to form a monodentate surface complex with a first shell of 7 atoms and a Lu−O distance of 2.28 Å. The longer Y−O distance found here for Y is consistent with its larger Y ionic radius. However, these authors could not detect any Lu−Al bonds in their EXAFS data. Other sorption studies of Eu onto γ-Al_2O_3 showed the formation of both monodentate and bidentate binuclear complexes.[20] In contrast to this study and to the results of Rabung et al. on Al oxides, EXAFS studies of lanthanides sorbed onto ferric oxides have shown a predominance of bidentate inner-sphere complexes.[47] Lu adsorbed onto ferrihydrite at pH ≥ 5.5 yielded an Lu−O coordination number of 7 at a distance of 2.30 Å, and a second coordination shell was identified with a Lu−Fe interatomic distance of 3.38 Å. These EXAFS results were complemented by time-resolved laser fluorescence spectroscopy measurements that showed five water molecules surrounding the metal cations, which was interpreted as a bidentate inner-sphere complex.[22] The similar distance to the second shell found by Dardenne et al.[22] and by us in these two different systems can be explained by the smaller size of Lu in comparison to that of Y, which is compensated for by the longer Fe−O bond distance in comparison to the Al−O bond, making possible a bidentate mononuclear sphere at 3.4 Å in Fe oxides and Al oxides. Another study by Estes et al. reported Eu K-edge EXAFS data of Eu(III) sorbed onto hematite.[19] They observed a decrease in the coordination number of the Eu−O bond from 8 to 5 upon adsorption accompanied by a smaller Eu−Fe bond distance of 3 Å. This result was interpreted via molecular simulations as being due to the formation of an inner-sphere bidentate mononuclear surface complex. Such a decrease in the coordination number was not observed in this study; the CN of the Y−O correlation was maintained at ∼8 ± 1 for both the aqueous and surface complexes.

Identification of Y Species in Waste Samples from AMD Treatment. The k^3-weighted EXAFS of the column samples (upper part) and standards (lower part) and their Fourier transform (FT) envelope functions with corrected phase shifts are shown in Figure 3. Visual comparisons of the

DOI: 10.1021/acs.est.9b01795
Environ. Sci. Technol. 2019, 53, 11153−11161

Table 3. Percentages of Y Species in the Column Samples Obtained from LCF of the EXAFS Spectra. *R*-Factor and χ^2 Are Defined in Chapter S3 of the SI

standard	C1-4	C1-5	C3-8	C3-9
B-YSO_4ads	0.719 ± 0.036	0.867 ± 0.038	0.495 ± 0.059	0.746 ± 0.061
YSO_4-solution	0.281 ± 0.069	0.133 ± 0.071	0.505 ± 0.084	0.254 ± 0.085
R-factor	0.14	0.14	0.29	0.30
$\chi 2$	133	154	371	392

EXAFS spectra of the column samples reveal a strong similarity between them, suggesting similar local order of Y in all samples. In addition, the EXAFS spectra of the column samples are very similar to those of the solid references (B-YSO_4-ads, B-Y-ads, B-Y-cop, and A-Y-ads). They have a shoulder at ~6.5 $Å^{-1}$, indicating a higher frequency, which is absent in the aqueous samples (see the arrow in Figure 3).

Based on the PCA analyses (see Chapter S3), the reconstructed spectra indicated that only two components were required to describe the samples (Figure S4). The two most likely Y species identified by target transformation of the standard spectra were the B-YSO_4-ads and B-Y-ads references (Figure S5). However, since their EXAFS signals are very similar, LCF of the EXAFS spectra of the waste samples from column treatments was performed using B-YSO_4-ads and YSO_4-sol (Figure 3A, upper part) to quantify the proportions of different Y species in the waste samples. The use of these two standards would correspond to YSO_4^+ adsorbed forming inner- and outer-sphere complexes, respectively.

The LCF results show that more than 72% of Y adopts a local geometry similar to that of the B-YSO_4-ads reference (with the exception of sample W-Alm-C3-8, for which the LCF indicated equal proportion of both YSO_4 presented as inner- and outer-sphere complexes (Table 3)). The waste samples were selected from the depth where the major proportion of Al precipitated, assuming basaluminite precipitation. However, other minor mineral species may have also been precipitated, such as Fe-oxyhydroxysulfate, due to the presence of a small amount of Fe in the solids. Specifically, samples from the Almagrera column (W-Alm-C3-8 and W-Alm-C3-9) presented higher Fe concentration than samples from Monte Romero treatment. REEs can also be scavenged by amorphous Fe hydroxides in AMD neutralization environments,[48] so a minor or almost negligible fraction of Y could be retained by the small proportion of ferric oxides precipitated in the selected samples, explaining the lower proportion of B-YSO_4-ads.

■ ENVIRONMENTAL IMPLICATIONS

The YSO_4^+ aqueous species has been characterized combining PDF analyses of aqueous solutions and AIMD simulations, confirming the formation of an inner-sphere Y−SO_4 ion pair with a monodentate configuration, with a Y−S interatomic distance of 3.5 Å. Results from the thermodynamic sorption model describe REE sorption onto basaluminite via sorption of aqueous $REESO_4^+$. The use of an atomistic model using this positively charged ion yields the best results for the EXAFS fitting of Y sorbed on basaluminite. However, the EXAFS technique cannot confirm the presence of YSO_4^+ sorbed onto basaluminite by itself, due to the low sensitivity to discern between Al and S neighbors. However, the EXAFS fitting, together with the PDF, can confirm the strong interaction and the formation of inner-sphere surface complexes of Y on basaluminite precipitates, via ligand exchange with AlO_6 units of its structure. EXAFS analyses of column waste samples show that most of the Y is retained as the same inner-sphere sorbed species, YSO_4^+, with a low proportion of YSO_4^+ in the outer-sphere configuration.

The description of the local structure of yttrium sorbed onto the basaluminite surface provided here complements the atomic configuration studies of other trace metals, such as As and Se elements in this mineral.[44] The chemical similarity between yttrium and other HREEs (from Tb to Lu) suggests that similar environments could be present for the other elements of the same group. This fact has important environmental consequences, as the HREE would be strongly sorbed, forming inner sphere complexes, which could result in their long-term immobilization at least until the host phase is dissolved or re-precipitated. A key question emerges about the long-term stability of the complex, particularly with an increase in the solution pH. The structural evolution of pure basaluminite with increasing pH showed its recrystallization onto boehmite, releasing sulfate into the solution.[45] Previous studies on poorly crystalline Fe phases from AMD, such as schwertmannite, have shown a release of adsorbed toxic elements during aging due to recrystallization processes.[49] The occurrence of such processes in REE-doped basaluminite could result in the remobilization of REEs and of other potentially adsorbed toxic elements. The extent to which these processes can occur in natural waters requires further investigation.

Besides, further studies on the potential uptake of LREEs by basaluminite are necessary to confirm and/or compare different structural mechanisms to those of their HREE counterpart These investigations will provide a better understanding of studies focused on a selective recovery of REEs from AMD wastes which could produce an economic value of the waste generated during the neutralization of AMD-affected waters.

■ ASSOCIATED CONTENT

Supporting Information

The Supporting Information is available free of charge on the ACS Publications website at DOI: 10.1021/acs.est.9b01795.

Synthesis of reference materials, analytical procedures and aqueous speciation calculations, synchrotron experiments and data analyses, molecular dynamics simulations, and the Phyton code used to generate PDF from AIMD simulations; samples used for EXAFS measurements and the modeling parameters from EXAFS fitting; and illustrating fitting of EXAFS spectra (PDF)

■ AUTHOR INFORMATION

Corresponding Author

*E-mail: alba.lozano@idaea.csic.es.

ORCID

Alba Lozano: 0000-0003-4050-6906

Alejandro Fernández-Martínez: 0000-0001-5073-9629

Mauro Rovezzi: 0000-0003-2539-6198

DOI: 10.1021/acs.est.9b01795
Environ. Sci. Technol. 2019, 53, 11153−11161

Notes

The authors declare no competing financial interest.

■ ACKNOWLEDGMENTS

This work was funded by the European EIT "Morerecovery" and the Spanish SCYRE (CGL2016-468 78783-C2-R) projects. A.L. was also funded by a FPI grant (BES-2014-069978) and the "Make Our Planet Great Again" short-stay program. A.F.-M. acknowledges a grant from Labex OSUG@2020 (investissements d'avenir, ANR10 LABX56) for financial support of this research. A.L. thanks J. Bellés, M. Cabañas, and R. Bartroli (IDAEA-CSIC) for their analytical assistance. D.D.T. is grateful to the U.K. Materials and Molecular Modelling Hub for computational resources, which is partially funded by EPSRC (EP/P020194/1). This research utilized Queen Mary's Apocrita HPC facility, supported by QMUL Research-IT. The authors would like to thank the ESRF for in-house beamtime allocation at ID31 and the SOLEIL review committee for beamtime allocation at BM30B-FAME on the French quota, proposal no. 30-02-1124.

■ REFERENCES

(1) Binnemans, K.; Jones, P. T.; Blanpain, B.; Van Gerven, T.; Yang, Y.; Walton, A.; Buchert, M. Recycling of rare earths: A critical review. *J. Clean. Prod.* **2013**, *51*, 1−22.

(2) Kumar, R.; Jiang, C.; Wang, J.; Cietek, D.; Roth, J.; Gell, M.; Jordan, E. H. Low Thermal Conductivity Yttrium Aluminum Garnet Thermal Barrier Coatings Made by the Solution Precursor Plasma Spray: Part II—Planar Pore Formation and CMAS Resistance. *J. Therm. Spray Technol.* **2018**, *27*, 794−808.

(3) Noack, C. W.; Dzombak, D. A.; Karamalidis, A. K. Rare Earth Element Distributions and Trends in Natural Waters with a Focus on Groundwater. *Environ. Sci. Technol.* **2014**, *48*, 4317−4326.

(4) Evangelou, V. P.; Zhang, Y. L. A Review: Pyrite Oxidation Mechanisms and Acid Mine Drainage Prevention. *Crit. Rev. Environ. Sci. Technol.* **1995**, *25*, 141−199.

(5) Coulton, R.; Bullen, C.; Hallet, C. The design optimisation of active mine water treatment plants. *Land Contam. Reclam.* **2003**, *11*, 273−280.

(6) Ackman, T. *Sludge Disposal from Acid Mine Drainage Treatment*, Report of Invest. 8672; U.S. Bureau of Mines: Pittsburg, PA, 1982; p 38.

(7) Viadero, R. C.; Wei, X.; Buzby, K. M. Characterization and Dewatering Evaluation of Acid Mine Drainage Sludge from Ammonia Neutralization. *Environ. Eng. Sci.* **2006**, *23*, 734−743.

(8) Hedin, R. S.; Watzlaf, G. R.; Nairn, R. W. Passive Treatment of Acid Mine Drainage with Limestone. *J. Environ. Qual.* **1994**, *23*, 1338−1345.

(9) Younger, P. L.; Banwart, S. A.; Hedin, R. S. *Mine Water Hydrology, Pollution, Remediation*; Springer Science & Business Media, 2002.

(10) Cravotta, C. A. Size and performance of anoxic limestone drains to neutralize acidic mine drainage. *J. Environ. Qual.* **2003**, *32*, 1277−1289.

(11) Watzlaf, G. R.; Schroeder, K. T.; Kleinmann, R. L. P.; Kairies, C. L.; Nairn, R. W. *The Passive Treatment of Coal Mine Drainage*, Laboratory Report DOE/NETL-2004/1202, U.S. Department of Energy, National Energy Technology: Pittsburgh, PA, 2004.

(12) Ayora, C.; Macías, F.; Torres, E.; Lozano, A.; Carrero, S.; Nieto, J.-M.; Pérez-López, R.; Fernández-Martínez, A.; Castillo-Michel, H. Recovery of Rare Earth Elements and Yttrium from Passive-Remediation Systems of Acid Mine Drainage. *Environ. Sci. Technol.* **2016**, *50*, 8255−8262.

(13) Ayora, C.; Caraballo, M. A.; Macias, F.; Rötting, T. S.; Carrera, J.; Nieto, J. M. Acid Mine Drainage in the Iberian Pyrite Belt: 2. Lessons Learned from Recent Passive Remediation Experiences. *Environ. Sci. Pollut. Res.* **2013**, *20*, 7837−7853.

(14) Bigham, J. M.; Nordstrom, D. K. Iron and Aluminum Hydroxysulfate Minerals from Acid Sulfate Waters. In *Sulfate Minerals, Crystallography, Geochemistry and Environmental Significance*; Jambor, J. L., Alpers, C. N., Nordstrom, D. K., Eds.; Mineralogical Society of America Reviews in Mineralogy and Geochemistry, 2000; Vol. *40*, pp 351−403.

(15) Carrero, S.; Fernandez-Martinez, A.; Pérez-López, R.; Lee, D.; Aquilanti, G.; Poulain, A.; Lozano, A.; Nieto, J.-M. The Nanocrystalline Structure of Basaluminite, an Aluminum Hydroxide Sulfate from Acid Mine Drainage. *Am. Mineral.* **2017**, *102*, 2381−2389.

(16) Gammons, C. H.; Wood, S. A.; Pedrozo, F.; Varekamp, J. C.; Nelson, B. J.; Shope, C. L.; Baffico, G. Hydrogeochemistry and Rare Earth Element Behavior in a Volcanically Acidified Watershed in Patagonia, Argentina. *Chem. Geol.* **2005**, *222*, 249−267.

(17) Lozano, A.; Ayora, C.; Fernández-Martínez, A. Sorption of rare earth elements onto basaluminite: the role of sulfate and pH. *Geochim. Cosmochim. Acta* **2019**, *258*, 50−62.

(18) Gimeno Serrano, M. J.; Auqué Sanz, L. F.; Nordstrom, D. K. REE Speciation in Low-Temperature Acidic Waters and the Competitive Effects of Aluminum. *Chem. Geol.* **2000**, *165*, 167−180.

(19) Estes, S. L.; Arai, Y.; Becker, U.; Fernando, S.; Yuan, K.; Ewing, R. C.; Zhang, J.; Shibata, T.; Powell, B. A. A Self-Consistent Model Describing the Thermodynamics of Eu(III) Adsorption onto Hematite. *Geochim. Cosmochim. Acta* **2013**, *122*, 430−447.

(20) Yang, S.; Sheng, G.; Montavon, G.; Guo, Z.; Tan, X.; Grambow, B.; Wang, X. Investigation of Eu(III) immobilization on γ-Al_2O_3 surfaces by combining batch technique and EXAFS analyses: Role of contact time and humic acid. *Geochim. Cosmochim. Acta* **2013**, *121*, 84−104.

(21) Fan, Q. H.; Tan, X. L.; Li, J. X.; Wang, X. K.; Wu, W. S.; Montavon, G. Sorption of Eu(III) on Attapulgite Studied by Batch, XPS, and EXAFS Techniques. *Environ. Sci. Technol.* **2009**, *43*, 5776−5782.

(22) Dardenne, K.; Schäfer, T.; Denecke, M. A.; Rothe, J.; Kim, J. I. Identification and Characterization of Sorbed Lutetium Species on 2-Line Ferrihydrite by Sorption Data Modeling, TRLFS and EXAFS. *Radiochim. Acta* **2001**, *89*, 469−479.

(23) Allen, P. G.; Bucher, J. J.; Shuh, D. K.; Edelstein, N. M.; Craig, I. Coordination Chemistry of Trivalent Lanthanide and Actinide Ions in Dilute and Concentrated Chloride Solutions FT Magnitude. *Inorg. Chem.* **2000**, *39*, 595−601.

(24) Lindqvist-Reis, P.; Lambe, K.; Pattanaik, S.; Persson, I.; Sandström, M. Hydration of the Yttrium (III) Ion in Aqueous Solution. An X-Ray Diffraction and XAFS Structural Study. *J. Phys. Chem. B* **2000**, *104*, 402−408.

(25) Yaita, T.; Narita, H.; Suzuki, S.; Tachimori, S.; Motohashi, H.; Shiwaku, H. Structural Study of Lanthanides(III) in Aqueous Nitrate and Chloride Solutions by EXAFS. *J. Radioanal. Nucl. Chem.* **1999**, *239*, 371−375.

(26) Duvail, M.; Ruas, A.; Venault, L.; Moisy, P.; Guilbaud, P. Molecular Dynamics Studies of Concentrated Binary Aqueous Solutions of Lanthanide Salts: Structures and Exchange Dynamics. *Inorg. Chem.* **2010**, *49*, 519−530.

(27) Kowall, T.; Foglia, F.; Helm, L.; Merbach, A. E. Molecular Dynamics Simulation Study of Lanthanide Ions Ln^{3+} in Aqueous Solution Including Water Polarization. Change in Coordination Number from 9 to 8 along the Series. *J. Am. Chem. Soc.* **1995**, *117*, 3790−3799.

(28) Ohta, A.; Kagi, H.; Tsuno, H.; Nomura, M.; Kawabe, I. Influence of Multi-Electron Excitation on EXAFS Spectroscopy of Trivalent Rare-Earth Ions and Elucidation of Change in Hydration Number through the Series. *Am. Mineral.* **2008**, *93*, 1384−1392.

(29) Rizkalla, E. N.; Choppin, G. R. Lanthanides and Actinides Hydration and Hydrolysis. In *Handbook on the Physics and Chemistry of Rare Earths*; Gschneider, K. A., Eyring, L., Choppin, G. R., Lander, G. H., Eds.; Lanthanides/Actinides: Chemistry; Elsevier Science B.V.: Amsterdam, The Netherlands, 1994; Vol. *18*.

DOI: 10.1021/acs.est.9b01795
Environ. Sci. Technol. 2019, 53, 11153−11161

(30) Duvail, M.; Spezia, R.; Vitorge, P. A Dynamic Model to Explain Hydration Behaviour along the Lanthanide Series. *ChemPhysChem* **2008**, *9*, 693−696.
(31) Janicki, R.; Starynowicz, P.; Mondry, A. Lanthanide carbonates. *Eur. J. Inorg. Chem.* **2011**, *2011*, 3601−3616.
(32) Jeanvoine, Y.; Miró, P.; Martelli, F.; Cramer, C. J.; Spezia, R. Electronic structure and bonding of lanthanoid(III) carbonates. *Phys. Chem. Chem. Phys.* **2012**, *14*, 14822−14831.
(33) Harris, S. M.; Nguyen, J. T.; Pailloux, S. L.; Mansergh, J. P.; Dresel, M. J.; Swanholm, T. B.; Gao, T.; Pierre, V. C. Gadolinium complex for the catch and release of phosphate from water. *Environ. Sci. Technol.* **2017**, *51*, 4549−4558.
(34) Luo, Y. R.; Byrne, R. H. Carbonate complexation of yttrium and the rare earth elements in natural rivers. *Geochim. Cosmochim. Acta* **2004**, *68*, 691−699.
(35) Torres, E.; Auleda, M. A Sequential Extraction Procedure for Sediments Affected by Acid Mine Drainage. *J. Geochem. Explor.* **2013**, *128*, 35−41.
(36) Parkhurst, D. L.; Appelo, C. A. J. *User's guide to PhreeqC (version 2.18) A computer program for speciation, and inverse geochemical calculations*; U.S. Department of the Interior, U.S. Geological Survey, 1999.
(37) Blanc, P.; Lassin, A.; Piantone, P.; Azaroual, M.; Jacquemet, N.; Fabbri, A.; Gaucher, E. C. Thermoddem: A Geochemical Database Focused on Low Temperature Water/Rock Interactions and Waste Materials. *Appl. Geochem.* **2012**, *27*, 2107−2116.
(38) Juhás, P.; Davis, T.; Farrow, C. L.; Billinge, S. J. L. PDFgetX3: a rapid and highly automatable program for processing powder diffraction data into total scattering pair distribution functions. *J. Appl. Crystallogr.* **2013**, *46*, 560−566.
(39) Proux, O.; Biquard, X.; Lahera, E.; Menthonnex, J. J.; Prat, A.; Ulrich, O.; Soldo, Y.; Trévisson, P.; Kapoujyan, G.; Perroux, G.; Taunier, P.; Grand, D.; Jeantet, P.; Deleglise, M.; Roux, J-P.; Hazemann, J-L. FAME A New Beamline for XRay Absorption Investigations of Very Diluted Systems of Environmental, Material and Biological Interests. *Phys. Scr.* **2005**, 970−973.
(40) Hutter, J.; Iannuzzi, M.; Schiffmann, F.; VandeVondele, J. CP2K: Atomistic Simulations of Condensed Matter Systems. *Wiley Interdiscip. Rev.: Comput. Mol. Sci.* **2014**, *4*, 15−25.
(41) Zhang, Y.; Yang, W. Comment on "Generalized Gradient Approximation Made Simple". *Phys. Rev. Lett.* **1998**, *80*, No. 890.
(42) Grimme, S.; Antony, J.; Ehrlich, S.; Krieg, H. A Consistent and Accurate Ab Initio Parametrization of Density Functional Dispersion Correction (DFT-D) for the 94 Elements H-Pu. *J. Chem. Phys.* **2010**, *132*, No. 154104.
(43) Juhás, P.; Farrow, C. L.; Yang, X.; Knox, K. R.; Billinge, S. J. L. Complex Modeling: A Strategy and Software Program for Combining Multiple Information Sources to Solve Ill Posed Structure and Nanostructure Inverse Problems. *Acta Crystallogr., Sect. A: Found. Adv.* **2015**, *A71*, 562−568.
(44) Carrero, S.; Fernandez-Martinez, A.; Pérez-López, R.; Poulain, A.; Salas-Colera, E.; Nieto, J. M. Arsenate and Selenate Scavenging by Basaluminite: Insights into the Reactivity of Aluminum Phases in Acid Mine Drainage. *Environ. Sci. Technol.* **2017**, *51*, 28−37.
(45) Lozano, A.; Fernández-Martínez, A.; Ayora, C.; Poulain, A. Local Structure and Ageing of Basaluminite at Different pH Values and Sulphate Concentrations. *Chem. Geol.* **2018**, *496*, 25−33.
(46) Cruz-Hernández, P.; Carrero, S.; Pérez-López, R.; Fernández-Martínez, A.; Lindsay, M. B. J.; Dejoie, C.; Nieto, J. M. Influence of As(V) on precipitation and transformation of schwertmannite in acid mine drainage-impacted waters. *Eur. J. Mineral.* **2019**, *31*, 237−245.
(47) Rabung, T.; Geckeis, H.; Wang, X. K.; Rothe, J.; Denecke, M. A.; Klenze, R.; Fanghäel, T. Cm(III) sorption onto γ-Al_2O_3: New insight into sorption mechanisms by time-resolved laser fluorescence spectroscopy and extended X-ray absorption fine structure. *Radiochim. Acta* **2006**, *94*, 609−618.
(48) Verplanck, P. L.; Nordstrom, D. K.; Taylor, H. E.; Kimball, B. A. Rare earth element partitioning between hydrous ferric oxides and acid mine water during iron oxidation. *Appl. Geochem.* **2004**, *19*, 1339−1354.
(49) Acero, P.; Ayora, C.; Torrentó, C.; Nieto, J. M. The Behavior of Trace Elements during Schwertmannite Precipitation and Subsequent Transformation into Goethite and Jarosite. *Geochim. Cosmochim. Acta* **2006**, *70*, 4130−4139.

DOI: 10.1021/acs.est.9b01795
Environ. Sci. Technol. 2019, 53, 11153−11161

Solid and aqueous speciation of yttrium in passive remediation systems of acid mine drainage

Alba Lozano[a,b*], *Alejandro Fernández-Martínez*[c], *Carlos Ayora*[a,b], *Devis Di Tommaso*[d], *Agnieszka Poulain*[e], *Mauro Rovezzi*[f], *Carlo Marini*[g]

[a] Institute of Environmental Assessment and Water Research, (IDAEA-CSIC), Jordi Girona 18-26, 08034 Barcelona, Spain

[b] Grup de Mineralogia Aplicada i Geoquímica de Fluids, Departament de Cristal-lografia, Mineralogia i Dipòsits Minerals, Facultat de Geologia, Universitat de Barcelona (UB), C/Martí Franquès, S/N, Barcelona, Spain

[c] Univ. Grenoble Alpes, Univ. Savoie Mont Blanc, CNRS, IRD, IFSTTAR, ISTerre, 38000 Grenoble, France

[d] School of Biological Sciences, Queen Mary University of London, Mile End Road, London, E1 4NS, UK

[e] ESRF, The European Synchrotron, 71 Avenue des Martyrs, Grenoble 38000, France

[f] Univ Grenoble Alpes, CNRS, IRD, Irstea, Météo France, OSUG, FAME, 38000 Grenoble, France

[g] CELLS-ALBA Synchrotron Radiation Facility, Carrer de la Llum 2-26,08290 Cerdanyola del Valles, Barcelona, Spain

Supporting Information

The Supporting information contains 19 pages, 3 tables and 5 figures.

*Corresponding author: Alba Lozano (alba.lozano@idaea.csic.es)

S1 SYNTHESIS OF REFERENCE MATERIALS

Basaluminite was synthesized following the method described by Adams and Rawajfih[1]. A solution of 214 mL of 0.015 M $Ca(OH)_2$ was added drop-by-drop to 30 mL of 0.05 M $Al_2(SO4)_3 \cdot 18H_2O$ (both commercial reagents) while being stirred until an OH:Al ratio of 2.14 was reached. The solid was washed three times to remove coprecipitated $CaSO_4 \cdot 2H_2O$ and dried for 48 hours at 40°C.

Nanoboehmite was synthesized following the method described by Xu et al.[2]. A solution of 0.5 M $AlCl_3 \cdot 6H_2O$ was mixed with 1 M NaOH. The titration was conducted drop-by-drop until reaching a pH of 8.1. The precipitate was washed three times with deionized water and dried for 72 hours at 40°C.

X-ray diffraction analyses were performed to ensure the purity of the samples. Digestions of 0.1 g of solids in 5 mL HNO_3 65% were carried out for 12 hours at 115°C for chemical characterization.

S2 DETAILS OF ANALYTICAL PROCEDURES AND AQUEOUS SPECIATION CALCULATIONS

Measurements of pH values were made with a Crison® glass electrode calibrated with buffer solutions of pH 2, 4, 7 and 9. Concentrations of major cations (S and Al) were measured by ICP-AES (Thermo Scientific – iCAP 6500, Radial acquisition) and Y was determined ICP-MS (Perkin-Elmer®SciexElan 6000). The detection limits were 1.6 and 1.0 µmol/L for S, Al and 0.2 µg/L for Y, respectively. Certified solutions (CPI International-CCV standard 1-solution A) were intercalated within the samples to check the analytical accuracy. The analytical precision error was estimated to be approximately 2% for ICP-AES and ICP-MS measurements. Two AMD laboratory standards supplied by P. Verplank (USGS), were also analyzed for REE accuracy, giving deviations lower than 5% of the recommended values, with the exception of Eu, giving values 25% below the recommended value[3].

The Donnee Thermoddem_V1.10.dat database[4] has been updated with the stability constants at zero ionic strength and 25°C for the following inorganic complexes for lanthanides and yttrium: $LnCO_3^+$, $LnCO_3^{-2}$ and $LnHCO_3^{+2}$ [5]; $LnSO_4^+$ [6]; $LnOH^{+2}$ [7], $LnOH_2^+$, $LnOH_3$ [8]; $LnCl^{+2}$, $LnCl_2^+$ [9]; LnF^{+2}, LnF_2^+ [10]; and $LnNO_3^{+2}$ [11] . Solubility products for REE $Ln(OH)_3$ and $Ln(OH)_{3(am)}$ solids have been complemented with those from the LLNL database (Johnson et al., 2000) and with those reported by Spahiu and Bruno[12] Scandium aqueous complexes, $Sc(OH)^{+2}$, $Sc(OH)_2^+$, $Sc(OH)_3$, $ScSO4^+$; and the solubility product for $Sc(OH)_3$ by Wood and Samson[13] were incorporated as well to the database. The aqueous speciation and saturation index of the solid phases were calculated with the PHREEQC code[28] using the Donnee Thermoddem_V1.10 database.

S3 SYNCHROTRON EXPERIMENTS AND DATA ANALYSES

S3.1 Pair Distribution Function analyses

HEXS measurements were performed at beamline ID31 at the European Synchrotron Radiation Facility (ESRF). Powder samples were loaded into polyamide capillaries. The samples and background measurements were performed at room temperature with incident X-rays of 70 KeV (λ=0.177 Å). The

incident X-ray energy was calibrated using a CeO_2 standard (NIST 674b). The 2D images were collected with a flat panel Pilatus3 X CdTe 2M detector. The obtained images were corrected and integrated using pyFAI[14]. Structure factors, S(Q), and pair distribution functions, PDFs, were obtained using the PDFgetX3 software[15]. Differential pair distribution functions (d-PDFs) were obtained by subtracting the PDF signal of pure synthetic basaluminite from the PDF of Y-doped basaluminite. Background subtraction of the aqueous samples was performed using a deionized water background. The background scale factor was adjusted to minimize the O-O correlation (~2.8 Å) in the PDFs.

S.3.2 EXAFS analyses

The EXAFS measurements of aqueous and solids B-Yads, B-Ycop, A-Ycop solid samples were performed at the Y K-edge (17.038 keV) on the FAME beamline[16] (the French bending magnet beamline, BM30B, at the ESRF), and B-YSO4-ads and Y_2O_3 sample on CLÆSS beamline (wiggler absorption beamline at the national Spanish light source, ALBA[17]). At Fame the X-ray optics configuration consisted of a pair of vertically focusing Rh-coated mirrors inclined at 2.7 mrad, providing harmonics rejection and vertical focusing. The monochromator was a cryogenically cooled and dynamic sagittal focusing double crystal monochromator equipped with a pair of Si(220) crystals. The beam size at the sample was approximately 100 × 200 μm^2 (vertical × horizontal). The energy calibration was performed at the first peak in the first derivative of the absorption spectrum of a Y foil and monitored with the same reference foil mounted in transmission after the sample. The incoming and transmitted beams were monitored with photodiodes reading the scattered signal from the X-rays passing through air-filled chambers. The partial fluorescence yield was measured with an energy dispersive high-purity Ge detector with thirty elements that was mounted at 90° on the scattering plane to minimize parasitic scattering. The strong fluorescence signal coming from the matrix of the samples was filtered with 150-μm-thick Al foil and a Sr filter of three absorption lengths. The measurements were performed at 20 K in a liquid He flow cryostat to reduce thermal vibrations (enhancing the EXAFS signal) and to avoid radiation damage. The spectra were acquired for approximately 40 minutes and repeated three to four times to obtain optimal statistics.

Room temperature EXAFS Spectra of B-YSO4-ads and, Y_2O_3, samples have been collected in transmission mode at CLÆSS beamline. This is the optical scheme of the beamline. The synchrotron radiation emitted by the multi-pole wiggler is first collimated vertically by the first mirror and then monochromatised using a liquid nitrogen cooled Si (311) double crystals monochromator. The x-ray beam is finally focused down to the sample at about 500 μm x 500 μm (H x V) by changing the radius of curvature of the second vertically focusing mirror. The incoming and outgoing photon fluxes have been measured by ionization chambers filled with an appropriate mixture of N2 and Kr gases. Beamline energy was calibrated on the edge position of the Y_2O_3 spectrum[18].

The solid samples were prepared as 5-mm-diameter pellets after fine grinding and diluting with BN. They were mounted on a PEEK (polyether ether ketone) sample holder and sealed with Kapton film. Frozen samples were prepared by depositing the aqueous solution onto the sample holder, which was kept in

liquid nitrogen vapor, sealed with Kapton film and kept in liquid N_2 until being mounted in the cryostat. All of the column samples, A-Yads reference and aqueous solutions were measured in fluorescence mode, whereas the Y reference compounds were measured in transmission mode. Multiple scans (3-5) were taken from each sample to obtain good statistics and signal-to-noise for EXAFS analysis. Each scan was checked for energy calibration and then a mean of 4 scans were merged.

The data reduction, normalization and EXAFS extraction were performed following the standard protocols implemented in the Athena software[17]. Normalization was performed using a linear pre-edge function and a second-order post-edge polynomial. The pre-edge and post-edge normalization range were,-150 to-30 eV and from 150 to 744 eV, respectively. The normalization used a linear pre-edge function and a quadratic post-edge polynomial. The EXAFS spectra were analyzed using the Athena software with two different procedures.

Principal component analysis (PCA) of the four EXAFS spectra obtained from the waste samples was performed in a k range of 3-12 $Å^{-1}$. The PCA determines the number of components that reproduces the EXAFS spectra for the set of column samples with the standards. The criterion used to estimate the number of species representative of each spectrum was to obtain a decrease in the R value of 20%, where R is defined as:

$$R = \frac{\sum_i^{N_{fit}} \left[\chi_i^{data} - \chi_i^{model}(x)\right]^2}{\sum_i^{N_{fit}} \left[\chi_i^{data}\right]^2}$$

where N_{fit} is the number of data points, X is the set of variables, Є is the noise level of the data, and N_{idp} is the number of independent data points.

This criterion was also checked by visual examination of the reconstructed spectra. Fig. S4 shows the experimental spectra reconstructed with combinations of two and three principal components (dashed lines). The first two components reproduce each spectrum reasonably well. Introducing a third component into the spectra gives a better reconstruction (improvement in R greater than 20%); however, the improvement to the fit is mostly in the k range > 9 $Å^{-1}$, where the signal is very noisy. Therefore, two components were considered to reproduce the experimental spectra satisfactorily.

After the examination of the components, the target transformation operation was performed to evaluate which references were the principal components. The two references with the lowest χ^2 values were B-Yads and B-Ycop, followed by A-Yads (Fig. S5). These three EXAFS spectra are nearly identical, and since basaluminite is amorphous, the yttrium geometry is expected to be the same in both solids. Thus, B-Yads and the following better reference, YSO4-sol, were selected, which represent yttrium attached to basaluminite as an inner sphere ligand and yttrium as a YSO_4^+ outer sphere ligand, respectively.

Linear combination fitting (LCF) was performed for each EXAFS spectrum of the waste samples with the B-Yads and YSO4-sol standards. The fraction of each standard spectrum is proportional to the amount of this species in the waste solid from the column treatments; thus, this result identifies the Y species in these solids. The precision of the fit is expressed by the error factor $\chi_v 2$, which is defined as:

$$\chi_v^2 = \frac{\chi^2}{(N_{idp} - N_{varys})}$$

where Nidp is the number of independent data points, Nvarys is the number of variables, and χ2 is defined as:

$$\chi^2 = \frac{N_{idp}}{\epsilon^2 N_{fit}} \sum_{i}^{N_{fit}} [\chi_i^{data} - \chi_i^{model}(x)]^2$$

The Artemis software[19] was used to estimate the backscattering phases and amplitude functions of the scattering paths. Atomistic models of aqueous solutions containing the YSO_4^+ complex were built from snapshots obtained from the molecular dynamics simulations. Atomistic structures of Y^{3+} adsorbed onto the AlO_6 octahedra from basaluminite were built from the structural model of basaluminite[20]. The K^3-weighted EXAFS spectra were fit in the range of 2.46-10.71 $Å^{-1}$. The coordination number (N), interatomic distance (R), Debye-Waller factor (σ^2) and ΔE_0 for the samples were allowed to vary and were linked to all of the shells during the fit. The goodness of the fit was evaluated by χ_v^2.

S4 MOLECULAR DYNAMICS SIMULATIONS

Ab initio (Born-Oppenheimer) molecular dynamics (AIMD) simulations were conducted with the electronic structure code CP2K/Quickstep, version 5.1[21]. CP2K implements DFT based on a hybrid Gaussian plane wave. Several studies have shown that generalized-gradient DFT approximations give radial distribution function for liquid water that are overstructured compared with experiments[22]. In this study, the revised Perdew–Burke–Ernzerhof (revPBE)[23] functionals were therefore augmented with the Grimme's dispersion correction termed DFT-D3[24]. The inclusion of van der Walls corrections to GGA functionals leads to a softer liquid structure[25,26]. Goedecker-Teter-Hutter pseudopotentials[27] were used to describe the core–valence interactions. All atomic species were represented using a double-zeta valence polarized basis set. The plane wave kinetic energy cut off was set to 1000 Ry. The *k*-sampling was restricted to the Γ point of the Brillouin zone. Simulations were carried out with a wave function optimization tolerance of 10^{-6} au that allows for 1.0 fs time steps with reasonable energy conservation. Periodic boundary conditions were applied throughout. AIMD simulations were carried out in the canonical (constant NVT) ensemble using a Nosé-Hoover chain thermostat to maintain the average temperature at T = 300K. AIMD of an aqueous solution of Yttrium(III) sulfate were carried out on a Y^3 – SO_4^{2-}–OH^- system embedded in a box of 61 water molecules. The initial configuration was generated starting from the last configuration of 200 ps of classical simulation of 64 water molecules in the isothermal–isobaric (T = 300 K and P = 1 atm) ensemble, which resulted in a equilibrated volume with cell vectors $\vec{a}$= (12.285, 0.000, 0.000), $\vec{b}$= (0.000, 12.285, 0.000), and $\vec{c}$= (0.000, 0.000, 12.285) (in Angstrom). Starting from the last configuration, one H_2O molecule was substituted with one Y^{3+}, and we conducted 40 ps of AIMD simulations. Finally, two H_2O molecules coordinated with Y^{3+} were substituted with one SO_4^{2-} and one OH^- ion, and we conducted further 15 ps simulations.

Pair Distribution Functions (PDF) and partial PDFs were generated from the AIMD trajectories using a home-built python code that makes use of the DiffPy-CMI library[28]. In order to minimize the contribution of bulk water and to be able to compare with the water-subtracted experimental PDFs of the aqueous YSO_4^+ complex, the O-O correlations were not included in the calculations.

S5 PYTHON CODE TO GENERATE PDF FROM AIMD SIMULATIONS

```
##################################################
## {Code to calculate PDFs from MD simulations
## (collection of snapshots in xyz format) using diffpy}
##################################################
## Author: {AlexFM}
## Copyright: {2019}, {Collaboration with IDAEA, EMPATIA project}
## Version: {1.0 Feb 2019}
## Email: {Alex.Fernandez-Martinez@univ-grenoble-alpes.fr}
##################################################
#


import numpy as np
import matplotlib.pyplot as plt
from diffpy.Structure import loadStructure, Lattice
from diffpy.srreal.pdfcalculator import DebyePDFCalculator
from diffpy.srreal.pdfcalculator import PDFCalculator

dpc = DebyePDFCalculator()
pc=PDFCalculator()


#Define parameters for PDF calculations
filename_experimental_pdf=''
filename_output=''

nframes=50000
pc.qmin=2
pc.qmax=25
pc.rmax=25
pc.qdamp=0.3

pc.setTypeMask('H','H',False)  #eliminates this pair
pc.setTypeMask('H','O',False)  #eliminates this pair
pc.setTypeMask('H','Y',False)  #eliminates this pair
pc.setTypeMask('H','S',False)  #eliminates this pair
pc.setTypeMask('O','Y',False)  #eliminates this pair
pc.setTypeMask('O','O',False)  #eliminates this pair
pc.setTypeMask('Y','Y',False)  #eliminates this pair
pc.setTypeMask('S','Y',False)  #eliminates this pair
pc.setTypeMask('O','S',True)   #includes this pair
pc.setTypeMask('S','S',False)  #eliminates this pair

#Read file containing MD trajectory
f = open('y_so4_m_oh_61w-pos-1.xyz', "r")
lines=f.readlines()
print 'lines read'
lines2=[]
for i in lines:
        j=i[:-1]
        lines2.append(j)
print 'lines corrected'

i=0
sizef=np.shape(lines)[0]
grall=[]

#Create lattice
```

```
box=Lattice(12.28519616,12.28519616,12.28519616,90,90,90)

while i<nframes:
    xyz=lines2[i:i+193]
    np.shape(xyz)
    np.savetxt('test.xyz',xyz,fmt='%s')
    cluster=loadStructure('test.xyz')

    #cluster.Uisoequiv=0.008
    for j in np.arange(cluster.element.shape[0]):
    #print cluster.element[i]
        if cluster.element[j]=='O':
                        #print cluster.element[i]
            cluster[j].Uisoequiv=0.015
                        #print cluster.Uisoequiv[i]
        elif cluster.element[j]=='Y':
                        #print cluster.element[i]
            cluster[j].Uisoequiv=0.001
                        #print cluster.Uisoequiv[i]
        elif cluster.element[j]=='S':
                        #print cluster.element[i]
            cluster[j].Uisoequiv=0.005
              #print cluster.Uisoequiv[i]
              cluster[187].Uisoequiv=0.005
              cluster[188].Uisoequiv=0.005
              cluster[189].Uisoequiv=0.005
        cluster[190].Uisoequiv=0.005
    cluster.placeInLattice(box)  #Place cluster in lattice
    r1, g1 = pc(cluster)
    grall.append(g1)
    #plt.plot(r1,g1)
    i=i+193
    print i


grall2=np.asarray(grall)
YSO4=np.loadtxt(filename_experimental_pdf,skiprows=27).T

#Plot results together with experimental PDF
plt.plot(YSO4[0],YSO4[1]*0.5,label='experimental')
plt.plot(r1,grall2.mean(axis=0),label='calculated')
plt.legend()
plt.show()

#Output to ascii file
np.savetxt(filename_output,np.transpose([r1,grall2.mean(axis=0)]))

f.close()
```

Table S1. Description of aqueous and solid standards. Type of synthesis, Y concentration in ppm and acquisition mode for EXAFS measurements.

Sample	mineral	Synthesis	ppm	Mode
B-YSO4-ads	Basaluminite	YSO4-adsorbed	20000	Transmission
B-Yads	Basaluminite	Y-adsorbed	20000	Transmission
B-Ycop	Basaluminite	Y-coprecipitated	80000	Transmission
A-Yads	Amorphous $Al(OH)_3$	Y-adsorbed	280	Fluorescence
Y-sol	1000 ppm Y, pH 4.6	Y aqueous	1000	Fluorescence
YSO4-sol	1000 ppm Y, 2000 ppm SO_4 (Na_2SO_4) , pH 3	Y aqueous	1000	Fluorescence

279 Table S2. Description of column samples, Y concentration and acquisition mode for EXAFS
280 measurements.

Sample	Part of colum	AMD Mine	Y ppm	EXAFS acquisition mode
W-MR-C1-4	Column Matrix	Monte Romero	37.5	Fluorescence
W-MR-C1-5	Column Matrix	Monte Romero	42.0	Fluorescence
W-Alm-C3-8	Column Matrix	Almagrera	7.8	Fluorescence
W-Alm-C3-9	Column Matrix	Almagrera	9.8	Fluorescence

281

Table S3. Modeling parameters for Y K-edge EXAFS in YSO_4^+ sorbed basaluminite sample (B-Yads) but taking into account free yttrium, Y^{3+}, at different inner sphere positions 1) Y as monodentate inner sphere ligand, 2) Y ion as bidentate mononuclear inner sphere ligand, and 3) Y ion as bidentate binuclear inner sphere ligand.

Sample	Model	path	N	σ^2	ΔE_0	R	Var.	χ_v^2
B-YSO4-ads	1. Monodent.	Y-O	9(1)	0.012 (1)	-5(1)	2.34 (1)	6	884
		Y-Al	2_{fix}	0.010 (3)	-5(1)	3.43(3)		
	2. Bident. Mononuc.	Y-O	9(1)	0.013 (1)	-6(2)	2.33(1)	6	481
		Y-Al	1_{fix}	0.006 (4)	-6(2)	3.42 (4)		
	3. Bident. Binuc.	Y-O	11(2)	0.014 (1)	-5(2)	2.33(1)	6	514
		Y-Al	2_{fix}	0.011 (6)	-5(2)	3.92(5)		

Figure S1. Y Aqueous speciation for aqueous solutions of (A) 0.1 M $Y(NO_3)_3$, (B) 0.1 M $Y(NO_3)_3$ plus 0.1 M Na_2SO_4, (C) 0.01 M YCl_3 and (D) 0.01 M YCl_3 plus 0.01 M Na2SO4, respectively, at pCO_2 3.5.

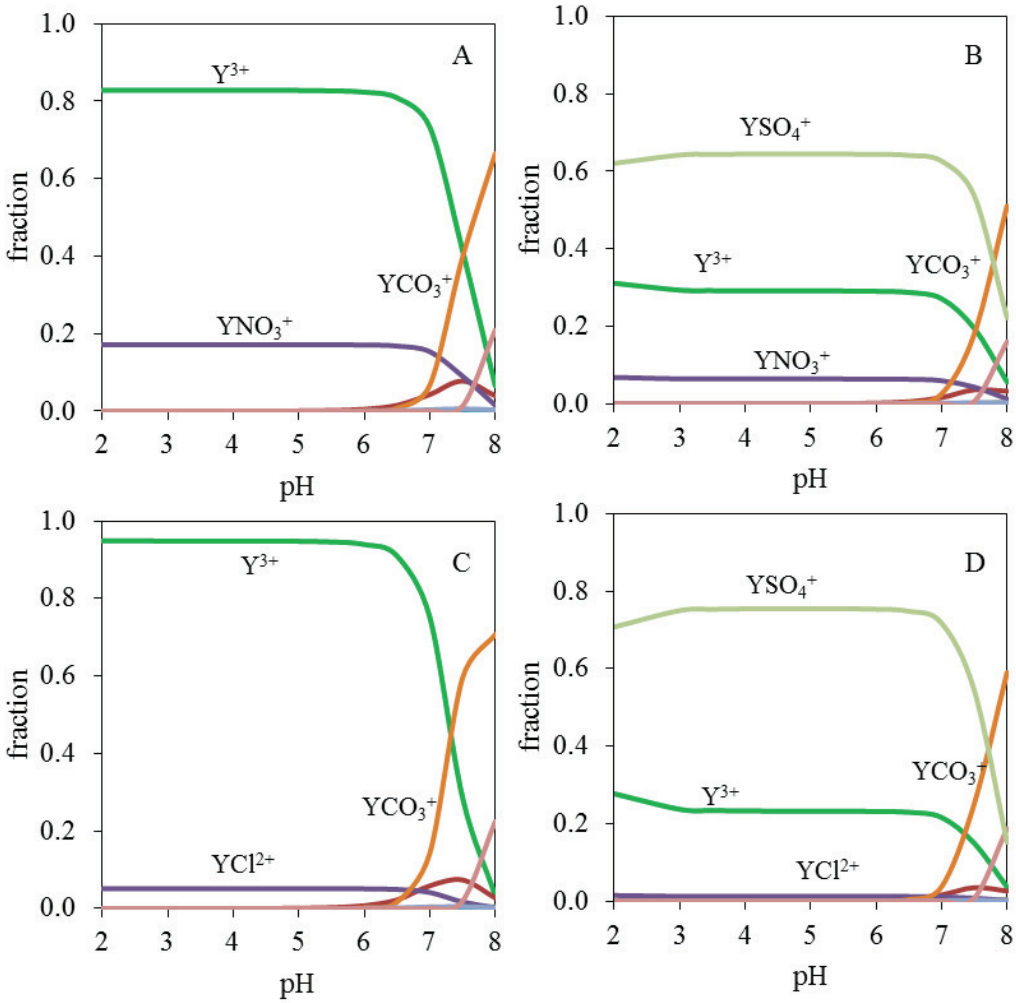

Figure S2. Atomistic representations of the three models of Y3+ adsorbed on Al-octaedral basaluminite water interface used to fit the EXAFS data of the B-YSO4-ads sample. The three models have an inner-sphere coordination with different oxygen atoms as ligands: (A) monodentate, (B) bidentate mononuclear, (C) bidentate binuclear.

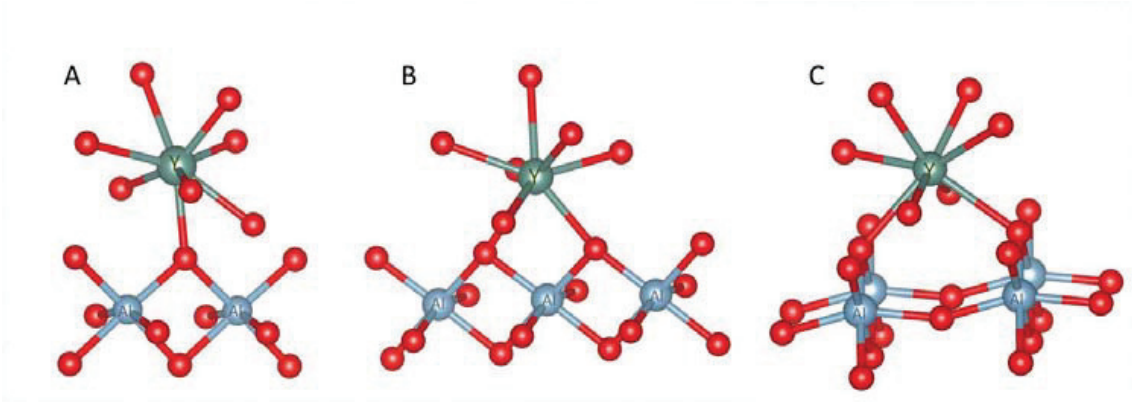

Figure S3. (A) K^3-weighted EXAFS spectra and (B) Fourier transform amplitude and real phase at Y K-edge absorbed onto B-YSO4-ads sample. Experimental and fits curves are displayed in black and red colors, respectively. Fits carried out with models represented in Fig. S2. K-range 3.41-12.20 $Å^{-1}$. R range 1.35-4.00 Å.

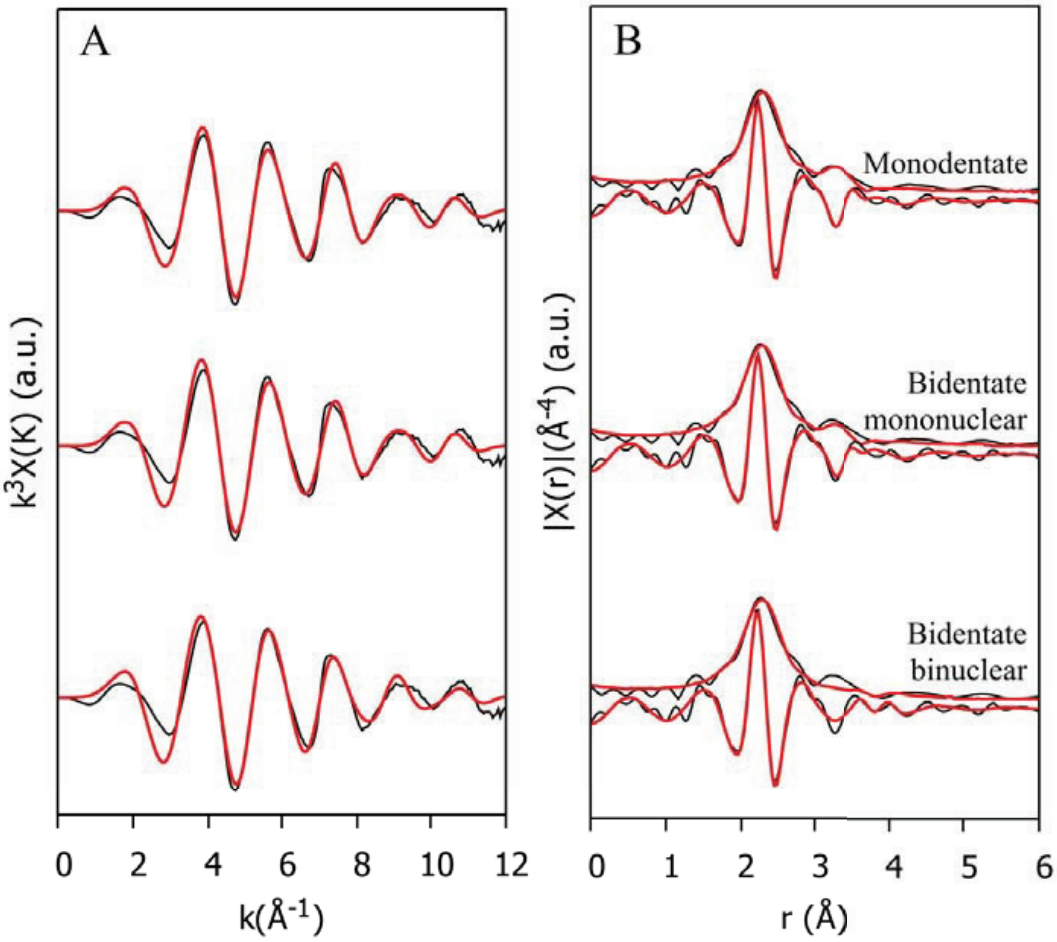

Figure S4. Experimental EXAFS spectra (solid lines) and the reconstructed spectra (red dashed lines) with 2 components (left) and with three components (right) for the four waste samples.

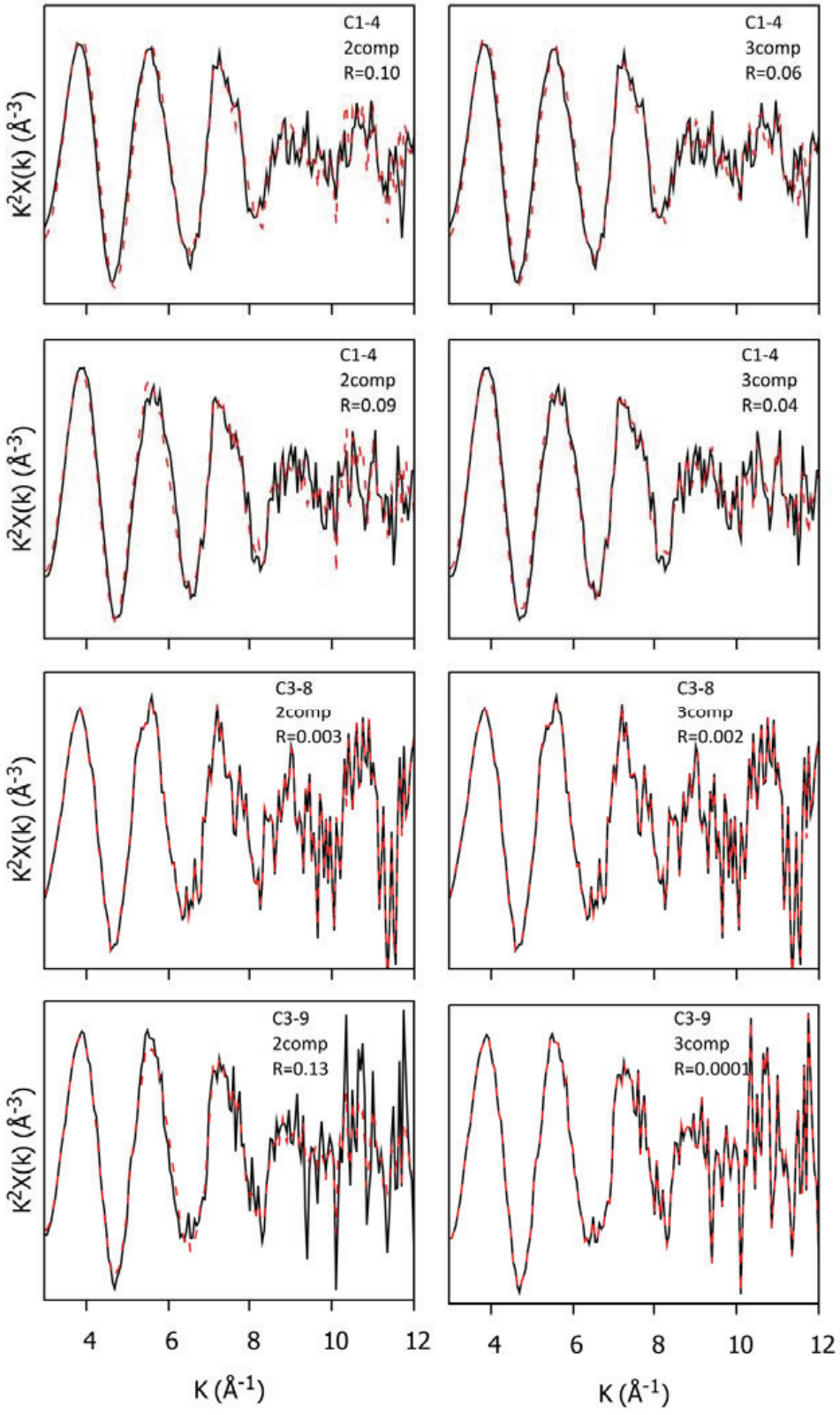

Figure S5. Target transformation (dashed lines) of waste samples EXAFS spectra (solid lines) for the six Y references. B-Yads: basaluminite with adsorbed Y^{3+}, B-Ycop: basaluminite coprecipitaetd withY^{3+}, B-YSO4-ads: basaluminite with adsorbed YSO_4^+, A-Yads: nanoboehmite with adsorbed yttrium;Y-sol: solution whith Y^{3+} as the main aqueous specie, YSO_4-sol: solution with YSO_4^+ as the main aqueous specie.

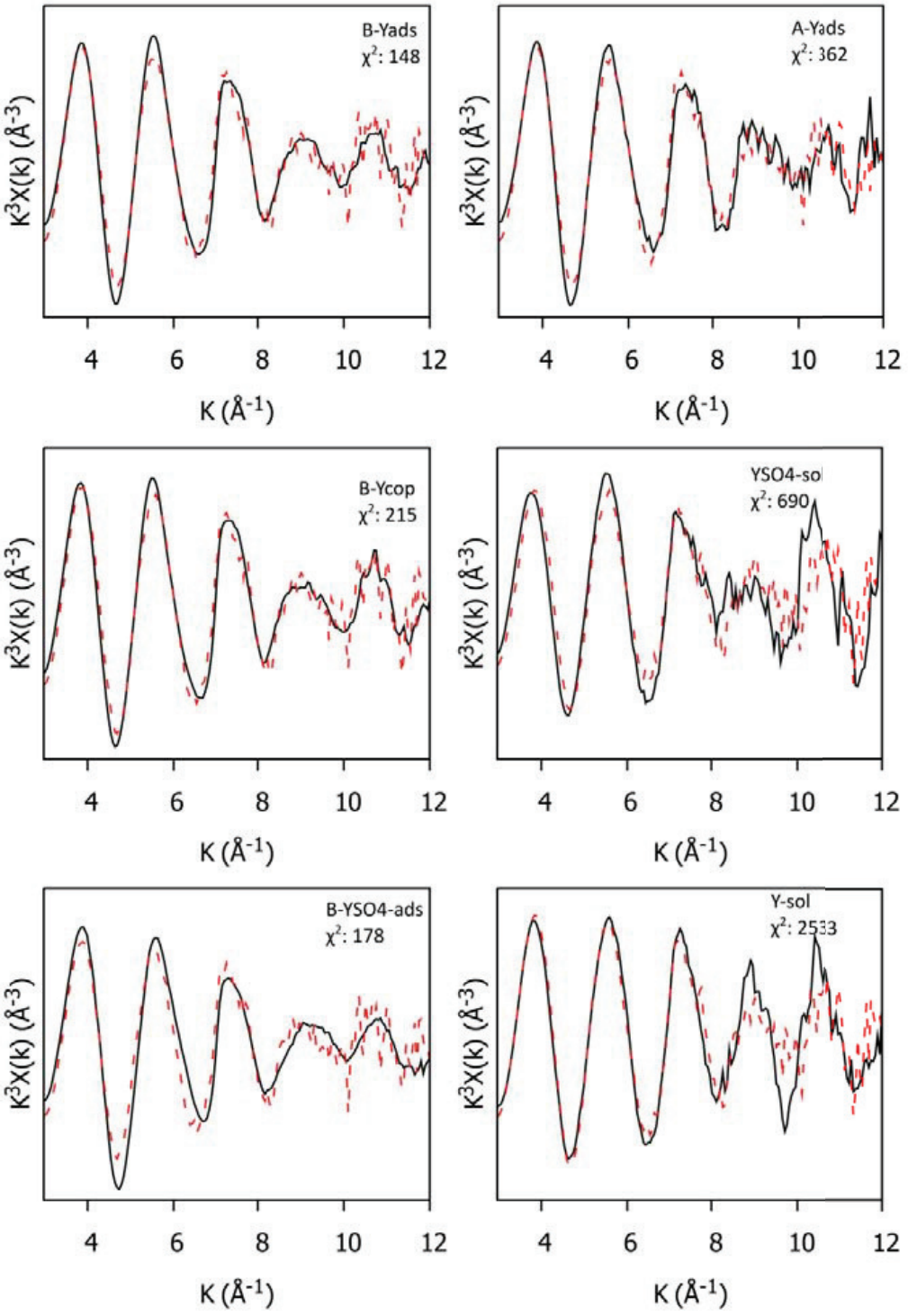

References

(1) Adams, F.;Rawajfih, Z. Basaluminite and alunite: A possible cause of sulfate retention by acid soils. *Soil Sci. Soc. Am. J.* **1977**, *41*, 686–692

(2) Xu, R.; Xiao, S.; Jiang, J.; Wang, Y. Effects of Amorphous $Al(OH)_3$ on the Desorption of Ca^{2+},Mg^{2+}, and Na^{+} from soils and minerals as related to diffuse layer layer overlapping. *J. Chem. Eng. Data* **2011**, *56*, 2536–2542.

(3) Verplanck, P. L.; Antweiler, R. C.; Nordstrom, D. K.; Taylor, H. E. Standard reference water samples for rare earth element determinations. *Appl. Geochem.* **2001**, *16*, 231–244.

(4) Blanc, P. H.; Lassin, A.; Piantone, P.; Azaroual, M.; Jacquement, N.; Fabbri, A.; Gaucher, E. C. Thermoddem: A geochemical database focused on low temperature water/rocinteractions and waste materials. *App.Geochem.,* **2012,** *27*, 2017-2216.

(5) Luo, Y. R.; Byrne, R. H. Carbonate complexation of yttrium and the rare earth elements in natural rivers. *Geochim. Cosmochim. Acta* **2004**, 68, 691–699.

(6) Schijf J.; Byrne R. H. Determination of SO4β1 for yttrium and the rare earth elements at I = 0.66 m and t = 25°C—Implications for YREE solution speciation in sulfate-rich waters. *Geochim. Cosmochim. Acta* **2004**, *68* (13) 2825-2837.

(7) Klungness G. D.; Byrne R. H. Comparative hydrolysis behavior of the rare earths and yttrium: the influence of temperature and ionic strength. *Polyhedron* **2000**, *19*, 99–107.

(8) Lee, J. H.; Byrne, R. H. Examination of comparative rare earth element complexation behavior using linear free-energy relationships. *Geochim. Cosmochim. Acta* **1992**, *56*, 1127–1137.

(9) Luo Y. R.; Byrne R. H. Yttrium and rare earth element complexation by chloride ions at 25 degrees. *C. J. Solution Chem.* **2001**, *30* (9), 837–845.

(10) Luo, Y.; Millero, F.J. Effects of temperature and ionic strength on the stabilities of the first and second fluoride complexes of yttrium and the rare earth elements. *Geochim. Cosmochim. Acta* **2004**, *68* (21), 4301–4308.

(11) Millero, F. J. Stability constants for the formation of rare earth inorganic complexes as a function of ionic strength. *Geochim. Cosmochim. Acta* **1992**, *56*, 3123–3132.

(12) Spahiu, K., Bruno, J. A selected thermodynamic database for REE to be used in HLNW performance assessment exercises. *SKB Technical Report* **1995**, 95-35, 88 pp.

(13) Wood, S. A.; Samson, A. M. The aqueous geochemistry of gallium, germanium, indium and scandium. *Ore Geology Reviews* **2006**, *28*, 57-102.

(14) Kieffer, J.; Karkoulis, D. PyFAI, a versatile library for azimuthal regrouping. *J. Phys. Conf. Ser.* **2013**, *425* (202012), 1–5.

(15) Juhás, P.; Davis, T.; Farrow, C. L.; Billinge, S. J. L. PDFgetX3: a rapid and highly automatable program for processing powder diffraction data into total scattering pair distribution functions. *J. Appl. Crystallogr.* **2013**, *46*, 560–566.

(16) Proux, O.; Biquard, X.; Lahera, E.; Menthonnex, J. J.; Prat, A.; Ulrich, O.; Soldo, Y.; Trvisson, P.; Kapoujyan, G.; Perroux, G.; Taunier, P.; Grand, D.; Jeantet, P.; Deleglise, M; Roux, J-P. and Hazemann, J-L. FAME A New Beamline for XRay Absorption Investigations of VeryDiluted Systems of Environmental, Material and Biological Interests. *Phys. Scr*. **2015**, 970-973.

(17) Simonelli, L.; Marini, C.; Olszewski, W.; Ávila Pérez, M.; Ramanan, N.; Guilera, G.; Cuartero, V.; Klementiev, K. CLÆSS: The hard X-ray absorption beamline of the ALBA CELLS synchrotron. *Cogent Physics* **2016**, *3*, 1231987.

(18) Tanaka, K.; Takahashi, Y.: Shimizu, H. Determination of the host phase of rare earth elements in natural carbonate using X-ray absorption near-edge structure. *Geochem. J.* **2009**, *43*, 143-149.

(19) Ravel, B.; Newville, M. ATHENA, ARTEMIS, HEPHAESTUS: Data Analysis for X-Ray Absorption Spectroscopy Using IFEFFIT. *J. Synchrotron Radiat*. **2005**, *12* (4), 537–541.

(20) Carrero, S.; Fernández-Martínez, A.; Pérez-López, R.; Lee, D.; Aquilanti, G.; Poulain, A.; Lozano, A; Nieto, J. M. The nanocrystalline structure of basaluminite, an aluminum hydroxide sulfate from acid mine drainage. Am. Mineral. **2017b**, *102*, 2381-2389.

(21) Hutter, Y.; Iannuzzi, M.; Schiffmann, F.; VandeVondele, J. CP2K: Atomistic Simulations of Condensed Matter Systems. *Wiley Interdiscip. Rev. Comput. Mol. Sci.* **2014**, *4*, 15–25.

(22) Sit, P. H-L.; Marzari, N. Static and dynamical properties of heavy water at ambient conditions from first-principles molecular dynamics., *J. Chem. Phys.* **2005**, *122*, 204510.

(23) Zhang, Y.; Yang, W. Comment on 'Generalized Gradient Approximation Made Simple". *Phys. Rev. Lett*. **1998,** *80,* 890–890.

(24) Grimme, S.; Antony, J.; Ehrlich, S.; Krieg H. A consistent and accurate ab initio parametrization of density functional dispersion correction (DFT-D) for the 94 elements H-Pu. *J. Chem. Phys*. **2010**, *132* (15), 154104.

(25) Wang, J; Román-Pérez, G.; Soler, J. M.; Artacho E.;. Fernández-Serra M.-V. Density, structure, and dynamics of water: The effect of van der Waals interactions, *J. Chem. Phys.* **2011**, *134,* 24516.

(26) Lin, I.-C.; Seitsonen, A. P.; Tavernelli, I.; Rothlisberger; U. Structure and Dynamics of Liquid Water from ab Initio Molecular Dynamics—Comparison of BLYP, PBE, and revPBE Density Functionals with and without van der Waals Corrections, *J. Chem. Theory Comput.* **2012**, *8*, 3902–3910.

(27) Goedecker, S.; Teter, M.; Hutter, J. Separable dual-space Gaussian pseudopotentials, *Phys. Rev. B,* **1996**, *54*, 1703–1710.

(28) P. Juhás, C. L. Farrow, X. Yang, K. R. Knox and S. J. L. Billinge, Complex modeling: a strategy and software program for combining multiple information sources to solve ill posed structure and nanostructure inverse problems, *Acta Crystallogr. A*. **2015,** *71*, 562-568.

Article 5

Geochemical behavior of rare earth elements in acid drainages: modeling achievements and limitations

To submit to: *Chemical Geology. Submitted.*

GEOCHEMICAL BEHAVIOR OF RARE EARTH ELEMENTS IN ACID DRAINAGES: MODELING ACHIEVEMENTS AND LIMITATIONS

Alba Lozano[a], Carlos Ayora[a], Francisco Macías[b], Rafael León[b], María José Gimeno[c], Luis Auqué[c]

[a] Institute of Environmental Assessment and Water Research, (IDAEA-CSIC), Jordi Girona 18-26, 08034 Barcelona, Spain

[b]Department of Earth Sciences & Research Centre on Natural Resources, Health and the Environment (RENSMA), Faculty of Experimental Sciences, University of Huelva, Campus "El Carmen", E-21071, Huelva, Spain

[c]Geochemical Modelling Group. Petrology and Geochemistry Area, Earth Science Department, University of Zaragoza, Spain C/ Pedro Cerbuna 12, 50009, Zaragoza

Corresponding author:

Alba Lozano (alba.lozano@idaea.csic.es)

ABSTRACT

Rare earth elements (REE) play a significant role in modern green technologies, but the global geographical distribution of these resources may cause supply risks to the market. However, the REE concentrations in acid mine drainage (AMD) are several orders of magnitude higher than those in other surface waters and could be a future supplementary source of highly valuable REE. Moreover, due to the common use of REE in modern industry, some toxicological studies suggest that REE could have pathogenic potential. Therefore, knowing the mobility constraints of REE in natural waters, particularly in AMD, is of interest.

Precipitation of schwertmannite and basaluminite occurs due to mixing of REE-enriched AMD streams and neutral streams. The REE fractionation between AMD and solid phases has been investigated in several localities in the Odiel-Tinto (SW Spain) and Arroyo del Val (N Spain) basins. The mobility of REE is related to the precipitation of Fe and Al phases that occurs at different pH values. The behavior of REE during the mixing is conservative under low pH conditions (pH<4 approximately), at which schwertmannite precipitates, whereas REE are scavenged under near-neutral pH conditions, at which basaluminite precipitates and what suggest that this phase could be responsible for REE retention. Indeed, when Fe and Al phases can be sampled separately, schwertmannite does not contain REE, which are entirely retained in basaluminite, confirming the REE removal by this later phase.

The validity and limitations of a recently proposed thermodynamic model of REE sorption on basaluminite have been assessed by comparing the model predictions with observations of samples recovered in the field. The model is able to predict the REE distribution pattern and confirms the preferential sorption of heavy REEs (HREEs) and Y over light REEs (LREEs) in all the samples. However, the lack of synchronicity between basaluminite precipitation and REE sorption during mixing in an open flow setting precludes an accurate prediction of the REE concentration in the solid phase.

Key words: lanthanides, yttrium, scandium, sorption, basaluminite, schwertmannite

1 INTRODUCTION

Lanthanide series (from La to Lu) plus scandium (Sc) and yttrium (Y) are referred to as rare earth elements (REE) according to the recommendation of the International Union of Pure and Applied Chemistry (Connelly et al., 2005). The lanthanide group can be arbitrarily divided into light REE (LREE: La to Nd), medium REE (MREE: Sm to Gd) and heavy REE (HREE: Tb to Lu). Due to its atomic size similarity to Ho, Y is often considered an HREE, whereas Sc has occasionally been left out of this group because of its small ionic radius (Chakhmouradian and Wall, 2012). The global demand for REE is constantly increasing due to their role in manufacturing permanent magnets, batteries, light-emitting diodes and alloys, among other technological advancements. However, most REE mineral deposits are concentrated in a few countries, and China dominates more than 90% of worldwide production (U.S. Geological Survey (USGS), 2019). Therefore, there is a need for alternative sources of REE (Alonso et al., 2012; European-Commission, 2017).

Notably, the acid mine drainage (AMD) is one of the most widespread forms of pollution affecting continental waters (Nordstrom, 2011; Nordstrom et al., 2015). The REE concentrations in AMD are several orders of magnitude higher than those of other surface waters and could be a future supplementary source of some highly valuable REE (Ayora et al., 2016; Stewart et al., 2017; Zhang and Honaker, 2018). Moreover, although REE have been considered a minor environmental concern due to their common use in modern industry, some toxicological studies suggest that they could have pathogenic potential (Dai et al., 2002; Pagano et al., 2015; Roncati et al., 2018; Zhuang et al., 1996). Therefore, knowing the mobility constraints of REEs in natural waters, particularly in AMD, is a matter of interest.

The mobility of REE in AMD is highly dependent on pH, as observed in several field studies. Verplanck et al. (2004) examined the concentrations of REE along two AMD-impacted streams with varying pH. Their results showed that REE behaved conservatively at pH values below 5 despite important Fe oxidation occurred. In contrast, REE were scavenged from the water at higher pH values. The authors discarded the precipitation of REE-bearing solids and attributed the REE removal to sorption onto Fe(III) precipitates. Similar depletion of the REE content was observed by Ferreira da Silva et al. (2009) when AMD in the Lousal mine area (S Portugal) mixed with a tributary stream and the pH increased from 3 to 6. (Gammons et al., 2005a) observed a similar REE behavior in a mountain stream affected by AMD. Sampling conducted at three stations, upstream (pH 3.3), intermediate (pH 5.5) and downstream (pH 6.8) showed that REEs remained in solution at the first two stations. The removal under high pH conditions was interpreted as sorption onto suspended

particles of undifferentiated Fe and Al hydroxides. In a similar study, Gammons et al. (2005b) collected samples along a 40 km stretch of the Patagonian Agrio river, which is initially acidic due to volcanic discharges. Most of the decrease in the REE load occurred immediately downstream of the confluence with a tributary that increased the pH of the Agrio river from 4.3 to 6.1. Due to the concomitant drop in Al concentration, these authors proposed that the loss of REE was due to sorption onto hydrous Al oxides.

Likewise, the REE mobility has also been assessed in response to AMD neutralization. Thus, the AMD percolation through a limestone-filled column induced the successive precipitation of schwertmannite and basaluminite. The REE were preferentially allocated in the basaluminite precipitates rather than in the schwertmannite (Ayora et al., 2016). Similar behavior was observed when a leachate from a coal debris was neutralized by the direct addition of NaOH (Zhang and Honaker, 2018). As schwertmannite forms at pH values below 4 and basaluminite forms at pH values above 4, these observations are consistent with the behavior observed in acidic streams. A minor fraction of Sc, however, was observed to be retained in the schwertmannite (Lozano et al., 2019c; Zhang and Honaker, 2018).

The process of REE transfer from water to solid phases is known to generate partitioning among the different REE. The preferential sequestration of the LREE by iron oxides in marine environments has been attributed to the stronger aqueous complexes formed between CO_3^{2-} and the HREE, which maintains the HREE in solution (Kawabe et al., 1999; Ohta and Kawabe, 2000; Sholkovitz, 1995). Besides, carbonate aqueous complexes can compete with natural organic matter, which also strongly complexes with REE favoring its stabilization in solution, as observed in several field studies in rivers (Pourret et al., 2007; Tang and Johannesson, 2003) and in seawater mixing zones (Adebayo et al., 2018). In contrast with these natural environments, in AMD systems, the HREE have been demonstrated to show a stronger affinity for the solid phase than the LREE (Gammons et al., 2005b; Verplanck et al., 2004). In AMD, aqueous complexes with SO_4^{2-} predominate, and their stability constants do not change with increasing atomic number; consequently, no REE fractionation would be anticipated from aqueous complexation in AMD (Gimeno et al., 2000). Therefore, REE fractionation (if any) should be intrinsic to the sorption process.

Bau (1999) studied the fractionation that results from the coprecipitation of REE and hydrous ferric oxide (HFO) due to the neutralizing of synthetic and natural acidic solutions. This author confirmed the strong pH dependence of REE retention by HFO. The author prepared solutions in which free REE cations predominated and demonstrated that fractionation occurred regardless of aqueous

speciation. Thus, in the experiments performed with synthetic solutions, LREE showed less preferential attachment to the HFO than MREE and HREE, but no preferential fractionation of HREE with respect to MREE was observed. However, an increase in incorporation into the solid phase from La to Lu was observed when a natural solution was used, and in addition to HFO, Al phases formed.

Recently, Lozano et al. (2019a) performed sorption experiments of Sc, Y and lanthanides on basaluminite. Sorption occurred at pH values between 4 and 7 and increased with the SO_4 concentration of the solution. The experiments also confirmed the existence of preferential fractionation, in which the affinity for the solid phase increased from La to Lu, with Y in an intermediate HREE position. These authors proposed a thermodynamic model in which the formation of monodentate surface complexes of sulfate-REE aqueous species explained the measurements. Because of its different aqueous speciation, Sc sorbed at pH values between 4 and 6 as bidentate surface complexes of both sulfate and hydroxyl-REE aqueous species. Similar sorption experiments were also conducted with schwertmannite (Lozano et al., 2019c). Here, REE sorption on schwertmannite occurred at pH ranges similar than that on basaluminite with the exception of Sc which sorbed at lower pH (between 3 and 5).

The aim of the present work is to test the validity of the thermodynamic model developed for REE sorption on basaluminite to predict REE behavior in AMD environments and to discuss the main limitations and uncertainties. Precipitation of schwertmannite and basaluminite occurs due to mixing of acidic (and REE-rich) and near-neutral streams. Several localities in two areas, Odiel-Tinto (SW Spain) and Arroyo del Val (N Spain), with high (>2 M) and low (<0.2 M) SO_4 concentrations, respectively, were selected for water and particulate sampling. The REE fractionation in the solid phase was predicted from the concentration in the acidic water and compared with the analytical values.

2 MATERIALS AND METHODS

2.1 Odiel river sites

The Odiel River, in southwestern Spain, is 122 km long and has a catchment area of 2300 km^2, extending from the Aracena Mountains in northern Huelva province to the Huelva estuary in the

south. The area has an inland Mediterranean climate, with fresh winters and warm and dry summers and an average rainfall of 800 mm, which falls mostly in winter. Approximately one hundred ancient mines and waste piles generating AMD have been detected in the Odiel watershed (Nieto et al., 2013; Sánchez-España et al., 2005).

The stretch of the river selected for the study is approximately 8 km long downstream of the first mine discharge of Mina Concepción (Fig. 1). The river flow varies greatly seasonally and annually. During the sampling campaign (February 2015), the Odiel river had a flow close to 1.5 m^3/s and an alkalinity of 130 mg/L eq. $CaCO_3$ prior to entering the mining area. In the selected section, the river receives four acidic tributaries with flows of 0.5 to 5 L/s and a final major input of 0.13 m^3/s from the Agrio river (Fig. 1). Because of these inputs, the Odiel remains acidic down to the estuary. The evolution of the water chemistry and precipitates in this stretch of the Odiel river has already been described by (Sánchez España et al., 2006).

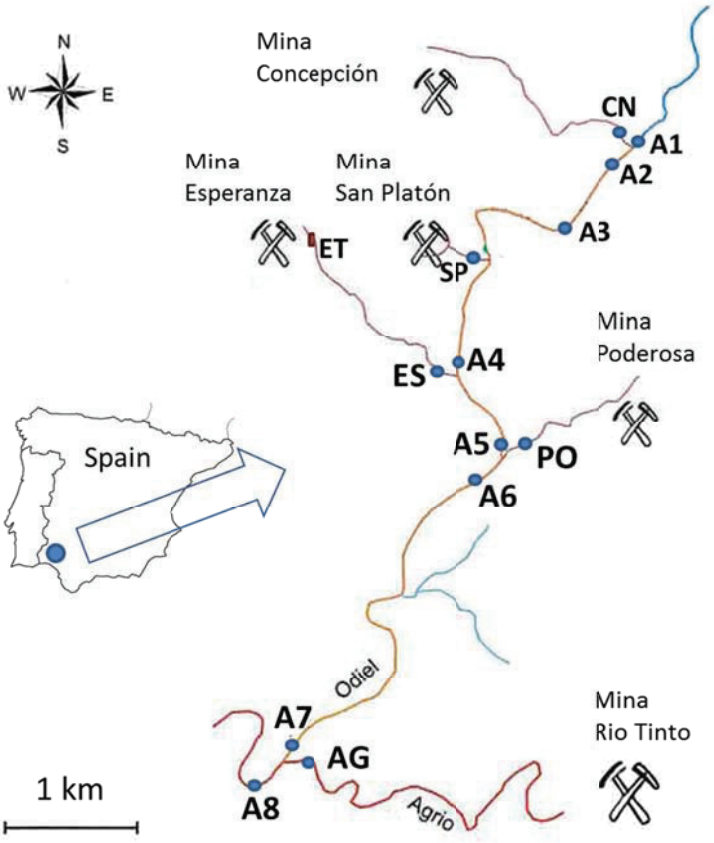

Figure 1. The studied stretch of the Odiel river and its acidic tributaries with the sampling points.

Water samples were collected from the five acidic water inputs (CN, SP, ES, PO and AG, Fig. 1) and from the Odiel river both upstream the confluences with the tributaries and more than 100 m downstream of the confluences, where water mixing was apparently complete (Fig. 1 and Table 1). Field parameters (temperature, pH, Eh and electric conductivity) were measured at each sampling

point. Water samples were filtered with 0.45 and 0.1 µm filters (Millipore), stored in 125 mL polyethylene bottles, acidified to pH < 2 with HNO_3, and cooled during transport. Solid samples were collected in 1 L bottles from the suspended precipitate clouds at the mixing points of acidic tributaries and the Odiel river (Fig. 2A). When possible, ochre and whitish precipitates were sampled separately (Fig. 2B). The water coexisting with the precipitates was labeled PO-mix, AG-mix1 (schwertmannite) and AG-mix2 (basaluminite). They were filtered in the laboratory the same day with 0.45 and 0.1 µm filters (more than one filter was needed). The filters were dried at 40°C and weighed. Then, they were digested with HNO_3 65% for 12 h at 115°C, and the solutions were stored for analysis. Additional filters were also kept for mineralogical observations.

2.2 Additional sites in the Odiel-Tinto catchments

The field sampling was completed with several localities from the same area. Thus, water samples and precipitates from Dehesa Boyal (DB) and Torerera mine (TO) correspond to the mixing of small acidic streams with less than 2 L/s (DB and TO, Table 2) with near-neutral water with greater flow (DB-neu and TO-neu, respectively). The solid samples from Dehesa Boyal and Torerera remained in the bottom (Fig. 2C), and the whitish precipitates extended for more than 500 m downstream the mixing point in Dehesa Boyal (Fig. 2D). The solid samples were collected with a syringe and left to settle in the bottle, dried and digested with HNO_3. The supernatant water was filtered, acidified and stored for analysis (DB-mix and TO-mix). The sampling campaigns were carried out in February-March, corresponding to the humid season. In summer, rainfall is almost absent, and the stream flows are a very small. Then, due to the perennial acidic discharges, the rivers become acid, and the whitish precipitates redissolve, whereas the reddish ones remain along the stream beds.

The Rio Tinto (RT) locality corresponds to the reverse situation. Upstream of the village of Niebla, a small neutral stream of less than 5 L/s discharges into the Rio Tinto main stream (1 m^3/s). Large amounts of whitish precipitates at the confluence of the two waters (Fig. 2E) and are carried down by the river flow until they redissolve one hundred meters downstream. Water samples were collected in the tributary (RT-neu) and the acidic river (RT). Precipitates were collected in the mixing zone inside the neutral discharge where the near-neutral water predominated. The samples of the solids in the suspended clouds were collected in 1 L bottles, left to settle and dried. The supernatant water (RT1-mix and RT2-mix) was filtered, acidified and stored for analysis.

Finally, a full-scale passive remediation system was in operation in 2007-8 at the Mina Esperanza site (ET in Fig. 1). The system consisted of a limestone sand filter through which the acidic water

flowed. A full description of the water and solid waste chemistry and mineralogy is provided in (Caraballo et al., 2011a, 2011b). Basaluminite precipitates appeared during the latter three months of the treatment life, and they were probably formed by the mixing of the near-neutral outflow of the treatment with untreated acidic water circulating through paths of exhausted reagent. Three solid samples of white precipitates were collected on different days from the outflow channel of the treatment plant (Fig. 2F). Similar to the previously described cases, the precipitates were collected, left to settle and dried, and the supernatant water was filtered and stored. Unfortunately, only major solute concentrations of the water samples coexisting with the solids were available (ET1-mix, ET2-mix, and ET3-mix in Table 2). No samples of the acidic water were collected at the moment of solid sampling. However, the chemistry of the pretreated AMD was fairly constant, and an averaged composition of the three later months of the treatment life compiled by Caraballo et al. (2016, Supplementary Information) was selected for modeling (ET, Table 2). The neutral outflow (ET-neu) was obtained as the average of monthly samples during the regular functioning of the treatment from April 2017 to June 2018.

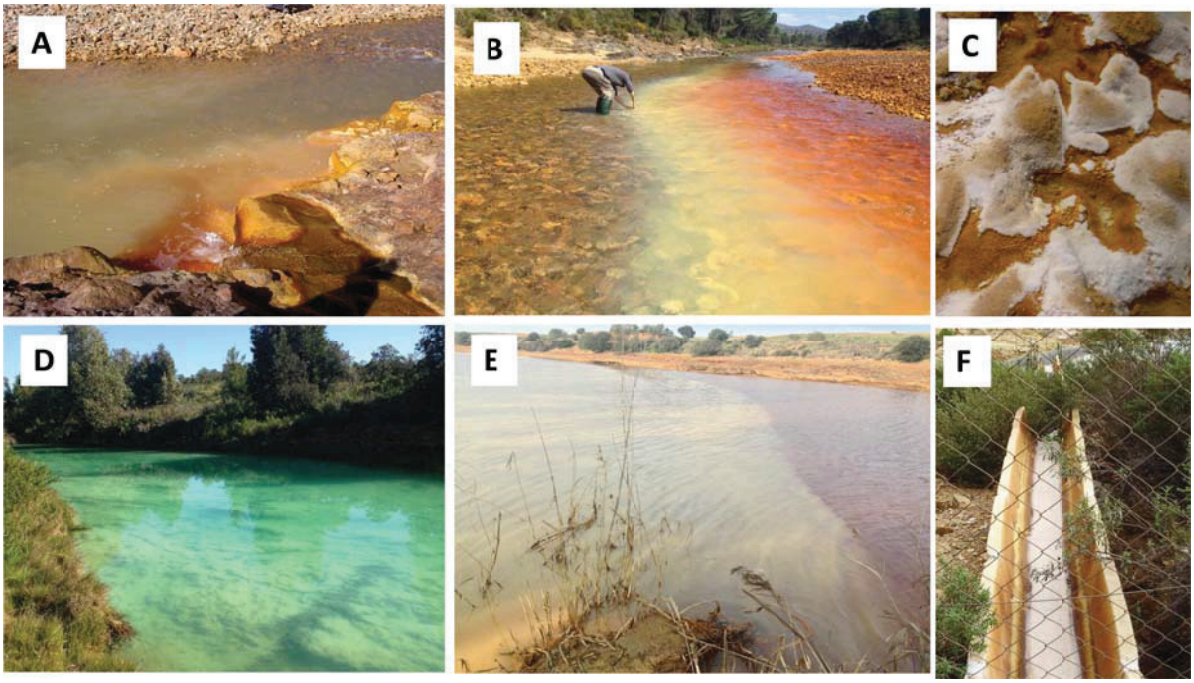

Figure 2. Pictures of the sampling sites: A) precipitation of ferrihydrite (reddish) and basaluminite (whitish) at the mixing point of the Mina Poderosa acidic discharge and the Odiel river; B) precipitation of schwertmannite (reddish) and basaluminite (whitish) at the mixing point of Agrio acidic discharge (right hand of the picture) and the Odiel river; C) detail of basaluminite precipitates in the Mina Torerera stream; D) basaluminite covering the bed of the Dehesa Boyal stream; E) basaluminite precipitation at the mixing point of a neutral stream (lower left) and the Tinto river (right); F) basaluminite precipitation at bottom of the outflow channel of the Mina Esperanza treatment plant.

2.3 Arroyo del Val site

The information corresponding to the Arroyo del Val area is mainly extracted from Auqué et al. (1993) and Gimeno (1999). The Arroyo del Val is located between the villages Luesma and Fombuena, approximately 70 km SW of Zaragoza, Spain. The area is in the Iberian Mountains, and it has an inland Mediterranean climate, with cold winters and warm and dry summers and an average rainfall of 500 mm, most of which falls in spring. The studied section of the Arroyo del Val stream is approximately 3 km long and features a flow rate of more than 10 L/s after rain events and less than 1 L/s during the summer. The stream flows across a monotonous series of dark brown to black shales of Silurian age that crop out in the drainage basin. The black shale contains abundant dispersed sulfides, mainly pyrite, which generates ubiquitous acid rock drainage (ARD) after weathering.

In contrast to most of the Odiel sites, the Arroyo del Val is an acidic stream that receives several neutral tributaries of near-neutral pH (Fig. 3). The mixing of waters yields iron-rich and especially aluminum-rich flocculates which are deposited at and downstream of the confluences. Water (labeled with a W) and solid (labeled with a C) samples were collected in three different campaigns, and only pairs of coexisting water and precipitate samples were selected: 1991 (W5-CV1), 1994 (W9-C9; W12-C12) and 1996 (Wexp-Cexp). As in the Odiel-Tinto area, the field parameters were measured, and the water samples were successively filtered through 2, 0.45 and 0.1 μm filters, acidified with ultrapure HNO_3 and refrigerated at 4°C until analysis. Solid samples were collected from the riverbed, dried and dissolved with HNO_3, and the solutions were stored for analysis.

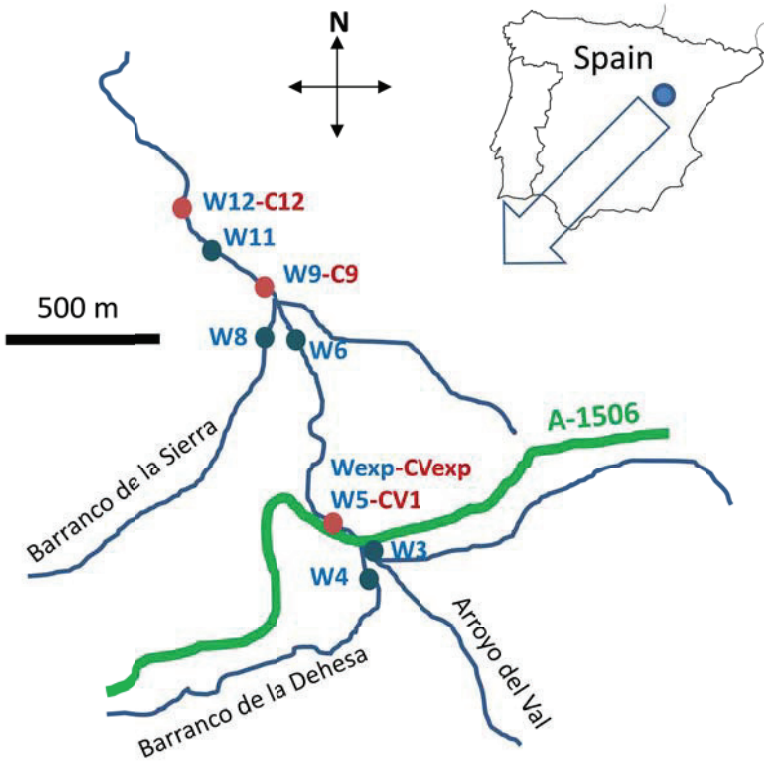

Figure 3. Sketch of the Arroyo del Val system. Each letter corresponds to different samples (W= water; C= precipitates).

2.4 Analysis

For the Odiel-Tinto sampling campaign, the field parameters, such as pH, Eh, temperature (T) and EC, were measured in situ with properly calibrated Hanna portable instruments (probe types HI9025C, HI9033 and HI9025).

The major cations (Na, K, Al, Fe, Ca, Mg, Zn, Fe, Mn and Si) and total S of the water samples and solid digestions were measured by inductively coupled plasma atomic emission spectroscopy (ICP-AES, Perkin-Elmer Optima 3200 RL), and the trace metals (Ni, Cd, Co, Pb) and REE (La, Ce, Pr, Nd, Sm, Eu, Gd, Tb, Dy, Ho, Er, Tm, Yb, Lu, Y and Sc) were measured with inductively coupled plasma mass spectrometry (ICP-MS, Perkin-Elmer SciexElan 6000). The detection limits were 0.1 mg/L for S, Na, and K; 0.05 mg/L for Ca, Mg, and Si; 0.02 mg/L for Fe, Zn, and Mn; 5 µg/L for Al; 1.5 µg/L for Cu and Ni; 0.5 µg/L for Pb; and 0.1 µg/L for As, Cd, Co and REE. Higher detection limits of up to 1 µg/L resulted from dilution of highly concentrated solutions. The analytical precision error was estimated to be approximately 7% for the ICP-AES measurements and 5% for the ICP-MS measurements. Two AMD laboratory standards were also checked for REE accuracy, yielding

deviations lower than 5% of the recommended values (Verplanck et al., 2001), except for Eu, which exhibited values 20% below the standard value.

The major mineral phases forming the solid samples were identified by X-ray diffraction (XRD) using a Bruker® D5005 X-ray diffractometer (XRD) with Cu Lα radiation. The samples were scanned from 0 to 60 degrees 2θ with a continuous scan at a rate of 0.025°/18 s. Granular material was also observed under a JEOL® JSM840 field emission scanning electron microscope with an Oxford Link® energy dispersive system (SEM-EDS).

For the Arroyo del Val site, the sampling and analytical procedures were very similar, and the details can be found in Auqué et al. (1993) and Gimeno (1999).

3 RESULTS

3.1 REE behavior in mixing streams

The chemical composition of the aqueous phase at each sampling point of the Odiel river stretch is listed in Table 1. These values will be compared with those resulting from the conservative mixing of the river and any acidic discharge. The theoretical concentration of any element in the river can be calculated as the addition of the concentrations of the element in the acidic tributary and in the river weighted based on their relative flows. The relative flows are calculated from the concentration of a conservative solute in the discharge and in the river upstream and downstream of the discharge by a simple mass balance calculation (Kimball et al., 2007). Magnesium was selected as a conservative solute because it forms very soluble salts and is practically absent in the solid phase analyses. Thus, the flow ratio between the discharge (Q_D) and the river (Q_1) was calculated as:

$$\frac{Q_D}{Q_1} = \frac{c_2 - c_1}{c_D - c_2} \quad (1)$$

where c_1 and c_2 are the Mg concentrations in the river upstream and downstream of the discharge point, respectively, and c_D is the Mg concentration in the discharge.

The measured concentration of several selected solutes in the river compared with that resulting from a theoretical conservative mixing is plotted in Fig. 4. Like Mg, most of the divalent metals (Ni, Co, Mn, Zn, and Cd) behaved conservatively and were not removed by the precipitates that formed

at the acidic discharge-river confluences, regardless of the final pH of the mixture (Fig. 4A). Although some amount of SO_4 was removed from the water by Fe and Al oxy-hydrosulfate precipitates, its high concentration made it a quasi-conservative solute (Fig. 4A). In contrast, Fe and As are clearly not conservative at both acidic and neutral pH values (Fig. 4B), indicating their removal by the precipitation of schwertmannite (Carlson et al., 2002; Fukushi et al., 2004). Aluminum and Cu showed an intermediate behavior (Fig. 4C). These elements are partially removed by precipitates in the upper part of the river, where its pH always remained above 6.5, and they behaved conservatively at low pH values when the acidic Agrio discharge caused the final pH of the river to be less than 3.5. Similar behavior was exhibited by the REE. The REE were completely removed by the precipitates that formed at pH values higher than 6.5, and they behaved conservatively at pH values below 3.5. This observation is consistent with the behavior described by previous authors (Ferreira da Silva et al., 2009; Gammons et al., 2005a; Verplanck et al., 2004) and suggests that, rather than schwertmannite, basaluminite is responsible for scavenging REE from water.

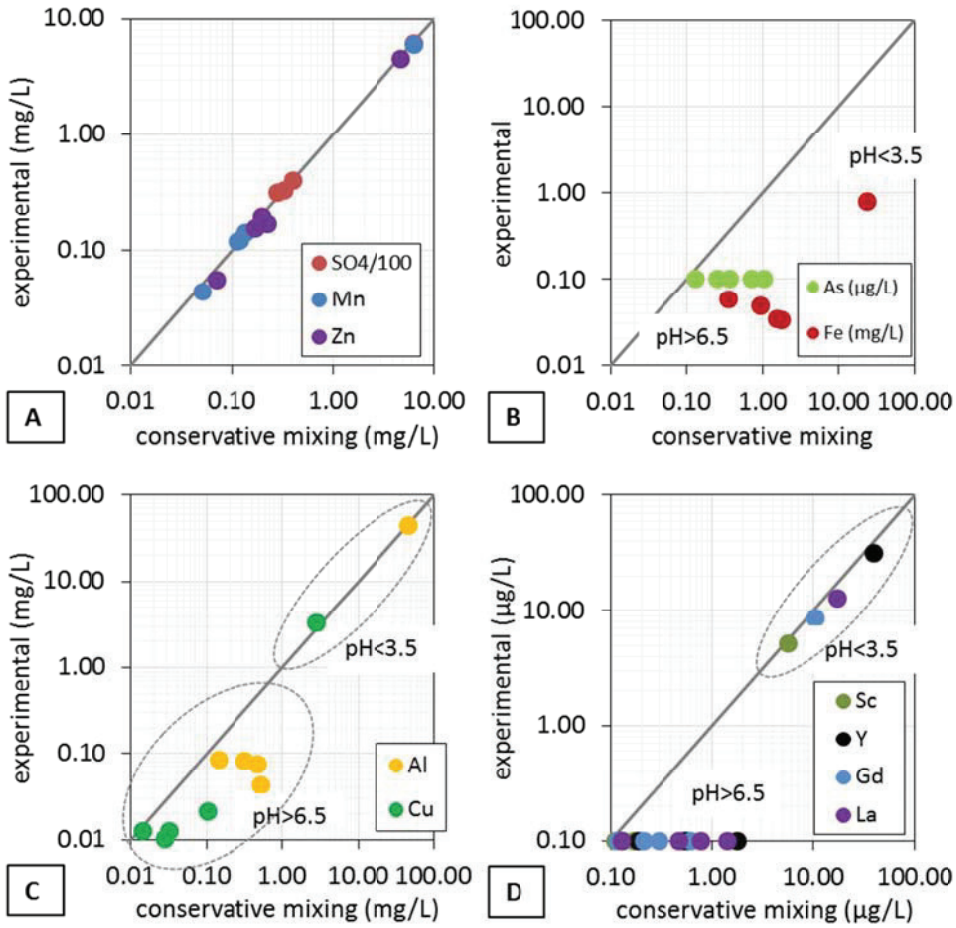

Figure 4. Comparison between experimental and conservative concentrations of selected elements in samples from the Odiel river after receiving acidic discharges.

The analyses of the acidic waters from the rest of the localities in the Odiel-Tinto area (DB, TO, RT and ET) are listed in Table 2. The Al and Fe concentrations varied from 120 to 750 mg/L, and their total REE concentrations ranged from 0.4 to 2 mg/L. These ranges are similar to those of the Odiel stretch described above (CN, SP, ES, PO and AG). Moreover, the filtrates coexisting with the solid precipitates sampled in the mixing zones were also analyzed for comparison (see the "-mix" samples in Table 2). These samples were clearly different from those of the acidic parent streams. With the exception of ET, these samples showed lower EC values, and the pH values ranged from 4.5 to 6.5; additionally, their Al, Fe and REE concentrations were all less than 13, 40 and 0.07 mg/L, respectively. The ET samples showed higher EC values because the treated water also had high sulfate concentrations, and Al and Fe were replaced by Ca from calcite dissolution.

The water analyses from the selected Arroyo del Val stretch are listed in Table 3. Unlike the Odiel-Tinto area, here, the main flow was acidic, and the tributaries supplied alkalinity to the mixture. Another relevant difference was the sulfate concentration of approximately 200 mg/L, which was lower than that in the Odiel-Tinto area by more than one order of magnitude. Additionally, the EC values and major and trace element concentrations were significantly lower. Thus, the Al and Fe concentrations were always less than 10 and 1 mg/L, respectively, and the REE concentrations were always less than 0.3 mg/L.

3.2 Precipitates

Reddish-ochre and whitish precipitates or mixtures were collected from all the localities. These materials are composed of spherical particles of less than 1 μm that clump together to form aggregates of larger size. In most of the reddish precipitates, the pink-cushion texture typical of schwertmannite can be distinguished, whereas only aggregates of spheres are observed in the whitish precipitates.

In general, the XRD profiles show many peaks corresponding to quartz, illite and feldspars. This makes the identification of poorly crystalline phases difficult unless silicates are absent or represent a very minor proportion. Thus, schwertmannite was only clearly identified in AG, DB and TO reddish precipitates floating in the water, and basaluminite was only clearly identified in whitish precipitates from AG, TO, DB and ET. In the rest of localities, the existence of basaluminite was deduced from the chemical analyses.

The analyses of the major and trace element concentrations in all the precipitates are shown in Table 4. The reddish precipitates from AG, which were identified as schwertmannite by XRD, showed a low Al content and a Fe/S ratio of 4.47 (Table 4, sample AG-r is an average of three samples), slightly lower than the range of 4.67 to 5.55 proposed for the natural variability of the mineral, $Fe_8O_8(OH)_{6-2x}(SO_4)_x \cdot nH_2O$, with x= 1 to 1.75 (Bigham et al., 1996). On the other hand, the whitish precipitates from AG, DB, TO and ET showed variable but minor Fe concentrations and Al/S ratios ranging from 4.32 to 6.26, higher than the theoretical basaluminite formula, $Al_4SO_4(OH)_{10} \cdot 5H_2O$, probably due to mixtures with Al hydroxides and/or the partial transformation of basaluminite into weakly crystalline boehmite and the release of SO_4 (Lozano et al., 2018). Finally, precipitates from PO and RT show high contents of both Al and Fe and have S concentrations below 3 wt% and (Fe+Al)/S ratios from 7.5 to 12, far above what is expected for schwertmannite and basaluminite. These samples are associated with water mixtures with pH values above 6, and the samples are interpreted as mixtures of schwertmannite and basaluminite with Al and Fe hydroxides (Bigham et al., 1996; Nordstrom and Alpers, 1999). Silica was present in all basaluminite analyses, with Al/Si molar ratios between 21 and 180, with the highest ratio in DB, 500 m from the water mixing. A similar distribution of Al/Si ratios was reported by Caraballo et al. (2019).

No mineral phases other than clay minerals, K-feldspar and plagioclase were identified in the precipitates from Arroyo del Val (Auqué et al., 1993). Chemical analyses of the bulk solids were also absent, although Gimeno (1999) reported that the precipitates were composed of Al (16 to 18 wt.%), Fe (25 to 29 wt.%) and S (6 to 11%), with minor amounts of Si (1 to 6 wt.%). Moreover, microprobe analyses of the whitish amorphous phase reveal the ubiquitous presence of S, with ((Al+Fe)/S) ratios close to 4, which indicates that schwertmannite and basaluminite could be the major phases.

More interestingly, REE were retained in the basaluminite from AG in a total amount higher than 400 mg/kg when this mineral was the major phase (AG, Table 4). In contrast, very low or below detection level concentrations were observed in the reddish precipitates of AG (AG-r, Table 4). This finding confirms that basaluminite rather than schwertmannite was responsible for the REE retention in the solid phase. This result is consistent with the composition of the pore water from the limestone columns used to treat the AMD. There, the REE concentrations in the pore water were similar or even higher than that of the AMD inflow in the schwertmannite zone, and REE concentrations decreased together with Al and Cu concentrations in the basaluminite zone (Ayora et al., 2016). A similar pattern was observed in the NaOH-based neutralization of an acidic leachate

from coarse coal debris. There, the REE were attached to Al-rich precipitates that formed at pH values between 4.8 and 6.1 and were absent in the schwertmannite that formed at lower pH values (Zhang and Honaker, 2018). Therefore, the REE partitioning between the aqueous and solid phases is modeled here assuming sorption onto basaluminite.

4 Discussion

4.1 Modeling REE concentrations in the solid phase

4.1.1 Aqueous speciation

The activity of the aqueous species was calculated by the PHREEQC code (Parkhurst and Appelo, 1999) using the Donnee Thermoddem_V1.10.dat database compiled by the Bureau de Recherches Géologiques et Minières (Blanc et al., 2012). The database has been updated with the stability constants at zero ionic strength and 25°C for the following inorganic complexes for lanthanides and yttrium: $LnCO_3^+$, $LnCO_3^{2-}$ and $LnHCO_3^{2+}$ (Luo and Byrne, 2001); $LnSO_4^+$ (Schijf and Byrne, 2004); $LnOH^{2+}$ (Klungness and Byrne, 2000), $LnOH_2^+$ and $LnOH_3$ (Lee and Byrne, 1992); $LnCl^{2+}$ (Luo and Byrne, 2001); LnF^{2+} and LnF_2^+ (Luo and Millero, 2004); and $LnNO_3^{2+}$ (Millero, 1992). The Sc aqueous complexes $Sc(OH)^{2+}$, $Sc(OH)_2^+$, $Sc(OH)_3$, and $ScSO_4^+$ were incorporated into the database (Wood and Samson, 2006). Log k values for aqueous species are compiled in Table S1 of the Supplementary Information.

The presence of sulfate in solution affects REE aqueous speciation because it forms strong complexes with REE (Gimeno et al., 2000). The proportion of the REE-sulfate complex (MSO_4^+) increases with sulfate concentration and is predominant at sulfate concentrations above 100 mg/L. Therefore, the aqueous species MSO_4^+ is the overwhelmingly dominant aqueous REE species in all the acidic streams and mixtures.

4.1.2 Surface complexation modeling

Lozano et al. (2019a) performed sorption experiments of REE onto basaluminite at different pH values and SO_4 concentrations. Owing to the predominance of sulfate complexes in the aqueous phase, the experiments were modeled by assuming that the aqueous MSO_4^+ complex exchanges with n protons from n surface sites XOH:

$$MSO_4^+ + nXOH = (XO)_nMSO_4^{1-n} + nH^+ \qquad K_M \qquad (2)$$

The equilibrium constant K_M of the reaction for each REE (M) is:

$$K_M = \frac{\{(XO)_nMSO_4^{1-n}\}\cdot a_{H^+}^n}{a_{MSO_4^+}\cdot\{XOH\}^n} \qquad (3)$$

Where $a_{MSO_4^+}$ and a_{H+} are the activities of the aqueous complex and proton, respectively, and $\{(XO)_nMSO_4^{1-n}\}$ and {XOH} account for the mole fraction of the sorbed species and free surface sites, respectively.

From the experimental values, (Lozano et al., 2019a) proposed a value of n=1 (monodentate complexes). This result is in agreement with the formation of a monodentate inner sphere complex of the YSO_4^+ aqueous species and basaluminite surface, suggested by Extended X-ray absorption fine structure (EXAFS) and high-energy X-ray scattering (HEXS) (Lozano et al., 2019b). Scandium speciation differed from the rest of the REE, and bidentate surface complexes with $ScSO_4^+$ and $ScOH^{2+}$ were proposed.

The equilibrium constants of Eq. 2 for basaluminite are listed in Table S2, and the variations in the sorbed fraction with pH resulting from the model at 2000 mg/L SO_4 are plotted in Fig. 5. The sorbed fraction curves for lanthanides and yttrium show a significant sorption from pH 5 whereas sorption of Sc occurs at pH values that are one unit lower, from pH 4.

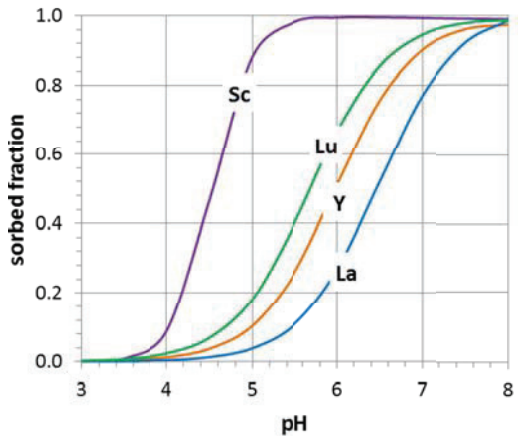

Figure 5. Variations in the sorbed fraction in basaluminite with pH for four selected REEs, as calculated from the model described in Lozano et al. (2019a) for a solid:liquid ratio of 1 g/L.

4.2 Comparison between predicted and analyzed concentrations

According to Eq. 2, the REE concentration of the aqueous phase (and the activity of its aqueous species, $a_{MSO_4^+}$), and the free sorption sites (obtained from the total sorption sites) were needed to predict the REE concentration in the solid phase.

The aqueous phase coexisting with the basaluminite precipitates at the mixing points from the Odiel-Tinto localities contained very low amounts of REE (the "–mix" samples in Tables 1 and 2) and cannot justify the REE concentration measured in the solid phase. This is because practically the entire REE content of the acidic tributaries has already been transferred to the solid particles, and the "–mix" aqueous phase is mainly composed of the main flow of neutral water carrying precipitates in suspension. Therefore, the REE concentration of the acidic stream was used as a base to calculate the activity of the aqueous species. In the case of Arroyo del Val, where the acidic water was the main flow, only a minor dilution took place, and the difference between the acidic water upstream and that of the mixing was used in the calculations (Table 3). To estimate the concentration of total sorption sites, T_{XOH} (mol/L), we assume that the entire Al was transferred from the aqueous to the solid phase and the difference between the Al concentration of the acidic stream and that of the mixture was used, and converted stoichiometrically into basaluminite:

$$T_{XOH} = \frac{[Al]\cdot M_{bas}\cdot}{4M_{Al}\cdot}\frac{S\cdot\sigma\cdot 10^{18}}{N_A} \qquad (4)$$

where the first fraction is the solid:liquid ratio (mg/L), [Al] is the Al concentration (mg/L) of the acidic stream minus that of the mixture; M_{Al} and M_{bas} are the molar masses of Al and basaluminite, respectively; S is the specific surface area (m^2/mg); σ represents the sites obtained from the basaluminite structure (4.6 sites/nm^2 according to Lozano et al. 2019a); and N_A is Avogadro's number. The specific surface area of the precipitates from IPB sites was also determined and ranged from 0.020 to 0.060 m^2/mg. These values were not available for samples from Arroyo del Val. Thus, the specific surface area of these precipitates was assumed to be 0.068 m^2/mg, the measured value for synthetic basaluminite (Lozano et al., 2019a). The resulting T_{XOH} values are also included in Table 4.

Both the calculated and measured REE concentrations in the solid phase were normalized to the North American shale composite (NASC) standard (Gromet et al., 1984) and compared. The predicted REE concentrations were higher or lower than the observed REE concentrations. This discrepancy could be due to several uncertainties and it is discussed below. In order to facilitate the comparison of the measured and calculated REE patterns, the calculated concentrations were

arbitrarily multiplied by a factor f until both observed and calculated Gd values coincided (Fig. 6A). Gadolinium was selected because it occupies a central location in the lanthanide series.

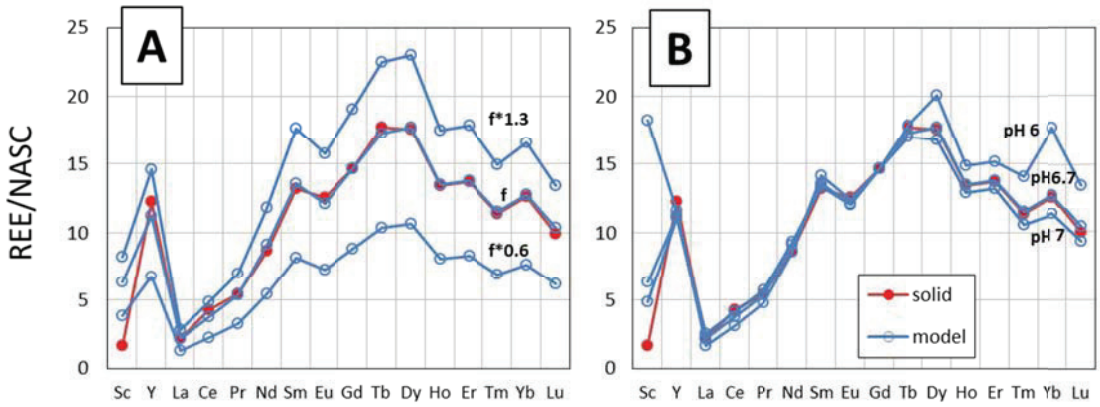

Figure 6. NASC-normalized REE distribution patterns in basaluminite calculated for three different factors f (A) and pH (B) values (blue symbols). The REE patterns measured in basaluminite (red circles) are plotted for comparison.

The pH value at which sorption occurred can be estimated from the REE distribution pattern. According to the sorption variation with pH calculated with the model, the different REE undergo very different sorption efficiencies at a given pH (Fig. 5). Thus, at pH 5, 85%, 19% and 4% of Sc, Lu and La are sorbed, respectively. At pH 7, sorption proportions are much more equilibrated, and 100%, 96% and 76% of Sc, Lu and La are sorbed, respectively. The consequence of this different sorption affinity on the REE distribution pattern is relevant (Fig. 6B). Thus, calculations performed at pH 6 predict more HREE and Sc to be sorbed than LREE, and their relative values are overpredicted with respect to measurements. The reverse reasoning can be made for calculations at pH 7 (Fig. 6B). Therefore, the REE distribution pattern is highly dependent on the sorption pH, and, inversely, the REE distribution pattern can provide information about the sorption pH. In summary, the final calculated patterns were obtained by manually selecting the factor f and pH values that allow the best fit between the predictions and the observations. The best fits of the REE patterns of calculated and measured solids together with the pH and factor f values are plotted in Figs. 7 and 8.

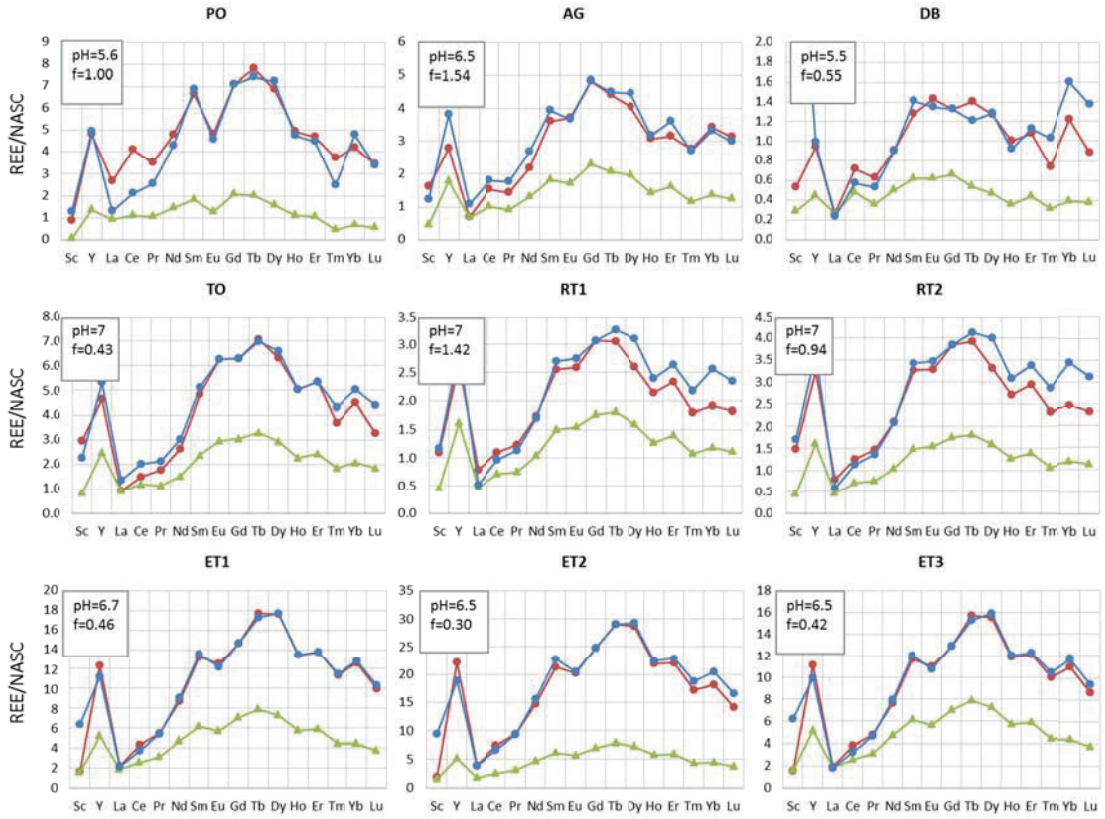

Figure 7. REE patterns of precipitates from the Odiel field area: analyzed (red) and predicted (blue). The concentrations in the parent AMD (green triangles) are also plotted for comparison. All the concentrations in the solids are normalized to the North American shale composite (NASC) and scaled to the same Gd value.

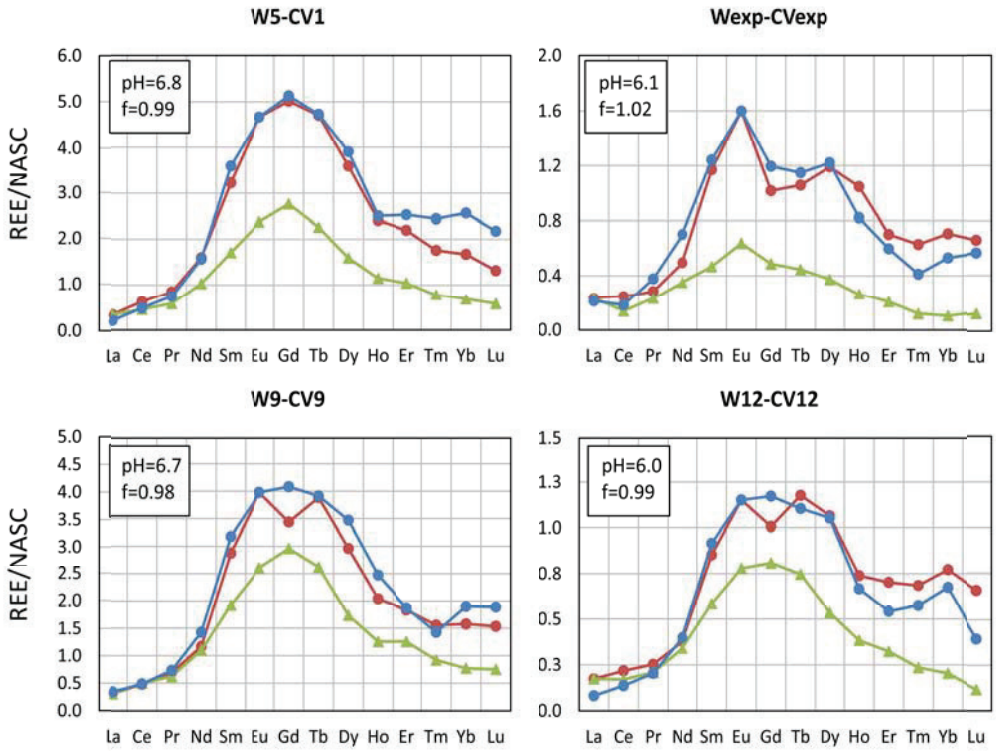

Figure 8. REE patterns of solid precipitates from the Arroyo del Val field area: analyzed (red) and predicted (blue). The concentrations of the parent AMD (green triangles) are also plotted for comparison. All the concentrations in the solids are normalized to the North American shale composite (NASC) and scaled to the same Eu value.

A f value lower than 1 indicates that the calculated values of REE sorption were higher than those measured from the collected solids, and the product by a factor lower than 1 was therefore required to fit the pattern. The reverse holds for f values higher than 1. The model predicted the observed trend of REE values within the order of magnitude (f varies from 0.3 to 1.5). The f values that are different from unity are attributed to uncertainties in one or several parameters used in the calculations: the specific surface area, which was not measured in some cases, the solid:liquid (S:L) ratio calculated from the Al removal from the acidic source (Eq. 4) and the exact pH at which sorption actually occurred.

Table 5. Effect of parameter variation on the factor f value to fit the observed patterns.

ET1	**S (m^2/g)**	**S:L (g/L)**	**pH**	**f**
Benchmarck	57	0.55	6.7	0.46
ΔpH	57	0.55	6.5	0.46*1.54
	57	0.55	6.9	0.46*0.64
ΔS	S*0.5	0.55	6.7	0.46*1.98
	S*2	0.55	6.7	0.46*0.49
ΔS:L	57	SL*0.5	6.7	0.46*1.98
	57	SL*2	6.7	0.46*0.49

To discuss the effect that the parameter uncertainty has on the factor f, a reasonable variation of each parameter keeping the rest constant was used in the calculations for the sample ET1 (Table 5). A variation of two decimals (±0.2) in the pH value still results in an acceptable manual fitting for the calculated REE patterns. If pH decreases only two decimals, sorption decreases and the factor f needs to increase by 1.54 times to fit the experimental pattern. Oppositely, if the pH increases two decimals, the factor f has to decrease 0.64 times. The specific surface area measured in the samples ranged from 16 to 57 m^2/g. If the model is run with a decrease of half or double of the specific surface area, an f factor almost double or half is required to fit the experimental pattern, respectively. Finally, since solid:liquid ratio multiplies the specific surface area in the calculation of total sorption sites (Eq. 4), their effect on f is equivalent to that described for the specific surface area.

From the comparison of the REE patterns of the original acid water and the solid phase (both measured and calculated), it is evident that the main trends of the REE distribution of the water are

transferred to the solid phase (Fig. 7 and 8). Thus, all the NASC-normalized REE patterns of waters and precipitates show a typical convex curvature indicating enrichment in MREE with respect to LREE and HREE, which has also been described for other acid drainages (Ferreira da Silva et al., 2009; Pérez-López et al., 2010; Sahoo et al., 2012). In detail, differences between calculated and measured REE concentrations in the solid are not systematic, and a particular element is sometimes slightly over- or underpredicted depending on the sample. This is especially true for some HREE and for some Arroyo del Val samples, where the concentrations are close to the analytical detection limit.

All the water samples from the Odiel-Tinto basins show a characteristic negative Eu anomaly, although this anomaly varies from acute in PO, ET and AG to less acute in other points of the Odiel-Tinto area (Fig. 7). Similar negative Eu anomalies have been described in samples recovered from felsic igneous rocks in a region of Eastern Canada (Leybourne and Johannesson, 2008). The Eu anomaly is absent in the samples from the Arroyo del Val site (Fig. 8). The reason for this different pattern seems related to the different lithological types found in the two regions, with felsic volcanic in the Odiel-Tinto area and sedimentary black shales in the Arroyo del Val. As an exception, some precipitates from Arroyo del Val show a negative anomaly in Gd that is not observed in the aqueous phase (and neither confirmed by the model), and could be due to an analytical artifact. In this case, the REE/NASC plots were scaled with Eu (Fig. 8).

According to laboratory experiments (Lozano et al., 2019c), REE sorption on schwertmannite occurs significantly at pH values higher than 5 (pH higher than 4 for Sc), and consistently, no REE was detected in three samples of schwertmannite precipitates (averaged as AG-r in Table 4) where the pH of the coexisting water ranged from 2.8 to 3.4 (AG and AG-mix1 in Table 1). This finding suggests that no REE (including Sc) would be scavenged by the schwertmannite precipitates that frequently cover the bed of many acidic streams and that they could be entirely recovered in treatment plants REE (Ayora et al., 2016; Zhang and Honaker, 2018). Nevertheless, owing to its much higher price, additional sampling of water and schwertmannite precipitates in acid drainages with pH values between 3 and 4 would be needed to confirm the Sc mobility.

Scandium samples from the Odiel-Tinto area showed no systematic differences between calculated and measured concentrations, with the exception of those from the Mina Esperanza treatment. There, the model systematically overpredicted the Sc concentration in the outflow of the treatment system (ETs, in Fig. 7). Therefore, part of the Sc from the acidic water seems to be selectively retained in a solid phase. Indeed, as observed in a column experiment emulating an AMD treatment with limestone, due to the high solid:liquid ratio, part of the Sc remained adsorbed on schwertmannite at pH as low as 3.5, whereas the rest of REE were completely mobile when the

acidic water front progressed in the treatment (Lozano et al., 2019c). Similar preferential fractionation of Sc to the solid phase at low pH values was observed when neutralizing a leachate from coal waste with NaOH (Zhang and Honaker, 2018).

The model matched the observed trend of REE values within the order of magnitude. But it is necessary to analyze the feasibility of the model to anticipate the REE concentration in the precipitates from the composition of the aqueous phases and the mixing ratios (blind prediction). Firstly, the amount of basaluminite particles that would form from the Al dissolved in the acidic stream can be diluted or dispersed in the mixture. This process could affect the solid:liquid ratio when sorption took place, and therefore account at least in part for the f factor value. The dilution of the acidic water in the final mixture (Q_D/Q_2 following the notation of Eq. 1) was independently calculated using the sulfate concentrations. Sulfate is a quasi-conservative solute with concentrations far above the detection limit and yields consistent mixing proportions in the samples from all the studied localities. According to Figure 9A, no correlation between dilution and the f factor values are observed, and therefore, no approximation to the f factor value can be anticipated from the composition of the mixing waters. Secondly, another source of uncertainty is the anticipation of the pH at which sorption occurs. Again, Figure 9B shows that no correlation can be observed between the pH obtained from the fitting of the measured REE patterns and the pH measured in the water coexisting with the collected precipitates. Similar lack of correlation can be deduced by comparing the adsorption pH with that pH anticipated from the mixing proportions of acidic and alkaline waters (not represented). All these calculations assume that all the reactions occur in a closed system. However, if reactions are not synchronous in an open flow setting, total masses may not be conservative. Thus, basaluminite starts to form early as the pH increases above 4, whereas significant REE sorption occurs at pH values between 5 and 7, at which point some of the basaluminite may have been transported downstream. Since the pH and f factor values required to fit the calculated and measured REE patterns cannot be independently anticipated from the composition and proportions of the mixing waters, the model cannot be used for blind predictions of the REE concentration of the precipitates in open flow systems.

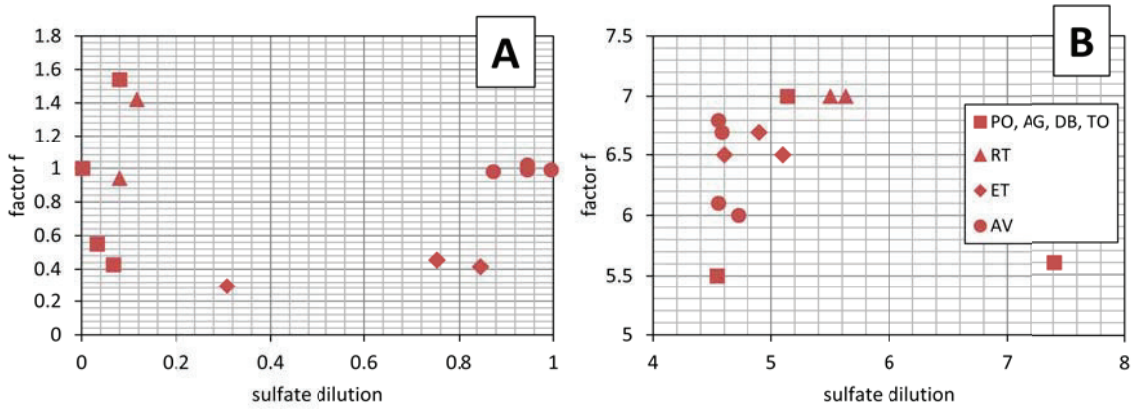

Figure 9. A) Dilution of AMD calculated from sulfate versus the f factor required to fit the observed and calculated REE patterns of the samples analyzed. B) pH measured in the water coexisting with the precipitates versus the pH obtained from fitting the REE concentrations measured and calculated with the model.

5 CONCLUSIONS

When an acid drainage mixes with a near-neutral stream, a mixture of schwertmannite and basaluminite precipitates. In all the cases studied, the behavior of REE during the mixing is conservative at low pH values (pH<4), whereas REE are scavenged by the flocculates at near-neutral pH values. This behavior is similar to that of Al and Cu and differs from that of Fe and As, which are partially removed at lower pH values, and different from that of divalent metals (Zn, Mn, Cd, and Co), which remain in solution at all observed pH values. This finding confirms the observations made by previous studies and suggests that Al phases could be responsible for REE retention. Indeed, when Fe and Al phases can be sampled separately, schwertmannite does not contain REE, which are entirely retained in basaluminite, confirming that the latter is the main phase responsible for the REE removal.

According to laboratory sorption experiments, both schwertmannite and basaluminite adsorb REE at pH values of 5 to 7. Therefore, the lack of REE in schwertmannite is attributed to the formation of this mineral at pH values below 4, whereas basaluminite precipitation occurs at pH values higher than 4. Scandium adsorbs onto the solid particles at pH values one unit lower than the rest of the REE (pH 4 to 6), but it seems to behave similar as the other REE in acidic streams with pH values below 4. Consequently, no REE including Sc would be scavenged in the schwertmannite precipitates frequently covering the bed of many acidic streams, and therefore, they could be entirely recovered in the AMD treatment plants.

A non-electrostatic surface complexation model of the MSO_4^+ aqueous species (M representing REE), with the exchange of one proton with the basaluminite surface, has been used to predict the REE removal in several cases of mixing between acidic and neutral waters. In the case of Sc, an additional species $Sc(OH)_2^+$ and the exchange of two protons were required. The sorption capacity of the solid phase can be estimated from the difference between the Al initially dissolved in the acidic water and the final concentration in the mixture. The model is able to match the REE distribution patterns observed in the solid phase, regardless of the sulfate concentration in the acid drainage. These distribution patterns confirm the preferential sorption of MREE, HREE and Y over LREE. However, the model fails to predict the REE concentrations in the precipitates from the composition and proportions of the mixing streams, due to the asynchronous precipitation of basaluminite and REE adsorption in an open fluid setting.

Acknowledgments

This work has been funded by the European EIT-Raw Materials 'Morecovery' and the Spanish SCYRE (CGL2016-78783-C2-R) and CAPOTE (CGL2017-86050-R) projects. A. L. was also funded by the FPI grant (BES-2014-069978). The authors wish to thank J. Bellés, M. Cabañas, R. Bartrolí and N. Moreno (IDAEA-CSIC) for their analytical assistance.

References

Adebayo, S.B., Cui, M., Hong, T., White, C.D., Martin, E.E., Johannesson, K.H., 2018. Rare earth elements geochemistry and Nd isotopes in the Mississippi River and Gulf of Mexico Mixing Zone. Front. Mar. Sci. 5, 1–18. https://doi.org/10.3389/fmars.2018.00166

Alonso, E., Sherman, A.M., Wallington, T.J., Everson, M.P., Field, F.R., Roth, R., Kirchain, R.E., 2012. Evaluating Rare Earth Element a Vailability : a Case With Revolutionary Demand From Clean Technologies. Environ. Sci. Technol. 46, 3406–3414. https://doi.org/10.1021/es203518d

Auqué, L.F., Tena, J.M., Gimeno, M.J., Mandado, J., Zamora, A., López Julián, P.L., 1993. Distribución de tierras raras en soluciones y coloides de un sistema natural de aguas ácidas (Arroyo del Val, Zaragoza). Estud. Geol. 49, 41–48. https://doi.org/10.3989/egeol.93491-2336

Ayora, C., Macías, F., Torres, E., Lozano, A., Carrero, S., Nieto, J.M., Pérez-López, R., Fernández-Martínez, A., Castillo-Michel, H., 2016. Recovery of Rare Earth Elements and Yttrium from Passive-Remediation Systems of Acid Mine Drainage. Environ. Sci. Technol. 50, 8255–8262. https://doi.org/10.1021/acs.est.6b02084

Bau, M., 1999. Scavenging of dissolved yttrium and rare earths by precipitating iron oxyhydroxide: Experimental evidence for Ce oxidation, Y-Ho fractionation, and lanthanide tetrad effect. Geochim. Cosmochim. Acta 63, 67–77. https://doi.org/10.1016/S0016-7037(99)00014-9

Bigham, J.M., Schwertmann, U., Traina, S.J., Winland, R.L., M., W., 1996. Schwertmannite and the chemical modeling of iron in acid sulfate waters. Geochim. Cosmochim. Acta 60, 2111–2121.

Blanc, P., Lassin, A., Piantone, P., Azaroual, M., Jacquemet, N., Fabbri, A., Gaucher, E.C., 2012. Thermoddem: A geochemical database focused on low temperature water/rock interactions and waste materials. Appl. Geochemistry 27, 2107–2116. https://doi.org/10.1016/j.apgeochem.2012.06.002

Caraballo, M.A., Macías, F., Nieto, J.M., Ayora, C., 2016. Long term fluctuations of groundwater mine pollution in a sulfide mining district with dry Mediterranean climate: Implications for water resources management and remediation. Sci. Total Environ. 539, 427–435. https://doi.org/10.1016/j.scitotenv.2015.08.156

Caraballo, M.A., Macías, F., Nieto, J.M., Castillo, J., Quispe, D., Ayora, C., 2011a. Hydrochemical performance and mineralogical evolution of a dispersed alkaline substrate (DAS) remediating the highly polluted acid mine drainage in the full-scale passive treatment of Mina Esperanza (SW Spain). Am. Mineral. 96, 1270–1277. https://doi.org/10.2138/am.2011.3752

Caraballo, M.A., Macías, F., Rötting, T.S., Nieto, J.M., Ayora, C., 2011b. Long term remediation of highly polluted acid mine drainage: A sustainable approach to restore the environmental quality of the Odiel river basin. Environ. Pollut. 159, 3613–3619. https://doi.org/10.1016/j.envpol.2011.08.003

Caraballo, M.A., Wanty, R.B., Verplanck, P.L., Navarro-Valdivia, L., Ayora, C., Hochella, M.F., 2019. Aluminum mobility in mildly acidic mine drainage: Interactions between hydrobasaluminite, silica and trace metals from the nano to the meso-scale. Chem. Geol. 519, 1–10. https://doi.org/10.1016/j.chemgeo.2019.04.013

Carlson, L., Bigham, J.M., Schwertmann, U., Kyek, ., Wagner, F., 2002. Scavenging of As from Acid Mine Drainage by Schwertmannite and Ferrihydrite : A Comparison with Synthetic Analogues Scavenging of As from Acid Mine Drainage by Schwertmannite and Ferrihydrite : A Comparison with Synthetic Analogues. Environ. Sci. Technol. 36, 1712–1719. https://doi.org/10.1021/es0110271

Chakhmouradian, A.R., Wall, F., 2012. Rare earth elements: Minerals, mines, magnets (and more). Elements 8, 333–340. https://doi.org/10.2113/gselements.8.5.333

Connelly, N.G., Hartshorn, R.M., Damhus, T., Hutton, A.T., 2005. Nomenclature of Inorganic Chemistry IUPAC Recommendations 2005, Royal Society of Chemistry.

Dai, Y., Li, Jian, Li, Jie, Yu, L., Dai, G., Hu, A., Yuan, L., Wen, Z., 2002. Effects of Rare Earth Compounds on Growth and Apoptosis of Leukemic Cell Lines. Vitr. Cell. Dev. Biol. - Anim. 38, 373–375. https://doi.org/10.1290/1071-2690(2002)038<0373:eoreco>2.0.co;2

European-Commission, 2017. Study on the review of the list of critical raw materials, European Commission. https://doi.org/10.2873/876644

Ferreira da Silva, E., Bobos, I., Xavier Matos, J., Patinha, C., Reis, A.P., Cardoso Fonseca, E., 2009. Mineralogy and geochemistry of trace metals and REE in volcanic massive sulfide host rocks, stream sediments, stream waters and acid mine drainage from the Lousal mine area (Iberian Pyrite Belt, Portugal). Appl. Geochemistry 24, 383–401. https://doi.org/10.1016/j.apgeochem.2008.12.001

Fukushi, K., Sato, T., Yanase, N., Minato, J., Yamada, H., 2004. Arsenate sorption on schwertmannite. Am. Mineral. 89, 1728–1734. https://doi.org/10.2138/am-2004-11-1219

Gammons, C.H., Nimick, D.A., Parker, S.R., Cleasby, T.E., McCleskey, R.B., 2005a. Diel behavior of iron and other heavy metals in a mountain stream with acidic to neutral pH: Fisher Creek, Montana, USA. Geochim. Cosmochim. Acta 69, 2505–2516. https://doi.org/10.1016/j.gca.2004.11.020

Gammons, C.H., Wood, S.A., Pedrozo, F., Varekamp, J.C., Nelson, B.J., Shope, C.L., Baffico, G., 2005b. Hydrogeochemistry and rare earth element behavior in a volcanically acidified watershed in Patagonia, Argentina. Chem. Geol. 222, 249–267. https://doi.org/10.1016/j.chemgeo.2005.06.002

Gimeno, M.J., Auqué Sanz, L.F., Nordstrom, D.K., 2000. REE speciation in low-temperature acidic waters and the competitive effects of aluminum. Chem. Geol. 165, 167–180. https://doi.org/10.1016/S0009-2541(99)00166-7

Gromet, L.P., Dymek, R.F., Haskin, L.A., Korotev, R.L., 1984. The “North American Shale Composite”: Its compilations, major and trace element characteristics. Geochim. Cosmochim. Acta 48, 2469–2482.

Kawabe, I., Ohta, A., Tokumura, M., Miyauchi, K., 1999. REE partitioning betweem Fe-Mn oxyhydroxide precipitates and weakly acid NaCI solutions : Convex tetrad effect and fractionation of Y and Sc from heavy lanthanides. Geochem. J. 33, 167–179.

Klungness, G.D., Byrne, R.H., 2000. Comparative hydrolysis behaviour of the rare earths and yttrium: the influence of temperature and ionic strength. Polyhedron 19, 99–107.

Lee, J.H., Byrne, R.H., 1992. Examination of comparative rare earth element complexation behavior using linear free-energy relationships. Geochim. Cosmochim. Acta 56, 1127–1137.

Leybourne, M.I., Johannesson, K.H., 2008. Rare earth elements (REE) and yttrium in stream waters, stream sediments, and Fe-Mn oxyhydroxides: Fractionation, speciation, and controls over REE + Y patterns in the surface environment. Geochim. Cosmochim. Acta 72, 5962–5983. https://doi.org/10.1016/j.gca.2008.09.022

Lozano, A., Ayora, C., Fernández-Martínez, A., 2019a. Sorption of rare earth elements onto

basaluminite: The role of sulfate and pH. Geochim. Cosmochim. Acta 258, 50–62. https://doi.org/10.1016/j.gca.2019.05.016

Lozano, A., Fernández-Martínez, A., Ayora, C., Di-Tomamaso, D., Poulain, A., Rovezzi, M., Marini, C., 2019b. Solid and Aqueous Speciation of Yttrium in Passive Remediation Systems of Acid Mine Drainage. Environ. Sci. Technol. https://doi.org/10.1021/acs.est.9b01795

Lozano, A., Fernández-Martínez, A., Ayora, C., Poulain, A., 2018. Local structure and ageing of basaluminite at different pH values and sulphate concentrations. Chem. Geol. 496, 25–33. https://doi.org/10.1016/j.chemgeo.2018.08.002

Luo, Y., Millero, F.J., 2004. Effects of temperature and ionic strength on the stabilities of the first and second fluoride complexes of yttrium and the rare earth elements. Geochim. Cosmochim. Acta 68, 4301–4308. https://doi.org/10.1016/j.gca.2004.05.025

Luo, Y.R., Byrne, R.H., 2001. Yttrium and Rare Earth Element Complexation by Chloride Ions at 25°C. J. Solution Chem. 30, 837–845.

Millero, F.J., 1992. Stability constants for the formation of rare earth inorganic complexes as a function of temperature and ionic strength. Geochim. Cosmochim. Acta 56, 3123–3132. https://doi.org/10.1016/j.gca.2006.09.019

Nieto, J.M., Sarmiento, A.M., Canovas, C.R., Olias, M., Ayora, C., 2013. Acid mine drainage in the Iberian Pyrite Belt: 1. Hydrochemical characteristics and pollutant load of the Tinto and Odiel rivers. Environ. Sci. Pollut. Res. 20, 7509–7519. https://doi.org/10.1007/s11356-013-1634-9

Nordstrom, D.K., 2011. Hydrogeochemical processes governing the origin, transport and fate of major and trace elements from mine wastes and mineralized rock to surface waters. Appl. Geochemistry 26, 1777–1791. https://doi.org/10.1016/j.apgeochem.2011.06.002

Nordstrom, D.K., Alpers, C.N., 1999. Chapter 6. Geochemistry of Acid Mine Waters, in: The Environmental Geochemistry of Mineral Deposits. pp. 133–160.

Nordstrom, D.K., Blowes, D.W., Ptacek, C.J., 2015. Hydrogeochemistry and microbiology of mine drainage: An update. Appl. Geochemistry 57, 3–16. https://doi.org/10.1016/j.apgeochem.2015.02.008

Ohta, A., Kawabe, I., 2000. Rare eath element partitioning between fe oxyhydroxide precipitates and aqueous NaCl solutions doped with NaHCO3: Determinations of rare earth element complexation constants with carbonate ions. Geochem. J. 34, 439–454. https://doi.org/10.2343/geochemj.34.439

Pagano, G., Guida, M., Tommasi, F., Oral, R., 2015. Health effects and toxicity mechanisms of rare earth elements-Knowledge gaps and research prospects. Ecotoxicol. Environ. Saf. 115, 40–48. https://doi.org/10.1016/j.ecoenv.2015.01.030

Parkhurst, D.L., Appelo, C.A.J., 1999. User's Guide to PHREEQC (VERSION 2) A Computer Program for Speciation, Batch Reaction, One Dimensional Transport, and Inverse Geochemical Calculations.

Pérez-López, R., Delgado, J., Nieto, J.M., Márquez-García, B., 2010. Rare earth element geochemistry of sulphide weathering in the São Domingos mine area (Iberian Pyrite Belt): A proxy for fluid-rock interaction and ancient mining pollution. Chem. Geol. 276, 29–40. https://doi.org/10.1016/j.chemgeo.2010.05.018

Pourret, O., Davranche, M., Gruau, G., Dia, A., 2007. Rare earth elements complexation with humic

acid. Chem. Geol. 243, 128–141. https://doi.org/10.1016/j.chemgeo.2007.05.018

Roncati, L., Gatti, A.M., Barbolini, G., Piscioli, F., Pusiol, T., Maiorana, A., 2018. In Vivo Uptake of Rare Earth Metals by Triple-Negative Breast Cancer Cells. Pathol. Oncol. Res. 24, 161–165. https://doi.org/10.1007/s12253-017-0209-3

Sahoo, P.K., Tripathy, S., Equeenuddin, S.M., Panigrahi, M.K., 2012. Geochemical characteristics of coal mine discharge vis-à-vis behavior of rare earth elements at Jaintia Hills coalfield, northeastern India. J. Geochemical Explor. 112, 235–243. https://doi.org/10.1016/j.gexplo.2011.09.001

Sánchez-España, J., López-Pamo, E., Santofimia, E., Aduvire, O., Reyes, J., Barettino, D., 2005. Acid mine drainage in the Iberian Pyrite Belt (Odiel river watershed, Huelva, SW Spain): Geochemistry, mineralogy and environmental implications. Appl. Geochemistry 20, 1320–1356. https://doi.org/10.1016/j.apgeochem.2005.01.011

Sánchez Espańa, J., Pamo, E.L., Pastor, E.S., Andrés, J.R., Rubí, J.A.M., 2006. The impact of acid mine drainage on the water quality of the Odiel river (Huelva, Spain): Evolution of precipitate mineralogy and aqueous geochemistry along the Concepción-Tintillo segment. Water. Air. Soil Pollut. 173, 121–149. https://doi.org/10.1007/s11270-005-9033-6

Schijf, J., Byrne, R.H., 2004. Determination of SO4β1 for yttrium and the rare earth elements at I = 0.66 m and t = 25°C- Implications for YREE solution speciation in sulfate-rich waters. Geochim. Cosmochim. Acta 68, 2825–2837. https://doi.org/10.1016/j.gca.2003.12.003

Sholkovitz, E.R., 1995. The aquatic chemistry of rare earth elements in rivers and estuaries. Aquat. Geochemistry 1, 1–34. https://doi.org/10.1007/BF01025229

Stewart, B.W., Capo, R.C., Hedin, B.C., Hedin, R.S., 2017. Rare earth element resources in coal mine drainage and treatment precipitates in the Appalachian Basin, USA. Int. J. Coal Geol. 169, 28–39. https://doi.org/10.1016/j.coal.2016.11.002

Tang, J., Johannesson, K.H., 2003. Speciation of rare earth elements in natural terrestrial waters: Assessing the role of dissolved organic matter from the modeling approach. Geochim. Cosmochim. Acta 67, 2321–2339. https://doi.org/10.1016/S0016-7037(02)01413-8

U.S. Geological Survey (USGS), 2019. Mineral Commodity Summaries, 2019th ed. Reston, Virginia.

Verplanck, P.L., Antweiler, R.C., Nordstrom, D.K., Taylor, H.E., 2001. Standard reference water samples for rare earth element determinations. Appl. Geochemistry 16, 231–244. https://doi.org/10.1016/S0883-2927(00)00030-5

Verplanck, P.L., Nordstrom, D.K., Taylor, H.E., Kimball, B.A., 2004. Rare earth element partitioning between hydrous ferric oxides and acid mine water during iron oxidation. Appl. Geochemistry 19, 1339–1354. https://doi.org/10.1016/j.apgeochem.2004.01.016

Wood, S.A., Samson, I.M., 2006. The aqueous geochemistry of gallium, germanium, indium and scandium. Ore Geol. Rev. 28, 57–102. https://doi.org/10.1016/j.oregeorev.2003.06.002

Zhang, W., Honaker, R.Q., 2018. Rare earth elements recovery using staged precipitation from a leachate generated from coarse coal refuse. Int. J. Coal Geol. 195, 189–199. https://doi.org/10.1016/j.coal.2018.06.008

Zhuang, G., Zhou, Y., Lu, H., Lu, W., Zhou, M., Wang, Y., Tan, M., 1996. Concentration of rare earth elements, As, and Th in human brain and brain tumors, determined by neutron activation analysis. Biol. Trace Elem. Res. 53, 45–49. https://doi.org/10.1007/BF02784543

GEOCHEMICAL BEHAVIOR OF RARE EARTH ELEMENTS IN ACID DRAINAGES: MODELING ACHIEVEMENTS AND LIMITATIONS

Tables

Table 1: Field parameters and chemical composition of the water samples from a selected Odiel river stretch

	A1	CN	A2	A3	SP	A4	ES	A5	PO	A6	A7	AG	A8	PO_mix	AG-mix1	AG-mix2
Sampling date	18/02/2015	18/02/2015	18/02/2015	18/02/2015	18/02/2015	18/02/2015	18/02/2015	18/02/2015	18/02/2015	18/02/2015	18/02/2015	18/02/2015	18/02/2015	18/02/2015	18/02/2015	18/02/2015
UTM X	706171.3	706120.8	706089.6	705606.7	704986	704839.5	704810.2	705189.6	705203.9	705121.6	703514.9	703481.4	703294.2	705203.9	703481.4	703481.4
UTM Y	4182969.4	4182952.1	4182906.3	4182340	4182025	4181329.5	4181227.3	4180732.4	4180651.7	4180570.7	4178344	4178232.8	4178192.1	4180651.7	4178232.8	4178232.8
pH	7.69	2.87	7.58	7.51	2.7	7.56	2.89	7.53	2.34	7.41	7.53	2.75	3.9	5.2	3.4	4.87
EC (mS/cm)	229	1085	233	233	6250	242	3779	246	4816	251	253	7250	1017	380	1271	407
Eh	327	679	310	220	570	312	648	321	704	303	294	657	455	254	449	427
temperature(ºC)	12.5	10.1	12.5	12.7	18.9	13	11.6	13.3	12.9	13.4	15.1	16.3	16.5	13.1	16.6	15
Alk (mg/L CaCO3)	130		115	118		115		111		108	102					
mg/L																
Al	0.08	23.49	0.04	0.04	222.9	0.08	90.7	0.08	171.5	0.08	0.10	605.0	44.12	3.1	79.0	1.1
Ca	19.68	18.06	19.55	19.69	162.7	20.41	258.2	19.73	137.8	20.04	20.05	170.9	30.20	19.7	47.0	30.0
Cu	0.00	1.39	0.01	0.02	13.5	0.01	3.1	0.01	39.2	0.02	0.02	36.6	3.35	0.1	7.5	0.8
Fe	0.07	44.64	0.05	0.05	1406.7	0.03	473.4	0.06	651.4	0.03	0.06	310.0	0.79	3.8	14.0	0.9
K	1.40	0.50	1.10	0.69	2.3	1.79	5.4	1.33	10.2	1.47	1.21	1.1	1.53	1.3	1.2	1.3
Mg	8.85	19.18	9.05	9.43	129.7	9.57	139.7	9.66	118.7	9.91	10.01	709.8	59.81	12.6	121.0	31.0
Mn	0.01	2.03	0.04	0.10	10.9	0.12	3.5	0.12	8.1	0.14	0.14	81.6	6.02	0.3	12.0	1.8
Na	10.27	10.01	10.59	10.40	25.3	10.80	29.1	10.74	59.1	10.54	10.52	31.0	17.47	10.7	15.0	14.0
SO4	11.10	471.26	19.45	21.96	5310.2	31.42	2669.9	32.75	3516.2	39.68	43.42	7726.8	613.81	142.5	441.0	239.0
Si	4.69	12.06	4.72	4.56	55.1	4.47	32.2	4.56	51.8	4.17	4.37	30.6	6.51	4.6	7.1	3.1
Zn	0.04	1.32	0.06	0.11	91.4	0.17	2.9	0.16	20.2	0.19	0.17	59.5	4.56	1.2	16.0	2.4
mg/L																
As	<0.1	1.7	0.1	<0.1	755.0	<0.1	226.5	<0.1	119.8	<0.1	<0.1	8.3	<0.1	<0.1	<0.1	<0.1
Cd	<0.1	6.3	0.1	<0.1	260.1	<0.1	23.8	0.1	129.8	0.1	0.1	372.5	31.0	<0.1	67.5	10.5
Co	<0.1	159.8	3.7	7.1	614.2	8.0	107.5	7.8	474.9	9.1	8.8	2053.5	160.7	27.4	405.0	69.1
Ni	<0.1	13.2	<0.1	1.6	80.0	1.5	47.4	1.9	96.7	2.0	2.0	945.8	79.9	8.1	207.9	30.3
Sc	<0.1	3.7	<0.1	<0.1	24.2	<0.1	15.8	<0.1	14.3	<0.1	<0.1	72.1	5.1	3.7	16.6	<0.1
Y	<0.1	22.3	<0.1	<0.1	379.3	<0.1	133.1	<0.1	735.5	<0.1	<0.1	508.7	31.8	11.1	140.4	7.6
La	<0.1	19.1	<0.1	<0.1	546.6	<0.1	45.0	<0.1	577.0	<0.1	<0.1	226.2	12.9	4.3	62.5	3.8
Ce	<0.1	46.9	<0.1	<0.1	1416.0	<0.1	109.3	<0.1	1479.5	<0.1	<0.1	718.2	42.6	19.3	198.4	11.0
Pr	<0.1	5.5	<0.1	<0.1	174.4	<0.1	22.3	<0.1	189.5	<0.1	<0.1	88.2	5.5	2.7	24.0	<0.1
Nd	<0.1	20.7	<0.1	<0.1	661.5	<0.1	105.4	<0.1	891.0	<0.1	<0.1	423.2	23.1	5.6	113.2	6.0
Sm	<0.1	5.3	<0.1	<0.1	163.3	<0.1	26.0	<0.1	219.4	<0.1	<0.1	115.6	7.3	1.8	31.4	<0.1
Eu	<0.1	0.1	<0.1	<0.1	21.7	<0.1	5.6	<0.1	31.8	<0.1	<0.1	22.8	1.2	<0.1	6.7	<0.1
Gd	<0.1	5.9	<0.1	<0.1	160.0	<0.1	22.7	<0.1	230.2	<0.1	<0.1	134.4	8.6	3.4	36.4	<0.1
Tb	<0.1	0.1	<0.1	<0.1	21.5	<0.1	4.5	<0.1	34.2	<0.1	<0.1	18.8	1.4	<0.1	5.6	<0.1
Dy	<0.1	5.0	<0.1	<0.1	100.3	<0.1	29.0	<0.1	174.9	<0.1	<0.1	116.0	7.9	2.1	30.7	<0.1
Ho	<0.1	0.1	<0.1	<0.1	15.0	<0.1	5.1	<0.1	28.3	<0.1	<0.1	19.2	1.4	<0.1	5.8	<0.1
Er	<0.1	2.4	<0.1	<0.1	33.7	<0.1	14.0	<0.1	69.0	<0.1	<0.1	56.4	3.9	1.3	15.3	<0.1
Tm	<0.1	0.1	<0.1	<0.1	3.4	<0.1	1.6	<0.1	5.0	<0.1	<0.1	6.6	<0.1	<0.1	1.8	<0.1
Yb	<0.1	1.9	<0.1	<0.1	19.3	<0.1	9.5	<0.1	42.9	<0.1	<0.1	45.4	3.0	<0.1	12.4	<0.1
Lu	<0.1	0.1	<0.1	<0.1	2.5	<0.1	1.3	<0.1	5.0	<0.1	<0.1	6.1	<0.1	<0.1	1.1	<0.1
∑REE		139.1			3742.6		550.2		4727.3			2577.8	155.6		702.2	28.4

Table 2: Field parameters and chemical composition of the water samples from several localities from the Odiel-Tinto rivers catchments

	DB	DB-neu	DB-mix	TO	TO-neu	TO-mix	RT	RT-neu	RT1-mix	RT2-mix	ET	ET-alc	ET1-mix	ET2-mix	ET3-mix
Sampling date	10/03/2015	10/03/2015	10/03/2015	01/02/2017	01/02/2017	01/02/2017	02/02/2017	02/02/2017	02/02/2017	02/02/2017	07 to 11/2008	2007-04/2008	29/09/2008	12/11/2008	22/10/2008
UTM X	662472.3	662366.4	665033.2	686048.1	685947.4	685977.8	710981.8	710948.8	709871.2	709871.2	704084.5	704166.2	704168.2	704166.2	704166.2
UTM Y	4156769	4156751.2	4155946.6	4162627.8	4162610.1	4162625	4143841.9	4143687.5	4142759.3	4142759.3	4181643.9	4181627.2	4181627.2	4181627.2	4181627.2
pH	2.58	6.54	4.54	2.44	6.12	5.14	2.62	6.44	5.5	5.63	2.6	6.1	4.9	4.6	5.1
EC (mS/cm)	6503	520	704	2465	261	269	1680	653	743	595	1760	1311	1403	1564	1633
Eh	629	102	369	493	216	393	397	74	240	66	397	213	283	320	301
temperature (ºC)	17.4	16.9	16.7	14.4	14.9	14.8	15.1	14	17.4	14.7	16.4	16.5			16.7
Alk (mg/L CaCO3)		130			50			225							
mg/L															
Al	742.00	0.0	6.2	350.14	0.1	3.8	136.88	0.30	12.4	10.2	149.7	0.2	22.0	18.0	5.7
Ca	123.42	39.0	33.8	200.01	15.7	17.6	50.69	100.90	95.6	96.8	181.4	692.0	482.0	522.0	643.0
Cu	78.13	0.5	1.7	9.99	0.0	0.1	25.09	0.01	2.5	1.8	24.6	0.1	11.2	12.0	3.7
Fe	490.07	0.0	0.2	128.81	0.0	1.3	503.40	0.30	40.3	34.4	1010.0	618.0	687.0	352.0	696.0
K	0.45	1.6	2.2	0.22	0.9	0.5	3.46	12.60	11.5	11.7	7.7	6.1	6.2	4.0	6.6
Mg	546.12	34.0	39.8	172.03	9.5	11.2	150.23	35.10	49.2	44.8	201.1	177.0	214.0	138.0	220.0
Mn	100.33	3.3	4.3	31.42	0.0	0.4	13.81	0.10	1.7	1.2	4.6	3.7	5.4	2.2	6.5
Na	16.22	41.0	36.5	5.60	14.7	14.2	27.54	72.30	67.9	69.1	41.23	20.60	28.0	22.0	29.0
SO4	8343.00	246.0	512.0	3681.18	39.3	283.3	2550.66	116.10	398.9	310.2	4010.1	2203.0	3563.0	2760.0	3735.0
Si	81.10	4.8	10.0	38.47	3.6	4.1	9.27	4.70	5.1	4.9	49.3	6.5	8.5	13.0	7.4
Zn	51.39	1.0	1.0	40.61	0.0	0.5	47.41	0.01	5.2	3.6	24.1	12.1	21.0	18.0	27.0
mg/L															
As	17.20	<0.1	<0.1	5.30	<0.1	<0.1	571.20	3.50	38.20	3.60	599.30				
Cd	249.80	0.60	8.20	52.00	<0.1	<0.1	142.00	<0.1	18.90	13.30	85.60				
Co	4867.00	9.50	35.20	415.10	<0.1	6.50	808.60	2.50	97.60	66.90	583.30				
Ni	2580.00	6.10	18.00	705.70	<0.1	11.20	147.90	<0.1	20.10	14.70	169.90				
Sc	97.20	<0.1	<0.1	21.90	<0.1	0.10	13.30	<0.1	0.10	0.10	23.80				
Y	268.60	<0.1	12.10	118.20	<0.1	2.00	87.30	<0.1	9.70	7.60	139.40				
La	185.40	<0.1	8.60	50.00	<0.1	<0.1	29.10	<0.1	3.40	2.70	56.90				
Ce	718.70	<0.1	25.30	139.90	<0.1	2.00	96.00	<0.1	10.50	8.60	169.60				
Pr	72.50	<0.1	2.70	18.20	<0.1	<0.1	13.70	<0.1	1.50	1.20	28.40				
Nd	340.50	<0.1	10.70	81.10	<0.1	1.20	63.10	<0.1	7.20	5.70	143.40				
Sm	82.90	<0.1	2.50	25.10	<0.1	<0.1	17.90	<0.1	2.00	1.60	36.80				
Eu	17.30	<0.1	<0.1	6.50	<0.1	<0.1	3.90	<0.1	<0.1	<0.1	7.00				
Gd	81.50	<0.1	3.00	29.20	<0.1	<0.1	19.40	<0.1	2.20	1.80	38.60				
Tb	10.30	<0.1	<0.1	4.90	<0.1	<0.1	3.10	<0.1	<0.1	<0.1	6.70				
Dy	57.90	<0.1	2.30	28.50	<0.1	<0.1	17.70	<0.1	2.00	1.70	40.30				
Ho	10.10	<0.1	<0.1	5.10	<0.1	<0.1	3.20	<0.1	<0.1	<0.1	7.30				
Er	32.20	<0.1	1.30	13.90	<0.1	<0.1	9.20	<0.1	1.10	<0.1	19.20				
Tm	3.90	<0.1	<0.1	1.80	<0.1	<0.1	1.20	<0.1	<0.1	<0.1	2.40				
Yb	27.20	<0.1	<0.1	11.30	<0.1	<0.1	7.40	<0.1	<0.1	<0.1	13.70				
Lu	3.80	<0.1	<0.1	1.50	<0.1	<0.1	1.00	<0.1	<0.1	<0.1	1.70				
∑REE	2010.0			556.9			386.2				735.2				

Table 3: Field parameters and chemical composition of the water samples from Arroyo del Val stream

	W-3	W-4	W-5	W-exp	W-6	W-8	W-9	W-11	W-12
Sampling date	1991	1991	1991	1996	1991	1991	1991	1991	1991
UTM X	654396.9		654345.6	654345.6	654190.8		654148.2	654055.6	653948.2
UTM Y	4556733.7		4556767.8	4556767.8	4557216.5		4557281.9	4557370.1	4557467.1
pH	3.32	7.45	4.55		3.90	7.02	4.58	4.39	4.72
EC (mS/cm)	539.00	570	465.00		518.00	315	453.00	449.00	428.00
Eh	839.00	322	672.00		731.00	498	614.00	721.00	685.00
temp ©	21.50	21.80	21.30		22.90	21.00	22.40	22.20	22.00
Alk (mg/L CaCO3)							11.59		
mg/L			4.50				3.70		1.20
Al	8.30	0.20	3.80		4.10	0.20	0.40	2.70	1.50
Ca	17.90	33.20	30.80		26.00	26.70	30.01	30.10	32.20
Cu	0.02	0.01	0.02		0.02	0.01	0.01	0.02	0.02
Fe	0.05	0.12	0.26		0.31	0.11	0.17	0.23	0.28
K	2.10	1.40	1.90		1.70	1.10	1.60	1.60	1.70
Mg	23.50	18.50	25.80		24.20	15.80	24.70	27.20	27.80
Mn	1.42	0.02	0.84		0.98	0.04	0.56	0.96	0.91
Na	10.00	10.00	10.00		10.10	8.00	9.00	11.00	11.00
SO4	221.00	72.00	209.00		199.00	69.00	174.00	209.00	208.00
Si	58.54	11.60	17.69		43.97	9.00	9.85	38.76	12.20
Zn	1.26	0.05	0.80		0.62	0.05	0.44	0.70	0.75
µg/L									
Sc									
Y	46.00		26.00		29.00		13.00	24.00	19.00
La	11.90		5.60	25.00	8.40		5.10	7.40	7.00
Ce	34.50		19.50	31.70	0.20		10.80	20.90	17.20
Pr	6.00		3.30	7.20	3.80		1.80	3.40	2.80
Nd	35.90		19.50	36.80	21.40		9.80	18.80	15.10
Sm	11.70		6.70	9.60	7.80		3.30	6.70	5.10
Eu	3.40		1.90	2.73	2.20		0.92	1.90	1.42
Gd	17.40		9.50	9.20	9.80		4.20	8.30	6.50
Tb	2.20		1.30	1.30	1.50		0.60	1.20	0.90
Dy	10.10		5.60	7.10	6.90		2.80	5.80	4.40
Ho	1.67		0.93	1.15	1.10		0.46	0.90	0.71
Er	3.90		2.40	2.30	2.50		1.00	2.00	1.50
Tm	0.48		0.29	0.22	0.30		0.12	0.30	0.20
Yb	2.40		1.40	1.10	1.60		0.60	1.30	1.00
Lu	0.30		0.20	0.20	2.30		<0.1	0.20	0.10
∑REE	187.85		104.12	135.60	98.80		54.50	103.10	82.93

Table 4: Chemical composition of the precipitates sampled from the Odiel-Tinto and Arroyo del Val area. SS accounts for basaluminite sorption sites.

	PO	AG	AG-r	DB	TO	RT	RT2	ET1	ET2	ET3	CV1	C5A	Cexp	C9	C12
wt %															
Al	13.65	27.52	1.24	20.94	25.76	11.45	14.05	27.48	27.63	28.28					
Fe	16.26	8.29	45.06	1.79	4.46	23.03	25.88	4.06	5.24	0.53					
S	3.41	5.49	5.77	4.56	7.51	2.24	2.66	7.53	7.27	6.81					
Si	0.670	1.330	0.010	0.120	1.100	0.170	0.170	0.621	0.652	0.814					
Al/S (molar)	4.75	5.94	0.26	5.44	4.07	6.06	6.26	4.32	4.51	4.92					
Fe/S (molar)	2.73	0.87	4.47	0.22	0.34	5.89	5.58	0.31	0.41	0.04					
(Al+Fe)/S	7.48	6.81	4.73	5.66	4.41	11.95	11.84	4.63	4.92	4.97					
Al/Si	21.12	21.46		180.93	24.29	69.85	85.71	45.88	43.95	36.02					
mg/kg															
Sc	12.9	24.2	<0.4	7.9	44.5	16.3	22.3	24.7	29.1	22.5					
Y	130.2	75.1	3.6	25.4	125.7	71.7	87.3	331.6	597.3	300.7					
La	82.7	21.3	8.0	8.3	28.8	24.5	24.4	67.7	123.7	58.6	10.40	5.98	7.30	9.60	5.40
Ce	274.8	103.1	17.9	48.2	100.7	73.4	84.1	286.9	493.3	252.8	41.50	22.50	16.60	32.30	14.60
Pr	31.9	13.1	2.1	5.7	16.2	11.2	13.4	49.4	85.5	43.8	7.70	4.20	2.60	6.30	2.30
Nd	145.9	66.0	9.2	27.4	80.7	52.9	64.4	263.8	449.7	231.9	48.60	23.50	15.10	35.50	11.50
Sm	39.8	21.5	1.8	7.7	28.9	15.3	19.5	79.0	127.1	70.0	19.30	11.50	7.00	17.20	5.10
Eu	6.0	4.6	<0.4	1.8	7.8	3.2	4.1	15.6	25.2	13.7	5.83	3.07	2.00	4.97	1.44
Gd	39.0	26.6	1.5	7.3	34.6	16.9	21.1	80.5	136.1	71.1	27.60	11.80	5.60	18.90	5.54
Tb	6.6	3.8	<0.4	1.2	6.0	2.6	3.3	15.1	24.7	13.4	4.00	2.00	0.90	3.30	1.00
Dy	38.2	22.4	1.0	7.1	34.9	14.4	18.4	97.6	159.0	86.3	19.90	10.30	6.60	16.40	5.90
Ho	6.3	3.9	<0.4	1.3	6.4	2.7	3.4	17.0	27.8	15.1	3.06	1.54	1.33	2.59	0.94
Er	15.4	10.3	<0.4	3.5	17.5	7.6	9.6	45.0	72.0	39.7	7.20	3.80	2.30	6.00	2.30
Tm	2.0	1.5	<0.4	<0.4	2.0	1.0	1.3	6.1	9.3	5.4	0.95	0.55	0.34	0.84	0.37
Yb	13.1	10.7	<0.4	3.8	14.0	5.9	7.7	39.1	56.6	34.5	5.20	3.30	2.20	4.90	2.40
Lu	1.6	1.4	<0.4	<0.4	1.5	0.8	1.1	4.5	6.5	4.0	0.60	0.40	0.30	0.70	0.30
basaluminite (g/L)	0.737	2.595		3.162	1.488	0.535	0.544	0.549	0.566	0.619	0.019	0.019	0.019	0.016	0.011
SSA (m^2/g)	31	20		23	32	16	16	57	57	57	68	68	68	68	
T_{XOH} (mol(/kgw)	3.826E-04	1.348E-03		1.643E-03	7.731E-04	2.779E-04	2.828E-04	2.851E-04	2.940E-04	3.215E-04	1.005E-05	1.005E-05	1.005E-05	8.259E-06	5.804E-06

Table 5. Effect of the parameter variation in the f factor to fit the fractionation patterns.

ET1	BET (m2/g)	SL (g/L)	pH	f
benchmarck	57	0.55	6.7	0.46
ΔpH	57	0.55	6.5	0.46*1.54
	57	0.55	6.9	0.46*0.64
ΔBET	BET*0.5	0.55	6.7	0.46*1.98
	BET*2	0.55	6.7	0.46*0.49
ΔSL	57	SL*0.5	6.7	0.46*1.98
	57	SL*2	6.7	0.46*0.49

GEOCHEMICAL BEHAVIOR OF RARE EARTH ELEMENTS IN ACID DRAINAGES: MODELING ACHIEVEMENTS AND LIMITATIONS

Annex

Table S1. Aqueous speciation constants for Sc, Y and lanthanides (M) with different ligands (L). References: a: Klugness & Byrne, 2000 ; b: Lee & Byrne, 92; c: Luo & Byrne, 2004;d: Millero, 92; e: Luo & Millero, 2004; f: Schijf & Byrne, 2004; g: Luo & Byrne,2001; h: Wood and Samson, 2006 (for Sc speciation).

Reaction	$\log {}_L\beta_n$	Sc	Y	La	Ce	Pr	Nd	Sm	Eu	Gd	Tb	Dy	Ho	Er	Tm	Yb	Lu	Ref
$M^{+3} + H_2O = M(OH)^{+2} + H$	$\log {}_{OH}\beta^*_1$	-4.31	-7.8	-8.81	-8.34	-8.32	-8.18	-7.84	-7.76	-7.83	-7.64	-7.59	-7.56	-7.52	-7.39	-7.45	-7.27	a
$M^{+3} + 2H_2O = M(OH)_2^{+} + 2$	$\log {}_{OH}\beta^*_2$	-9.7	-16.4	-18.14	-17.6	-17.27	-17.04	-16.51	-16.37	-16.37	-16.18	-16.1	-16.07	-15.96	-15.88	-15.74	-15.67	b, h
$M^{+3} + 3H_2O = M(OH)_3 + 3$	$\log {}_{OH}\beta^*_3$	-16.1	-25.99	-27.9	-27.23	-26.63	-26.4	-25.91	-25.41	-25.28	-25.08	-24.83	-24.56	-24.35	-24.18	-23.85	-23.85	b, h
$M^{+3} + CO_3^{-2} = MCO_3^{+}$	$\log {}_{CO3}\beta_1$	-	7.48	6.73	7.06	7.23	7.28	7.46	7.48	7.39	7.46	7.56	7.55	7.61	7.68	7.81	7.75	c
$M^{+3} + HCO_3^{-} = MHCO_3^{+3}$	$\log {}_{HCO3}\beta_1$	-	2.32	2.34	2.31	2.25	2.28	2.34	2.47	2.36	2.46	2.5	2.46	2.49	2.52	2.53	2.49	c
$M^{+3} + 2CO_3^{-2} = M(CO3)_2^{-}$	$\log {}_{CO3}\beta_2$	-	12.63	11.3	11.76	12.08	12.17	12.53	12.63	12.48	12.78	12.91	13	13.12	13.27	13.3	13.37	c
$Ln^{+3} + NO_3^{-} = LnNO_3^{+2}$	$\log {}_{NO3}\beta_1$	-	-	0.58	0.69	0.69	0.79	0.78	0.83	0.47	0.51	0.15	0.25	0.15	0.2	0.25	0.56	d
$M^{+3} + F^{-} = MF^{+2}$	$\log {}_F\beta_1$	-	3.97	3.11	3.29	3.35	3.29	3.61	3.72	3.71	3.83	3.88	3.78	3.77	3.77	3.84	3.74	e
$M^{+3} + 2F^{-} = MF_2^{+}$	$\log {}_F\beta_2$	-	6.35	5.16	5.48	5.66	5.66	5.99	6.11	6.07	6.24	6.29	5.98	5.96	6.09	6.31	6.31	e
$Ln^{+3} + SO_4^{-2} = LnSO_4^{+}$	$\log {}_{so4}\beta_1$	4.18	3.5	3.61	3.61	3.62	3.6	3.63	3.64	3.61	3.59	3.57	3.54	3.51	3.48	3.46	3.44	f,h
$M^{+3} + Cl^{-} = MCl^{+2}$	$\log {}_{Cl}\beta_1$	-	0.65	0.65	0.65	0.65	0.65	0.65	0.65	0.65	0.65	0.65	0.65	0.65	0.65	0.65	0.65	g

Table S2. Equilibrium constants for the REE surface complexation reactions onto basaluminite (Lozano et al., 2019a).

Element	Surface Complex	Log K
Sc	$(XO)_2ScSO_4^-$	-5.19
	$XOSc(OH)_2$	-5.81
Y	$XOYSO_4$	-2.48
La	$XOLaSO_4$	-2.95
Ce	$XOCeSO_4$	-2.81
Pr	$XOPrSO_4$	-2.69
Nd	$XONdSO_4$	-2.60
Sm	$XOSmSO_4$	-2.48
Eu	$XOEuSO_4$	-2.50
Gd	$XOGdSO_4$	-2.50
Tb	$XOTbSO_4$	-2.48
Dy	$XODySO_4$	-2.37
Ho	$XOHoSO_4$	-2.40
Er	$XOErSO_4$	-2.40
Tm	$XOTmSO_4$	-2.27
Yb	$XOYbSO_4$	-2.13
Lu	$XOLuSO_4$	-2.19